Turbulent boundary layers perturbed by an array of cylinders

A DISSERTATION
SUBMITTED TO THE FACULTY OF
UNIVERSITY OF MINNESOTA
BY

Yan Ming Tan

IN PARTIAL FULFILLMENT OF THE REQUIREMENTS
FOR THE DEGREE OF
DOCTOR OF PHILOSOPHY

Ellen K. Longmire, Adviser

September 2017

Acknowledgements

I am lucky for being able to meet and work with many exceptional individuals during the course of this work. First, I would like to thank my adviser, Prof. Ellen Longmire for her expert guidance and unwavering patience throughout this work. Her passion and dedication to scientific work has had a huge impact on my professional development. Furthermore, her mentorship made me a better problem solver and substantially improved my verbal and written communication skills. I consider myself privileged to have been able to work with her.

I would also like to thank my committee members and reviewers – Professor Krishnan Mahesh, Professor Joseph Nichols, and Professor Michele Guala for lending me their expertise by providing helpful feedback for this work. In fact, Professor Krishnan Mahesh's Aerodynamics course in my undergraduate years inspired me to specialize in fluid mechanics. Professor Joseph Nichols enthusiasm and willingness to share his immense theoretical knowledge helped me improve my understanding of fluid mechanics. Professor Michele Guala's experiences in conducting field measurements and various experiments inspired me to be a better experimenter.

I also want to thank Mitchell Ryan for teaching me how to conduct hot-wire anemometry experiments in the wind-tunnel which resulted in my master's work. In addition, I want to also thank Dr. Shaokai Zheng who taught me how to maintain and run the water channel facility. Furthermore, he was also instrumental in teaching me the art of stereoscopic particle image velocimetry measurements. I want to thank Dave Hultman for helping us fix the water channel when it broke down. That was a challenging time and we were

fortunate to have had Dave's help. I also want to thank Kale Hedstrom for all his help in resolving hardware issues and providing great ideas whenever we need advice.

I am grateful to Dr. Wing Lai, Dr. Daniel Troolin, Dr. Matt Stegmeir and Dr. Aaron Boomsma from TSI Inc USA for lending us their state of the art 3-D volumetric PTV system, and for their support and discussion regarding the 3-D PTV measurements and analysis.

I want to also thank all lab and work mates for their mentorship, camaraderie and help over the years: Dr. Deepak Adhikari, Dr. Omid Amili, Dr. Diogo Barros, Dr. Ankur Bordoloi, Dr. Anwar Chengala, Dr. Pietro Ferrero, Dr. Andras Nemes, Dr. Zhengzhong Sun, Dr. Mostafa Toloui, Dr. Kyle Winters, Alonso Alvarado, Luci Baker, Kee Onn Fong, Sahar Jalal, Anand Kartha, Daniel Krizan, Jeshwanth Kundem, Yixuan Li, Tristan van de Moortele, Alec Petersen and Yi Hui Tee. I am grateful that I met all of you. The moments that we share will be cherished for many years to come.

I am extremely grateful to my partner, Lavynnia Low, for her patience, support and encouragement when things seemed impossible.

Last but not least, I want to thank my family, especially my parents and late grandparents for never giving up on me. I would never be writing this now if it were not for their sacrifices to ensure access to education for me and my sister. Their strong emphasis on the importance of education resulted in me having the opportunity to complete this work. I want to also thank my younger sister for her tireless work ethic that led her to achieve many extraordinary feats. She will always be an inspiration to me.

Dedication

To my parents, late grandparents and sister for their tremendous support, encouragement and love over all the years.

Abstract

Turbulent boundary layers (Re_τ = 2500) were perturbed by a spanwise array of cylinders, and the effects on the large-scale flow organization within the logarithmic layer were investigated. Boundary layer and vortex packet recovery trends were quantified downstream of several arrays. Two array spacings, each with two cylinder heights were considered. For S = 0.2δ arrays, cylinder heights of H = 0.2δ (H^+ = 500, aspect ratio, AR = 4) and H = δ (H^+ = 2500, AR = 20) were investigated. For the S = 0.6δ arrays, cylinder heights were H = 0.2δ and H = 0.05δ (H^+ = 125, AR = 1).

Stereoscopic and planar PIV measurements were acquired in both fixed and flying configurations at three measurement heights across the logarithmic layer, z^+ = 125, 300 and 500. Furthermore, 3-D PTV volumes were acquired downstream of the S= 0.2δ arrays over a depth of $155 < z^+ < 465$. Results of time-averaged velocity statistics, instantaneous velocity fields and structural analyses of low and high uniform streamwise momentum zones were discussed. In addition, a vortex packet identification algorithm (VPIA) was developed to quantify relaxation trends of individual packet signatures in the flow downstream of the arrays.

All of the arrays affected mean and RMS streamwise velocities averaged across the span downstream, due to the blockage posed to the oncoming flow. Undulating wakes due to Karman shedding occurred behind the cylinders, while the average wake structure at the cylinder tips suggested formation of streamwise aligned tip vortices.

For the S = 0.2δ array, relaxation trends differed for the two cylinder heights, H = 0.2δ and H = δ. Downstream of the H = δ array, instantaneous PIV and VPIA results showed a bottom-up mechanism for the recovery of the large-scale flow organization. Flow features recovered first closer to the wall (z^+ = 125), then later at z^+ = 300, while hardly any recovery was seen at z^+ = 500 up to 7δ downstream of the array, the furthest measurement location. In contrast, some indications of top-down recovery were observed for the flow perturbed by the shorter H = 0.2δ array. In this case, however, flow features and packets closer to the wall at z^+ = 125 remained altered up to 7δ downstream, even though streamwise velocity statistics relaxed substantially to the unperturbed values. The difference in recovery trends between the two cylinder heights was related to weaker and stronger outer-inner interactions respectively, relative to the unperturbed flow.

For the S = 0.6δ arrays, perturbations to mean and RMS velocity statistics were weaker than for the S = 0.2δ arrays as blockage was reduced substantially. Nevertheless, the flow downstream of the S = 0.6δ, H = 0.2δ array was profoundly affected, such that the energy contained in the 0.6δ spanwise wavelength was increased throughout the logarithmic layer over a distance of 7δ. The energy increase was related to the array preferentially re-aligning incoming high and low uniform momentum zones to spanwise locations corresponding to cylinder locations and the regions between them respectively. The re-alignment effects were stronger for low and high momentum zones that were longer than 0.5δ. The H = 0.05δ case also showed similar but much weaker trends.

Table of Contents

List of Tables

List of Figures

Nomenclature

+	Superscript represents normalization using inner variables
‾	Over bar denotes average

Abbreviations

TBL	turbulent boundary layer
PIV	particle image velocimetry
PTV	particle tracking velocimetry
PPIV	planar particle image velocimetry
SPIV	stereoscopic particle image velocimetry
FPIV	flying particle image velocimetry
FOV	field of view
BNC	berkeley Nucleonics
RMS	root mean square
VPIA	vortex packet identification algorithm
CMR	coherent momentum region
LMR	low momentum region
HMR	high momentum region
ACR	auto-calibration reconstruction
Q2	quadrant two event, ejection
Q4	quadrant four event, sweep

Greek symbols

δ	unperturbed turbulent boundary layer thickness
θ	momentum thickness
ν	kinematic viscosity of fluid
α	angle between camera central line of sight and z-axis
κ	von Karman constant

χ chi square distribution value

σ standard deviation of dataset

γ number of degrees of freedom for Chi squared distribution

β level of significance

ζ Random uncertainty parameter

λ_{ci} Swirl strength

λ_y Spanwise wavelength

λ_x Streamwise wavelength

Roman symbols

x streamwise coordinate

y spanwise coordinate

z wall-normal coordinate

z^+ wall-normal coordinate normalized by inner units

Δz wall-normal separation between cross-correlated planes

$\bar{U}$ streamwise time averaged mean velocity

$\bar{V}$ spanwise time averaged velocity

$\bar{W}$ wall-normal time averaged velocity

U streamwise velocity

V spanwise velocity

W wall-normal velocity

u streamwise fluctuating velocity

v spanwise fluctuating velocity

w wall-normal fluctuating velocity

u_{rms} streamwise RMS velocity

v_{rms} spanwise RMS velocity

w_{rms} wall-normal RMS velocity

$\delta\bar{U}$	averaged streamwise velocity uncertainty
$\delta\bar{V}$	averaged spanwise velocity uncertainty
$\delta\bar{W}$	averaged wall-normal velocity uncertainty
δu_{rms}	streamwise RMS velocity uncertainty
δv_{rms}	streamwise RMS velocity uncertainty
δw_{rms}	streamwise RMS velocity uncertainty
δu	instantaneous streamwise velocity uncertainty
δv	instantaneous spanwise velocity uncertainty
δw	instantaneous wall-normal velocity uncertainty
P_0	systematic uncertainty of PIV measurement
P_u	systematic uncertainty for streamwise velocity
P_v	systematic uncertainty for spanwise velocity
P_w	systematic uncertainty for wall-normal velocity
U_τ	friction velocity
U_∞	freestream velocity
Re_τ	Reynolds number, wall units
Re_θ	Reynolds number based on momentum thickness
D	cylinder diameter
H	obstacle/Cylinder height
S	cylinder array spacing
AR_c	aspect ratio of cylinders
Δt	time between laser pulses
Δt_d	Q-switch delay time
L_v	vector spacing
N	number of realizations
k	wave number
k_y	spanwise wave number

E_{uu} streamwise energy spectrum

R_{uu} streamwise velocity correlation coefficient

R_{ww} wall-normal velocity correlation coefficient

k_{max} maximum resolvable wave number

k_{min} minimum resolvable wave number

$N_{p/f}$ number of packets per field

$N_{s/L}$ number of swirls per length

$N_{s+/s-}$ number of positive to negative swirls ratio

L_{sk} length based on skeleton of packet signature

W_{sk} width based on skeleton of packet signature

L_{ex} length based on extrema of packet signature in streamwise direction

W_{ex} width based on extrema of packet signature in spanwise direction

W_m mean width

S_c convex solidity

N_h number of enclosed holes

A_h area of holes

AR aspect ratio of packet signatures

R_{AB} correlation coefficient

C log law intercept

Chapter 1

Introduction

1.1 Motivation

For any object moving within a fluid, significant energy is expended to overcome retarding drag forces. For streamlined bodies, the dominant portion of the drag is produced within turbulent boundary layers (TBLs), which is the thin chaotic layer of fluid adjacent to the solid boundary. Within a TBL, the average fluid velocity changes drastically from near zero up to the body speed over a short distance normal to the body surface. The thickness of a TBL on a modern airliner wing is only a few centimeters, while the change in average velocity across the layer is hundreds of meters per second. Evidently, tremendous shearing forces must be present in this region, giving rise to large skin friction drag forces associated with severe losses and inefficiencies in many applications. For example, skin friction drag can contribute up to 50% of the total drag on a modern aircraft, 70% on large ships, and up to 90% on oil pipelines and submarines. Thus, any fuel savings using drag reduction strategies derived from fundamental understanding of turbulent boundary layers will have a huge impact on the economics of present day transportation.

Over the last two decades, it has become apparent that the motions in the TBL are not completely chaotic, but instead contain coherent eddies organized into recurring patterns. These coherent eddies or vortices (swirling regions of fluid) are frequently shaped like hairpins, and are often organized into groups termed hairpin packets (Adrian, Meinhart &

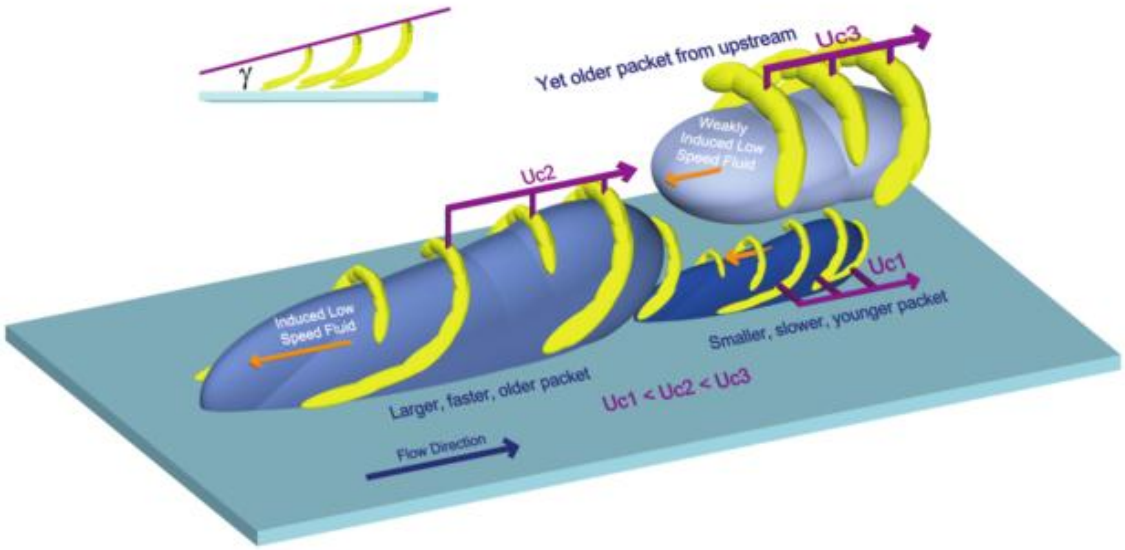

Figure 1-1: Conceptual sketch of multiple hairpin packets in a turbulent boundary layer. Reproduced from Adrian, Meinhart & Tomkins (2000).

Tomkins 2000). A hairpin packet (see Figure 1-1) includes multiple hairpin vortices aligned in the dominant flow direction, moving at approximately the same velocity. These packets are of interest because they are thought to contribute substantially to the production of drag (Ganapathisubramani *et al.* 2003). Hence, it may be possible to alter these packet structures to achieve drag reduction.

This study attempts to exploit present understanding of large-scale organization of eddies to alter turbulent boundary layer behavior. Previously, Zheng and Longmire (2014) successfully perturbed vortex packets in the logarithmic region using a spanwise array of wall-mounted cylinders, and documented the effects using PIV at a single measurement height. The spanwise spacing between cylinders was chosen to either disrupt the natural packet modes (preferred spanwise spacing between adjacent vortex packets) and

therefore weaken the packet structures, or to enhance the natural modes and reinforce the packet structures. Key findings show packet signatures disrupted by a narrowly spaced array reappear shortly downstream. Conversely, the array spaced at the natural packet mode reinforced incoming packet signatures downstream, such that they persist with less spanwise meandering to the end of the measurement domain. Many questions remain, e.g., how do packet signatures reappear so quickly after being strongly disrupted? How and why do packets get reinforced downstream of the wider spaced array? Specifically, how do these effects vary throughout the logarithmic region, since the previous findings were documented only at a single measurement height. Therefore, an experimental investigation is carried out in a turbulent boundary layer perturbed by an array of cylinders using combinations of planar and stereoscopic particle image velocimetry (PIV) at three wall-parallel measurement planes. Furthermore, three-dimensional particle tracking velocimetry (PTV) measurements in a volume were conducted to evaluate flow structure connectivity across the logarithmic layer, downstream of the perturbation.

1.2 Previous work

In this section, previous work relevant to the study of turbulent boundary layers and the effects of both small and large-scale perturbations on turbulent boundary layers is reviewed. Section 1.2.1 reviews studies of unperturbed turbulent boundary layers, while section 1.2.2 highlights previous studies on feature extraction algorithms applied to boundary layer data. This is followed by section 1.2.3 covering studies on perturbations to turbulent boundary layers. Section 1.2.4 will highlight studies on boundary layer recovery from perturbations, followed by the objectives of the present dissertation in section 1.3.

The co-ordinate system used in this dissertation is as follows: The streamwise direction is along the x-axis, the spanwise is y and the wall-normal direction is along the z axis. The velocity components U, V, and W correspond to the streamwise, spanwise and wall-normal velocity components respectively. Quantities normalized by inner variables in the present dissertation are denoted by a superscript '+'. The normalization is computed based on kinematic viscosity of fluid, ν and the skin friction velocity $U_\tau = (\tau_w/\rho)^{1/2}$, where τ_w is the wall shear stress, and ρ is the density of the fluid. The turbulent boundary layer thickness is δ, and when normalized by inner units $\delta^+ = \delta U_\tau/\nu$ is known as the friction Reynolds number represented by Re_τ.

1.2.1 Turbulent boundary layers

The no-slip condition necessitates the formation of a boundary layer, where the velocity varies from zero to the bulk velocity over a thin transition layer. The canonical example of a boundary layer is the flow over a flat plate, where the boundary layer initiates at the leading edge. The thickness of the initially laminar boundary layer grows along the streamwise direction. After some distance downstream of the leading edge, the boundary layer undergoes transition due to instabilities, resulting in a turbulent boundary layer (see Figure 1-2). The present study considers only turbulent boundary layers.

The turbulent boundary layer can be subdivided into several regions, based on the relative magnitudes of the viscous and turbulent stresses. The viscous stresses are significant in the near wall region, defined as $z^+ < 30$. The mean streamwise velocity profile varies linearly in the viscous sublayer ($0 < z^+ < 5$) where viscous processes dominate over inertial effects. On the other hand, the maximum of the turbulent kinetic energy production occurs within the buffer layer ($5 < z^+ < 30$).

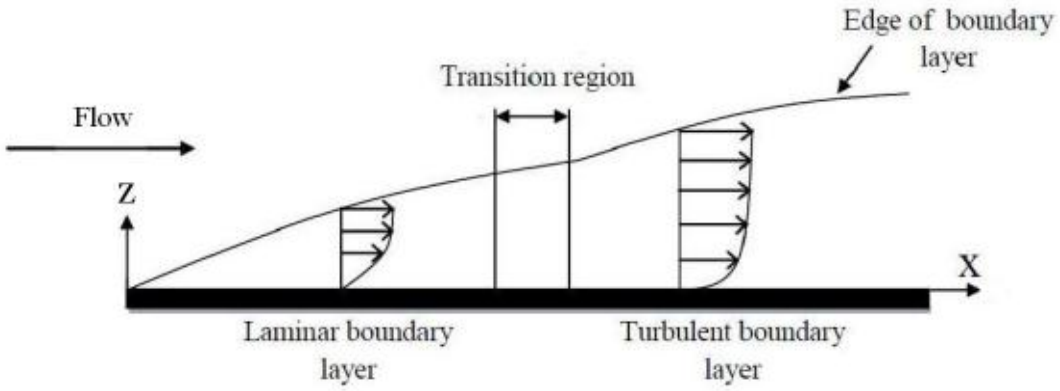

Figure 1-2: Evolution of the mean stream-wise velocity profile of a boundary layer over a flat plate. Reproduced from Gao (2011).

The region $30 < z^+ < 0.2\delta$ is defined as the logarithmic region, where the turbulent or Reynolds stresses dominate relative to the viscous stresses, and where production approximately equals dissipation. The mean velocity profile here follows a logarithmic law defined as $\bar{U}^+ = (1/\kappa) \ln z^+ + C$, where the von Karman constant κ is typically taken to be 0.41, and the intercept C to be 5.1 (Pope 2000). This dissertation focuses on the effects of perturbations within the logarithmic layer. This area is of interest to many researchers in boundary layer flows, as the velocity profiles within this layer collapse for different Reynolds numbers, suggesting the existence of a single universal logarithmic curve. Therefore, turbulent motions within the logarithmic layer can be similar for different Reynolds numbers; hence results from studying the logarithmic layer in a boundary layer with a specific Reynolds number may be generalized to other Reynolds numbers, ultimately making the boundary layer problem more tractable. Beyond the logarithmic region lies the wake region ($0.2\delta < z < \delta$), where the changes in mean streamwise velocity are more gradual in contrast to the other regions.

1.2.1.1 Coherent structures

Turbulence is historically associated with chaotic changes in flow quantities where analytical solutions are possible only in the simplest flow geometries and limited to low Reynolds numbers. Many flows in engineering applications have high Reynolds numbers, implying orders of magnitude separation between the largest and the smallest scales in the flow, posing significant challenges to modeling and simulations. For boundary layers, this problem may be tackled by representing the boundary layer with a hierarchy of characteristic coherent structures (Townsend 1976).

Over the past few decades, significant evidence has emerged confirming the existence of recurring patterns in wall-bounded flows, in what researchers in the field refer to as coherent structures. Structures can be deemed coherent when they persist spatially for a reasonable period of time (long enough to be qualitatively recognized by the human eye) whilst contributing significantly to the time averaged statistics of the flow (Adrian 2007). Some of the first important coherent structures identified were alternating high and low-speed streaks within the near wall region ($z^+ < 30$) of the TBL spaced at 100 wall units (Hama 1957; Kline *et al.* 1967; Corino & Brodkey 1967). The streaks were associated with Q2 (ejection, $u < 0$, $w > 0$) and Q4 (sweep, $u > 0$, $w < 0$) events and were shown to be major contributors to the Reynolds stresses in the near-wall region (Wallace, Eckelmann & Brodkey 1972). The Q2/Q4 events were attributed to quasi streamwise vortices lifting viscously retarded fluid upwards from the inner region (Bogard & Tiederman 1986; Robinson 1989). Readers who wish to dive deep into the history of coherent structure research are strongly encouraged to read the excellent review on numerous coherent structure studies up till 1990 by Robinson (1991). A graphic by

Robinson (1991) reproduced in Figure 1-3 illustrates the types of coherent structures corresponding to the different regions in wall bounded flows. The schematic shows the prevalence of quasi stream-wise structures close to the wall, a mixture of quasi stream-wise vortices and arch-like structures in the log region, and the dominance of arch like structures in the wake region.

1.2.1.2 Hairpin vortices

In 1952, Theodorsen proposed the model of a hairpin/horseshoe vortex as a representative structure in boundary layers (Figure 1-4). The parts that make up the hairpin vortex have been referred to as the legs, neck and head regions (Figure 1-4b). The legs correspond to quasi-streamwise vortices near the wall, and the head consists of a compact region of spanwise vorticity or swirling motions, located furthest away from the wall. The head is connected to the legs through the necks inclined at ~ 45° to the wall.

The first observation of hairpin vortices was reported in visualization experiments performed by Offen & Kline (1975), then Falco (1977), followed by the monumental visualizations by Head and Bandyopadhyay (1981) showing the prevalence of hairpin shaped structures over a range of $500 < Re_\theta < 17{,}500$ in the logarithmic and outer parts of a canonical turbulent boundary layer. Here, θ is the momentum thickness. In their high Re visualizations, elongated hairpin vortices with origin at the wall frequently extended through most of the boundary layer thickness, δ. The observed hairpins were mostly inclined with respect to the wall with angles 40 - 50°. Furthermore, the authors noted that individual hairpins could group together to form longer coherent structures with characteristic interfaces at an angle of 20° relative to the wall (Figure 1-5).

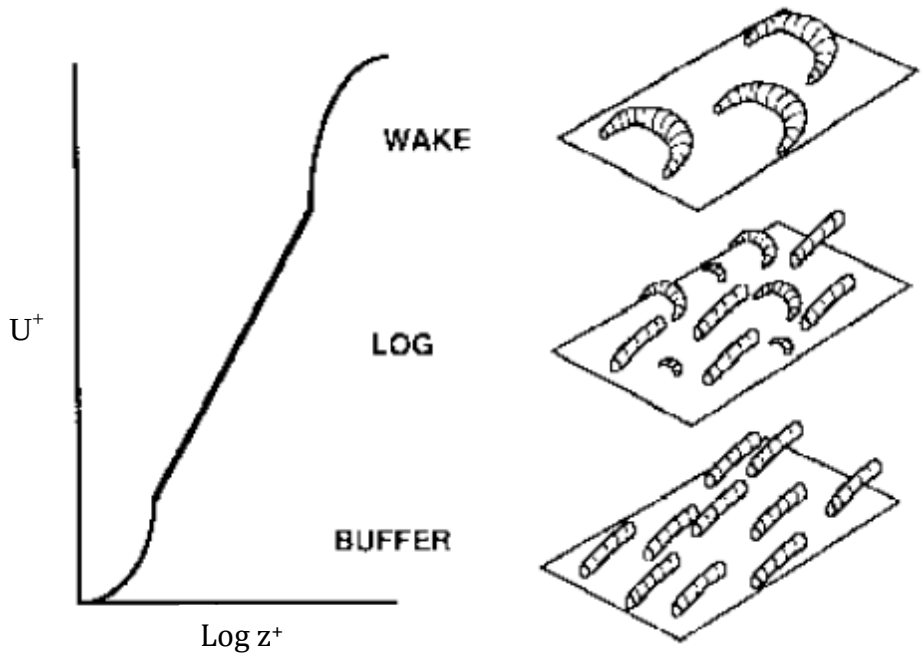

Figure 1-3: Schematic of vortical structures in different regions of the turbulent boundary layer. Reproduced from Robinson (1991).

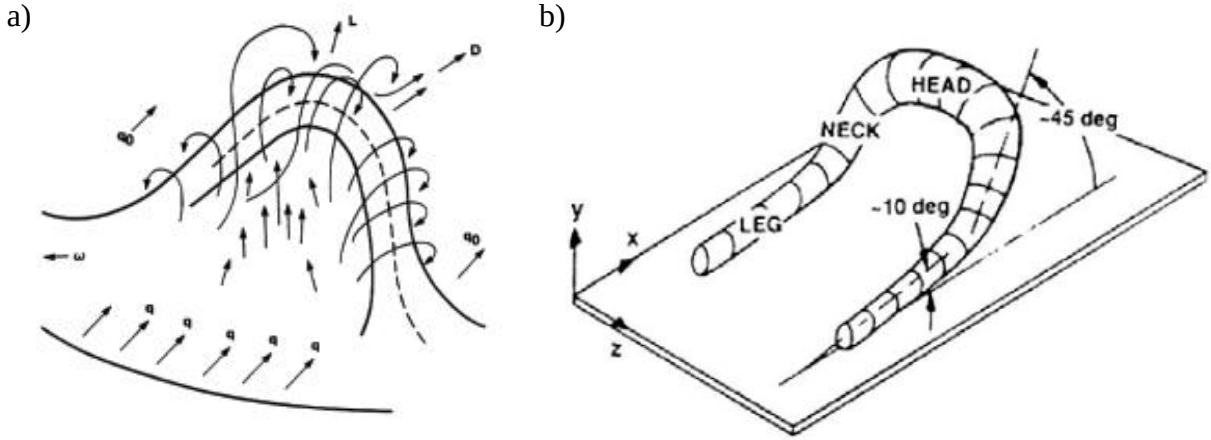

Figure 1-4: a) Theodorsen's (1952) illustration of a hairpin/horseshoe vortex and b) nomenclature. Reproduced from Robinson (1991).

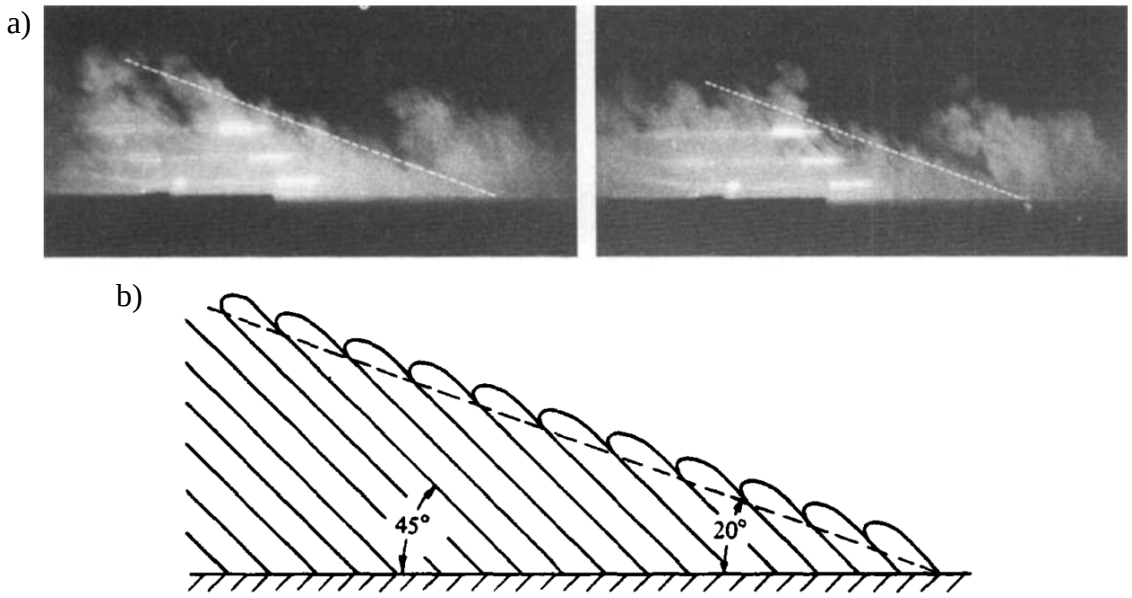

Figure 1-5: Example of visualizations showing inclined hairpin structures grouping together resulting in an interface inclined ~20° relative to the wall. Flow is from right to left. a) Visualization results at Re_θ = 17500. b) Schematic of inclined structures and interface. Reproduced from Head & Bandyopadhay (1981).

Since then, the hairpin vortex has played a significant role in explaining many of the features observed in wall turbulence. An idealized hairpin vortex signature is shown in Figure 1-6. Notable features include the ejection event (Q2) roughly perpendicular to the inclined plane containing the head and neck of the hairpin, the Q4/Q2 stagnation point, and the low-speed region close to the wall. In many experiments and computational studies, the observed hairpins are rarely symmetric, often manifesting as one-sided arches or 'cane' like vortices (Smith *et al.* 1991; Robinson 1991). In this dissertation, the term hairpin will be used to denote arch, horseshoe, and cane vortices as they are believed to be variations of the same basic structure (Adrian, Meinhart, Tomkins 2000).

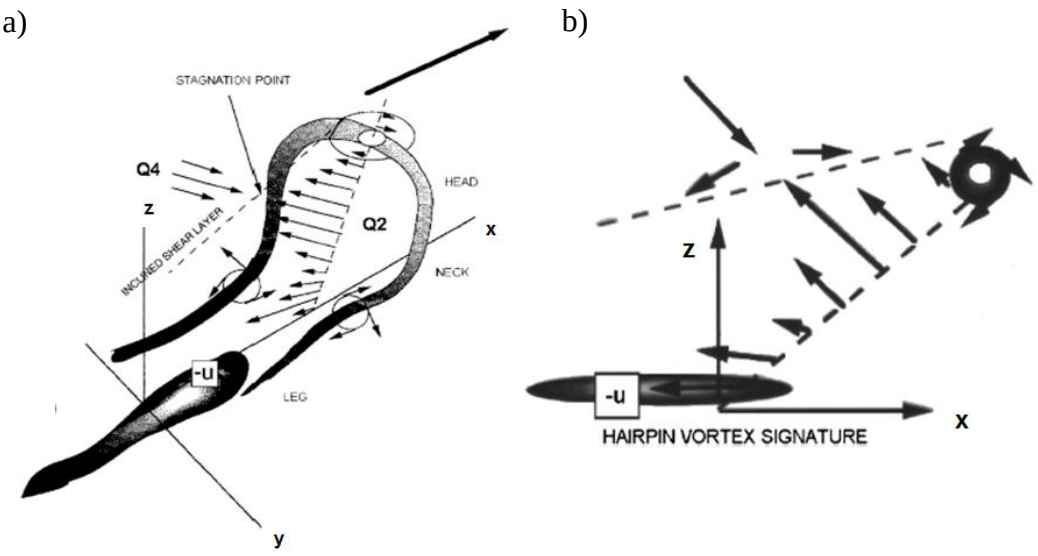

Figure 1-6: a) Schematic of idealized hairpin eddy attached to the wall; b) signature of hairpin eddy in the stream-wise wall normal plane. Reproduced from AMT (2000).

1.2.1.3 Hairpin packets

Most importantly, 5-10 hairpin vortices sharing a common convection velocity can form streamwise aligned groups in what is referred to now as hairpin packets. These packets were frequently observed in the landmark PIV measurements of wall-normal planes by Adrian, Meinhart & Tomkins (AMT) (2000) in canonical turbulent boundary layers (355 < Re_τ < 1490). The hairpins within a packet appeared as compact regions of vorticity associated with circular streamlines (when U_c, convection velocity is subtracted), located above and downstream of strong ejection events (see Figure 1-7). These signatures were abundant in the logarithmic and outer regions. Furthermore, the authors noted that individual packets grew upwards in the streamwise direction with a mean angle of approximately 12° relative to the wall, extending up to ~1.4δ in the streamwise direction. Hairpin packets also populated supersonic turbulent boundary layers (Re_τ = 7080) as seen in Tomographic PIV measurements of Elsinga *et al.* (2010) over a depth of 0.15 < z/δ <

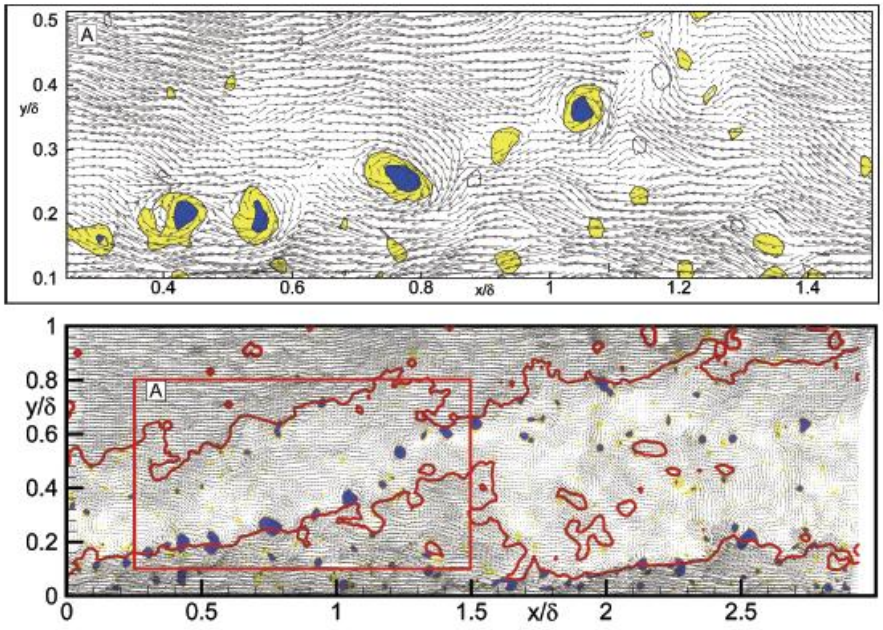

Figure 1-7: Example of hairpin vortex packets at Re_θ = 7705, red solid lines show contours of constant streamwise velocity at 70% and 94% of the free-stream velocity. Filled closed contours denote regions of swirling and can be associated with the heads of hairpin vortices. Both velocity fields subjected to Galilean decomposition where a constant convection velocity, U_c is subtracted. Reproduced from Adrian (2007).

0.47. Comparisons between the hairpin vortices of packets in subsonic flow versus supersonic flow indicate shape and size similarities between the two, suggesting universality of these structures. Aspects of hairpin packet organization and dynamics have since been investigated in many additional experimental studies (e.g. Dennis & Nickels 2011; Schröder *et al.* 2007; Wu & Christensen 2006; Gao *et al.* 2011; Gao *et al.* 2013; Elsinga *et al.* 2007; Elsinga *et al.* 2010; Ganapathisubramani *et al.* 2003; Christensen & Adrian 2001; Tomkins & Adrian 2003; Jodai & Elsinga 2017).

Hairpin packets make significant contributions to time averaged statistics of wall turbulence. Linear stochastic estimates conditioned on a strong swirling event yielded results that were consistent with hairpin packets in both x-y and x-z planes (Christensen

& Adrian 2001; Ganapathisubramani *et al.* 2005; Wu & Christensen 2006; Hambleton *et al.* 2006). Moreover, Ganapathisubramani *et al.* (2003) showed that hairpin packets carried up to 25% of the Reynolds shear stress despite occupying less than 4% of the total area in x-z stereoscopic PIV (SPIV) measurement planes of a canonical turbulent boundary layer (Re_τ = 1060). This is consistent with the hypothesis of AMT (2000) stating that multiple hairpins within a packet can create additional stresses through cooperative transfer of momentum between the individual hairpins, leading to long low speed zones.

The formation of hairpin vortices from quasi streamwise vortices, in addition to generation of additional hairpin vortices by pre-existing hairpin vortices (i.e auto-generation) were conjectured as a possible mechanism for hairpin packet formation (Zhou *et al.* 1996 & 1999; AMT 2000). This conjecture was based on results from experiments (Acarlar & Smith 1987; Smith *et al.* 1991) and computational (Zhou *et al.* 1996 & 1999) studies. Acarlar & Smith (1987) and Smith *et al.* (1991) showed additional hairpins generated from a strong initial hairpin like vortex in laminar boundary layers through visualization studies. This phenomenon was also observed in direct numerical simulations of a channel with a mean turbulent field by Zhou *et al.* (1996 & 1999). The auto-generation process persisted in a channel with a turbulent mean profile subjected to high levels of background noise (Kim, Sung Adrian 2008), giving rise to hairpin packets with greater asymmetry and complicated features, suggesting that hairpins can still auto-generate in highly noisy environments. This was then supported by the time-resolved Tomographic PIV measurements in a fully developed turbulent boundary layer (Re_τ = 782) by Jodai & Elsinga (2016), where they showed numerous auto-generation events on

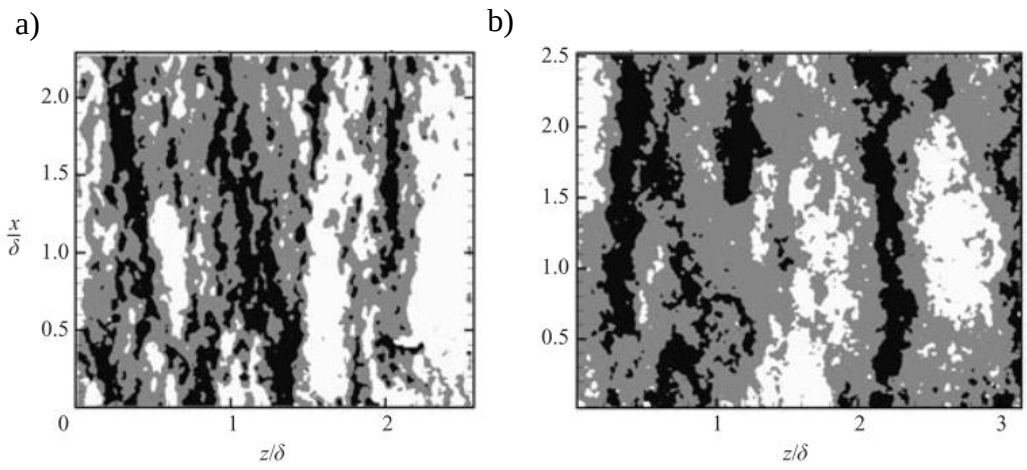

Figure 1-8: Instantaneous u-velocity contours showing elongated low-momentum regions at $Re_\theta = 7705$. Black regions < $-0.1\bar{U}$, white regions > $0.1\bar{U}$, where $\bar{U}$ is the local time averaged mean velocity. a) $z^+ = 100$, $z/\delta = 0.045$; b) $z^+ = 440$, $z/\delta = 0.2$. Reproduced from Tomkins & Adrian (2003).

a time scale of 20-30 viscous time units (ν/u_τ^2) in the near wall region of their boundary layer. Moreover, they also detailed the evolution of a hairpin packet developing from quasi streamwise vortices on either side of a low momentum zone.

A dominant feature in x-y measurement planes within the logarithmic region is alternating low and high speed regions elongated in the streamwise direction (see Figure 1-8). Packet signatures appear as coherent low momentum regions (LMRs) bounded by counter-rotating swirling regions of fluid, which can be cross sections of the hairpin legs or neck (Tomkins & Adrian 2003; Ganapathisubramani *et al.* 2003). These signatures were abundant in the PIV measurements of Tomkins & Adrian (2003) from the buffer layer up to the top of the log layer ($21 < z^+ < 440$) in TBLs with $Re_\tau = 426$ and 2216 and the PIV measurements of Ganapathisubramani *et al.* (2003) in a TBL with $Re_\tau = 1060$.

Tomkins & Adrian (2003) also showed that average spanwise length scales increased linearly with z through qualitative visualization and linear stochastic estimation, consistent with self-similar growth. This is impossible to observe in an instantaneous field. Based on views of instantaneous fields, the authors conjectured spanwise scale growth mechanisms through merging and re-connection of individual vortical structures on an eddy by eddy basis, as proposed previously by other groups (Offen & Kline 1975; Perry & Chong 1982; Wark & Nagib 1989). Tomkins & Adrian (2003) also considered multiple merging scenarios in addition to annihilation of neighboring vortex legs of merging vortices. The three mechanisms proposed by Tomkins & Adrian (2003) are shown in Figure 1-9. The scenario in Figure 1-9b illustrates the outcome of the merging when the vortex legs completely annihilate or cancel each other out, while Figures 1-9a and 1-9c show other possible outcomes; both result in a larger downstream hairpin vortex, and a smaller upstream hairpin. The smaller upstream hairpin retains the sense of rotation in the direction of the mean shear for figure 1-9a, while undergoing the opposite rotation for the scenario in figure 1-9c. All three mechanisms were hypothesized as a means for smaller hairpin packets closer to the wall to form larger ones extending further from the wall, and manifested in their data as merging of spanwise neighboring LMRs into wider ones (illustration shown in figure 1-9d). This was also observed in the Tomographic PIV measurements in a Re_τ = 2480 TBL by Gao *et al.* (2013), where not only did neighboring packet structures merge to form one packet, but an individual packet could also break into two parts due to strong spanwise shearing.

Extensive studies have been conducted on the average sizes of coherent structures in boundary layers (Christensen & Adrian 2001; Tomkins & Adrian 2003;

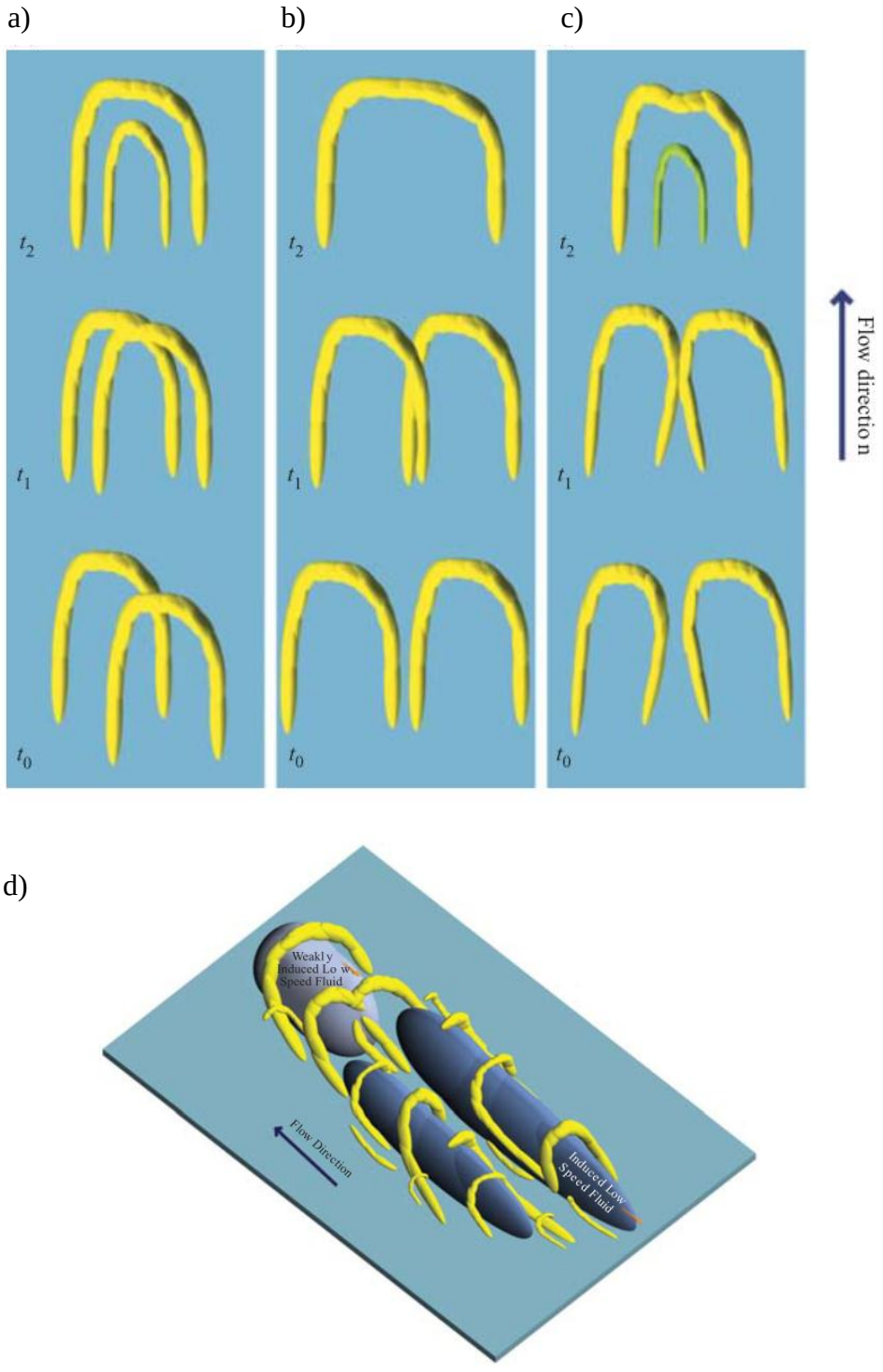

Figure 1-9: Schematic of idealized vortex merging scnearios. a) overlap and pairing of outer structure, residual structure has rotation in direction of mean shear; b) merging with inner-leg annihilation; c) merging of outer structures without overlap, residual structure rotates in opposite direction of mean shear; d) idealized schematic of merging vortex packets through vortex re-connection. Reproduced from Tomkins & Adrian (2003).

Ganapthisubramani 2005; Wu & Christensen 2006; Hutchins & Marusic 2007a; Tutkun *et al.* 2009). On the contrary, fewer studies have examined the spanwise distribution of vortex packets in boundary layers, which is critical to turbulent wall-models (de Silva *et al.* 2016). The spanwise spacings between hairpin packets have been reported to be within the range 0.5δ to δ (Hutchins, Ganapathisubramani & Marusic 2005; Elsinga *et al.* 2010; Gao 2011; Zheng & Longmire 2014). Hutchins, Ganapathisubramani & Marusic (2005) investigated the spanwise periodicity of LMRs in DNS data at $Re_\tau = 1100$ through examination of the dominant spanwise Fourier modes of streamwise velocity fluctuations at $z^+ = 150$. They observed a 0.6δ preferential spanwise spacing of the LMRs. In fact, 93% of the total energy represented in the PIV data was contained within spanwise wavelengths between 0.5δ and 0.75δ. Elsinga *et al.* (2010) observed spacings of LMRs to vary between 0.5δ and 1δ in a supersonic turbulent boundary layer. Separately, Gao (2011) proposed that the spanwise spacing of LMRs within the logarithmic region was greater than 0.5δ, consistent with Elsinga *et al.* (2010). They inferred this based on the lack of instances where two packets appeared simultaneously in their 0.5δ wide Tomographic PIV volumes, across depths of $z^+ = 100 – 300$ and $z^+ = 300 – 500$.

Hairpin packets or coherent LMRs have also been shown to have very long streamwise length scales (Jimenez 1998; Kim & Adrian 1999), even greater than 20δ in a high Reynolds number atmospheric boundary layer, $Re_\tau = 660{,}000$ (Hutchins & Marusic 2007a). Kim & Adrian (1999) suggested the concatenation of multiple hairpin packets in the streamwise direction as a possible reason for their formation (see Figure 1-10). The DNS studies of Lee & Sung (2014) of a $Re_\tau = 930$ turbulent channel flow showed frequent merging of long LMRs with streamwise length between 1-3δ along the

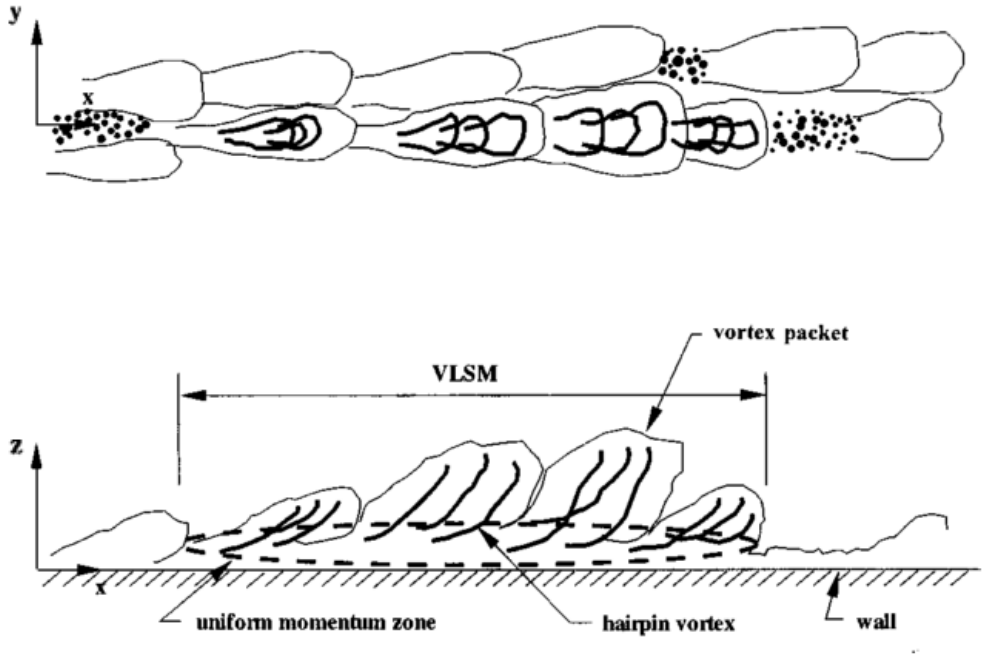

Figure 1-10: Conceptual illustration of hairpin packet concatenation resulting in very long stream-wise length scales. Reproduced from Kim & Adrian (1999).

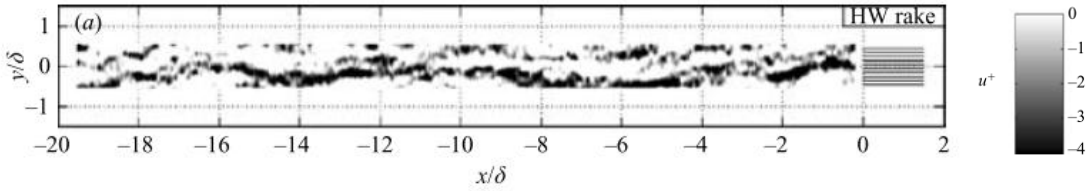

Figure 1-11: Example of hot-wire rake signal reconstructed using Taylor's hypothesis and convection velocity based on local mean showing meandering low momentum zone at $z/\delta = 0.15$ for $Re_\tau = 14380$. Reproduced from Hutchins & Marusic (2007a).

streamwise direction, supporting Kim & Adrian's hypothesis. They proposed that this mechanism may be the key prerequisite for the formation of the very long LMRs. Hutchins and Marusic's (2007a) hot-wire rake measurements coupled with Taylor's hypothesis in various boundary layers ($1120 < Re_\tau < 19960$) also confirmed the existence of very long superstructures populating the logarithmic region. These features could

extend to over 20δ in length. Instantaneous views showed that these superstructures meander significantly along their length in the spanwise direction (Figure 1-11). The authors suggested the meandering behavior as a reason for the underestimation of the average length scales of flow structures derived from two-point spatial correlations and pre-multiplied spectral analyses.

The large-scale energy containing motions in wall turbulence have been shown to influence the small-scale motions, especially with increasing Reynolds numbers (e.g. Hutchins & Marusic 2007b; Marusic, Mathis & Hutchins 2009; Bernardini & Pirozzoli 2011; Guala, Metzer & Mckeon 2011; Marusic, Mathis, Hutchins 2010; Mathis *et al.* 2011; Ganapathisubramani *et al.* 2012; Agostini & Leschziner 2014; Baars, Hutchins & Marusic 2017). Hutchins & Marusic (2007b) showed evidence of modulation of the small-scale fluctuations in the near wall region by very large scale features in the logarithmic region. The authors discovered this by decomposing the streamwise fluctuation velocities into large-scale and small-scale components, and observed that the amplitudes of the small scale fluctuations were suppressed in the presence of a large-scale negative fluctuation, and amplified when accompanied a large-scale positive fluctuation (i.e amplitude modulation). Based on the amplitude modulation effect and the attached eddy hypothesis (Townsend 1976), Mathis *et al.* (2011) proposed a model that successfully predicted streamwise velocity statistics in the near wall region of a canonical boundary layer, using data acquired from a single measurement point taken at the location of the energetic outer peak in streamwise pre-multiplied energy spectra, in the logarithmic layer. The model assumes the existence of a universal inner region, interacting with the outer motions through superposition and modulation. Statistics such

as spectra, turbulence intensity, skewness, flatness and moments up to the sixth order were reconstructed accurately.

1.2.1.4 Modeling with the hairpin packet paradigm and the attached eddy hypothesis

A hairpin vortex model was applied successfully by Perry, Marusic and colleagues to reproduce statistics of wall turbulence based on the attached eddy hypothesis, proposed by Townsend in 1967 (Perry & Chong 1982; Marusic & Perry 1995; Marusic 2001; Woodcock & Marusic 2015; de Silva *et al.* 2016). The hypothesis states that wall turbulence can be represented by a hierarchy of geometrically self-similar eddies whose size scales with the distance from the wall. Perry and Chong (1982) reproduced the logarithmic profile for mean velocity using a hierarchy of randomly distributed Λ-shaped vortices (idealization of hairpins). They postulated scale growth mechanisms for the attached eddies by pairing of individual vortices to form larger vortices, thus establishing discrete hierarchies. Separately, they suggested that individual vortices could also grow by drawing vorticity from the mean flow. The zonal-like organization of uniform momentum zones as shown in experiments (Meinhart & Tomkins 1995; AMT 2000) was reproduced in the synthetic datasets of de Silva *et al.* (2016a) with a theoretical boundary layer represented by a hierarchy of randomly located hairpin packets as in Marusic (2001) following the attached eddy hypothesis. In addition, the linear increase in the number of uniform momentum zones with increasing Reynolds number observed in experiments was also reproduced in the synthetic data. This lends further support to a boundary layer represented by a hierarchy of hairpin packets. Using the hairpin packet as the representative structure, coupled with further refinements to Townsend's attached eddy hypothesis through rigorous mathematical treatment, Woodcock & Marusic (2015)

were able to reliably estimate structure functions and higher order moments of the velocity fluctuations in turbulent wall flows with results comparable to data from experiments, although the authors noted discrepancies in the predicted flatness of the streamwise velocity fluctuations. This was later resolved by de Silva *et al.* (2016) by imposing minimum distances between adjacent model hairpin packets, instead of a random distribution where packets can lie atop of one another directly. This result demonstrated the importance of spatial exclusion between packets in modeling turbulent wall flows, and the importance of understanding the distribution of hairpin packets within wall-bounded flows.

1.2.2 Feature extraction algorithms in turbulent boundary layers

The present dissertation includes the development of a feature extraction algorithm to extract LMRs associated with packet structures. Several previous studies have employed feature extraction algorithms to analyze statistics of specific coherent structures in boundary layers (e.g. Ganapathisubramani *et al.* 2003; Lin *et al.* 2007; Lee & Sung 2011; Nolan & Zaki 2013).

Ganapathisubramani *et al.* (2003) extracted regions associated with hairpin packets in streamwise-spanwise vector fields derived from SPIV measurements of a turbulent boundary layer with Re_τ = 1060. The legs of hairpin vortices can appear as neighboring cores of positive and negative wall-normal vorticity roughly aligned in the streamwise direction. For a hairpin packet, one might observe multiple pairs of cores aligned approximately in the streamwise direction, while also bordering LMRs, as collectively, the multiple hairpins act to induce a longer region of low streamwise momentum. A region growing algorithm was developed to identify regions of strong Reynolds shear

stress bounded by strong negative vorticity beneath and positive vorticity above. These regions were used as the seed points, where based on streamwise velocity, neighboring points lying within local thresholds of streamwise velocity were connected, such that a final coherent region was a patch of relatively uniform momentum. The final step involved connecting patches adjacent to one another in the streamwise direction, provided that the streamwise distance between the patches was less than the average widths of the patches being merged. Identified patches at $z^+ = 92$ and 150 were typically aligned in the streamwise direction; Occasionally however, patches were inclined at small angles in the spanwise direction. Further from the wall at $z/\delta = 0.2$, no long LMRs were identified, which may be a consequence of the algorithm. The authors noted many cases of individual short patches separated by distances of about 100 wall units in the streamwise direction that were not merged by the algorithm. They believed that these short patches in reality could be part of longer patches with length of order δ.

Lee & Sung (2011) modified the aforementioned algorithm to specifically extract large (long) and very large scale features in their DNS of a spatially developing turbulent boundary layer with $Re_\theta = 570 – 2560$. Patches with length greater than 3δ accounted for more than 40% of the total number of patches identified, and contributed to approximately 45% of the total Reynolds shear stress from all the patches, demonstrating the importance of these long structures to the Reynolds shear stress production and transport.

Lin *et al.* (2007), on the other hand, employed an algorithm to extract regions of low and high streamwise momentum in the buffer region of a canonical turbulent boundary layer with $Re_\theta = 7800$ in planes from $z^+ = 14.5$ to $z^+ = 48$ from SPIV data. Thresholds

dependent on the standard deviation of streamwise velocity were employed to define coherent regions corresponding to low speed streaks and these regions were subsequently refined by erosion and dilation of the binarized images. In a separate study, Nolan and Zaki (2013) employed a feature detection algorithm to track and acquire amplitudes of streaks based on local extrema in the streamwise velocity fluctuations from a DNS of a transitional boundary layer.

1.2.3 Perturbations to turbulent boundary layers

Many studies have sought to perturb turbulent boundary layers to achieve desirable effects such as drag reduction or delay of flow separation, while others have characterized perturbations or roughness effects, relevant to practical flows. A majority of these studies can be loosely grouped based on the wall normal and stream-wise length scales of the perturbations.

Two groups will be considered:

a) Small scale perturbations with large streamwise extent
b) Small and large scale perturbations with small streamwise extent

1.2.3.1 Small scale perturbations with large streamwise extent

Wall roughness has been investigated extensively as a means of perturbing boundary layer organization. Typically, the roughness elements are much smaller than the boundary layer thickness, and distributed over a significant streamwise distance relative to the boundary layer thickness. With this approach, the goal is to modify or disrupt the near-wall cycle of turbulence production to potentially reduce skin-friction drag. The present review differentiates between ordered rough surfaces, in the transitionally rough

regime and the irregularly rough surfaces in the fully rough regime. Two key parameters come to mind for roughness studies: the roughness Reynolds number, $k_s^+ = (kU_\tau)/\nu$, quantifying the effect of roughness on the buffer layer, and k/δ, the roughness height to boundary layer thickness ratio.

Irregular rough surfaces on boundary layers have been extensively studied and a review of many of these studies can be found in Jimenez (2004). Roughness effects on the mean flow can be characterized by a roughness function (ΔU^+) manifesting as a downward shift of the logarithmic law corresponding to the rise in momentum deficit compared to the smooth wall case (Clauser 1954; Hama 1954).

More recently it has been shown that the effects of irregular rough surfaces in the fully rough regime were confined to the inner layer, such that the coherent structures in the outer flow resembled those in smooth-wall boundary layers (Volino *et al.* 2007; Squire *et al.* 2016). This lends support to Townsend's wall-similarity hypothesis, stating that the turbulent motions outside the region affected by the roughness (roughness sublayer) are independent of the wall boundary condition (Flack *et al.* 2005; Flack & Schultz 2014). In general, irregular rough surfaces contribute to an increase in wall shear stress largely due to the form drag contributed from the roughness elements in the fully rough regime, or both viscous and form drag of the roughness elements in the transitionally rough regime (Flack & Schultz 2014).

On the other hand, ordered rough surfaces such as riblets on the other hand have been shown to reduce skin friction drag within boundary layers (e.g. Walsh 1980; Goldstein 1995; Bechert *et al.* 1997; Bechert *et al.* 2000; Lee & Lee 2001; Garcia-Mayoral & Jimenez 2011; Nugroho *et al.* 2013; Kevin *et al.* 2017). Walsh (1990) reviews many

studies on riblets aligned in the streamwise direction. Sawtooth riblets with a triangular cross-section (Walsh 1980) were shown to produce a 5.1% reduction in measured turbulent shear stresses in a boundary layer flow. To investigate possibly larger reductions, Bechert *et al.* (1997) studied different riblet geometries and spacings and were able to achieve ~9% drag reduction using riblets shaped like blades. The mechanism for drag reduction was attributed to the suppression of cross stream velocity fluctuations near the wall. The spacing between the peaks of the riblets was found to be a critical parameter, such that surfaces with smaller spacings between riblets led to a decrease in the magnitude of the drag reduction (Bechert *et al*. 1997).

Ordered rough surfaces have also been shown to profoundly affect the flow far above the surface, instead of being limited to the inner layer as in irregular rough surfaces. Nugroho *et al.* (2013) showed that converging-diverging riblets ($H/\delta \sim 0.01$) in a canonical turbulent boundary layer ($771 < Re_\tau < 2310$) imposed large-scale spanwise periodicities on the mean velocity, turbulent intensities and boundary layer thickness. Furthermore, pre-multiplied energy spectra indicated that large-scale energy was amplified over converging regions while being suppressed over diverging regions. The authors hypothesized that this could be due to the riblets preferentially re-aligning the large scale motions above. Separate y-z SPIV measurements by Kevin *et al.* 2017 in a TBL (Re_τ = 3900) over similar type riblets also yielded a pronounced spanwise periodicity in all single point statistics. The authors also reported counter-rotating roll modes accompanying the spanwise periodicities, such that upward motions occur above regions of convergence and downward motions above diverging regions of the riblet surface. Separately, Vanderwel & Ganapathisubramani (2015) showed that long strips of Lego

bricks with H = 0.09δ and spanwise spacings of 0.3δ – 1.8δ also imposed significant secondary flows within a boundary layer with Re_τ ~ 4200. The spanwise spacing between the roughness surfaces profoundly influenced the resulting secondary flows, where the strongest and largest coherence occurred for spacings of 0.88δ.

1.2.3.2 Perturbations with short streamwise length scale

The present study differs from previous rough wall studies in two ways. In our study, the streamwise extent of the perturbing elements is substantially shorter, and the elements protrude further into the logarithmic layer or beyond.

Many studies have examined large-eddy break up (LEBU) devices (e.g. Yajnik & Acharya 1979; Corke *et al.* 1981; Hefner *et al.* 1981; Plesniak & Nagib 1985; Savill & Mumford 1988; Wark *et al.* 1990; Hutchins & Choi 2002; Park *et al.* 2011). Typically, these LEBU devices extend significantly into the boundary layer while posing a relatively small frontal blockage to the oncoming turbulent boundary layer area. Several studies have shown the potential of LEBU devices to reduce skin friction drag (Corke *et al.* 1981; Wilkinson 1988; Wark *et al.* 1990; Hutchins & Choi 2002; Park *et al.* 2011), and in some cases the effect of reduced skin friction lasted up to 150δ downstream of the devices (Plesniak & Nagib 1985). The suppression of large-scale motions within the boundary layer due to interaction of LEBU wakes with existing turbulent eddies was postulated as the mechanism for the skin-friction drag reduction (Wark *et al.* 1990; Wilkinson 1988). Corke *et al.* (1981) examined the flow downstream of four wall-parallel plates with narrower wall-normal spacing closer to the wall. The flat plate manipulators protruded significantly into the boundary layer with H = 0.8δ, but remained fairly porous at a 4% frontal blockage to the oncoming boundary layer (Re_τ ~ 1900).

Their hot-wire results showed a deficit in streamwise velocity relative to the unperturbed flow for $z < 0.5\delta$. In addition, streamwise root mean square (RMS) velocities for $z/\delta < 0.1$ were suppressed up to ~ 9δ downstream of the manipulators. They attributed the reduced RMS velocities to the plates' inhibition of wall-normal velocity fluctuations which impeded flow interactions across the depth of the boundary layer. Boiko & Kornilov (2009) also observed similar results in measurements within a logarithmic region (Re_τ ~ 400) perturbed by an array of vertically oriented wall-mounted flat plates ($H/\delta = 0.5$, frontal blockage = 22%), spaced 0.2δ apart. Streamwise RMS velocities were suppressed up to 7δ downstream, which was their last measurement location. Notably, they observed a stable decrease in the local skin friction coefficient from $x = 0.1\delta$ downstream of the array, up to a distance of 7-8δ, with a maximum reduction of ~ 28% of the unperturbed local skin friction coefficient at $x = 6\delta$. Hutchins and Choi (2002) investigated the effects of two streamwise aligned vertical plates spaced at 0.2δ extending to $H/\delta = 0.5$ on a turbulent boundary layer with Re_τ ~ 400. Their hot-wire measurements also indicated suppression in streamwise RMS velocity within the logarithmic region up to 7δ downstream. Interestingly, RMS velocities were also suppressed downstream of a 2-D fence with 65% porosity, posing a significant blockage to the oncoming turbulent boundary layer (Lee & Kim 1999). Moreover, the fence in this case extended well beyond the boundary layer thickness to H/δ ~ 10. Their results also showed sustained deficits in streamwise velocity for $z/\delta < 1$ up to 7δ downstream corresponding to the last measurement location.

Studies of sparse obstructions with limited height compared to δ also show profound effects on the flow downstream. These effects extended above the height of the elements

(Tomkins 2001; Guala *et al.* 2012; Jacobi & Mckeon 2011; Tan 2015). As far as we know, few studies examined the effects of perturbations on hairpin packets in boundary layers. Tomkins (2001) and Guala *et al.* (2012) examined the effects of periodic arrays of wall mounted hemispheres ($H/\delta = 0.09$) on the packet organization in the outer layer of a turbulent boundary layer with $Re_\tau \sim 2200$. Reduction in streamwise length scales of the packets in the outer layer were observed, in addition to the steepening of the inclination angles of existing packet signatures beyond the height of the perturbation. On the other hand, Jacobi & Mckeon (2011) used four 2-D spanwise bars ($H/\delta = 0.06$) staggered in the streamwise direction spanning a distance of δ to perturb a $Re_\tau \sim 970$ canonical turbulent boundary layer. Hot-wire and x-y PIV measurements were conducted. Results showed that the perturbation redistributed the population of swirl structures in the wall-normal direction, increasing the number at $z/\delta = 0.2 - 0.3$, whilst decreasing the population of swirl structures closer to the wall. Additionally, they observed a velocity deficit immediately downstream of the perturbation for $z/\delta < 0.3 - 0.4$, that persisted over a distance of 15δ. Furthermore, the authors observed an increase in streamwise RMS velocity, peaking at the bar height immediately downstream of the perturbation which decayed in strength and propagated away from the wall with increasing streamwise distance.

In studies downstream of high and low aspect ratio perturbations, Rodriguez-Lopez *et al.* (2016a&b) observed key differences in the recovering boundary layer. In their study, they artificially generated a high Re boundary layer with properties resembling canonical boundary layer by perturbing the initial canonical boundary layer. The two types of perturbations considered were two rows of cylinders ($H/\delta \sim 1$, $S = 0.5\delta$) and a sawtooth

fence tilted downstream at 50° with respect to the wall ($H/\delta \sim 0.75$). The blockage for the sawtooth fence varied with wall-normal location, with the blockage being 100% at the wall, while the percentage blockage was constant across the height of the cylinders. The authors observed a much shorter adaptation region downstream of the two rows of cylinders, where the length of the adaptation region was defined as the location where canonical properties of the boundary layer is recovered downstream of the perturbation elements. In contrast, the boundary layer properties did not recover downstream of the sawtooth fence within their measurement domain ($x \sim 150\delta$). They attributed the observed difference in recovery behavior to differences in boundary layer formation mechanisms downstream of the perturbations. A wall-driven mechanism was proposed to explain the behavior downstream of the two rows of cylinders, such that structures near the wall remain intact, then grow outwards by entraining the cylinder wakes. Moreover, later results (Rodriguez-Lopez *et al.* 2016b) showed that wall-normal motions were suppressed, limiting the influence of the outer layer on the near wall region. In comparison, a wake-driven mechanism was proposed to govern the formation of the boundary layer downstream of the sawtooth fence, such that a strong re-circulation region generated strong wall normal motions, increasing the influence of the energetic motions in the outer layer on the near wall region, and was related to the very long adaptation region (Rodriguez-Lopez *et al.* 2016a&b). The authors noted that this result was consistent with previous studies by Alving & Fernholz (1996) and Castro & Epik (1998), where both studies suggested that outer energetic motions influenced the relaxation process of a turbulent boundary layer downstream of a mild separation event, such that the inner layer was much slower to recover than the outer layer.

Previous studies in our lab have examined the effects of an array of cylinders in a turbulent boundary layer (Ryan *et al.* 2011; Ortiz-Dueñas *et al.* 2011; Zheng & Longmire 2014). The wake behind finite wall-mounted cylinders is highly three-dimensional and includes free end tip structures associated with generating downwash (e.g. Kawamura *et al.* 1984; Park & Lee 2000; Sumner *et al.* 2004; Wang *et al.* 2006). Karman-like vortices are also generated along most of the cylinder height, and a horseshoe vortex occurs near the base of the cylinder (Sumner *et al.* 2004; Pattenden *et al.* 2005). Illustrations from previous works of the aforementioned wake structures are shown in Figure 1-12. An in-depth review of the wake structure and associated vortex patterns can be found in Sumner (2013). Key parameters that strongly influence the resulting wake of the finite wall-mounted cylinder are the Reynolds number, inflow condition: laminar or turbulent (Wang *et al.* 2006), cylinder height to boundary layer thickness ratio, H/δ (Wang *et al.* 2006) and the cylinder aspect ratio (Sakamoto & Arie 1983; Sumner *et al.* 2004). The cylinder wakes become more complex when the cylinders are placed closely along the spanwise direction, with the additional parameter being the cylinder spacing (e.g. Sumner *et al.* 1999; Park & Lee 2003). Results show that the flow between the cylinders interacts with vortices shed off the cylinders, altering the formation length (Park & Lee 2003). On top of that, small spacings between the cylinders result in different wakes behind each of the cylinders. On the other hand as the cylinders are spaced further apart, the cylinder wakes become increasingly more similar to one another (Sumner *et al.* 1999).

The array of cylinders profoundly affected the mean and RMS velocity statistics of the turbulent flow downstream. Ryan *et al.* (2011) studied the flow downstream of cylinder arrays ($H/\delta = 0.13$) with spacings of $S = 0.26\delta$ and 0.5δ immersed within the log region

a)

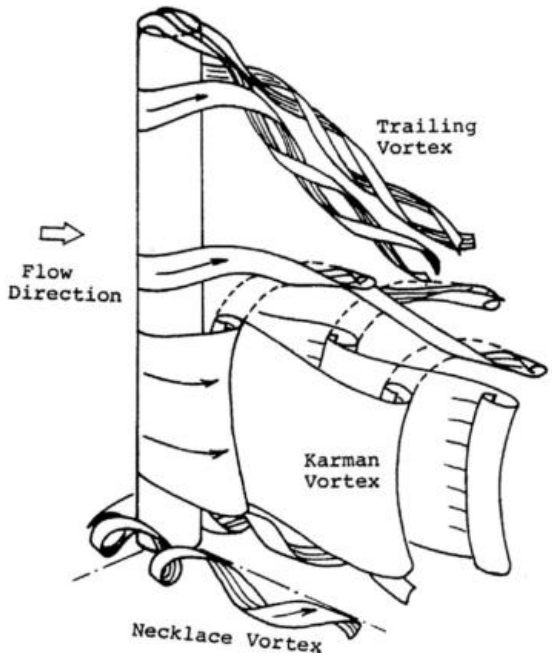

b)

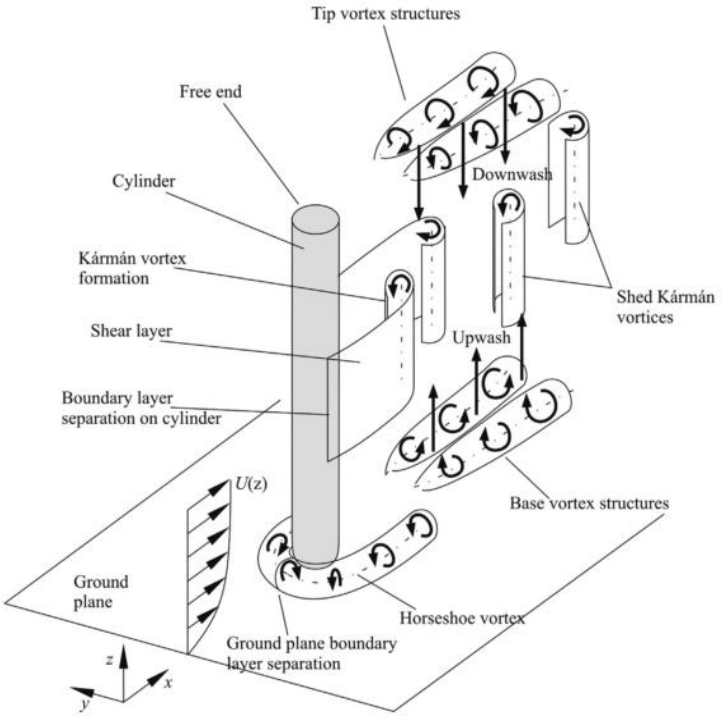

Figure 1-12: Illustrations of wake structures downstream of a finite wall-mounted cylinders reproduced from a) Kawamura *et al.* (1984) and b) Einian *et al.* 2010.

of a boundary layer (Re_τ = 1200) using hot-wire anemometry. Results showed that the deficit in the mean velocity remained confined to the log region, at least until x = 0.5δ downstream, which was the furthest extent of their measurements. Both arrays initially shifted the peak in turbulence intensity away from the wall towards the top of the log region. Also, the perturbations to the streamwise RMS velocity profile propagated outward beyond the log region, eventually extending to 2-3H at a distance 7δ downstream (Tan 2014). This result was similar to trends in Jacobi & Mckeon (2011).

The spanwise organization of flow structures downstream of the array of cylinders was significantly affected as well. Ortiz- Dueñas *et al.* (2011) considered spanwise arrays of cylinders (H/δ = 0.2) with spanwise spacings, S = 0.2δ and 0.4δ with PIV and volumetric PTV at Re_τ = 2500 at a measurement height of z^+ = 300 and volumes across depth $52 < z^+ < 1000$ respectively. Immediately downstream of both arrays, averaged results showed initial splitting and divergence of the wakes, followed by pairing with neighboring wake structures at a downstream location scaling with the array spacing. Downstream of the S = 0.2δ array, the split wakes were observed to pair more than once, while the spanwise location of low speed zones downstream varied significantly. By comparison, the pairing of the wakes downstream of the S = 0.4δ array seemed to result in a relatively stable flow where low speed zones tend to align in the mid span between cylinders on average, up to x = 4δ. Volumetric measurements indicated that on average, within the logarithmic region, the cylinder wake structures seemed to have a dominant streamwise and wall-normal vorticity component that diminishes by x = 0.5δ.

Ryan (2011) and Zheng and Longmire (2014) showed that although the incoming packet organization downstream of a narrowly spaced array (S = 0.2δ) was initially disrupted at

$z^+ = 300$, the upstream packet organizations reappeared relatively quickly downstream at roughly similar spanwise locations. Zheng & Longmire (2014) investigated the effects of an array of cylinders with height $H = 0.2\delta$ ($H^+ = 500$) and cylinder spacing of $S = 0.2\delta$ on packet organization. They used SPIV and flying PIV, where the PIV system moves at the local convection velocity of the flow to capture flow evolution. In measurement planes at $z^+ = 300$, packets were disrupted immediately downstream of the $S = 0.2\delta$ array, where wakes with Karman-like shedding patterns appeared directly behind each cylinder. The individual wakes interacted strongly with one another in the spanwise direction resulting in highly disorganized flow downstream, as well as a shift of the mean velocity deficit into the regions between cylinders. On average, flow was induced to move towards the wall in the cylinder wakes by structures shedding off of the cylinder tips and away from the wall in the mid-span between each cylinder, resulting in a highly three dimensional flow on average. Flying PIV measurements at $z^+ = 300$ frequently showed the re-emergence of the incoming packet organization beginning about 2δ downstream of the array. Based on this result, Zheng and Longmire (2014) hypothesized that the recovery of previously existing packet signatures was due to the unperturbed packet organization above the array propagating towards the wall. This idea is consistent with the result of modulation of near wall structures by the larger scales in the outer layer (Hutchins & Marusic 2007; Mathis, Hutchins & Marusic 2009; Ganapathisubramani *et al.* 2012).

Separately, Zheng & Longmire (2014) also investigated packet organization downstream of a $S = 0.6\delta$ array, which matched the natural scaling of vortex packets in the spanwise direction found by Hutchins *et al.* (2005) and Tomkins & Adrian (2003). At $z^+ = 300$, the instantaneous flow downstream depended significantly on flow conditions upstream. In

general, the authors observed that incoming packet signatures passing close to the cylinders ingested the cylinder wakes, resulting in stronger slow moving zones. Also, the packets were shifted gradually to the spanwise location corresponding to the region between the cylinders with increasing streamwise distance. This effect was attributed to the tip downwash effect, bringing faster moving fluid towards the wall, which displaced existing flow structures.

A Fourier method was employed to extract the dominant spanwise scales in the flow and showed the strongest amplification to the 0.6δ spanwise mode at the furthest measurement location. Citing previous hot-wire results from Ryan *et al.* (2011) who examined the effects of reduced cylinder array height and cylinder diameter, Zheng and Longmire (2014) hypothesized that the aforementioned effects could be achieved with a reduced array height. This is one of the hypotheses that will be tested in the present dissertation.

1.3 Objectives and approach

The objective of the present dissertation is to further understanding of perturbation effects by a spanwise array of cylinders on the large-scale organization within the logarithmic region, with focus on the spanwise distribution of low/high coherent momentum zones. Also, trends in the relaxation of the flow structure organization and features downstream are investigated. In addition, questions posed from the collective work of Zheng & Longmire (2014), Ryan *et al.* (2011) and Ortiz- Dueñas *et al.* (2011) are addressed. Two array spacings are considered, S = 0.2δ and 0.6δ. For the S = 0.2δ array, we seek to test the hypothesis proposed by Zheng & Longmire (2014) of whether packet signatures

reappear downstream due to the influence of packet signatures in planes above. On the other hand, for the S = 0.6δ array, we investigate whether the stabilizing effect downstream of the S = 0.6δ, H = 0.2δ array (Zheng & Longmire 2014) can be achieved with a shorter array.

The following questions are addressed:

1. *How do velocity statistics and structural characteristics of coherent momentum regions (CMRs, low and high) change relative to the unperturbed flow across the depth of the logarithmic layer?*
2. *How do the velocity statistics and structural features of CMRs evolve with increasing streamwise distance?*
3. *What are the trends in relaxation (if any) of the velocity statistics and structural features of CMRs downstream of the perturbations? Also, how do they vary across the logarithmic region?*

The following questions are specific to the S = 0.2δ array:

1. *Do packet signatures reappear downstream of the S = 0.2δ, H = 0.2δ array due to the influence of unperturbed packet signatures above?*
2. *How does the vertical extent of packet signatures across the logarithmic layer compare between the perturbed and unperturbed flows?*

Questions specific to the S = 0.6δ array are as follows:

1. *How do spanwise distribution of CMRs vary across the logarithmic layer, downstream of the S = 0.6δ, H = 0.2δ array?*

2. *How does these effects compare when the array height decreases? What are the effects in planes above the array height?*

To address the aforementioned questions, a series of experiments were conducted. Velocity data were acquired using PIV at three wall-parallel measurement planes to assess trends across the logarithmic region. For the S = 0.2δ array, two cylinder heights (H = 0.2δ and H = δ) were selected to test the top-down hypothesis proposed by Zheng and Longmire (2014). The H = δ cylinders were selected to disrupt packet organization throughout the boundary layer depth, while it is assumed that packet signatures persist above the H = 0.2δ array. Relaxation trends downstream of both arrays across the logarithmic layer will be compared. In addition, volumetric measurements at select streamwise locations downstream of both arrays were acquired, and used to assess how structures relate across the logarithmic layer between the perturbed and unperturbed flows.

For the S = 0.6δ array, two cylinder heights were also considered, H = 0.2δ and H = 0.05δ. Three PIV measurement planes were also considered for both arrays, such that trends across the logarithmic layer could be assessed. The shorter array allowed us to investigate whether effects reported for the H = 0.2δ array at z^+ = 300 (Zheng & Longmire (2014) were still evident for a weaker perturbation.

The rest of the dissertation is organized as follows: Chapter 2 describes the experimental facilities, and methodologies used for data processing and reduction. Chapter 3 shows the unperturbed flow results. Chapter 4 shows and discusses results corresponding to the S = 0.2δ arrays, while chapter 5 covers the S = 0.6δ arrays. Chapter 6 discusses and presents conclusions, followed by recommendations for future work.

Chapter 2

Facilities, experiments and methodologies

This chapter first describes the water channel facility and the cylinder arrays used to perturb the oncoming turbulent boundary layer (Section 2.1). Section 2.2 covers the particle image velocimetry (PIV) experiment setup, measurement hardware (e.g. laser, cameras, etc.), data processing and reduction methodologies, and measurement uncertainty. Section 2.3 discusses the volumetric particle tracking velocimetry (PTV) measurements.

2. 1 Water channel facility and cylinder arrays

Experiments were performed in the water channel facility (Figure 2-1) at the Department of Aerospace Engineering & Mechanics, University of Minnesota. The test section of the channel measures 8 m long, 1.12 m wide and 0.61m in depth. For all experiments, the water free surface in the no-flow condition was 0.41m above the bottom wall of the test section, equivalent to roughly 5000 gallons of water. Flow was driven by three propellers connected to a 50HP Reliance Electric AC motor with a variable input frequency from 6 – 60 Hz. The propellers were located beneath the end of the test section where recirculation occurs from outlet to inlet. The individual shafts of the propellers were connected to a 3:1 ratio gear system. Prior to the inlet of the test section, the flow passes through a honeycomb and a series of screens followed by an asymmetric 5:1 contraction.

2.1.1 Flow conditions

The motor was driven at 45 Hz for all experiments conducted, resulting in a water depth of 0.39m from the bottom wall of the test section. A 3mm circular trip-wire was adhered

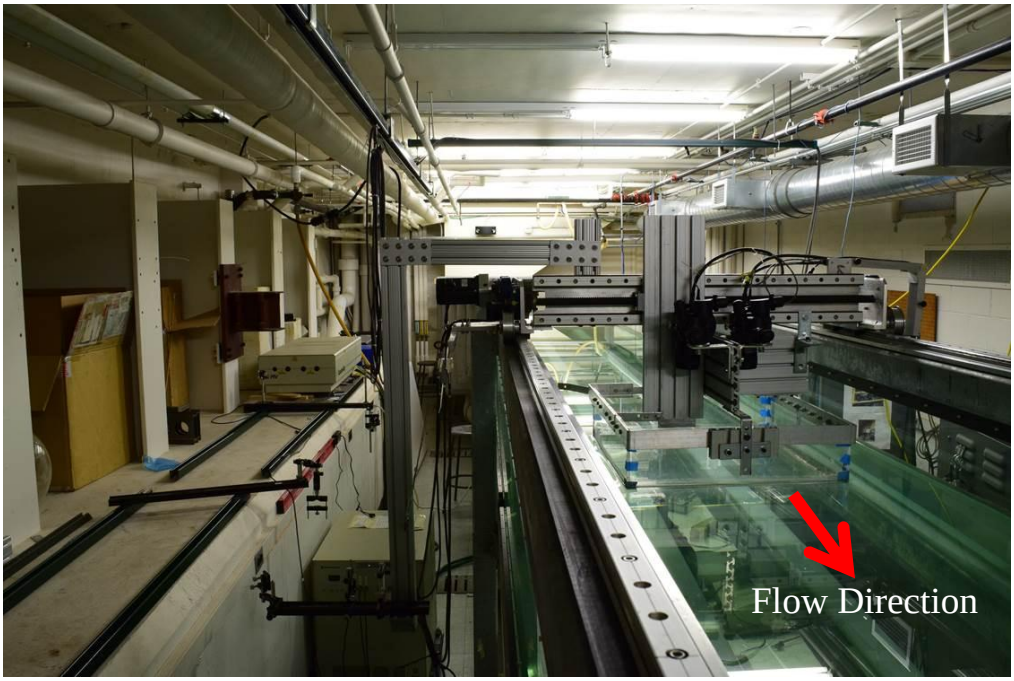

Figure 2-1: Picture of water channel facility

to the bottom wall at the entrance of the test section with silicone adhesive. The trip wire serves to optimally trip the boundary layer into becoming turbulent. The boundary layer then develops along the bottom wall throughout the test section. For all experiments, images were acquired with lines of sight passing through an interface box with a bottom surface made out of optical glass. The interface box was mounted to the traverse carriage. The main purpose of the interface box is to mitigate the effects of the water free surface. The box also doubles as a fail-safe against potential water damage to the PIV cameras due to human error during the camera mounting process. The flow speed increases slightly through the area where partial immersion of the interface box occurs. Further details on this effect can be found in Gao (2011).

Measurements were acquired starting 6.1m downstream of the trip wire, defined as the location where x = 0. The boundary layer height at this location was δ = 125.5 mm, and the Reynolds number based on the skin friction velocity was Re_τ = 2500. The Reynolds number based on momentum thickness was Re_θ = 6200 while the freestream velocity U_∞ was 0.508 m/s. The free stream turbulence intensity was evaluated to be $0.014U_\infty$ (Gao 2011). Relevant parameters to the present dissertation are tabulated in Table 2-1 below. Further details on the facility and various base flow parameters can be found in Gao (2011).

Table 2-1: Flow parameters reproduced from Gao (2011).

Parameters	With box	Without box
Streamwise distance from trip, x_{trip}	6.12 m	6.12 m
Water height, H_w	390 mm	390 mm
Motor frequency	45 Hz	45 Hz
Freestream velocity, U_∞	0.508 m/s	0.485 m/s
Boundary layer thickness, δ	125.5 mm	134.4 mm
Skin friction velocity, U_τ	0.0198 m/s	0.0180 m/s
Momentum Thickness Reynolds number, Re_θ	6200	7050
Friction Reynolds number, Re_τ	2500	2410

2.1.2 Cylinder arrays

The present study uses a spanwise array of cylinders to perturb the oncoming turbulent boundary layer. The diameter of the cylinders, D was fixed at 6.35 mm. The cylinders were mounted in a single row all across the test section width at location x = 0 (e.g. Figure 2-2a). The cylinder spacing was aligned using a ruler. The ruler was aligned to be perpendicular to the side walls of the test section using a steel square frame. Two cylinder spacings were selected for the present study, S = 0.2δ and 0.6δ. In addition to that, three cylinder heights were considered, H = 0.05δ, 0.2δ and δ.

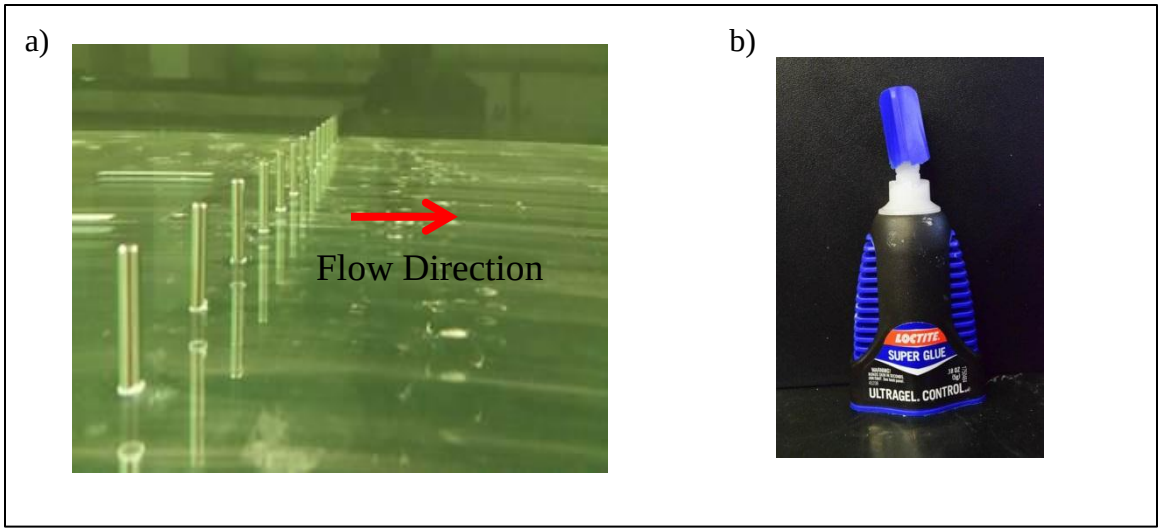

Figure 2-2: a) Picture showing H = 0.2δ cylinder array with S = 0.6δ in water channel. b) Picture of recommended adhesive for mounting cylinders.

The H = 0.05δ and 0.2δ cylinders were stainless steel dowel pins ordered off the shelf from McMaster-Carr. On the other hand, the H = δ cylinders were fabricated from steel rods. The cylinders were mounted to the bottom surface of the test section using super-glue (cyanoacrylate), specifically Loctite super glue - Ultragel control (see Figure 2-2b), which performed best among the many adhesives tested. The H = 0.05δ and 0.2δ cylinders were mounted without draining the water from the channel.

The H = δ cylinders were the most difficult to mount out of the three cylinder heights considered as they protruded the most into the boundary layer. These cylinders experienced larger frontal forces due to the oncoming flow resulting in them having a higher tendency to topple over during an experiment run. To circumvent this, the H = δ cylinders were mounted in a dry channel, to allow the glue to set in dry conditions. Moreover, additional glue underneath and around the base of the cylinders was applied to ensure sustained adhesion during experiments. Additionally, the channel was

incrementally started from rest to prevent the cylinders from falling over due to the abrupt change in flow speed.

Details on the various experimental cases studied, along with the aspect ratios of the cylinders, and percentage frontal blockage with respect to the frontal area of the oncoming turbulent boundary layer are documented in Tables 2-2, 2-3 and 2-4, for the stereoscopic PIV (SPIV), planar PIV (PPIV) and flying PIV (FPIV) measurements.

Table 2-2: List of planar PIV data sets. * denotes data from Zheng (2011).

Data set name	**Cylinder height, H**	**Cylinder Spacing, S**	**Aspect Ratio, AR_c**	**% Frontal Blockage**	**Measurement Height, z^+**
pnoc_z125	N/A (no cylinders)				125
pnoc_z300					300
pnoc_z500					500
p02d_z125	0.2δ	0.2δ	4	5%	125
p02d_z300					300
p02d_z300					500
p02dt2_z125	δ		20	25%	125
p02dt2_z300					300
p02dt2_z500					500
p06d_z125	0.2δ	0.6δ	4	1.7%	125
p06d_z300*					300
p06d_z500					500
p06dt3_z125	0.05δ		1	0.4%	125
p06dt3_z300					300
p06dt3_z500					500

Table 2-3: List of stereo PIV data sets. * denotes data from Zheng (2011).

Data set name	Cylinder height, H	Cylinder Spacing, S	Aspect Ratio, AR_c	% Frontal Blockage	Measurement Height, z^+
snoc_z125	N/A (no cylinders)				125
snoc_z300					300
snoc_z500					500
s02d_z300*	0.2δ	0.2δ	4	5%	300
s02d_z500					500
s02dt2_z300	δ		20	25%	300
s02dt2_z500					500
s02dt3_125	0.05δ		1	1.25%	125
s02dt3_z300					300
s06d_z300*	0.2δ	0.6δ	4	1.7%	300
s06d_z500					500
s06dt2_z500	δ		20	8.5%	500
s06dt3_z125	0.05δ		1	1.6%	125
s06dt3_z300					300

Table 2-4: List of flying planar PIV data sets

Data set name	Cylinder height, H	Cylinder Spacing, S	Aspect Ratio, AR_c	% Frontal Blockage	Measurement Height, z^+
fnoc_z125	N/A (no cylinders)				125
fnoc_z300					300
fnoc_z500					500
f02d_z125	0.2δ	0.2δ	4	5%	125
f02d_z300					300
f02d_z300					500
f02dt2_z125	δ		20	25%	125
f02dt2_z300					300
f02dt2_z500					500
f06d_z125	0.2δ	0.6δ	4	1.7%	125
f06d_z300					300
f06d_z500					500
f06dt3_z125	0.05δ		1	0.4%	125
f06dt3_z300					300
f06dt3_z500					500

2.2 PIV Experiments

A PIV system consists of camera(s), laser(s), optics and single or multiple synchronizers. The present experiment uses a dual head Spectra Physics Nd:YAG laser capable of 370 mJ/pulse. The laser optics for beam shaping included multiple mirrors, spherical lenses and cylindrical lenses. This resulted in a laser sheet that was roughly 1 mm in thickness.

The flow was seeded with silver coated hollow glass spheres from Potters Industries LLC (SH400S20) with an average diameter of 13 um and average density of 1.6 g/cm^3. The particles were first mixed in a separate container with water from the channel, before being introduced at the settling chamber at the end of the test section. The quality of the seeding was assessed in real time through live-streaming of the PIV images. The imaged particles were typically larger than 2 pixels.

2.2.1 Measurement setup

The PPIV measurement setup consists of two cameras oriented roughly normal to the bottom wall of the test section (see Figure 2-3). The two cameras were 12 bit TSI 4MP PowerView Cameras with 2048 x 2048 pixels. Both cameras were angled slightly with respect to the bottom surface of the channel, or the wall-parallel plane in order to provide some spanwise overlap between the individual fields of view (FOV) to acquire a relatively wide field of view. Nikon Micro-Nikkor 60 mm lenses were used with f number of 11, resulting in a magnification of 0.08. The cameras were both equipped with Scheimpflug adapters to minimize distortion around the edges of the FOVs. The resulting FOV for the PPIV measurements was $1.1\delta \times 2.1\delta$ in the streamwise and spanwise directions respectively.

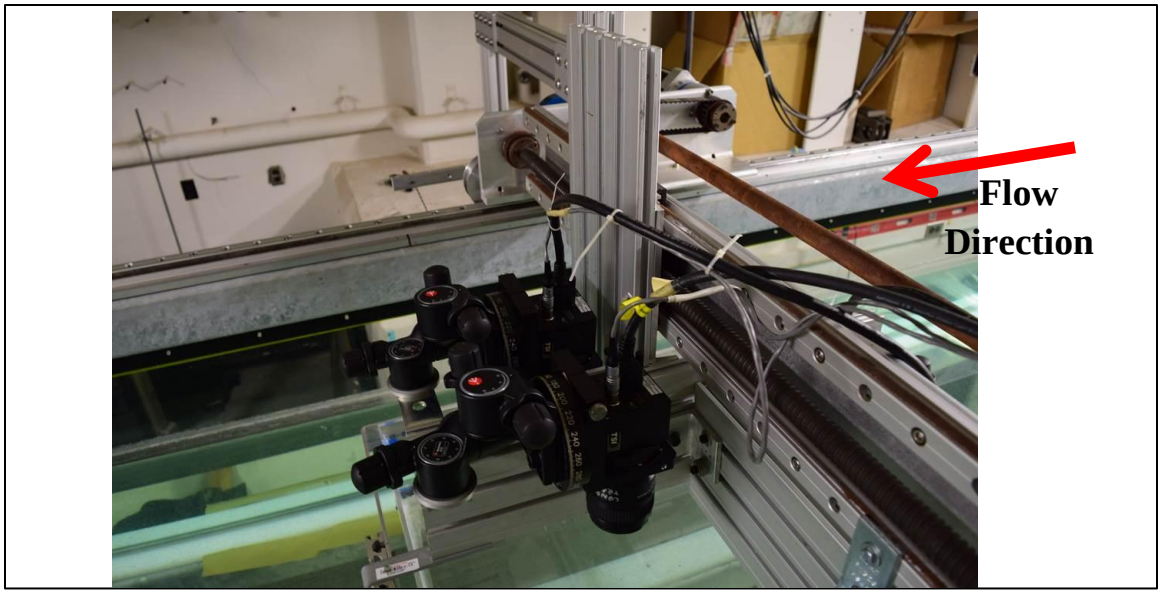

Figure 2-3: Picture of the planar PIV set up. Both cameras were angled at α ~ 5° with respect to the z-axis.

For the SPIV measurements, the two cameras were tilted at an angle α of ~ 30° with respect to the z-axis. In this configuration, the camera views were mostly overlapped, resulting in a FOV of 1.1δ × 1.1δ. A diagram illustrating the top view of the measurement setup for both the SPIV and PPIV measurements relative to the incoming laser sheet is shown in Figure 2-4. The center line between the SPIV cameras was aligned in the flow direction while the PPIV cameras were aligned perpendicular to the flow direction. The SPIV arrangement allowed for an increase in α relative to the PPIV camera arrangement. This α was not possible in the PPIV camera arrangement and it would not offer any advantage in the PPIV measurements.

Images were acquired at six streamwise locations spanning $0.1 \leq x/\delta \leq 7.5$ for both the SPIV and PPIV measurements. The first measurement location was taken to be slightly offset from the cylinder location as the light sheet was partially cut off due to the

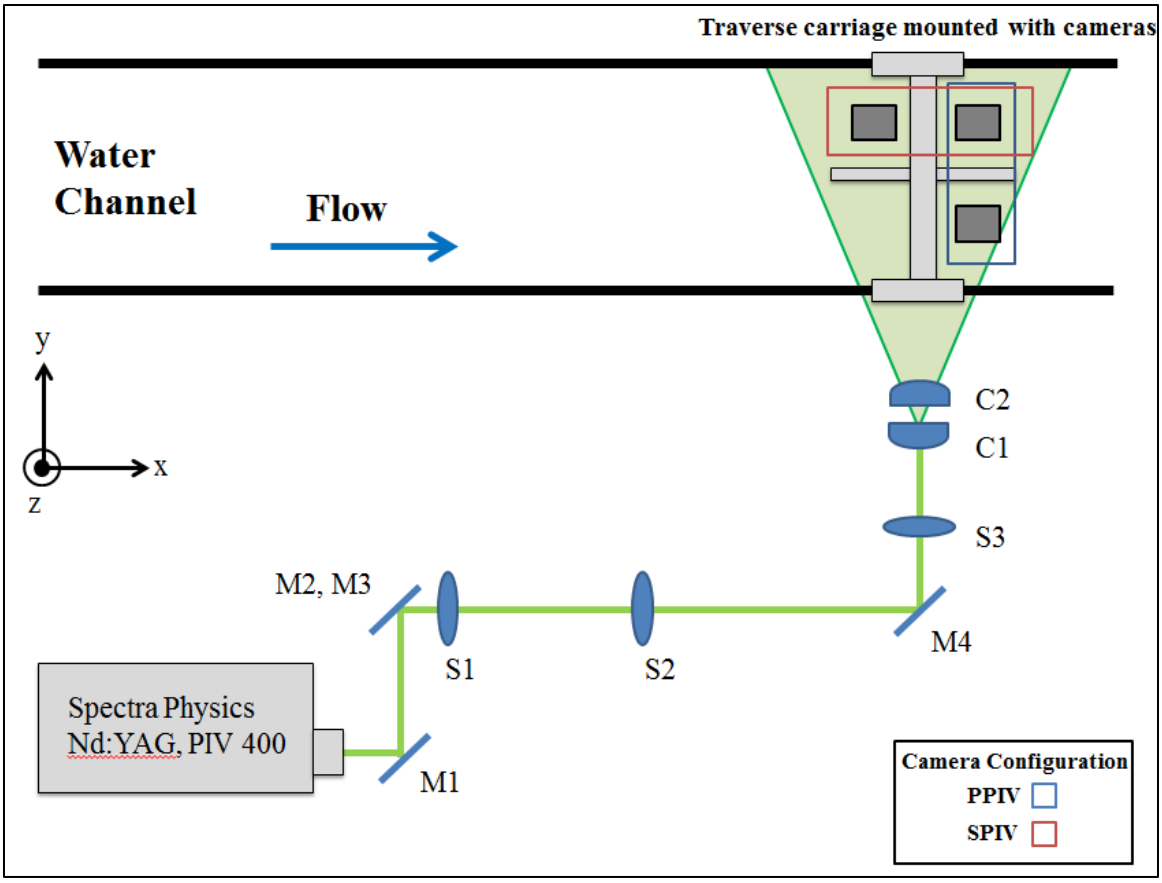

Figure 2-4: Diagram showing top view of PPIV and SPIV setup, also depicted are the optical arrangements for shaping the beam into a laser sheet. M#, mirror (number in order), S# - spherical lens, and C# – cylindrical lens. Diagram not to scale.

blockage posed by the cylinders closest to the oncoming light sheet. This was also exacerbated by a slight approach angle of the oncoming light sheet with respect to the normal of the side wall of the channel. The locations of the six streamwise measurement regions are illustrated in the schematic shown in Figure 2-5 for both the SPIV and PPIV measurements. The measurement domain consists of five consecutive zones with streamwise lengths of 1.1δ directly downstream of the cylinder array, followed by a zone in the far field at 6.4δ to 7.5δ.

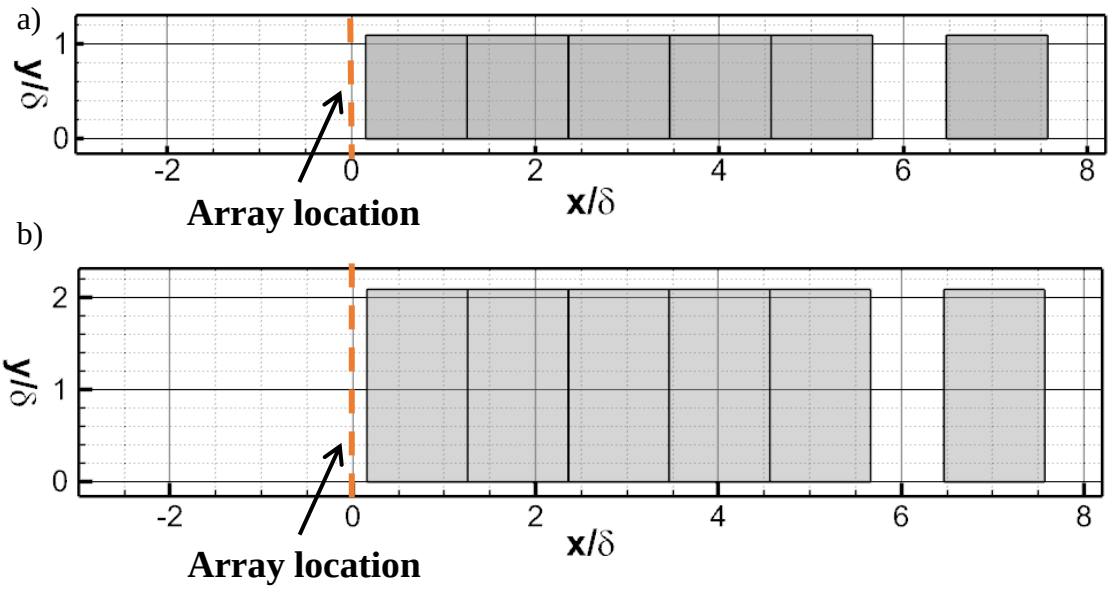

Figure 2-5: Schematic of a) SPIV data fields, b) PPIV data fields

For the SPIV and PPIV measurements, at all measurement locations, 1000 independent PIV fields were captured at a rate of ~0.5Hz determined by the write speed of the hard drive of the acquisition computer. The flow at measurement height of $z^+ = 300$ would have travelled ~ 6δ downstream between successive image captures, which can be considered reasonably independent. The time between the laser pulses (Δt) was 1800 us, resulting in an average displacement of ~7-9 pixels in measurements of the unperturbed flow for all measurement heights considered.

For the flying PIV (FPIV) measurements, the extent of the measurements covered a range of $-2 < x/\delta < 7.5$ (see figure 2-6). The traverse speed was set to the local time-averaged velocity of the corresponding measurement height. Δt was increased to 2400 us to acquire a reasonable average particle pixel displacement between the frames in the convective reference frame. The particle displacements were evaluated to be ~ 1-2 pixels.

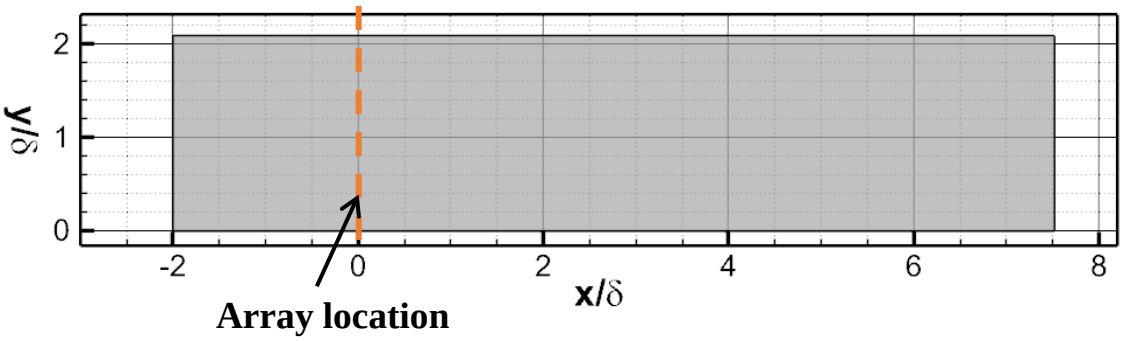

Figure 2-6: Extent of FPIV measurements, note zones are not demarcated in the above illustration.

Sufficient time before the start of the PIV triggering during the FPIV runs was allocated for the traverse to accelerate to the designated speed, and for transient vibrations to damp out. Forty-five runs were captured for each case.

2.2.2 Laser-sheet generation and alignment

The optics used for laser sheet generation consisted of a series of mirrors, spherical lenses and cylindrical lenses. The diagram in Figure 2-4 illustrates the order of the various components used to generate the light sheet. First, the laser beam from the output of the laser is directed via mirrors M1, M2 and M3 then collimated using spherical lenses, S1 and S2, both with focal length of 500 mm. Then, the beam is redirected towards the channel test section using mirror M4, which is mounted on the optical rail attached to the traverse carriage. The laser beam then passes through the other components on the optical rail consisting of a spherical lens, S3 with focal length of 1000 mm. It then also passes through two convex cylindrical lenses with focal length of 60mm, after which it enters the channel and forms the light sheet.

The z-location of the light sheet was re-aligned multiple times to the various measurement heights considered in this investigation. All the measurement heights were located within the logarithmic region, at z^+ = 125, 300 and 500. z^+ is the wall-normal coordinate normalized by viscous units according to the formula, $z^+ = zU_\tau/\nu$ where U_τ is the skin-friction velocity estimated from the Clauser chart method (Gao 2011), and ν the kinematic viscosity of the fluid, which in our case is water at room temperature.

A key challenge was to ensure that the light sheet remained parallel throughout the measurement domain at the desired measurement height. An iterative method was employed to achieve this and is described next.

Two TSI dual-plane calibration plates equipped with the mirror slit attachment (Fig. 2-7) were placed on the bottom surface of the water channel. The first plate was centered at the most upstream end of the measurement domain ($x = -2\delta$), while the second plate at the last measurement location ($x = 7\delta$). The face of the mirror slit attachment was initially aligned with the spanwise edge of the measurement domain closest to the oncoming light sheet. Depending on the desired measurement height, the calibration target was elevated using blocks or shims. The laser light reflection off the mirror slits provided feedback on the height of the laser sheet.

Next, the laser sheet was aligned in the x-direction to the x-location of the calibration plate within the channel by moving the traverse carriage. The vertical alignment of mirror M4 was sometimes adjusted to ensure that the light sheet contacts the mirror slit attachment, and further fine tuning was required to ensure that it struck the mirror slit corresponding to the desired measurement height.

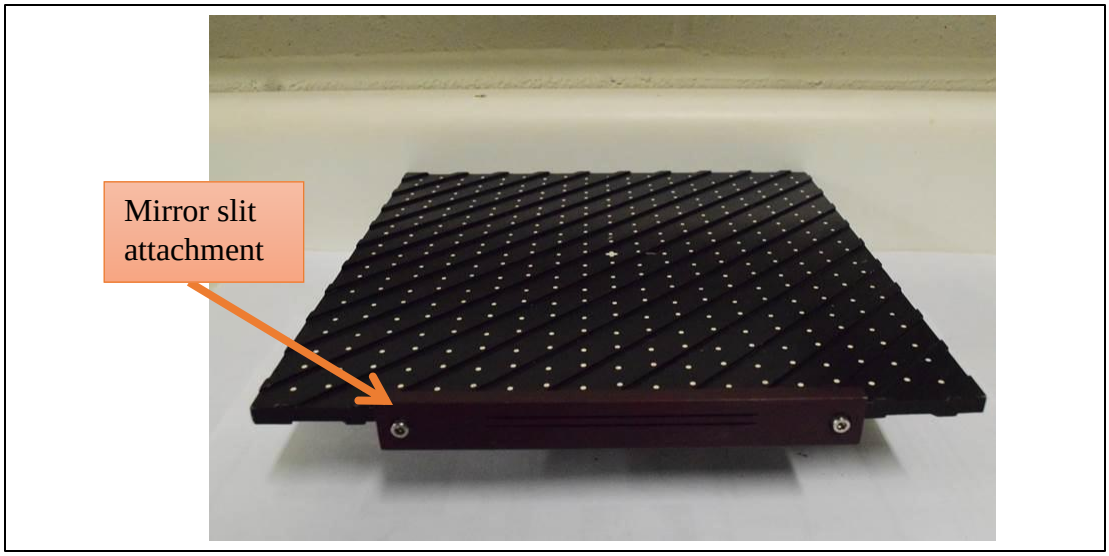

Figure 2-7: Picture of TSI calibration plate with mirror slit attachment

Following that, two checks were performed to evaluate the variation in the height of the light sheet relative to the channel bottom surface. The first check required that the front face of the mirror slit attachment be moved to align with the spanwise edge of the measurement domain furthest from the incoming light sheet to estimate the variation in height of the light sheet across the channel width. The second check required moving the traverse to align the laser sheet in the x-direction with the calibration plate at the furthest downstream measurement location. This gave the variation in height of the light sheet along the streamwise direction of the channel. Similarly, the first check could be performed at the furthest downstream measurement location. Vertical alignment of the M4 mirror affected the height of the laser sheet across the channel width whilst the alignment of the M3 mirror affected the variation in height along the streamwise direction.

Ideally, the height of the light sheet should be the same in all four locations (two streamwise and two spanwise locations) examine. Practically, a minimum deviation of 0.1° in the light sheet across a distance of 9δ in the streamwise direction with respect to the wall parallel plane was desired. A larger tolerance in deviation angle was accepted in the spanwise direction at a minimum of 0.5°. This translated to a deviation in z height of roughly 30 wall units in the streamwise and 40 wall units in the spanwise direction respectively.

In the case where the adjustment of both the M3 and M4 mirrors was insufficient to achieve the aforementioned condition, the heights of the mirrors M3 and M4 with respect to the bottom wall of the channel was adjusted. Typically, when this occurred, the heights of the spherical lenses S1, S2 and S3 with respect to the bottom wall of the channel were also adjusted to ensure that the beams hit the center of these lenses.

2.2.3 Data acquisition system and synchronization

Two computers were required to operate the PIV acquisition system. One computer was dedicated to PIV image acquisition (referred to as the acquisition computer) whilst the other was used for controlling the traverse (referred to as the traverse computer). The cameras were connected to the acquisition computer through a 64-bit Sapera Frame Grabber. Data transfer from the cameras was handled through TSI's software (Insight 4G). The cameras were synchronized with the laser pulses via triggers generated by two Berkeley Nucleonics (BN) pulse generators (Models 500-A and 500-C, see figure 2-8). A TSI LaserPulse synchronizer (Model 610034, figure 2-8) was on the receiving end of the triggers from the BN pulse generators as well and served as a conduit for triggering the camera acquisition.

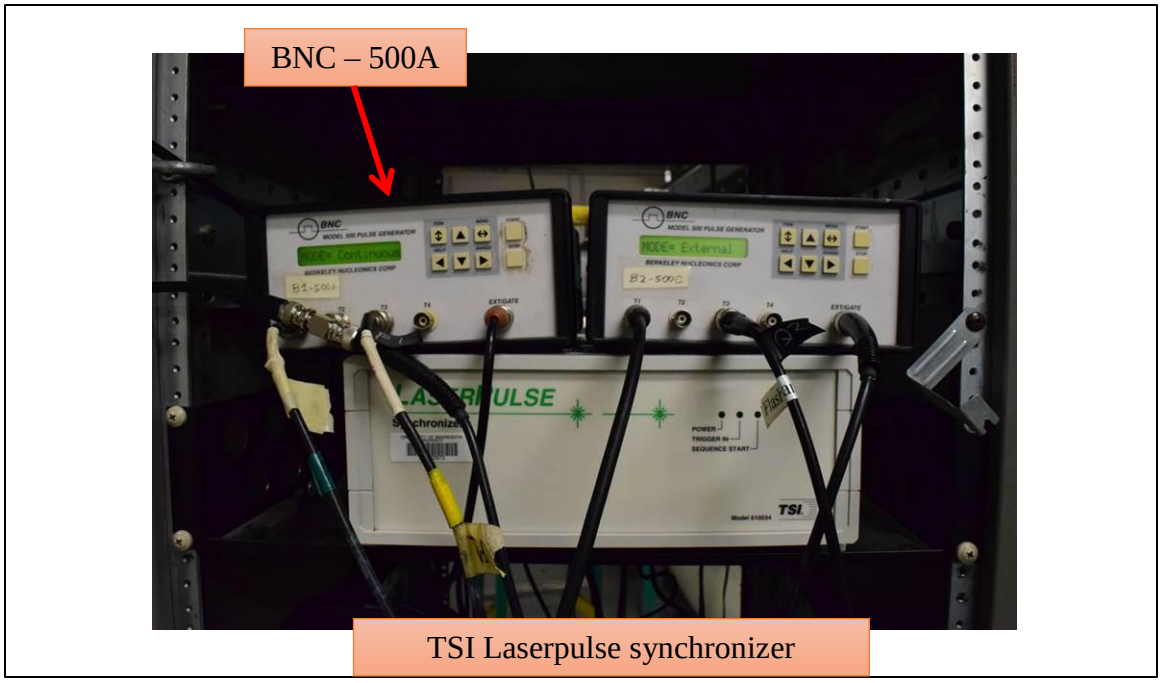

Figure 2-8: Picture of PPIV and SPIV synchronization components

The primary BN box, model 500-A was designated as the master box providing the signal source, and was operated in continuous mode. In the continuous mode of operation, the primary BN box was started manually by hitting the start button on the BN box. The four output ports on it are labeled as T1, T2, T3 and T4, while the single input port provides a means for the primary BN box to be externally triggered, although this was not used in this case. The T1 and T3 ports were used to trigger flash lamp 1 (F1) and flash lamp 2 (F2) on the laser. T2 was connected to the input port of a separate BN pulse generator (model 500-C) which serves as a slave box operating in the external trigger mode. The T2 signal was also split to trigger the camera.

The slave BN box also has four output ports designated (S1-4), where ports S1 and S3 were used to trigger the Q-switches on the heads of the lasers designated Q1 and Q2. The

repetition frequency of the slave box was determined by the repetition frequency prescribed in the settings of the master BN box. The camera trigger signal originating from the T2 port was split two-ways with one going to the external trigger port on the TSI LaserPulse synchronizer and the other to the external trigger on the 64-bit Frame Grabber mounted within the acquisition computer. An illustration of the timing diagram used for PPIV and SPIV is shown in Figure 2-9. The optimum Q-switch time delay, Δt_d for maximum power output on the laser was 180μs.

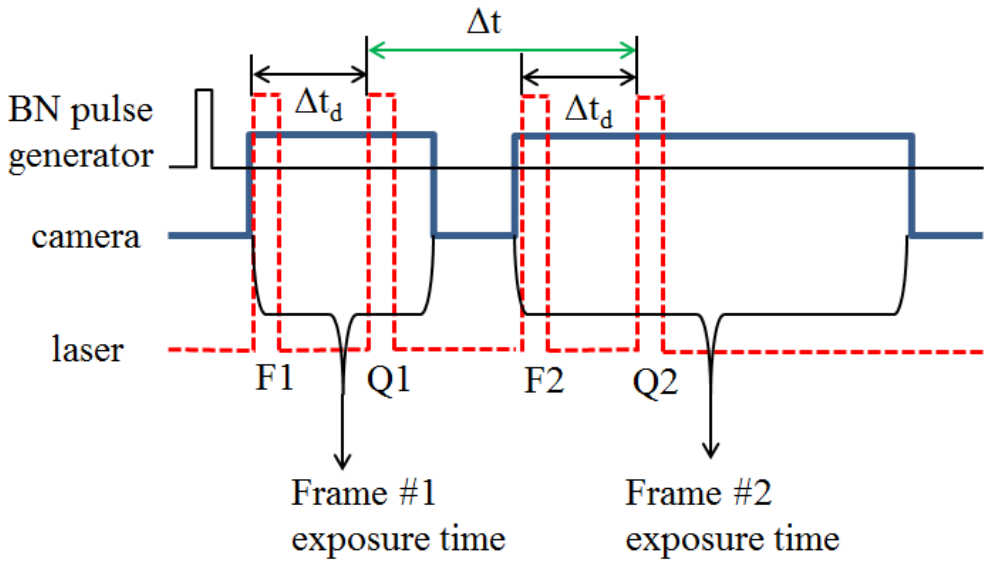

Figure 2-9: Timing diagram for PPIV and SPIV

2.2.4 FPIV setup and synchronization

The FPIV data acquisition system required additional components and modifications to the synchronization methodology. The FPIV acquisition system was designed to track a region of fluid along the streamwise direction, starting at the same location for every run. The key challenge was to synchronize the PIV triggering with the exact traverse location.

This step was integral to ensure that separate runs could be compiled and statistically analyzed.

The main components used for synchronizing the PIV system with the traverse location included a magnetic proximity switch (Littelfuse Inc, MDSM-4R-12-18, Figure 2-10) coupled with a Dual D-Type Flip Flop Chip (Texas Instruments, SN74S74, Figure 2-11). The magnetic proximity switch was mounted on the frame of the water channel (Figure 2-11). A magnet was attached to the body of the traverse carriage via a cantilever rod at a height aligned to match with the location of the proximity switch.

As the traverse moved along the streamwise direction, the magnet would trigger the proximity switch briefly, sending a pulse which set the flip flop chip. The flip flop chip was powered by a 5V power supply shown in figure 2-12a. Prior to the input to the flip flop chip, the signal from the magnetic switch passed through a low pass filter (Frequency Devices model 9002, figure 2-12a) set to 8 kHz to eliminate high frequency content detrimental to detecting the passage of the magnet on the traverse carriage. When the input of the flip flop chip saw a transition to high, then to low again, it set the initially low output of the flip flop chip to high. The output of the flip flop chip was then connected to the input port of a function generator which served as a gate (Exact Model 200MSTPC, figure 2-12b). A sketch of the circuit diagram for the flip flop chip and its connectivity with various other components are shown in Figure 2-13.

The function generator only output pulses when the incoming signal from the flip flop chip was high. Initially, the BN pulse generator was used directly as it too also had a gate function, but for undetermined reasons, there was an unpredictable delay of ~10ms – 100ms between the positive edge input trigger to the time when it began outputting

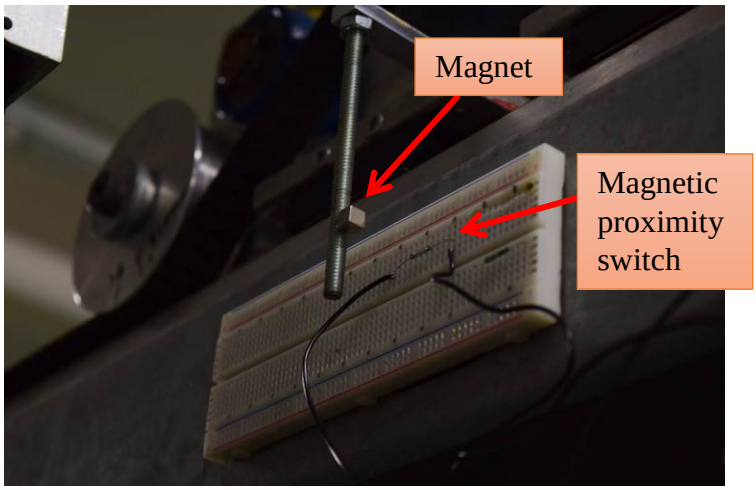

Figure 2-10: FPIV synchronization components

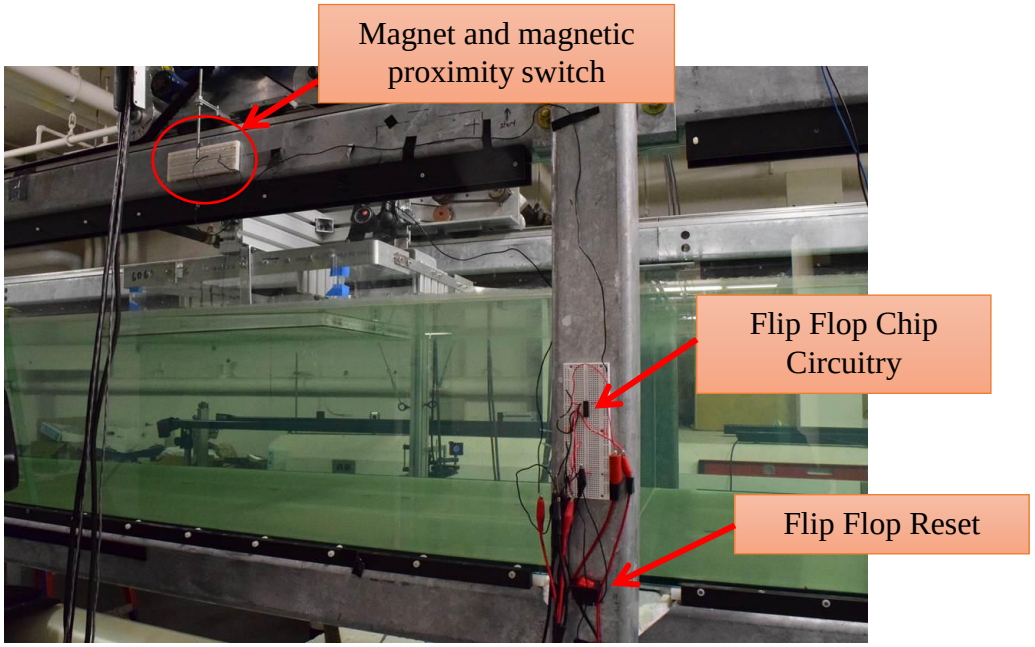

Figure 2-11: Picture of the location of the magnet and magnetic proximity switch, flip flop chip circuitry and the flip flop reset switch

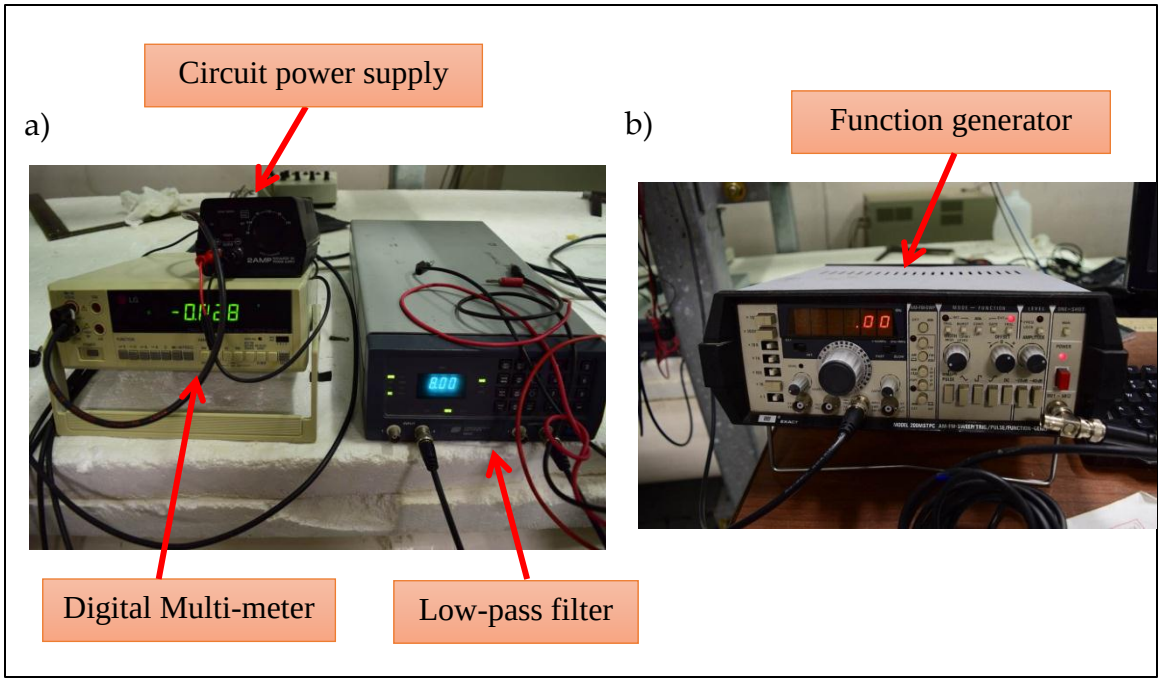

Figure 2-12: FPIV synchronization components, a) picture of circuit power supply, and frequency devices low pass filter, and the digital multi-meter used to monitor the flip flop chip's output state. b) Picture of function generator.

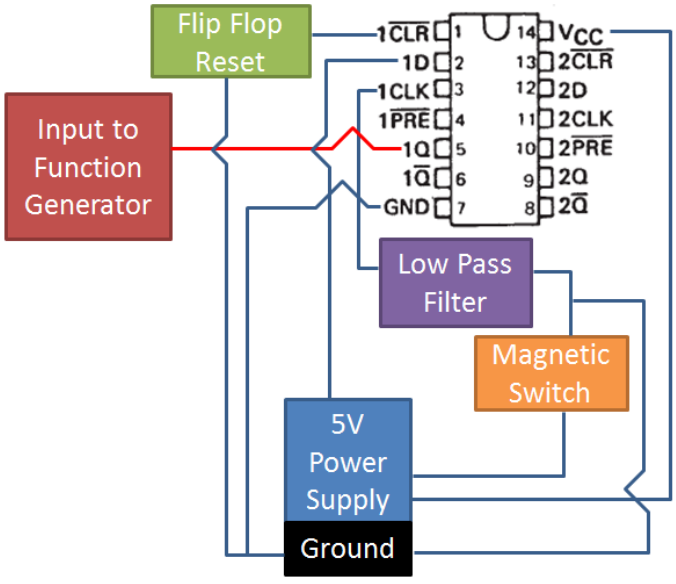

Figure 2-13: Sketch of circuit for flip flop chip, illustrating connectivity between various components.

pulses. This caused a large uncertainty in the start location of the PIV triggering. Interestingly, operating the BN pulse generators in external triggering mode was delay free. Thus, to avoid the uncertainty due to the timing delay, the function generator was used to output pulses to trigger the BN pulse generators.

The function generator was set to output pulses at an interval of 7.43 Hz (measured on a digital oscilloscope). This specific acquisition frequency was determined from a trial and error process and was found to stably trigger the frame grabbers for the TSI cameras in 'capture to memory mode'. Operating in this mode allowed the cameras to acquire at a faster rate as data were saved to the on-board memory on the acquisition computer as opposed to transferring the images directly to the acquisition computer's hard drive. Once a run was completed, the flip flop chip had to be reset manually by grounding the first pin on the chip. The reset switch is shown in Figure 2-11.

The uncertainty in the starting location for separate runs was quantified by comparing the pixel locations of images of known markers within the channel test section between separate runs. The resulting uncertainty in starting location was small. The worst case was evaluated to be 0.3mm or 5 pixels. This uncertainty had only a minimal effect on subsequent statistical analyses of the compiled FPIV runs.

With the above processes in place, a separate issue related to transient laser power at the start of every run needed to be resolved. The problem arises when starting up a run, specifically when the PIV triggering begins cold (i.e long time interval between separate runs). In this situation, the laser takes a substantial amount of time (~ 10δ at traverse speed ~ 0.37m/s) to reach maximum output power. This resulted in relatively poor illumination at the beginning of the run versus the end of the run, causing errors to

propagate into the vector fields. In order to mitigate this, a pre-triggering routine to warm up the laser was followed before activating the PIV triggering system.

The warm up routine required another BN pulse generator (Model-500D, Figure 2-14) to keep the laser firing whenever the input gate signal remained active. The input gate of the BN pulse generator was enabled and connected to the breakpoint trigger output on the traverse controls, via the traverse National Instruments card (see Fig. 2-15). The breakpoint trigger was used to output a low or high signal when the relative encoder count exceeded a threshold set by the user. The encoder counts correspond to the streamwise location of the traverse. The break point location was deliberately set at a streamwise location upstream of the point where PIV triggering began corresponding to the magnetic proximity switch location. This allowed sufficient time for the warm up routine to be disabled, and for the PIV triggering to begin. In this specific application, the unknown delay in the triggering from using the gate function on the BN pulse generator was not critical. This was because the offset in streamwise location between the break point trigger and the start of the PIV triggering exceeded the maximum of the unknown time delay introduced. All in all, this method allowed the laser to quickly reach maximum output power, which substantially improved the illumination throughout the FPIV run. A summary of the various steps required to complete a run is shown in the block diagram in Figure 2-16.

2.2.5 Calibration

Two separate dual-plane calibration plates (Fig. 2-17) were used depending on the measurement height of the corresponding experiment. The laser sheet was aligned to the region between the first and second planes of the calibration plates.

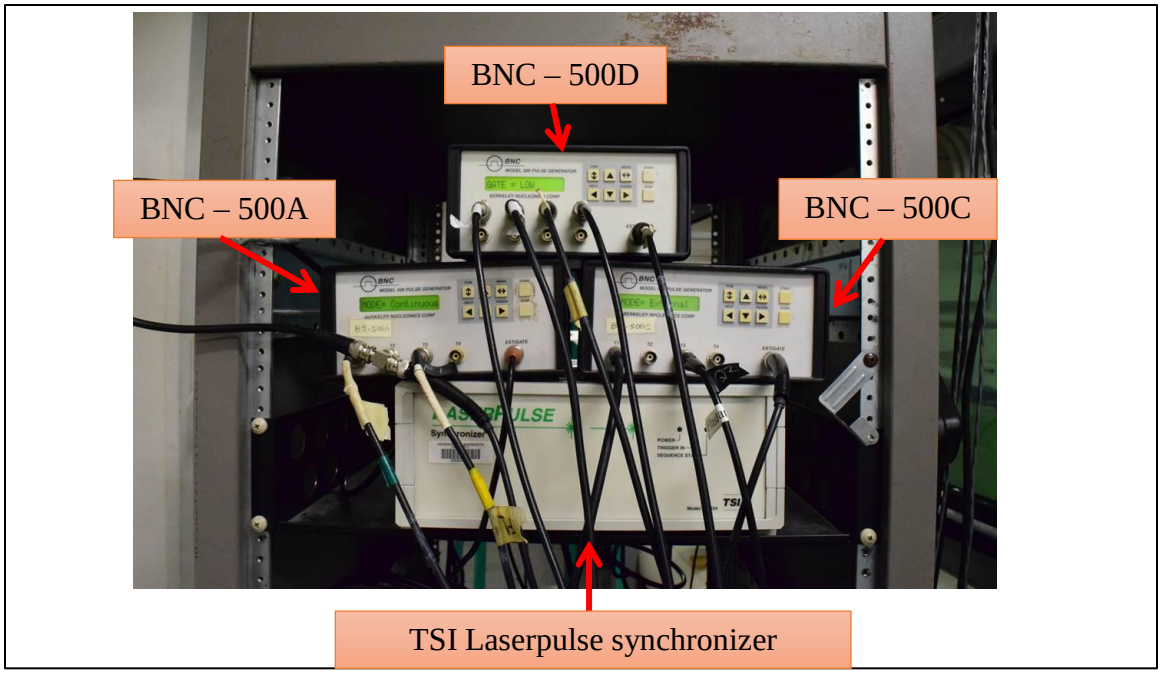

Figure 2-14: FPIV synchronization components used, note the BNC model 500-D which has 8 output channels.

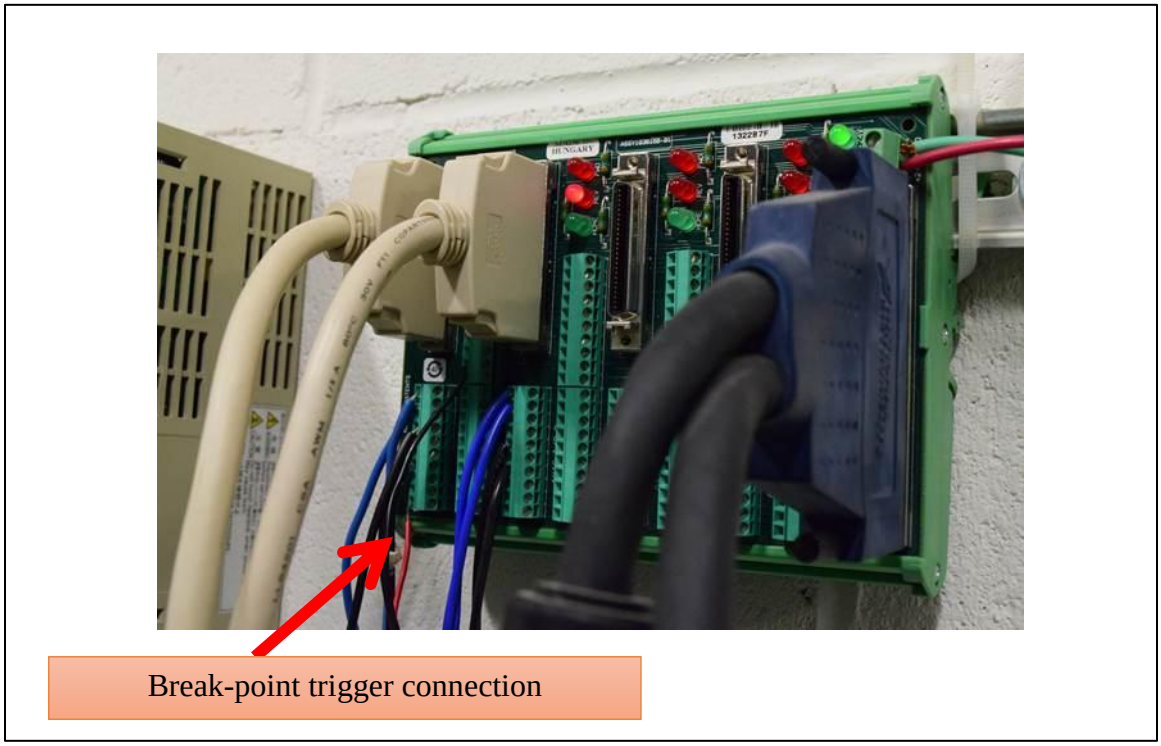

Figure 2-15: National instruments card in Lab 30A and break point trigger in.

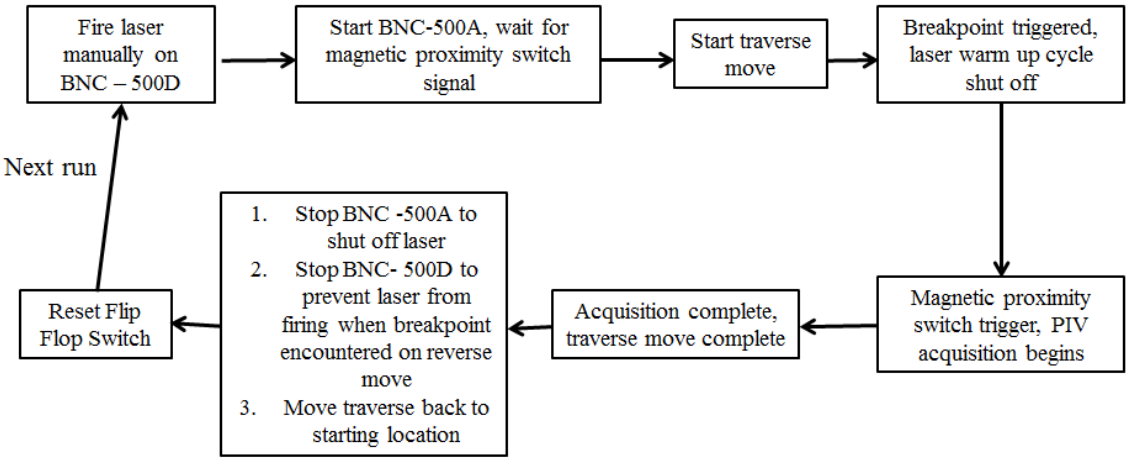

Figure 2-16: Block diagram of steps to complete a run for FPIV measurements

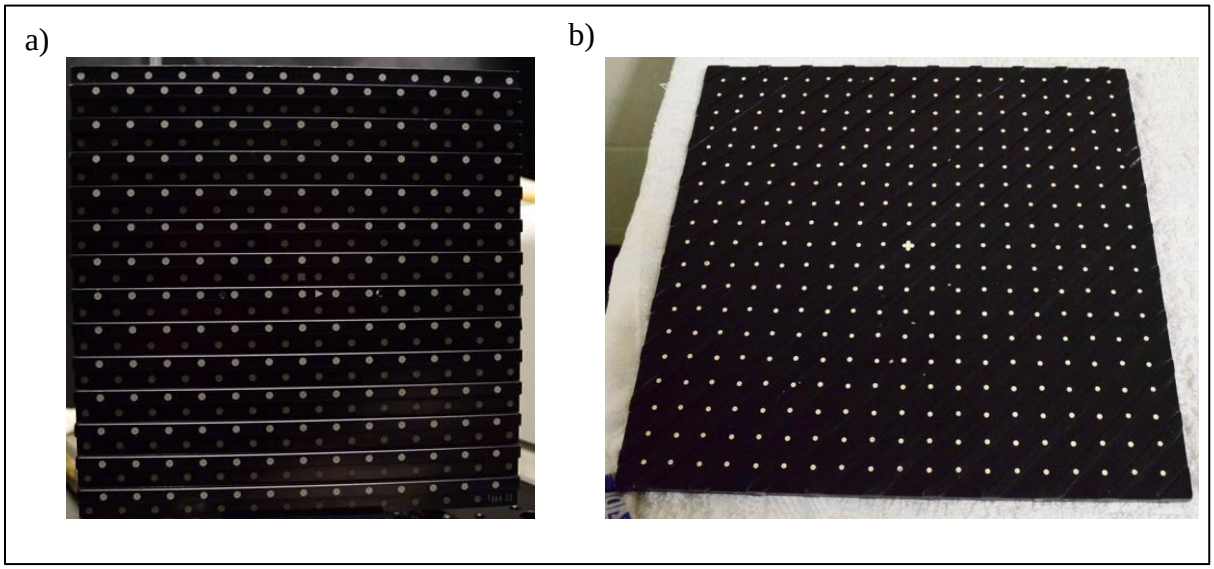

Figure 2-17: Pictures of a) LaVision and b) TSI calibration plates.

For the measurements at height z^+ = 300 and 500, the LaVision type 22 dual plane calibration plate was used. For z^+ = 125, calibration was not possible using the LaVision calibration plate due to its thickness. With the calibration plate placed directly on the bottom wall, the calibration plane closest to the wall was higher than z^+ = 125. Thus, a

thinner TSI calibration plate was used instead, which required custom input parameters of the calibration target size and spacing into Davis (version 8.1.4), the PIV processing software by LaVision.

The calibration plate used was carefully aligned to ensure perpendicularity to the channel side wall. This was achieved by using steel framing squares. For the PPIV experiments, the two cameras together captured a field of view much wider than the width of the calibration plate, thus two separate calibration images were acquired for each camera. In contrast, the SPIV measurements only required a single capture as the FOVs were overlapped. Additionally, the SPIV calibration was subjected to self-calibration (Wieneke 2008) to correct for possible misalignment of the calibration plane with respect to the plane of the laser sheet. All calibration images were acquired in the flow 'on' condition at experiment flow speeds to account for the tilting of the interface box due to the forcing from the flow where the box was partially immersed in water.

For all experiments, the calibration acquired at $x = 0$ was used for data acquired at the other stream-wise locations. This is fairly reasonable as the bottom wall of the channel was assessed to be relatively flat in the region where measurements were acquired (Gao 2011). Furthermore, for data collection runs taken within hours from one another, the same calibration was used.

2.2.6 Data processing

All PIV data was processed using Davis (version 8.1.4). The raw images were masked to remove the edges of each field of view. Then, image pre-processing was used to suppress noise present in the cropped raw images. A sliding background subtraction was used to

suppress large scale intensity fluctuations in the background while preserving the high frequency fluctuations in intensity corresponding to the particle locations. Additionally, a min/max filter also known as particle intensity normalization was used. This filter determines the upper and lower bounds of the local image intensity within a specified neighborhood, subtracts the lower bound and normalizes the local image intensity with the difference between the lower and upper bounds, thus maximizing the dynamic range of the digital image field (Adrian & Westerweel 2011).

For the SPIV and PPIV datasets, a multi-pass interrogation strategy was used where the initial window size was 64 x 64 pixels then reduced to 32 x 32 pixels for the final passes. An overlap of 50% were used for the interrogation windows, resulting in a vector spacing of L_v = 1.2 mm, or L_v^+ = 23. For the FPIV data sets, the interrogation size was chosen to be 48 x 48 pixels with a 50% overlap. The corresponding vector spacing was L_v = 1.7mm or L_v^+ = 34. The resolution was twice the vector spacing due to the 50% overlap.

The resulting vectors were post processed using both median filters and velocity range filters to remove outliers from erroneous correlations. First, three passes of a 3 x 3 median filter were applied to remove vectors with absolute magnitudes greater than 3 times the standard deviation of the neighboring vectors. After this post-processing step in DAVIS, the PIV vectors were fed through a filtering routine developed in Matlab. The Matlab algorithm removed outliers that were 3σ away from the mean of that data set. Then, the time averaged mean and standard deviation were re-computed. These statistics were then fed to the global velocity range filter in DAVIS, and applied to remove and replace vectors that were ±3σ away from the re-computed mean. Typically, most of the filtering and replacement occurred on the edges of the PIV field.

A substantial portion of the velocity data analysis was performed in Matlab. A small non-zero component in spanwise mean velocity was present in most of the data sets acquired. This was most likely caused by a misalignment of the view of the cameras with the flow direction, and was accounted for via a rotation (< 0.2°) of the vector fields in Matlab, the magnitude of rotation was selected such that the mean spanwise velocity was reduced to zero.

2.2.7 Uncertainty analysis of PIV experiments

The instantaneous vectors from PIV were affected by two sources of uncertainty. The first source was from the calibration. The error was estimated to be ~0.1 pixels from a root mean square fit error of the third order polynomial fit for the calibration markers in DAVIS. The second error originated from the random error in estimating the subpixel location of the correlation peak. For a 32 x 32 interrogation window size, the error, P_0 is typically about 0.1 pixels (Willert 1996; Westerweel 1997). Both errors were propagated using the square root of the sum of the squares method, resulting in an uncertainty of 0.14 pixels for the instantaneous vectors. For the SPIV results, the uncertainty of the out of plane component of velocity is a function of the angle α between the central line of sight of the camera to the z-axis, and the uncertainty of the in-plane velocity component. As α for the SPIV measurement was ~ 30^o, the uncertainties in the out of plane velocity components were greater than the in-plane velocity components (Prasad 2000), such that the errors of each velocity component are a function of P_0 and α, resulting in the following relations:

$$P_u = P_0/(2)^{0.5} \quad (2\text{-}1)$$

$$P_v = (2/3)^{0.5}P_0 \quad (2\text{-}2)$$

$$P_w = (2)^{0.5}P_0 \quad (2\text{-}3)$$

resulting in uncertainties of $P_u = 0.0084U_\infty$, $P_v = 0.0096U_\infty$ and $P_w = 0.017U_\infty$ for the instantaneous SPIV vectors. The values of the uncertainty for the instantaneous vectors did not vary much with measurement height, as changes to magnification were minimal. For the PPIV measurements the uncertainty was estimated to be $0.012U_\infty$ for all components of the instantaneous vectors.

The mean velocity statistics were also affected by uncertainty, and dominated by the random uncertainty following the equation below.

$$\delta u, v, w = \pm \frac{1.96\sigma}{\sqrt{N}} \quad (2\text{-}4)$$

σ is the standard deviation of the corresponding velocity component while N represents the number of statistically independent realizations in the data set. The uncertainty in the mean velocity statistics for SPIV measurements were $0.009U_\infty$ for $\bar{U}$, $0.005U_\infty$ for $\bar{V}$, and $0.008U_\infty$ for $\bar{W}$. For the PPIV measurements, the uncertainties in mean velocities were determined to be $0.005U_\infty$ for $\bar{U}$ and $0.003U_\infty$ for $\bar{V}$.

The uncertainty interval in the root mean square (RMS) velocity statistics were estimated using a chi-squared distribution following the equation:

$$\frac{(N-1)\sigma^2}{\chi^2_{\gamma,\beta/2}} \leq \sigma^2_{u,v,w} \leq \frac{(N-1)\sigma^2}{\chi^2_{\gamma,1-\beta/2}} \quad (2\text{-}5)$$

where σ is the standard deviation of the corresponding velocity component and N is the number of realizations. χ^2 is the Chi-Squared distribution, acquired for $\gamma = 999$,where γ is the number of degrees of freedom (N-1), and $\beta = 0.025$ for a 95% confidence level.

The uncertainties for the sample RMS velocities were fairly small. For both the PPIV and SPIV measurements, the estimated uncertainty for the streamwise RMS velocity was $0.004U_\infty$ while the spanwise RMS velocity uncertainty was $0.0025U_\infty$. The SPIV wall normal RMS velocity uncertainty was estimated to be $0.005U_\infty$. The uncertainties are tabulated in Table 2-5 below.

Table 2-5: Estimated velocity uncertainties for SPIV and PPIV measurements

	SPIV	**PPIV**	**3-D PTV**
$\delta\bar{U}/U_\infty$	0.009	0.005	0.010
$\delta\bar{V}/U_\infty$	0.005	0.003	0.005
$\delta\bar{W}/U_\infty$	0.008	N/A	0.014
$\delta u_{rms}/U_\infty$	0.004	0.004	0.004
$\delta v_{rms}/U_\infty$	0.003	0.003	0.003
$\delta w_{rms}/U_\infty$	0.005	N/A	0.007
$\delta u/U_\infty$	0.008	0.012	0.010
$\delta v/U_\infty$	0.001	0.012	0.010
$\delta w/U_\infty$	0.017	N/A	0.030

2.2.8 Data reduction methodology

This section details the reduction techniques used to treat and reduce the data for analysis.

2.2.8.1 Fourier method for extracting dominant spanwise modes

A Fourier method for extracting the dominant spanwise modes (Zheng 2011) was used to reduce the PPIV data for analysis. First, the instantaneous deviations in streamwise

velocity with respect to the local mean velocity, $\bar{U}$ were computed. Then, the spanwise slice of streamwise velocity at every streamwise location was subjected to a low pass filter to minimize aliasing errors while applying the Fourier transform. The parameters for the low pass filter corresponded to the maximum wave number k_{max} divided by 2, as per Nyquist's Theorem. Wavenumber is defined as $k = 2\pi/\lambda$ where λ is wavelength. The wavelength λ is equal to the vector spacing $L_v = 1.1$mm for k_{max}, the maximum resolvable wave number. This can change depending on dataset, and measurement height, and is computed for every dataset. Then, the filtered streamwise fluctuations at every streamwise location were Fourier transformed to the wave number domain.

Two key issues were addressed by Zheng (2011) in the application of this analysis. Firstly, the span of the FOV limits the longest resolvable wavelength, and thus defines a minimum resolvable wave number $k_{min.}$ Thus the non-zero energy content contained within the band 0 to k_{min} was deemed unphysical and subsequently set to zero. In a similar manner, the energy content for wave numbers larger than $k_{max}/2$ cannot be resolved by the PPIV, and thus was set to zero as well.

The second issue relates to the coarse resolution when examining wave numbers close to $k_{min.}$ This was attributed to the evenly spaced wave number domain, which when transformed into real space corresponds to unevenly spaced intervals (see Zheng 2011). Thus, a curve fit was applied incorporating points adjacent to the detected peak associated with the most energetic mode (largest energy amplitude). Five points were considered for the curve fit, including the detected peak. This was necessary to extract a continuous distribution of the dominant spanwise modes as a better resolution may be attained through this method. The wavelength associated with the maximum of the

resulting curve fit was selected as the dominant spanwise mode. An example of this is given in Figure 2-18. The figure shows the result from Fourier transforming an instantaneous spanwise slice of streamwise velocity at a single x-location. The peak (green cross) from the curve fit (red) was shown to be the selected dominant spanwise mode. This method was applied to every spanwise slice of streamwise velocity at every streamwise location and for all realizations, resulting in a distribution of the dominant spanwise modes.

The peak fitting process was improved by conditionally adjusting the number of points required in the curve fit, based on the amplitudes of the points adjacent to the detected peak. Initially, five points were considered for the curve fit, consisting of the two points on either side of the detected peak and the detected peak itself. Based on many qualitative assessments of the curve fit on the data, in some cases, a four point fit worked best, while in others a three point fit was sufficient. Building off of that information, the following strategy was devised to improve the curve fitting. The sign of the difference in amplitudes between the two points on the left/right side of the detected peak decides whether the first/last point would be omitted in the curve fit. The evaluated slope should be positive from left to right on the left side of the detected peak, while it should be negative from left to right on the right side of the detected peak. For example, see figure 2-18. Here, to the left of the detected peak (black cross), the two points had a negative difference, and the result of using five points is shown in the black curve. The red curve on the other hand omits the left most point, as it failed the aforementioned criteria set, and the resulting fit appears more reasonable with the selected dominant mode being at the green cross. This method was similarly applied to the right portion of the curve.

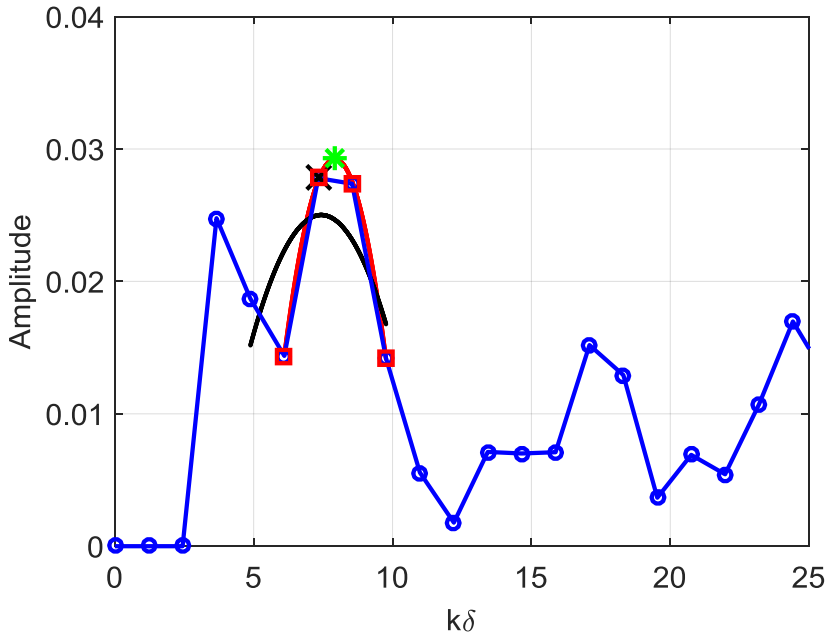

Figure 2-18: Example result of Fourier transform on a spanwise slice of streamwise velocity at a single x-location (blue curve). Black cross denotes detected maximum. Black curve shows result of fit using five points. Red curve denotes conditional curve fit, and green star shows the final selected dominant spanwise mode.

Separately, another curve fitting issue was addressed which concerned the band 0 to k_{min} that was set to zero. In some instances, the dominant mode occurs very close to k_{min}, resulting in the left most points of the curve fit to include points within the band that was set to zero energy content (e.g. Fig. 2-19). A fit in this scenario was not possible due to the ambiguity in one-sided fits. Therefore, this scenario is excluded from the statistics to improve the accuracy on the estimation of the dominant spanwise modes.

Finally, the extracted dominant spanwise modes for every instance and every streamwise location within a measurement zone was binned and analyzed. A bin size of 0.1δ was found to work well in suppressing noise while retaining sufficient resolution between spanwise modes for analysis of spanwise content in the data.

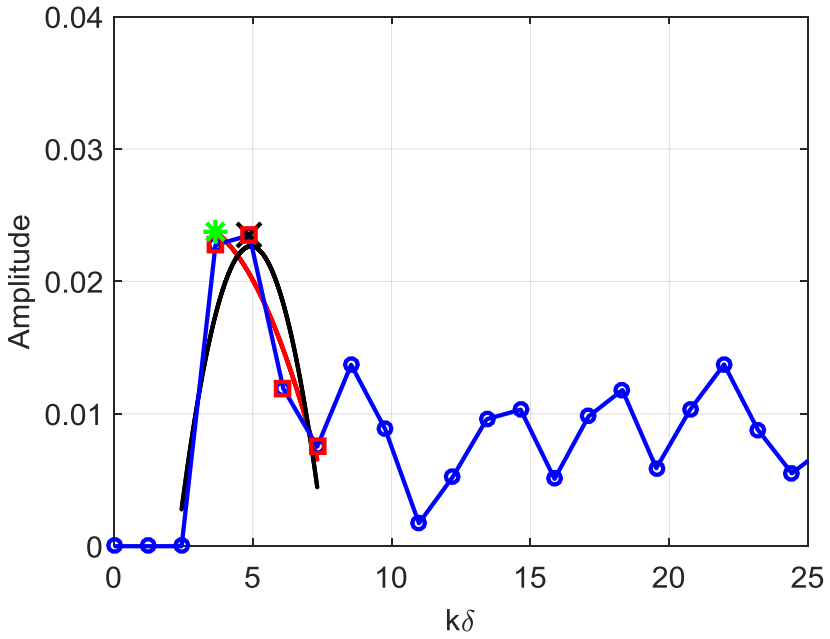

Figure 2-19: Sample Fourier transform result from dominant spanwise mode analysis. For legend see figure 2-18. Neither red curve nor black curves fit well close to k_{min}.

2.2.8.2. Vortex packet signature identification algorithm

A vortex packet signature identification algorithm (VPIA) was developed to quantitatively investigate vortex packet recovery downstream of the narrowly spaced (S = 0.2δ) cylinder arrays. The algorithm employs aspects of multiple features to detect and extract individual vortex packet signatures from wall parallel measurement planes in both unperturbed and perturbed velocity fields derived from the PPIV measurements. The terms packet and packet signatures are used interchangeably in this dissertation.

As the VPIA was to be used for comparison purposes, i.e. perturbed vs. unperturbed flow, the goal was to identify only 'individual' packet signatures not complicated by spanwise merged or merging structures. In addition, packet signatures intersecting the spanwise edges of the PIV fields were not considered. Furthermore, the algorithm was devised to be restrictive, i.e. the strategy was to minimize false positives, rather than to

identify every individual packet signature within the data. Under this restriction, the aim was to capture as many individual packet signatures as possible. Based on previous literature (Ganapathisubramani *et al.* 2003; Tomkins & Adrian 2003) and with present experience analyzing many instantaneous streamwise-spanwise fields, packet signatures were defined as coherent slow moving regions bounded by counter rotating swirls (signed by wall-normal vorticity direction). In this context, swirl or swirling strength is defined as the imaginary part of the eigenvalues of the two-component velocity gradient tensor (Zhou *et al.* 1999) where in this case, swirling structures could be cross sections of hairpin necks or legs. The essence of the algorithm is to employ image processing functions to automatically extract and catalogue packet signatures with criteria guided by experience viewing many instances of packet signatures. The algorithm was conditioned based on packet signatures observed in unperturbed flow, then applied to both unperturbed and perturbed data.

The algorithm description is as follows:

Step 1: A threshold was applied to the PIV velocity data to identify regions of $U < 0.95\bar{U}$ where $\bar{U}$ is the mean velocity at the measurement height.

Step 2: The thresholded velocity field was binarized, and Matlab image processing functions were used to detect connected regions. The resulting output corresponding to the sample field in Figure 2-20a is shown in Figure 2-20b.

Step 3: Erosion and dilation were performed on the structures identified to separate weakly connected regions. The resulting output from this step is shown in Figure 2-20c.

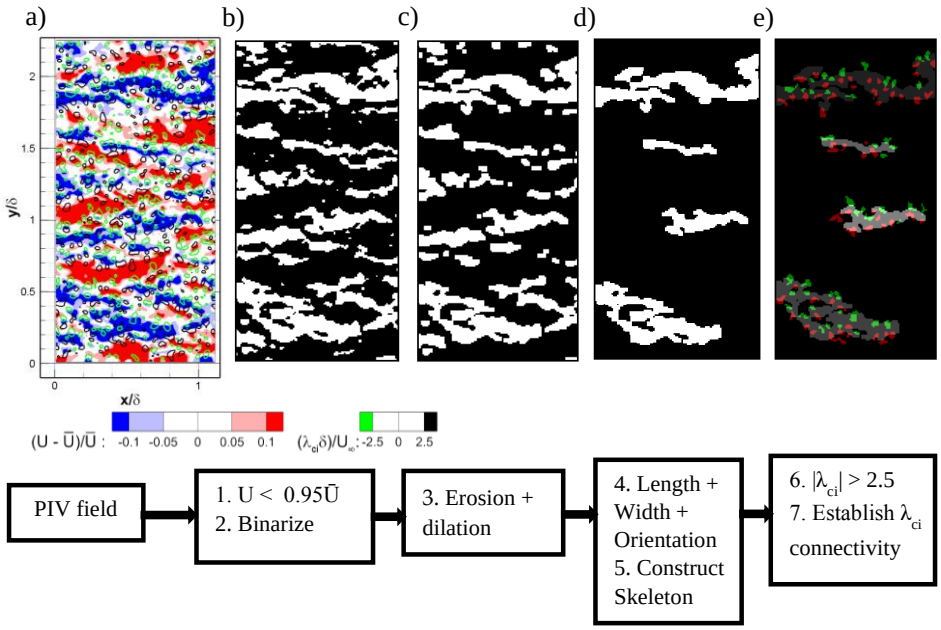

Figure 2-20: VPIA process on a sample field. a) Sample input to VPIA, intermediate outputs after b) steps 1-2, c) step 3, d) steps 4-5, e) after steps 6-7

Step 4: The length, width and orientation of the detected regions were computed. The length and width were determined based on the streamwise and spanwise extrema of the detected region respectively. The orientation was determined by fitting an ellipse to the outline of the structure, and taking the angle between the major axis and the streamwise direction. Minimum thresholds were set for the length (0.5δ) and width (0.05δ) in order to extract structures with significant streamwise and spanwise extent. The length threshold was designed to include structures with a minimum of about five hairpins based on streamwise spacing between hairpin heads reported by AMT (2000). The width threshold was based on the finding of Tomkins & Adrian (2003) that coherent low speed regions at $z^+ = 100$ typically exceeded 0.04δ in width. Additionally, structures with large spanwise inclinations to the streamwise direction (β >25°) were removed as packet

signatures in unperturbed flow tend to have little spanwise inclination (see e.g. Tomkins & Adrian 2003). The output of Steps 1 through 4 applied to a sample unperturbed field is shown in Figure 2-20d.

Step 5: Streamwise scans of the remaining structures were performed in order to construct a skeleton. First, the width of the structure at every streamwise location was computed and averaged, to acquire an estimate of the mean width. Then, the skeleton was constructed by connecting regions for which the local width was greater than 50% of the mean width. Structures with large gaps in the skeleton (>245 wall units or 0.1δ) were removed as they did not look like packet signatures in the unperturbed flow. An example of a detected skeleton in unperturbed flow is shown in Figure 2-21a. Figure 2-21b shows an identified structure from perturbed flow that was removed due to the large gap in its skeleton.

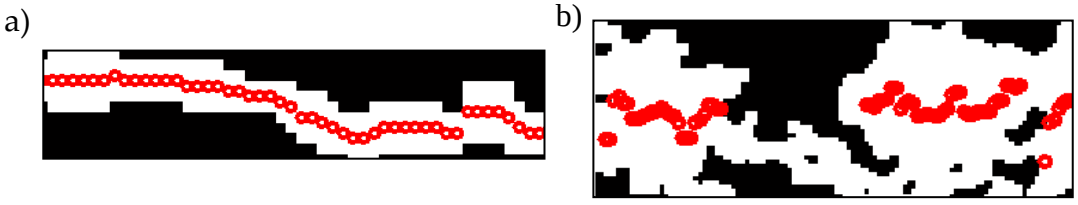

Figure 2-21: Sample skeletons acquired from the streamwise scan of the structure width

Step 6: The swirling strength, λ_{ci}, was computed where the velocity gradients were obtained via central difference and normalized by the freestream velocity and δ. A threshold of $|\lambda_{ci}| > 2.5$ was applied, and the resulting swirl fields were binarized. This threshold was selected to suppress noise whilst retaining as many swirl structures as possible. Using similar connection and extraction methods as in steps 1-2, all swirling structures were separated and labeled. The minimum length and width of the detected

swirl structures based on the extrema was set at 3 grid points (75 wall units) to suppress noise. The minimum length and width of the detected swirl structures was set at 3 grid points (75 wall units or 0.03δ) to suppress noise.

Step 7: Swirling regions that overlapped low momentum regions (LMRs) were identified. Prior to swirl identification, the low momentum regions were dilated with a rectangular kernel of length 5 (123 wall units) and width 3 grid points (75 wall units). The dilation allowed for swirling structures that were slightly offset from but still associated to the parent LMR to be included. The number of swirls per length ($N_{s/L}$) and the ratio of positive to negative swirls ($N_{s+/s-}$) based on the sign of the wall normal vorticity associated with each LMR were computed. Figure 2-20e shows all swirling structures that have been associated with the detected LMRs.

The steps described above were applied to sets of 100 PIV fields for unperturbed flow at all three measurement heights. Then, the structures identified were compared manually against the original PIV plots that overlaid swirling structures and streamwise velocity contours (e.g. Figure 2-20a). Structures identified by the algorithm were separated into the following categories: packets, non-packets, merging/merged packets, and edge structures. The comparison revealed a number of false positives at each height. To decrease the number of false positives, threshold criteria based on $N_{s+/s-}$ and $N_{s/L}$ were added. The former helped eliminate structures that intersected the spanwise edges of the field, while the latter helped eliminate merged/merging structures. Note $N_{s/L}$ has units of $1/\delta$. Additionally, both criteria were effective at eliminating some structures that lacked associated swirls. The threshold values can be found in Table 2-6.

After applying these additional criteria at $z^+ = 125$ and $z^+ = 300$ in the unperturbed flow, no non-packets were present in the VPIA output from the unperturbed data sets examined. On the other hand, 3% of the detected structures at $z^+ = 500$ were classified as non-packets. At all measurement heights, a small number of structures detected were classified as merged/merging packets. These structures were difficult to remove as their statistics could closely resemble those of individual packet signatures. More restrictive thresholds on $N_{s/L}$ could exclude these structures but only at a cost of losing a greater number of individual packets.

The algorithm, including the additional thresholds on $N_{s+/s-}$ and $N_{s/L}$, was next applied to the perturbed boundary layer data at downstream locations greater than $x/\delta = 2.4$. The algorithm was not applied to locations with $x/\delta < 2.4$ as wakes from the cylinders could be dominant, and they were difficult to exclude from identification by the algorithm. To evaluate algorithm accuracy, the output of the algorithm and PIV data fields centered on $x/\delta = 2.9$ and $x/\delta = 7$ were compared manually, repeating the process followed for the unperturbed data. The comparison showed a large number of false positives associated with wake-like structures. Hence, additional criteria were devised based on examination of many samples. Generally, the false positives (or wake-like structures) tended to have the following visual characteristics:

i. Many enclosed ‘holes’ within structures caused by local zones of larger streamwise velocity
ii. Many appendages attached to main structure
iii. Significant width variation along the streamwise direction
iv. Low aspect ratio
v. Little obvious association between swirls on opposite sides of structure

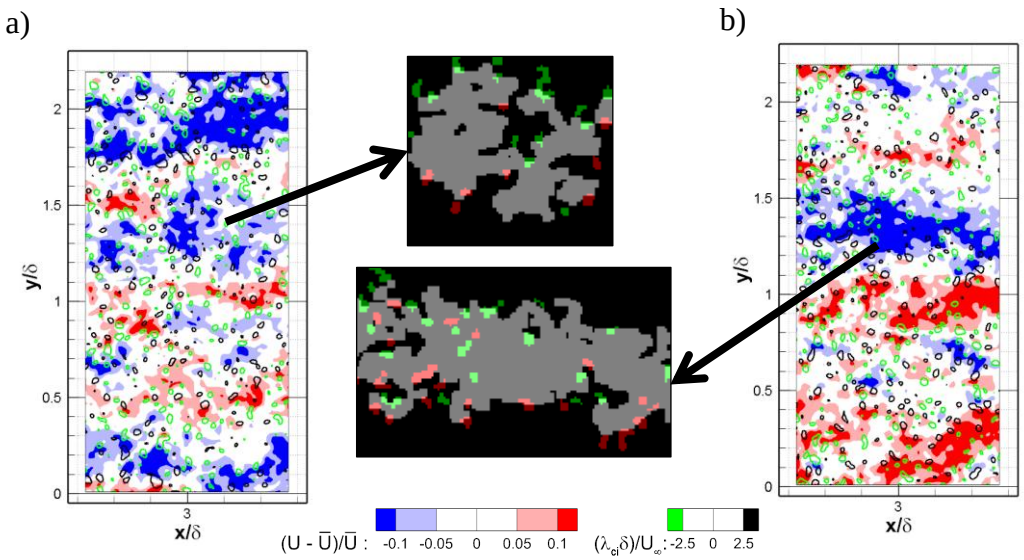

Figure 2-22: Two samples of false detections behind H= δ array at x/δ = 2.9, z^+ = 500. Green and red depict counter rotating swirls within the detected structures; gray contours show region associated with detected structure.

Two examples of false positives from the perturbed data are shown in Figure 2-22. The structure in Figure 2-22a looks highly irregular and has a large width compared to its length. Furthermore, it lacks obvious swirl pairing. The structure in Figure 2-22b, which possibly results from spanwise merging packets, also lacks obvious swirl pairing. In addition, it includes seven holes. In order to filter out structures exhibiting the above characteristics, many criteria were examined, and amongst all criteria tested, the following were deemed most effective at minimizing false positives:

1. **Convex Solidity, S_c**

The ratio of the area of the structure over the area of the smallest possible convex polygon fitted to the outline of the structure. See Figure 2-23.

2. **N_h**

Number of enclosed holes within the structure.

a) b)

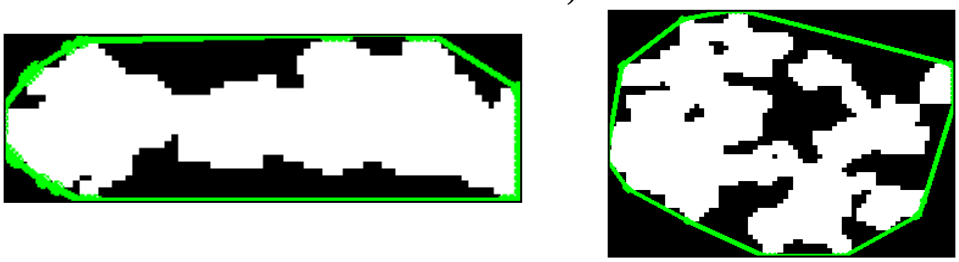

Figure 2-23: Ratio of structure area (white) over area bounded by green line gives the measure of convex solidity. Two sample structures: a) unperturbed, b) perturbed.

3. **A_h**

Ratio of the area of the structure over the area of the structure with holes filled.

4. **L_{sk}/L_{ex}**

Sum of the lengths of identified skeleton segments divided by the distance between the streamwise extrema points.

5. **Mean Width, W_m**

The average of the widths measured at every streamwise location of the structure.

6. **Aspect ratio (AR)**

Ratio of length to width based on extrema points.

The first three criteria (Sc, N_h, A_h) were selected to exclude structures with the first two characteristics (i & ii) listed above. These criteria, which are different measures of structure porosity, work better when applied together. For example, a structure with a single large hole would satisfy the N_h criterion, but would be excluded based on A_h. Meanwhile, the convex solidity measure would exclude a structure with multiple appendages (e.g. Fig. 2-22a), but no holes.

The skeleton length ratio (L_{sk}/L_{ex}) criterion was selected to exclude structures that vary substantially in local width but lack significant streamwise gaps in the skeleton. Recall that the skeleton is constructed only where the local width of the structure exceeds 50% of the mean width. For wavy structures typical of cylinder wakes, the local width can vary significantly over short streamwise intervals yielding short gaps in the skeleton. Therefore, this measure could exclude wavy structures with multiple short gaps (shorter than the threshold used in Step 5).

Separately, the mean width (W_m) was used to exclude structures that were merged or merging with spanwise adjacent structures. The aspect ratio (AR) also performs a similar function while also eliminating structures with lower aspect ratios than typical packet signatures in the unperturbed flow.

A large percentage of the false packet detections were eliminated with the above criteria. Those that remained still included the visual characteristics listed above (i – v). The threshold values could be adjusted to eliminate the remaining false detections, but only at a cost of eliminating many more real packet signatures.

The assigned thresholds for the above criteria are given in Table 2-6. All thresholds were assessed for sensitivity. First, the basic criteria listed in Steps 1 and 4 ($\bar{U}$, L_{ex}, W_{ex}, β) were subjected to variations of 10% of their set threshold values in either direction. Then, the additional criteria ($N_{s+/s-}$, $N_{s/L}$, S_c, N_h, A_h, L_{sk}/L_{ex}, W_m, AR) were subjected to the same tests. Although the absolute numbers of identified packets varied with the threshold values, none of the threshold variations changed the trends in the results presented below.

Based on the assigned thresholds, tests were performed to ascertain statistical convergence for the number of packet signatures detected per field, $N_{p/f}$. Here, we define statistical convergence as being achieved when the variation of $N_{p/f}$ as the number of fields considered increases is bounded within an interval ±2% of the final value of $N_{p/f}$. Estimates for the number of shorter structures (e.g. $0.475\delta < L_{sk} < 0.525\delta$) per field converged by N = 300, while $N_{p/f}$ for structures longer than the field of view converged by N = 800. On the other hand, the number of swirls per field was statistically converged by N = 700.

Table 2-6: Values of thresholds applied to unperturbed and perturbed data at each measurement height.

Criteria	$z^+ = 125$	$z^+ = 300$	$z^+ = 500$
U	$< 0.95\bar{U}$		
$\mathbf{L_{ex}}$	$> 0.5\delta$		
$\mathbf{W_{ex}}$	$> 0.05\delta$		
$\mathbf{W_m}$	$< 0.2\delta$	$< 0.25\delta$	$< 0.3\delta$
$\mathbf{N_h}$	< 4		
AR	> 2	> 2	> 1.5
$\mathbf{A_h}$	> 0.97		
$\mathbf{N_{s+/s-}}$	0.5 - 1.5		
$\mathbf{N_{s/L}}$	15 - 40		
$\mathbf{L_{sk}/L_{ex}}$	N/A	N/A	> 0.77
$\mathbf{S_c}$	N/A	N/A	> 0.58

The results from the VPIA were subject to both bias error and random uncertainty. The bias error was due to over-counting from false positives. To assess over-counting, structures identified from VPIA with criteria in Table 2-6 applied were compared with those identified manually in 100 sample fields. False positives were identified and counted. The greatest number of false positives occurred downstream of the $H = \delta$ array,

x/δ = 2.9, z^+ = 500, corresponding to 0.06/field. Typical values for other cases were 0.02/field.

Random uncertainty was determined for every case and streamwise location. In the unperturbed flow, the random uncertainties were 0.07/field at z^+ = 125, 0.05/field at z^+ = 300 and 0.04/field at z^+ = 500 at all streamwise locations. The random uncertainties for the perturbed flow were slightly larger. Downstream of the H = δ array, the random uncertainty was 0.09/field at z^+ = 125, 0.07/field at z^+ = 300 and 0.06/field at z^+ = 500. As for the H = 0.2δ array, the random uncertainties were 0.08/field at z^+ = 125, 0.07/field at z^+ = 300 and 0.07/field at z^+ = 500. The uncertainties affecting VPIA results for both unperturbed and perturbed flow are given in Tables 2-7 and 2-8 respectively. Relative uncertainties for the perturbed flow were not included in Table 2-8 as values varied with cylinder height, measurement height and streamwise location. The total uncertainty was assessed with the root mean sum of squares methodology to incorporate bias with random uncertainty, where in the vast majority of cases, the random uncertainty was dominant.

Table 2-7: Unperturbed flow. Uncertainty values for number of packets per field, $N_{p/f}$ and $N_{\lambda/f}$ at all measurement heights. Percentage values computed as a fraction of averaged counts over all streamwise locations.

Measurement height, z^+	**$\delta N_{p/f}$**	**$\delta N_{p/f}$ (%)**	**$\delta N_{\lambda/f}$**	**$\delta N_{\lambda/f}$ (%)**
125	0.07	5.0%	0.74	0.2%
300	0.05	5.6%	0.90	0.4%
500	0.04	10.0%	0.81	0.5%

Table 2-8: Uncertainty values for $N_{p/f}$ and $N_{\lambda/f}$ at all measurement heights in the perturbed flow.

Case	Measurement height, z^+	$\delta N_{p/f}$	$\delta N_{\lambda/f}$
H = δ	125	0.08	0.85
	300	0.07	0.83
	500	0.06	0.69
H = 0.2δ	125	0.08	0.93
	300	0.07	0.84
	500	0.07	0.86

2.2.8.3 Two point correlation analysis

The spatial coherence and statistical significance of features within the PPIV velocity fields were quantified using two-point correlations of the fluctuating velocity field considered. The two-point correlation coefficient between two quantities R_{AB} is defined as:

$$R_{AB}(\Delta x, \Delta y) = \frac{\overline{A(x,y)B(x+\Delta x, y+\Delta y)}}{\sigma_A \sigma_B} \qquad (2\text{-}6)$$

where σ_A and σ_B are the standard deviations of the instantaneous fields A and B respectively, Δx and Δy are the separations distances within the plane between the two correlated fields. The overbar represents an ensemble average over all the realizations within a data set. The two-point spatial correlations were computed in Matlab using FFTs. The results were against a result acquired with a direct spatial correlation method which agreed to within machine zero. The correlation coefficient results were normalized by the local standard deviation of the two correlated quantities, and the number of

elements participating in the correlation computation, which varies with the separation distance (Δx, Δy).

In the flow perturbed by the S = 0.6δ array, the extent of the correlated field was refined to include an integer amount of cells as shown in Figure 2-24. A cell is defined as the region containing a single perturbation element. The same method was applied to the correlation of the unperturbed flow to ensure consistent comparisons. In contrast, the entire S = 0.2δ velocity fields were included in the correlation computations as the effect of a non-integer amount of cells would be weak due to the large number of cells contained within these fields.

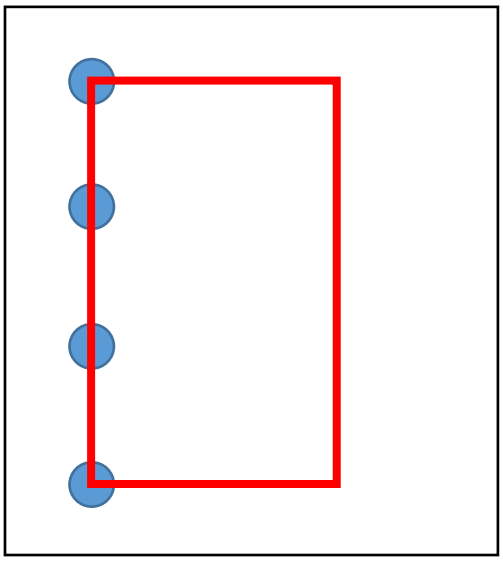

Figure 2-24: Cell definition for autocorrelations in flow downstream of the S = 0.6δ arrays. Not to scale.

2.3 Volumetric PTV Experiments

A four camera PTV system was used to acquire volumetric velocity fields in unperturbed and flow perturbed by an array of narrowly spaced cylinders (S = 0.2δ). Two cylinder heights (H = 0.2δ and H = δ) were considered for the volumetric measurements.

2.3.1 Measurement setup

Four TSI Powerview 8MP cameras fitted with Scheimpflug adapters and 60 mm Nikon Micro-Nikkor lenses were mounted above the water channel in a rectangular configuration with approximately 250 mm between cameras, aimed downward to view the boundary layer through the transparent interface box (Figure 2-25). All cameras had array sizes of 3320 x 2496 pixels, and were capable of image acquisition rates up to 8.5 Hz.

Two lasers were used simultaneously to illuminate the volume of interest. The Spectra Physics PIV -400 laser was capable of outputting ~370mJ/pulse while the Evergreen laser outputted nominally ~200mJ/pulse at 532 nm. The original laser optics used for PIV measurements with the PIV-400 system were modified slightly to generate the volume. Spherical lens, S3 (see figure 2-4) with focal length 1000 mm was replaced with a different spherical lens with focal length 500 mm. Cylindrical lenses C1 and C2 were removed and replaced with a concave cylindrical lens with focal length of -200 mm. On the other hand, two cylindrical lenses were used to shape the beam output from the Evergreen laser, one with a focal length of 300 mm and the other -25mm. Both lasers were positioned on opposite sides of the channel. The edges of the laser beams were masked using tape on the channel side walls prior to entering the channel test section to

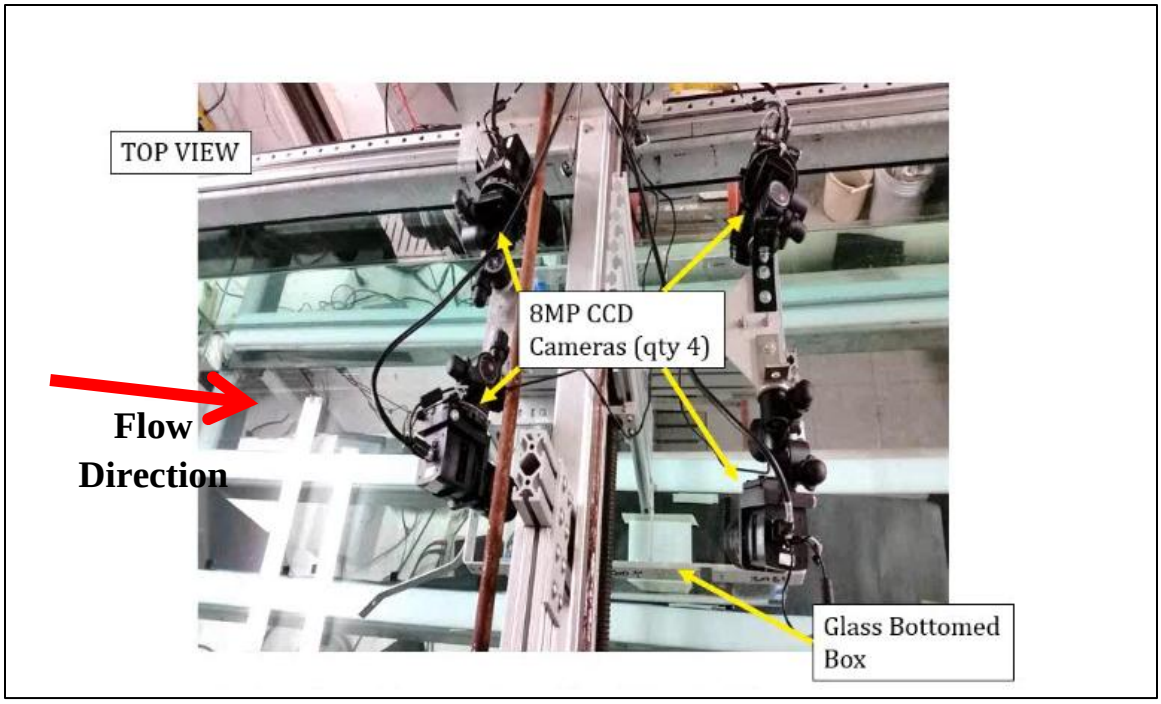

Figure 2-25: Picture showing volumetric PTV setup

reduce unnecessary illumination away from the measurement volume. The resulting measurement volume was 88 mm × 115 mm ×16 mm (0.7δ × 0.9δ × 0.12δ) in the x, y and z directions respectively. The measurement location for the unperturbed flow was selected to cover a streamwise range of $0.15 < x/\delta < 0.85$. Data was acquired at three measurement locations downstream of the respective cylinder arrays. For the flow downstream of the $H = 0.2\delta$ array, the measurement locations covered $0.15 < x/\delta < 0.85$, $2 < x/\delta < 2.7$ and $3.3 < x/\delta < 4$. For $H = \delta$, the locations spanned $0.15 < x/\delta < 0.85$, $2.2 < x/\delta < 2.9$ and $4.3 < x/\delta < 5.0$. Schematics of the data fields are shown in Figure 2-26.

The Evergreen laser and all four cameras were synchronized via a TSI model 610036 synchronizer box (see figure 2-27) coupled with software control from Insight V3V 4G. The start signal from the TSI model 610036 box was routed to also trigger the BN model

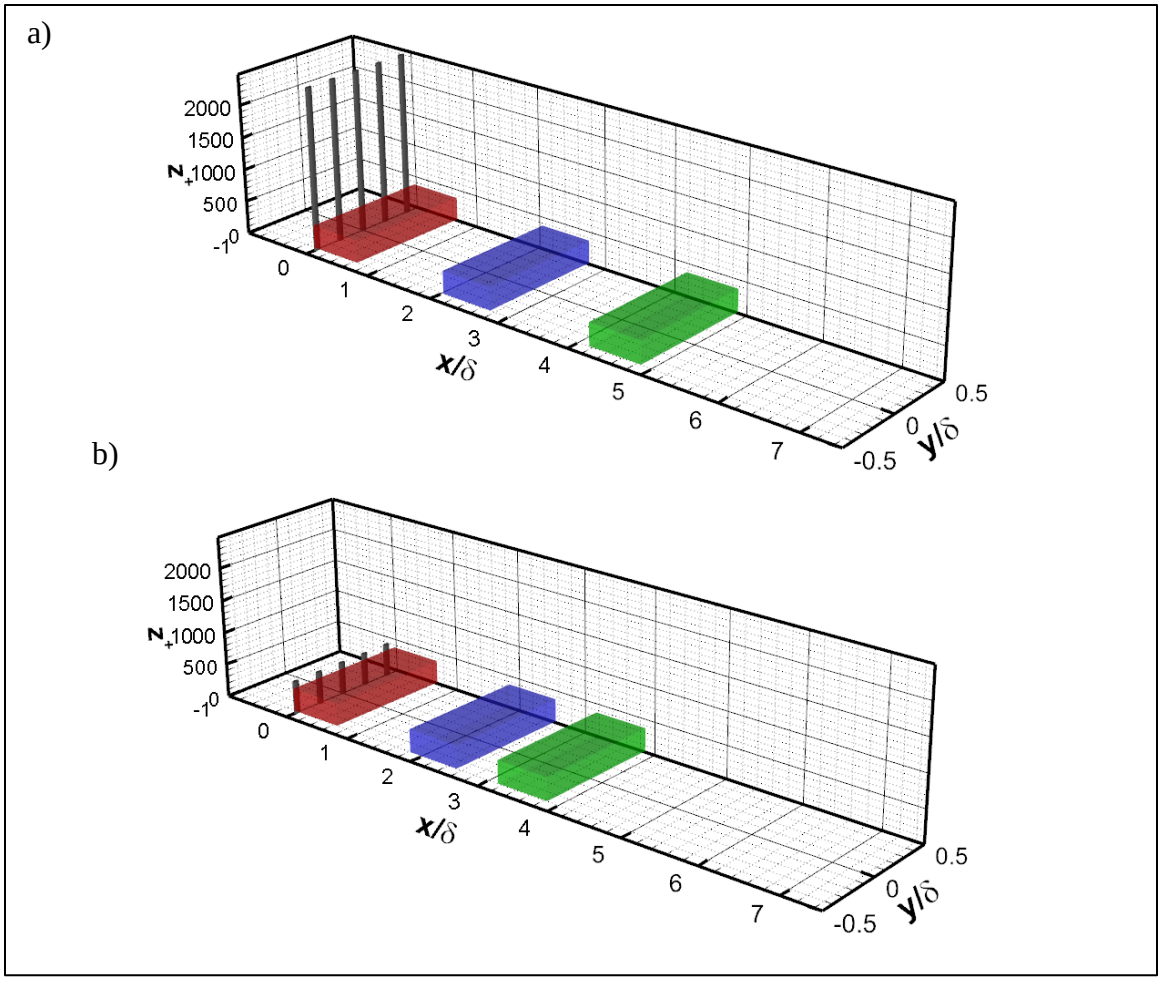

Figure 2-26: Schematic of measurement volumes for a) H = δ and b) H = 0.2δ. Cylinders spaced at 0.2δ.

500A master box which then triggered the BN model-500C slave box, both serving to fire the PIV - 400 laser.

2.3.2 Volumetric PTV Calibration

The four camera system was calibrated using a single-plane, back-lit calibration target with a grid of dots spaced evenly at 5 mm apart (Figure 2-28). The calibration process was performed in the unperturbed flow at experiment conditions. The calibration plate was attached to a vertical traverse through a series of stainless steel rods. The vertical

Figure 2-27: Picture of TSI model 610036 synchronizer box

Figure 2-28: Picture of the single plane, back-lit calibration target.

traverse was mounted to a horizontal strut that rested on the top surface of the side walls on the water channel (see Figure 2-29). The calibration plate thickness was roughly 6 mm. The first calibration location in the z direction was such that the calibration plate was slightly offset from the bottom wall of the test section. The plate was then traversed

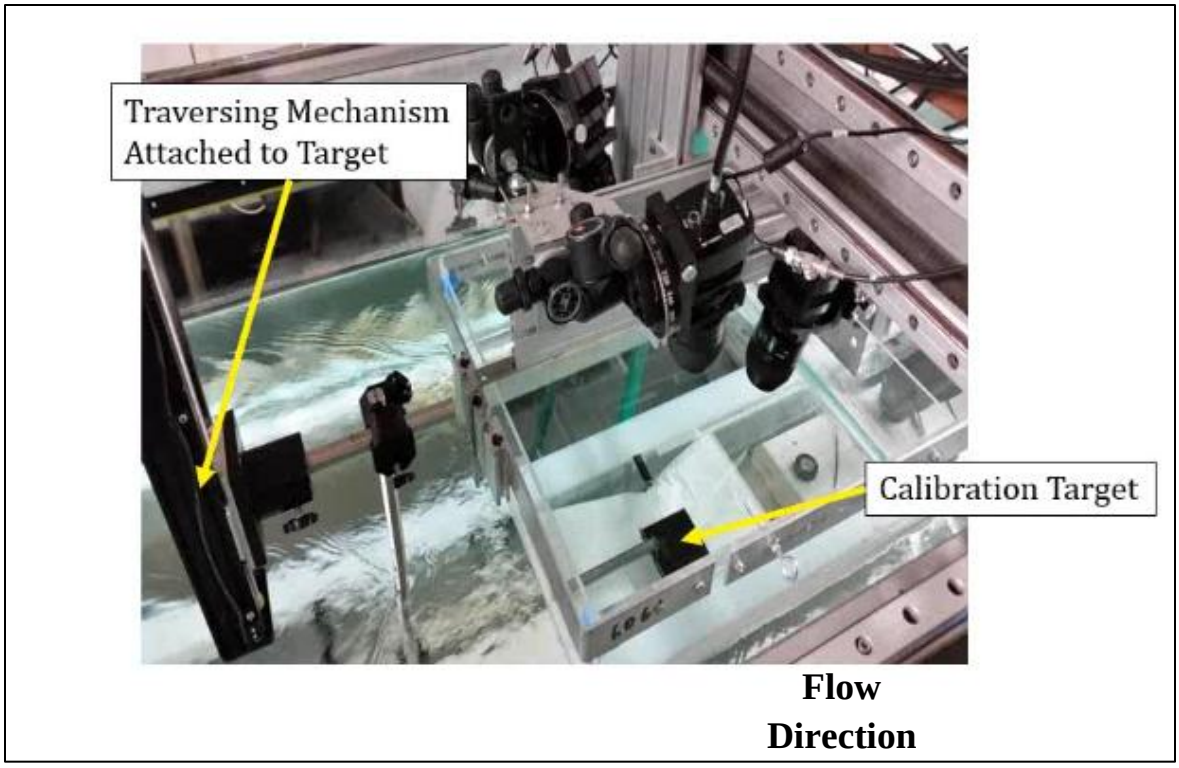

Figure 2-29: Picture of the calibration setup.

upwards in increments of 1mm from the bottom-most location through the depth of the measurement volume, with calibration images being acquired for all four cameras after every increment in z. Due to the inherent thickness of the calibration plate, the calibration depth did not extend all the way to the bottom of the measurement volume, thus additional calibration planes were determined via extrapolation. The extrapolation used the trajectories of the calibration points with increasing z, performing a linear fit on this curve, and later extracting the sub pixel location of the calibration points for the three planes closest to the wall. These were then used to add calibration planes to the existing calibration.

This calibration was then used for every data collection zone. Calibration was difficult in the case where cylinders were present in the measurement domain. The cylinders introduced significant unsteadiness in the flow, acting to vibrate the cantilevered calibration plate in the measurement domain. This resulted in larger uncertainty in the calibration markers, which caused the software to fail at generating a stable calibration. Thus, only the calibration in the unperturbed flow was used for all the experiments. The slight variations in the calibration due to movement of the laser sheet and cameras to different streamwise locations were accounted for using a correction determined from an auto-calibration reconstruction (ACR) technique based on examining particle images from the corresponding data set. This technique is described in detail in Boomsma *et al.* (2016).

2.3.3 Volumetric PTV data processing

The Δt between successive frames was 750 μs such that the pixel displacement between frames was roughly 7 to 9 pixels. The measurements were captured at 0.5 Hz. Sets of 1500 images were acquired for every case at every stream-wise location.

The raw images were processed using Insight V3V 4G. An example of a raw image is shown in Fig. 2-30a. First, the raw images were pre-processed to suppress noise. The images were first assessed qualitatively to determine the base level noise in the background (regions where no apparent particles were present), and subsequently the magnitude of intensity associated with it. Then, this level of intensity was subtracted from all the images. Next, a 5×5 median filter was applied to the images, and the result was then subtracted from each image to remove features present in the background. Then, the images were multiplied by a constant number to increase the absolute difference

between the peaks corresponding to particle locations and remaining noise. Finally, the images were smoothed with a 3 × 3 Gaussian kernel with weight of 0.5 to facilitate the particle identification process. A sample of the pre-processed image is shown in Fig. 2-30b.

The sub-pixel centers of the individual particles were identified on the 2-D images through thresholding and a 2-D Gaussian fit. The particle detection threshold varied between data sets, due to the varying levels of illumination, likely from the process of

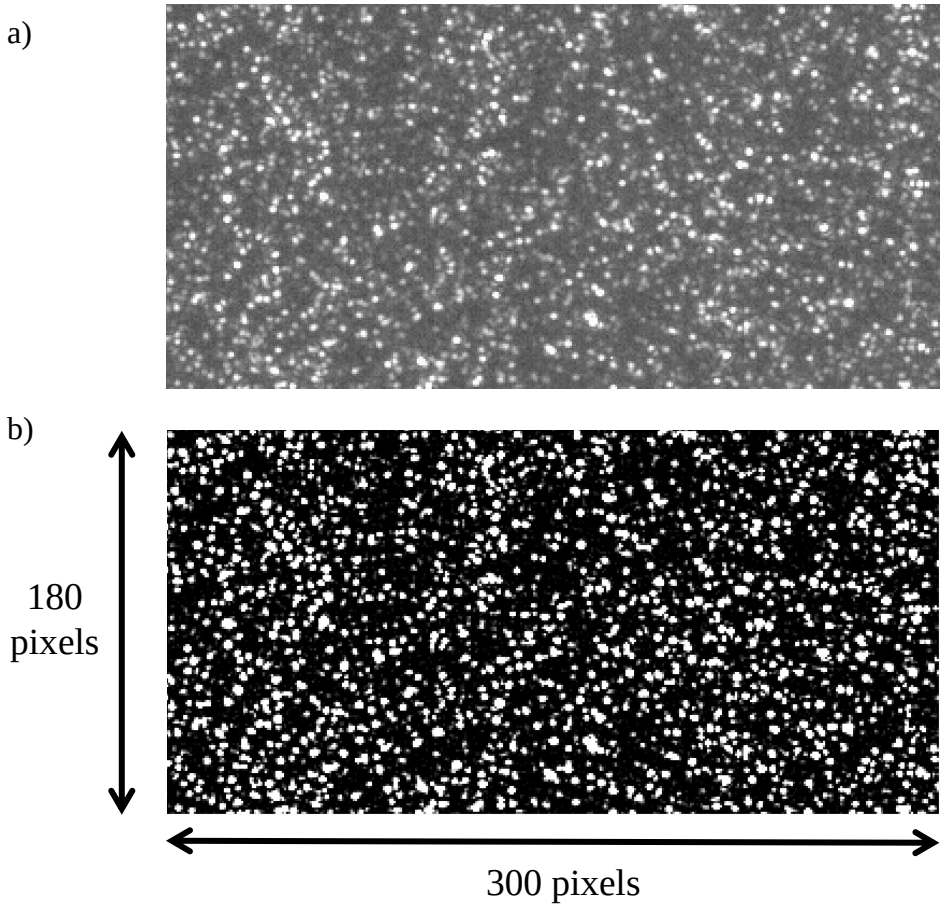

Figure 2-30: Sample a) raw image from one of the four cameras. b) Result of image pre-processing applied to raw image.

laser-alignment when moving from one streamwise location to another. The value of the particle detection threshold was optimized to identify ~150,000 particles per image. The particle thresholds could differ between frames and cameras as illumination could vary with the viewing angle, while illumination differences between frames could occur due to mismatched laser power levels between the two pulses. Although more particles could be identified by decreasing the threshold, there exists a lower limit (based on user judgement) beyond which a large number of these particles were false detections. This effect could be examined by overlaying the locations of the centroids of the particles with the images.

The next stage in the processing pipeline was particle matching, where the particle locations were matched between all cameras for a single frame to determine their 3-D location in real-world space, resulting in a particle cloud at two times, t and Δt. The mapping was done using a polynomial function derived from the calibration. Not all particles identified were matched, therefore, when the particle detection threshold was set to low, a large number of particles were unmatched and removed. This was sub-optimal as these erroneous particles still took up CPU time, but did not result in an increase in the number of matched particles. The number of particles matched between the frames also depends on the radius of the search tolerance. The particle search tolerance (microns) was applied in two stages, a coarse search, and later a finer search. The coarse and fine search tolerances were 130 μm and 65μm for all datasets, and were determined through a trial and error process, depending on the results from the particle vector calculation stage. The coarse and fine search tolerances were essentially the maximum allowable deviations between the centroids of a particle identified in separate camera views. Additional

parameters specified were the minimum and maximum particle radius for the Gaussian fit at 1 and 2 pixels respectively, and the percentage allowable overlap between separate particles within that image, which was set to 65%. Increasing the values of the aforementioned parameters resulted in untenable processing times and is not recommended (see Insight V3V software instructions for further details).

The particle displacements were tracked between the two time instances using a robust point matching technique described in Stellmacher and Obermayer (2000) to arrive at a volumetric velocity field. The only parameter specified for the technique was the particle group size, at 256. In addition, a universal median filter (7) and global velocity range filters were used. The intervals of the global velocity range filter were set to $\pm U_\infty$ for all components to filter out outliers. As a result, the particle volumes contained between 30,000 – 50,000 randomly spaced particle vectors per field (e.g. Fig. 2-31). The variation in the number of particle vectors between separate instances may be due to vibrations induced from various sources such as the vibration from running the water channel, and possibly from the water impacting the interface box. To suppress variations in the final volumetric field due to variation in number of particle vectors, only fields that contained greater than 35,000 particle vectors were compiled for the subsequent analyses. The spacings between particle vectors with its nearest neighbors were roughly ~ 1mm (20 wall units).

The volumes of the randomly spaced particle vectors were interpolated using a Gaussian weighted interpolation scheme in a rectangular grid with node dimensions of 7 mm × 4 mm × 3 mm (140 × 80 × 60 in wall units) in the streamwise, spanwise and wall normal directions respectively with a node volume overlap of 75%. This resulted in vector

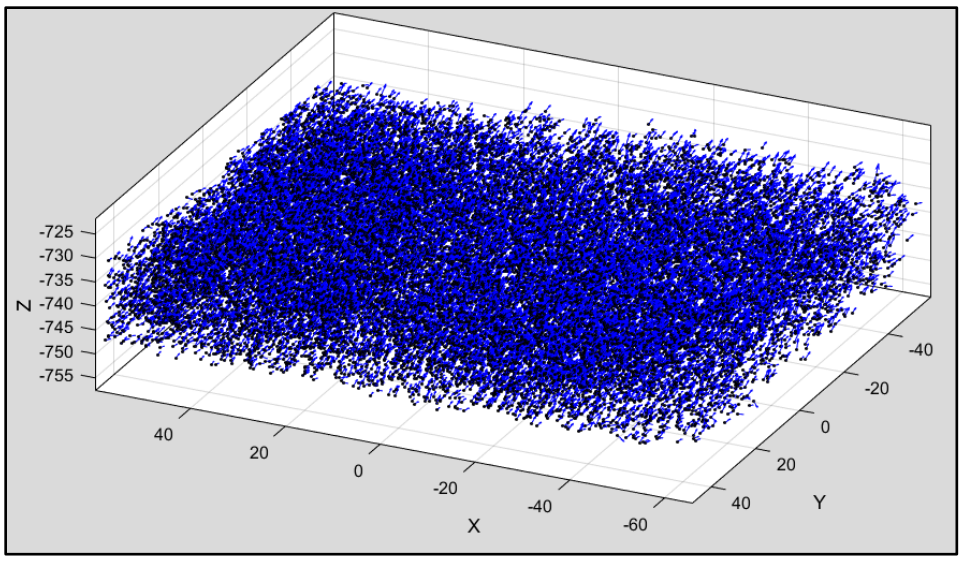

Figure 2-31: Example of particle vectors from an instantaneous volume from 3-D PTV measurements.

spacings of 35 × 20 × 15 wall units. This specific grid dimension was selected as the dominant motions in this flow are elongated in the streamwise direction, while being narrower along the spanwise direction. In addition, the smallest dimension was along the z-direction, and this was specified to better capture the variations across the logarithmic layer.

The uncertainty in the particle position measurement is a function of a number of experimental parameters including the number of cameras, the angle between cameras, the accuracy of the 2D Gaussian fit (which depends on the magnification, particle size, and pixel size), and the least squares mapping error. A root sum of squares uncertainty analysis was performed for the parameters in the current study resulting in an uncertainty of 4.5 microns in the streamwise and spanwise directions, and 14 microns in the wall-normal direction. The uncertainty in the velocity measurements depends on particle displacement uncertainty as well as the time between laser pulses. For the current study

the velocity uncertainty was $0.01U_\infty$ for a given particle track in the streamwise and spanwise directions and $0.03U_\infty$ in the wall-normal direction. The uncertainties associated with the mean and RMS values derived from 3-D PTV measurements are tabulated in Table 2-5.

Chapter 3

Results & Discussion: Unperturbed turbulent boundary layer

In this chapter, the unperturbed turbulent boundary layer results are presented. The results from this chapter will be used for comparison with the perturbed flow in subsequent chapters. First, single-point velocity statistics are presented to assess measurement quality. Then, instantaneous flow structure variation across the measurement heights is evaluated qualitatively and quantitatively. The first streamwise measurement location starts 6m downstream of the trip-wire location, corresponding to x = 0. Unless otherwise specified, all results in this chapter were obtained at this location.

3.1 Time-averaged results

The average streamwise velocity contour maps for the unperturbed flow acquired from PPIV are shown in Figure 3-1 for three measurement heights. Notably, all fields show variations across the span-wise direction that were typically greater than the estimated uncertainty computed in Chapter 2 (see Table 2-5). For z^+ = 125(Fig. 3-1a), the deviations away from the local mean velocity are greater over certain spanwise locations. For example, in Figure 3-1, a slow moving region spans $1.6 < y/\delta < 2$ while a fast moving zone is seen at $0.8 < y/\delta < 1.4$. These variations were within $\pm 0.02U_\infty$ from the field average. On the other hand, for z^+ = 300 (Fig. 3-1b) and 500 (Fig. 3-1c), the variations are smaller at $\pm 0.01U_\infty$ and $\pm 0.015U_\infty$ respectively. The observed deviations in $\bar{U}$ are likely due to the existence of very long low momentum zones within the logaritmic layer. Hutchins & Marusic (2007a) found lengths of low momentum zones that could extend over 20δ in a Re_τ = 14,380 canonical boundary layer. In our case, a structure of length

20δ would remain correlated for four samples, thus effectively reducing the number of statistically independent samples we have by a factor of four. In this case, the uncertainty in the mean velocity would rise to $0.02U_\infty$, possibly accounting for the observed variations at $z^+ = 125$ (Fig. 3-1a). Previous experiments in our facility also revealed that debris stuck in the flow conditioning section 10 meters upstream of the measurement test section could yield locations of average faster and slower regions larger than uncertainty. This could also be a possible contributor to the result at $z^+ = 125$. These variations could at times be $\pm 0.04U_\infty$ and therefore, the flow conditioning sections were cleaned regularly to mitigate this effect. All in all, the low speed zones do not always occur in the same location, if it were so, the deviations at a single spanwise location would be much greater than what was observed at $z^+ = 125$ (Fig. 3-1a). Separately, for all measurement heights, the deviations in average spanwise velocity (Fig. 3-2) were minimal and largely within measurement uncertainty.

Streamwise and spanwise RMS velocity fields from PPIV measurements are shown in Figure 3-3 and 3-4 for all measurement heights. The variations were also minimal for all measurement heights, except at the edges of the field at $z^+ = 125$ (Fig. 3-3a) in the streamwise component. The larger variations there are likely due to more erroneous vectors as a result of the particles moving out of the PIV field of view, therefore, these regions are not considered for analyses and computations.

For the SPIV measurements in unperturbed flow, the average streamwise velocity results are shown in Figure 3-5 at all measurement heights. Similar to the PPIV results (Fig. 3-1), deviations at certain spanwise locations are observed (e.g Fig. 3-5a & b). For $z^+ = 300$ (Fig. 3-5b), the average streamwise velocity increases with increasing spanwise location.

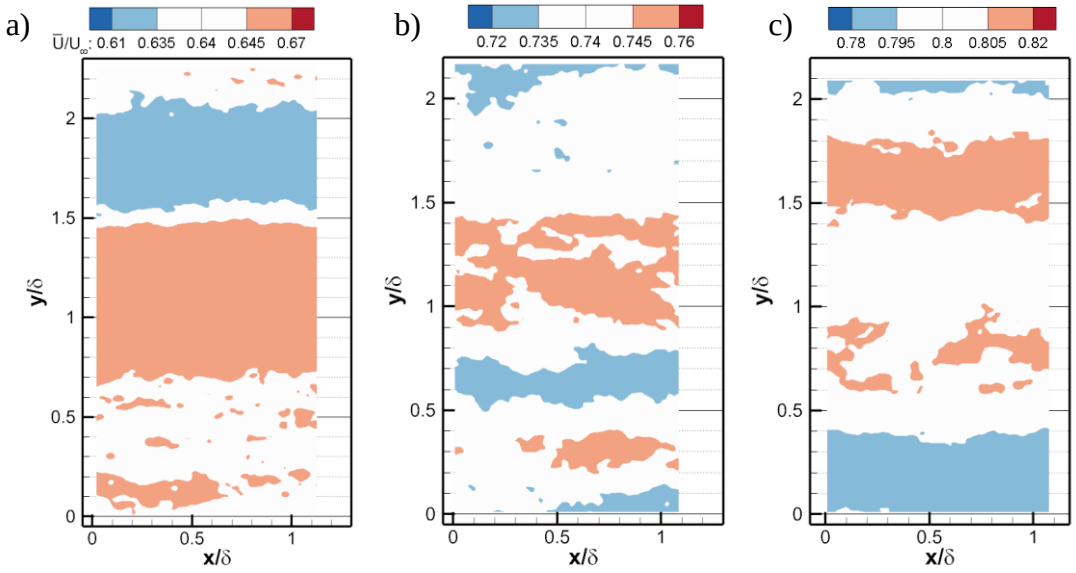

Figure 3-1: Unperturbed flow. Average streamwise velocity results from PPIV at measurement height a) z^+ = 125, b) 300 and c) 500.

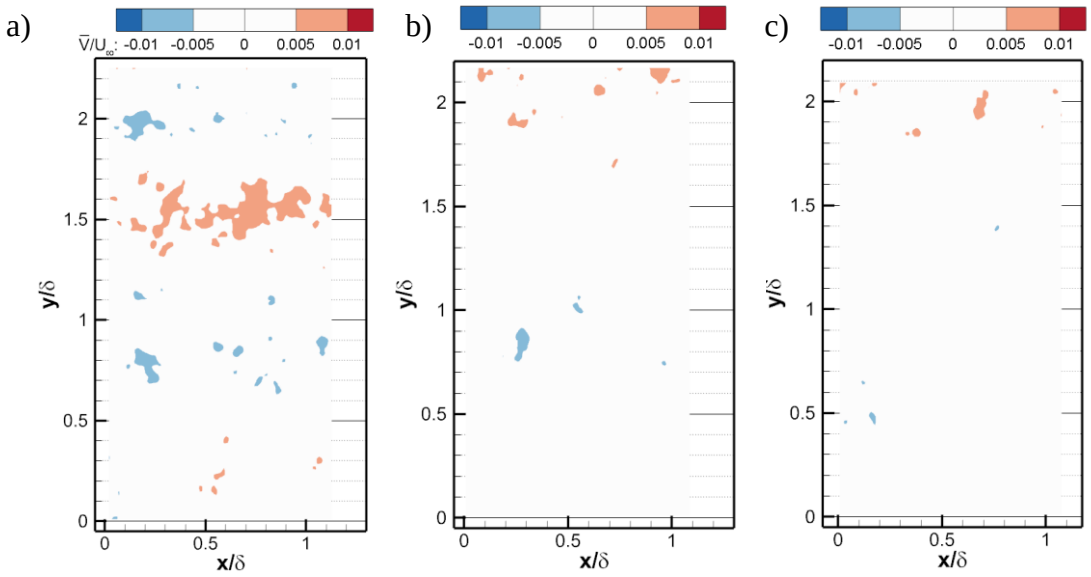

Figure 3-2: Unperturbed flow. Average spanwise velocity results from PPIV at measurement height a) z^+ = 125, b) 300 and c) 500.

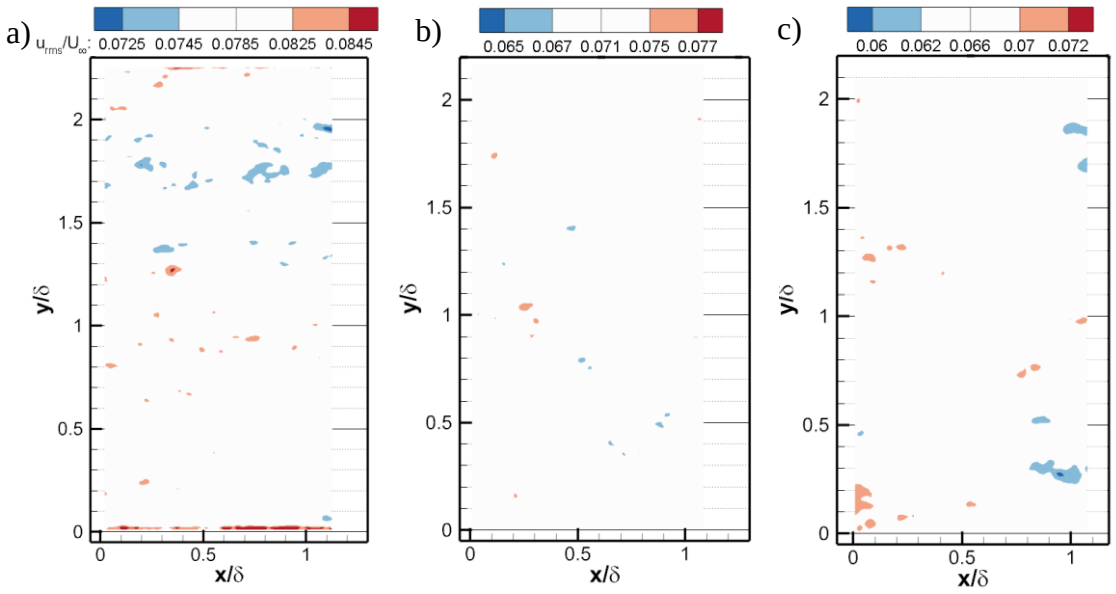

Figure 3-3: Unperturbed flow. Streamwise RMS velocity results from PPIV at measurement height a) $z^+ = 125$, b) 300 and c) 500.

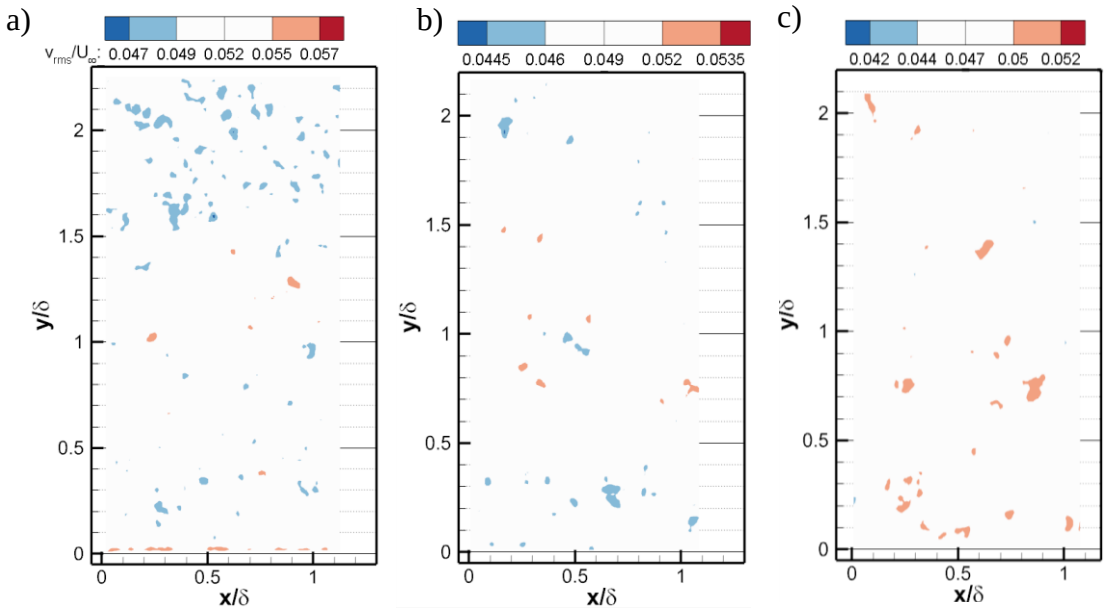

Figure 3-4: Unperturbed flow. Spanwise RMS velocity results from PPIV at measurement height a) $z^+ = 125$, b) 300 and c) 500.

This can either be attributed to a small tilt of the laser sheet estimated to be around 0.5° or as a result of laser sheet expansion with increasing y-location (0.5 mm to 1mm, or 10 wall units and 20 wall units respectively). The deviations were $\pm 0.02U_\infty$ away from $\bar{U}$ at $z^+ = 125$ (Fig. 3-5a) and 300 (Fig. 3-5b), in comparison to $\pm 0.01U_\infty$ (Fig. 3-5c) for $z^+ = 500$. Deviations in the average spanwise velocity (Figure 3-6) were largely within uncertainty. The maximum deviation occurs at $z^+ = 125$ (Fig. 3-6a) with a magnitude of $\pm 0.007U_\infty$.

For $z^+ = 125$ (Fig. 3-7a) and 500 (Fig. 3-7c), deviations in average wall-normal velocity field were within uncertainty. Deviations are observed at $z^+ = 300$ (Fig. 3-7b) where the errors are from the calibration procedure. This is discussed in detail in Zheng (2011) where the calibration plate was rotated 45° about the z-axis such that the grooves are perpendicular to the streamwise direction.

The RMS velocity variations for all velocity components from SPIV are shown in Figures 3-8, 3-9 and 3-10 for all measurement heights. Deviations within the RMS velocity fields were minimal and largely within uncertainty for both the streamwise and spanwise velocity. On the other hand, distinct deviations are observed for the wall-normal RMS velocity (Fig. 3-10) at $z^+ = 300$, where this can be attributed to the errors introduced by the calibration procedure (see Zheng 2011).

Velocity statistic averaged across planar fields were computed for both SPIV and PPIV and compared with DNS statistics from Sillero *et al.* (2013) for a canonical turbulent boundary layer with $Re_\tau = 1989$ (Table 3-1). The wall-normal RMS velocity at $z^+ = 300$ deviates from the DNS result due to the errors introduced in the calibration procedure (Zheng 2011). While mean streamwise velocities show deviations away from DNS values

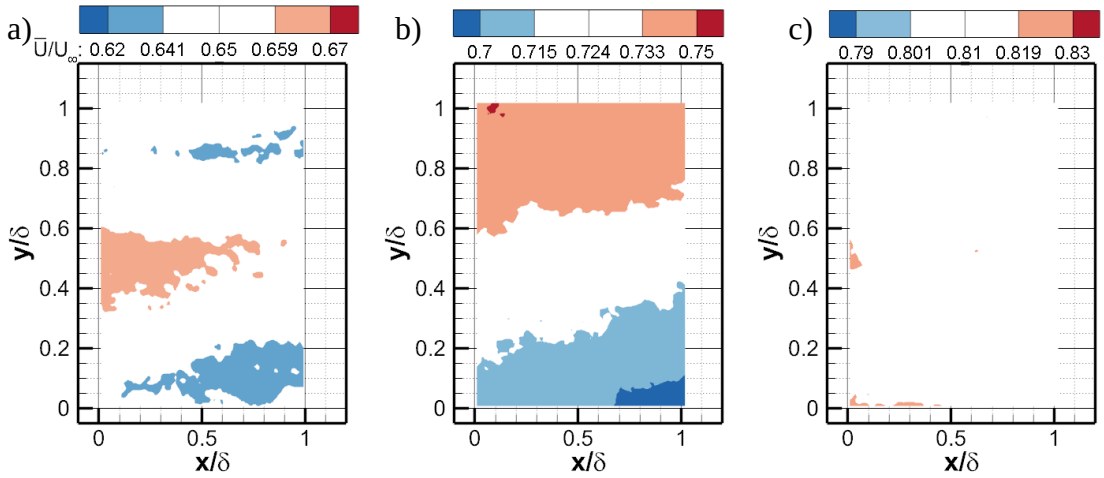

Figure 3-5: Unperturbed flow. Average streamwise velocity results from SPIV at a) z^+ = 125, b) 300 and c) 500.

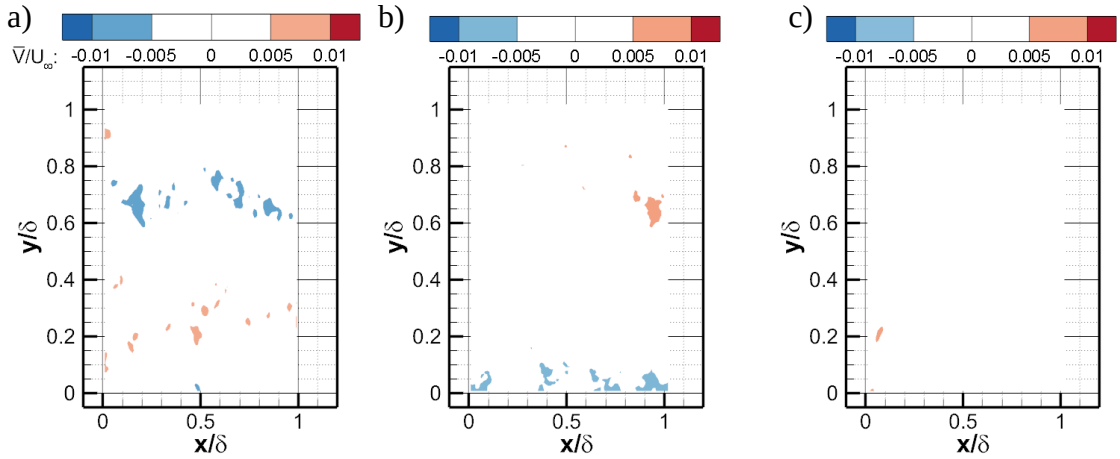

Figure 3-6: Unperturbed flow. Average spanwise velocity results from SPIV at a) z^+ = 125, b) 300 and c) 500.

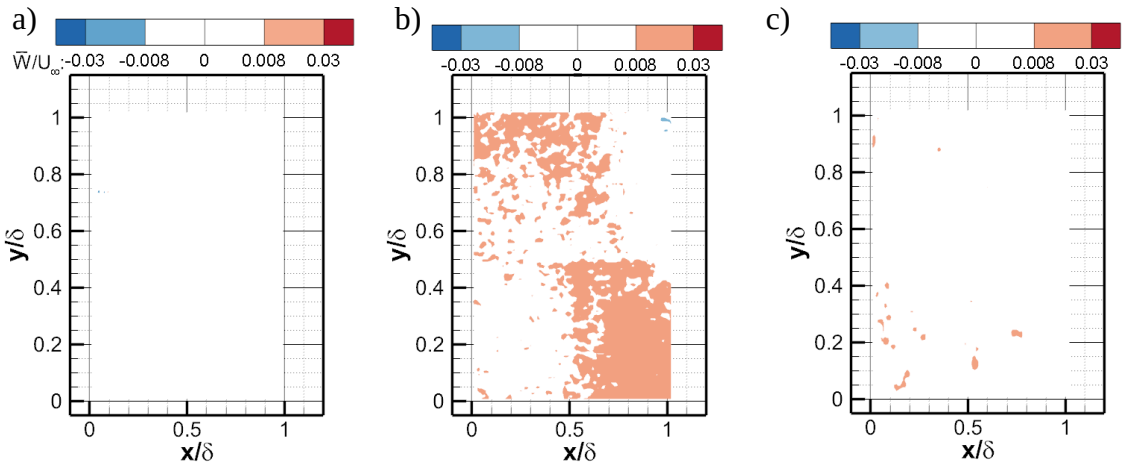

Figure 3-7: Unperturbed flow. Average wall-normal velocity results from SPIV at a) z^+ = 125, b) 300 and c) 500.

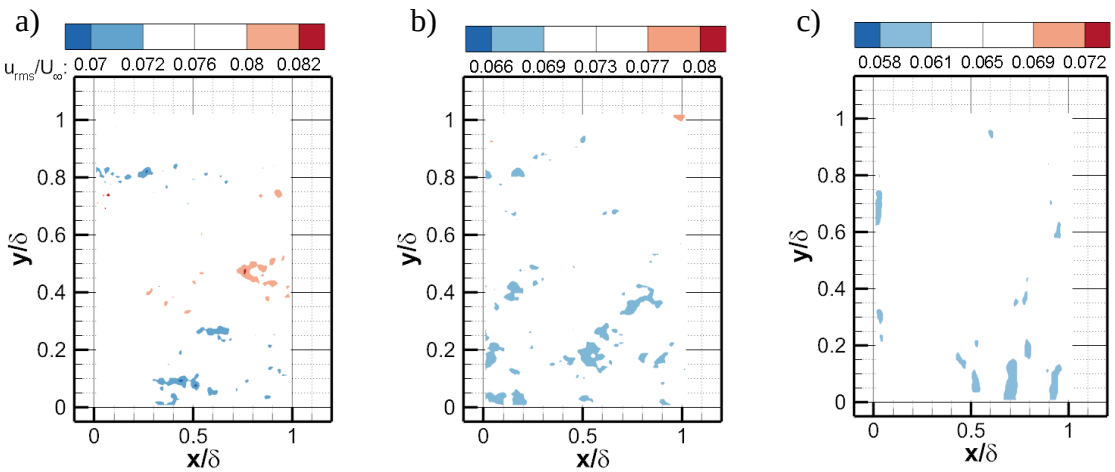

Figure 3-8: Unperturbed flow. Streamwise RMS velocity results from SPIV at a) z^+ = 125, b) 300 and c) 500.

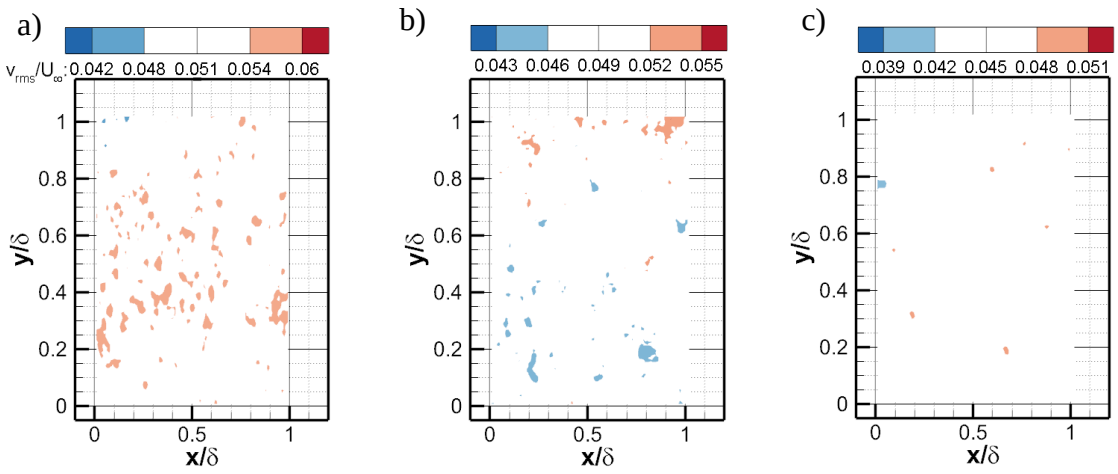

Figure 3-9: Unperturbed flow. Spanwise RMS velocity results from SPIV at a) z^+ = 125, b) 300 and c) 500.

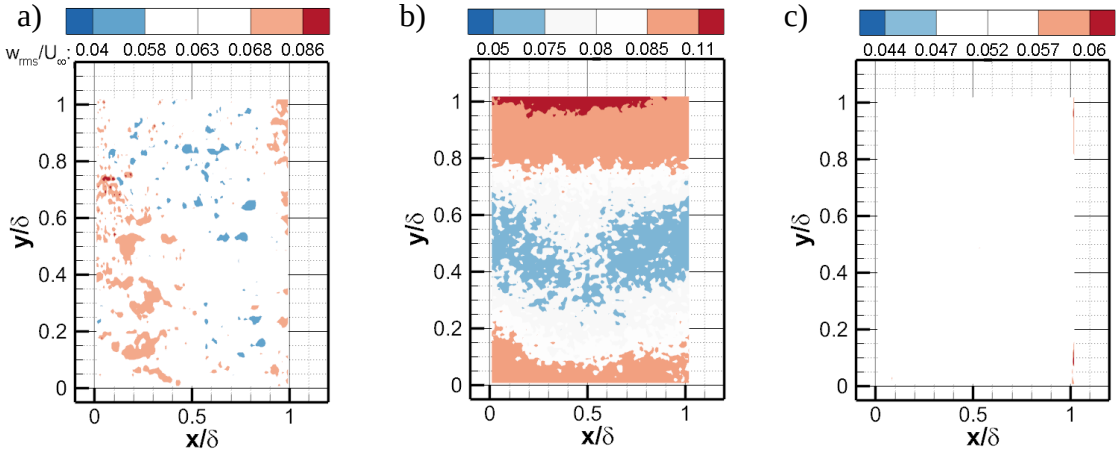

Figure 3-10: Unperturbed flow. Wall-normal RMS velocity results from SPIV at a) z^+ = 125, b) 300 and c) 500.

Table 3-1: Mean and RMS velocity statistics for the unperturbed flow acquired using both SPIV and PPIV compared with DNS data from Sillero *et al.* (2013). *SPIV and PPIV data from Zheng & Longmire (2014).

Measurement Height		SPIV(Re_τ = 2480)	PPIV(Re_τ = 2480)	DNS (Re_τ =1989)
z^+ = 125	$\bar{U}/U_\infty$	0.649±0.009	0.640±0.005	0.624
	$\bar{V}/U_\infty$	0.004±0.005	0.002±0.003	0.001
	$\bar{W}/U_\infty$	0.007±0.008	--	0.005
	u_{rms}/U_∞	0.075±0.004	0.078±0.004	0.080
	v_{rms}/U_∞	0.051±0.003	0.051±0.003	0.043
	w_{rms}/U_∞	0.052±0.005	--	0.055
z^+ = 300*	$\bar{U}/U_\infty$	0.725±0.009	0.740±0.005	0.705
	$\bar{V}/U_\infty$	0.002±0.005	0.003±0.003	0.001
	$\bar{W}/U_\infty$	0.007±0.008	--	0.005
	u_{rms}/U_∞	0.071±0.004	0.071±0.004	0.075
	v_{rms}/U_∞	0.0487±0.003	0.049±0.003	0.043
	w_{rms}/U_∞	0.0846±0.005	--	0.052
z^+ = 500	$\bar{U}/U_\infty$	0.809±0.009	0.802±0.005	0.764
	$\bar{V}/U_\infty$	0.004±0.005	0.003±0.003	0.002
	$\bar{W}/U_\infty$	0.003±0.008	--	0.006
	u_{rms}/U_∞	0.064±0.004	0.061±0.004	0.070
	v_{rms}/U_∞	0.045±0.003	0.047±0.003	0.043
	w_{rms}/U_∞	0.052±0.005	--	0.050

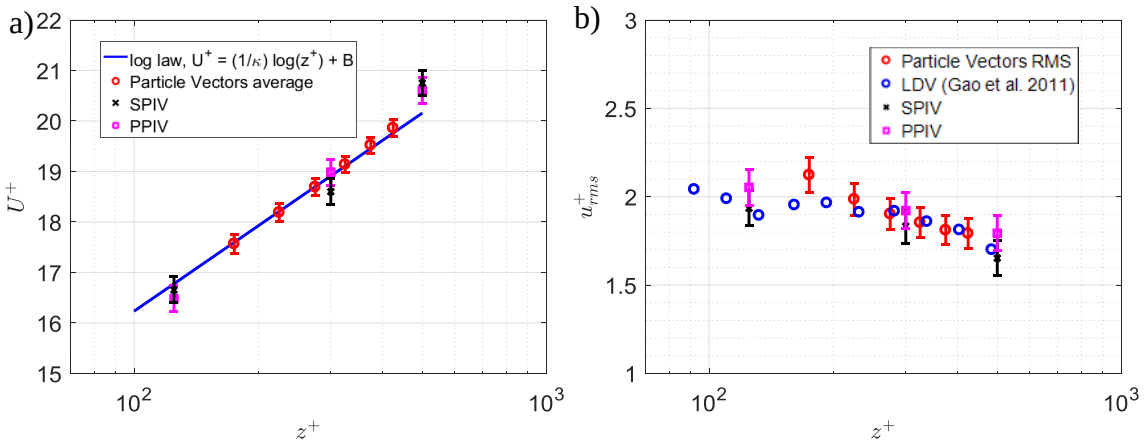

Figure 3-11: a) Mean & RMS velocity from 3-D PTV measurements, SPIV and PPIV versus wall-normal location. Particle vectors grouped into bins with depth of 50 wall units, then averaged.

which can be due to the effect of the viewing box (see Gao 2011 and discussion in Chapter 2, section 2.1.1). Other than that, values from experiments agree well to within uncertainty with DNS values.

Mean and RMS streamwise velocity profiles across the depth of 3-D PTV measurement volumes in the unperturbed flow are shown in Figure 3-11. Results from SPIV and PPIV are shown as well for comparison. The velocity statistics from the 3-D PTV measurements are derived from the averaging of individual particle vectors within bins of depth $\Delta z^+ = 50$, or ~2.5mm. The 3-D PTV mean velocities plotted in Figure 3-11a agreed well with the law of the wall with $\kappa = 0.41$ and $B = 5.0$. The mean velocities from SPIV and PPIV measurements at $z^+ = 500$ deviates from the law of the wall which might be expected considering this is the location at the top of the log layer ($z/\delta = 0.2$) where the applicability of the law of the wall diminishes.

On the other hand, RMS velocity statistics from 3-D PTV (Fig. 3-11b) also agreed well with previous LDV measurements acquired in similar flow conditions by Gao (2011). Both SPIV and PPIV RMS velocity statistics agree well with previous measurements to within uncertainty.

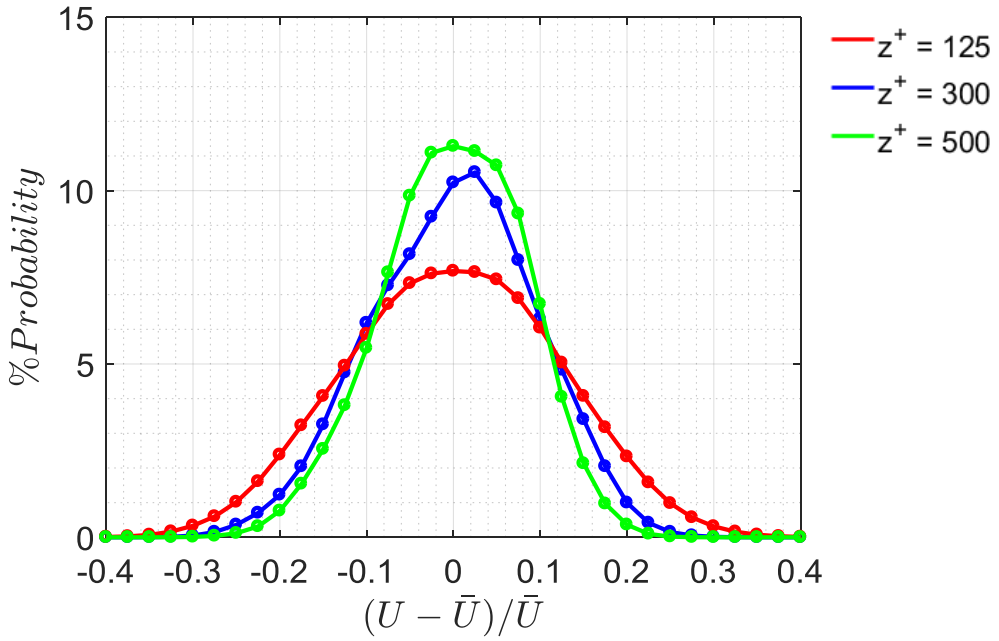

Figure 3-12: Probability density function of streamwise velocity fluctuations normalized by local mean velocity in the unperturbed flow for all measurement heights.

The probability density functions (PDFs) of streamwise velocity fluctuations for all measurement heights in the unperturbed flow from PPIV measurements are shown in Figure 3-12. The velocity fluctuations are defined as the deviation away from the local time averaged velocity. With increasing measurement height, the distributions become narrower, consistent with decreasing streamwise RMS velocity. Notably, the skewness of the PDFs becomes increasingly negative with increasing height. The PDF is relatively symmetric at z^+ = 125 with a small skewness value of -0.01. The negative skewness

increases with wall-normal distance to -0.13 at $z^+ = 300$, and -0.19 at $z^+ = 500$. These values are consistent with skewness values in a TBL with $Re_\tau = 2800$ (Mathis *et al.* 2011). The negative skewness values imply a longer tail for slow moving regions in the PDFs, i.e, there are more extreme negative values for slow moving regions versus less extreme positive values for fast moving regions.

3.2 Instantaneous Results

Figure 3-13 shows examples of instantaneous velocity fields from the unperturbed flow at three measurement heights. The rest of this dissertation will show instantaneous examples from PPIV measurements, unless specified otherwise. This is because the PPIV fields have a wider span, enabling visualizations of multiple structures within a single instance. The contour colors reflect slow (blue) and fast (red) moving regions relative to the local mean velocity of the measurement height. The dominant features across all measurement heights are alternating low and high momentum zones, consistent with Tomkins & Adrian (2003), Ganapathisubramani *et al.* (2003) and Hutchins & Marusic (2007a). We consider a hairpin packet signature as a relatively long and narrow streamwise-coherent slow-moving region bounded by counter-rotating swirling structures (depicted by black and green contours), aligned with the definition of Ganapathisubramani *et al.* (2003) and Tomkins & Adrian (2003). The low momentum zones or packets observed at $z^+ = 125$ (Figure 3-13a) are typically long and narrow, for example at $y/\delta = 0.15$, 1.9 and possibly 1.6. At $z^+ = 300$ (Figure 3-13b), the slow moving zones becomes wider (e.g. $y/\delta = 0.3$, 0.8 and 1.6) and fewer swirling structures are observed. These trends continued at $z^+ = 500$ (e.g. Figure 3-13c, $y/\delta = 0.65$ and 1.2). Generally, packets tend to become wider and occasionally shorter with increasing height, consistent with Tomkins & Adrian (2003).

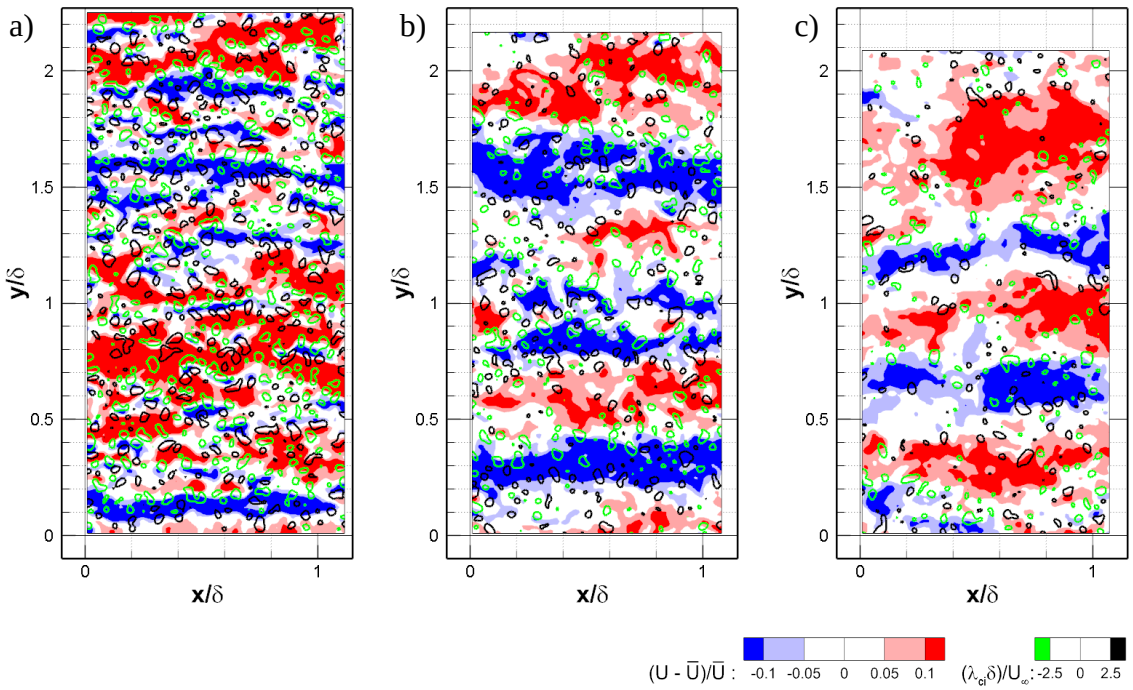

Figure 3-13: PPIV data of unperturbed flow at a) z^+ = 125, b) z^+ = 300 and c) z^+ = 500. Blue and red contours show deviation from local mean velocity at the measurement height, also normalized by the same local mean velocity.

Instantaneous examples of FPIV runs at all measurement heights for the unperturbed flow are shown in Figure 3-14. The PIV system was traversed at $U_T = \bar{U}$ of the respective measurement height determined from PPIV measurements. For all measurement heights, many of the structures within the flow appear to convect downstream at a velocity close to $\bar{U}$, as many features at $x/\delta \sim -2$ tend to correspond to features at the last measurement location, $x/\delta \sim 7$. Consistent with the PPIV results, with increasing measurement height, packet signatures also become wider and sometimes shorter.

Notably, the FPIV results showed several instances involving two separate LMRs merging into a single wider LMR, consistent with results from Gao *et al.* (2013) and Tomkins & Adrian (2003). One such example is shown in Figure 3-14a, at z^+ = 125, where two low momentum zones (y/δ = 1.5 and 1.8) converged on one another starting at

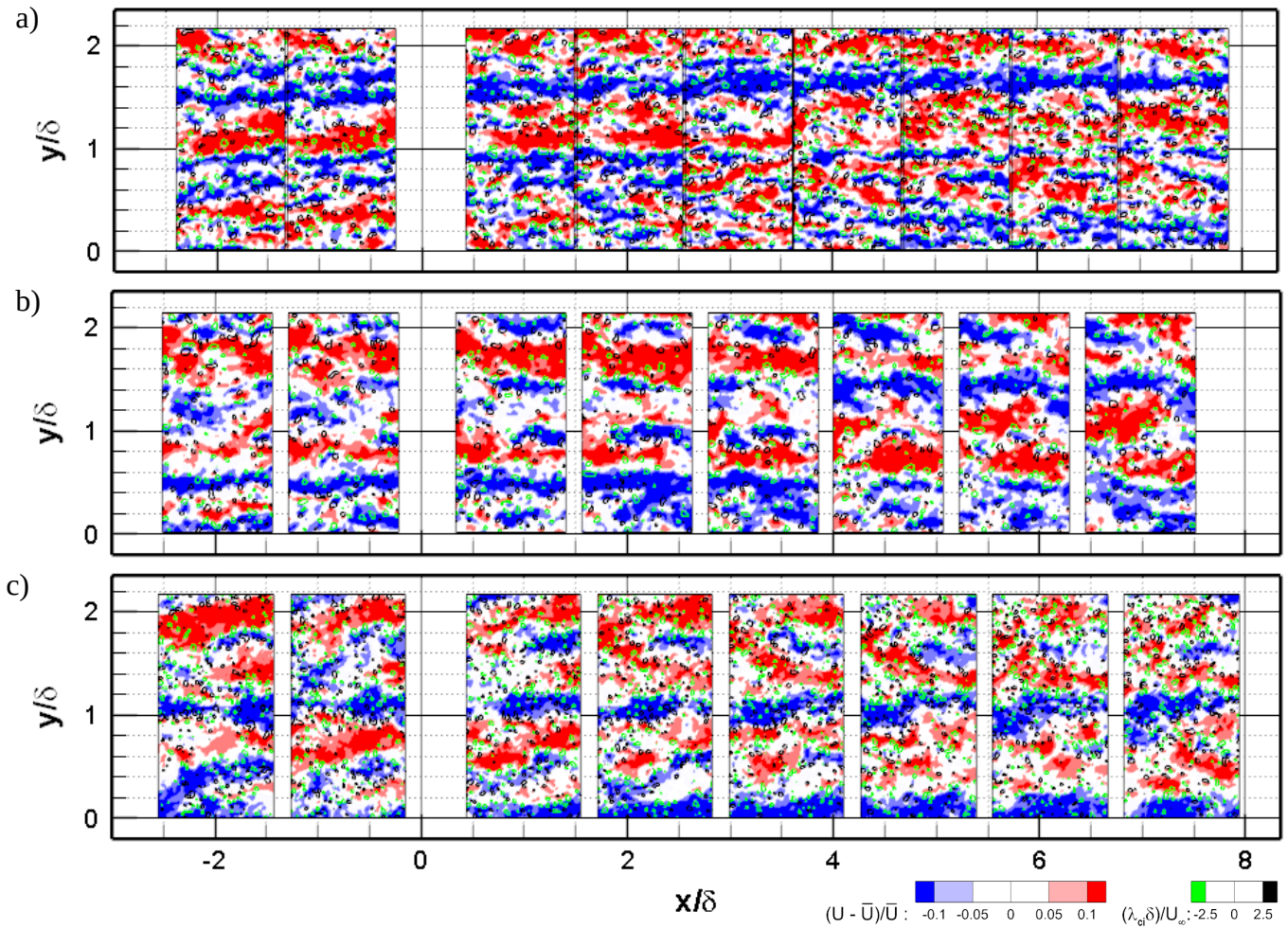

Figure 3-14: Unperturbed flow. FPIV runs at a) $z^+ = 125$, b) $z^+ = 300$ and c) $z^+ = 500$.

x/δ = -0.5, and later appeared as a single LMR by $x/\delta \sim 3$. This is consistent with the spanwise scale growth mechanism proposed by Tomkins & Adrian (2003) for wall-bounded flows.

3-D PTV measurement volumes (e.g. Fig. 3-15) in the unperturbed flow show hairpin packet signatures frequently extending across the depth of the volumes ($155 < z^+ < 465$). This observation is consistent with previous measurements by Gao *et al.* (2011) who performed tomographic PIV on volumes spanning z^+ = 100-300 and 300-500. Figure 3-15a shows an instantaneous volume in which a coherent LMR at $y/\delta \sim 0.15$ extends across the entire depth as well as the streamwise domain. Trends across the measurement depth are consistent with those inferred from PPIV measurements, such that packet signatures close to the wall are frequently narrow and long, while becoming shorter and wider with increasing height. For example, a narrow and long LMR can be seen in Figure 3-15b at $z^+ = 155$ ($y/\delta = 0.2$). The signature of the same packet was observed at roughly the same spanwise location at both $z^+ = 300$ and 465 (Figs. 3-15c & d). The packet looks wider at $z^+ = 300$ and shorter at $z^+ = 465$.

3.3 Structural Features

3.3.1 Regions of uniform streamwise momentum

Coherent momentum regions (CMRs) in the unperturbed velocity fields were extracted using similar methodology as the VPIA (see Ch. 2, section 2.2.8.2), except with fewer thresholds. CMRs refer to both the LMRs and high momentum regions (HMRs). The detected structures were subjected to the following thresholds only; $(U - \overline{U})/\overline{U} > |0.05|$, $L_{ex} > 0.1\delta$ and $W_{ex} > 0.05\delta$. Different from the VPIA, high momentum zones were

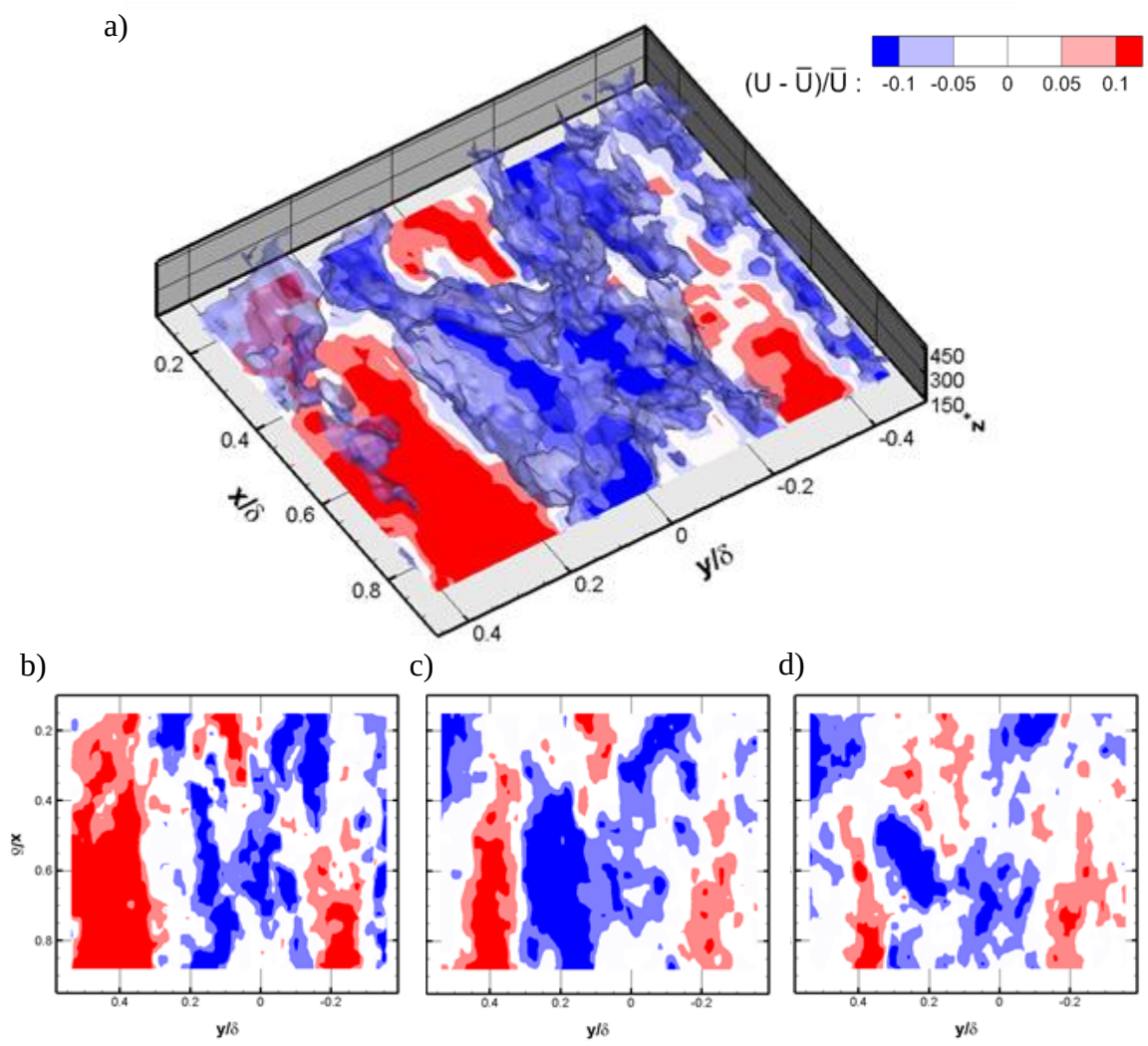

Figure 3-15 Unperturbed flow. a) Instantaneous volume from 3-D PTV. Colors show the fractional deviation of streamwise velocity from the local mean velocity for the plane at $z^+ = 155$. Iso-surfaces show regions with $U < 0.95\overline{\overline{U}}$. Streamwise spanwise slices of streamwise velocity at b) $z^+ = 1255$, c) $z^+ = 300$ and d) $z^+ = 465$.

extracted as well. This serves as a useful tool to corroborate the trends inferred from the instantaneous visualizations.

Figure 3-16a shows length histograms of the detected CMRs for all measurement heights. The histograms indicate that slow moving packets are frequently narrower and longer close to the wall, while becoming wider and shorter with increasing measurement height, supporting trends inferred from visualizations. The bin for $L_{ex} = \delta$ shows the largest percentage of LMRs at $z^+ = 125$ (15%) compared to 13% at $z^+ = 300$ followed by 11.3% at $z^+ = 500$, of the number of detected LMRs at the measurement heights respectively. Also, with increasing measurement height, HMRs become increasingly long with respect to LMRs. For $z^+ = 125$, the percentage of LMRs with value $L_{ex} = \delta$ is 15% compared to 11% for the HMRs. The percentages become comparable at $z^+ = 300$, 13.5% for LMRs vs 12.5% for HMRs. Then at $z^+ = 500$, the percentage of long HMRs is greater at 12.5% compared to 11% for long LMRs. These effects were difficult to ascertain from instantaneous visualizations of the streamwise velocity fields.

Mean width histograms for detected CMRs are shown in Figure 3-16b. Trends are supported by observations in instantaneous visualizations, with narrower LMRs closer to the wall and wider above. The width histograms show the largest percentage of LMRs for $z^+ = 125$ (82%) at the bin corresponding to the smallest width (0.075δ), consistent with visualizations. In comparison, the percentages for $z^+ = 300$ and 500 for that width dropped to 65% and 62% respectively. On the other hand, for the largest width value (0.275δ), the percentages were greatest for $z^+ = 500$ and least at $z^+ = 125$, for both LMRs and HMRs. The histograms also suggest that HMRs tended to be wider than LMRs at $z^+ = 300$, and more so at $z^+ = 125$.

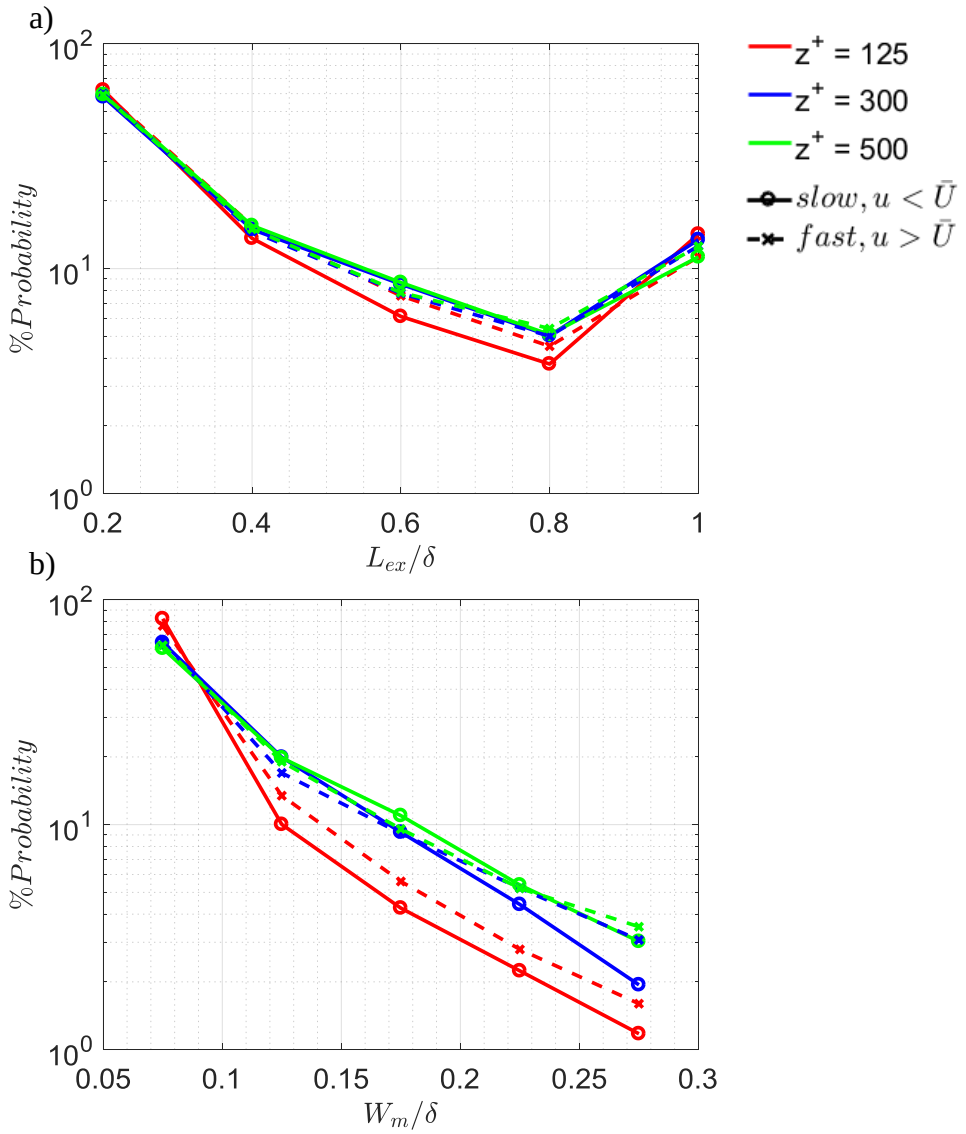

Figure 3-16: Coherent momentum regions in unperturbed flow. Distribution of a) L_{ex}, extrema length, and b) W_m, mean widths normalized by the corresponding number of slow or fast moving coherent momentum zones respectively with $(U - \bar{U})/\bar{U} > |0.05|$, $L_{ex} > 0.1\delta$ and $W_{ex} > 0.05\delta$. Colors show measurement height. Solid lines and circles show statistics for low momentum zones while dashed lines and crosses show statistics for high momentum zones, relative to the local mean velocity.

Figure 3-17 shows distributions of the absolute magnitudes of the deviation in streamwise velocity away from the local mean velocity within extracted low/high momentum regions in the unperturbed flow for all measurement heights. The distributions were separated into two groups sorted by extrema length of the detected regions, $L_{ex} > 0.5\delta$ and $L_{ex} < 0.5\delta$. The trends in the plot show that indeed more extreme deviations occur within LMRs compared to HMRs for both $z^+ = 300$ (Fig. 3-17b) and 500(Fig. 3-17c), where the skewness values are negative. In comparison, at $z^+ = 125$(Fig. 3-17a), the deviation magnitudes are similar between the HMRS and LMRs. These trends are observed for both the $L_{ex} > 0.5\delta$ and $L_{ex} < 0.5\delta$ CMRs.

3.3.2 Autocorrelations of streamwise velocity

Streamwise ($\Delta y = 0$) and spanwise ($\Delta x = 0$) slices of the auto-correlation contours of streamwise velocity fluctuations averaged over 1000 samples are shown in Figure 3-18 for all measurement heights. In general, autocorrelation magnitudes for the $\Delta y = 0$ autocorrelations (Figure 3-18a) increased for $\Delta x/\delta < 0.5$ with increasing z^+, while decreasing for $\Delta x/\delta > 0.5$. At $z^+ = 125$, the correlation coefficient decreases at a faster rate for $\Delta x/\delta < 0.5$, relative to both $z^+ = 300$ and 500. On the other hand, a slower decrease is shown at $z^+ = 125$ for $\Delta x/\delta > 0.5$ compared to $z^+ = 300$ and 500, resulting in a greater non-zero correlation at $\Delta x/\delta = \pm 1$. This suggests more flow structures on average with characteristic lengths greater than $\Delta x/\delta > 0.5$ at $z^+ = 125$, relative to $z^+ = 300$ and 500. Also, this could mean a greater number of structures on average with length scales of $\Delta x/\delta < 0.5$ at $z^+ = 300$ and 500 relative to $z^+ = 125$. This interpretation is consistent with the instantaneous observations of packet signatures becoming shorter with increased measurement height.

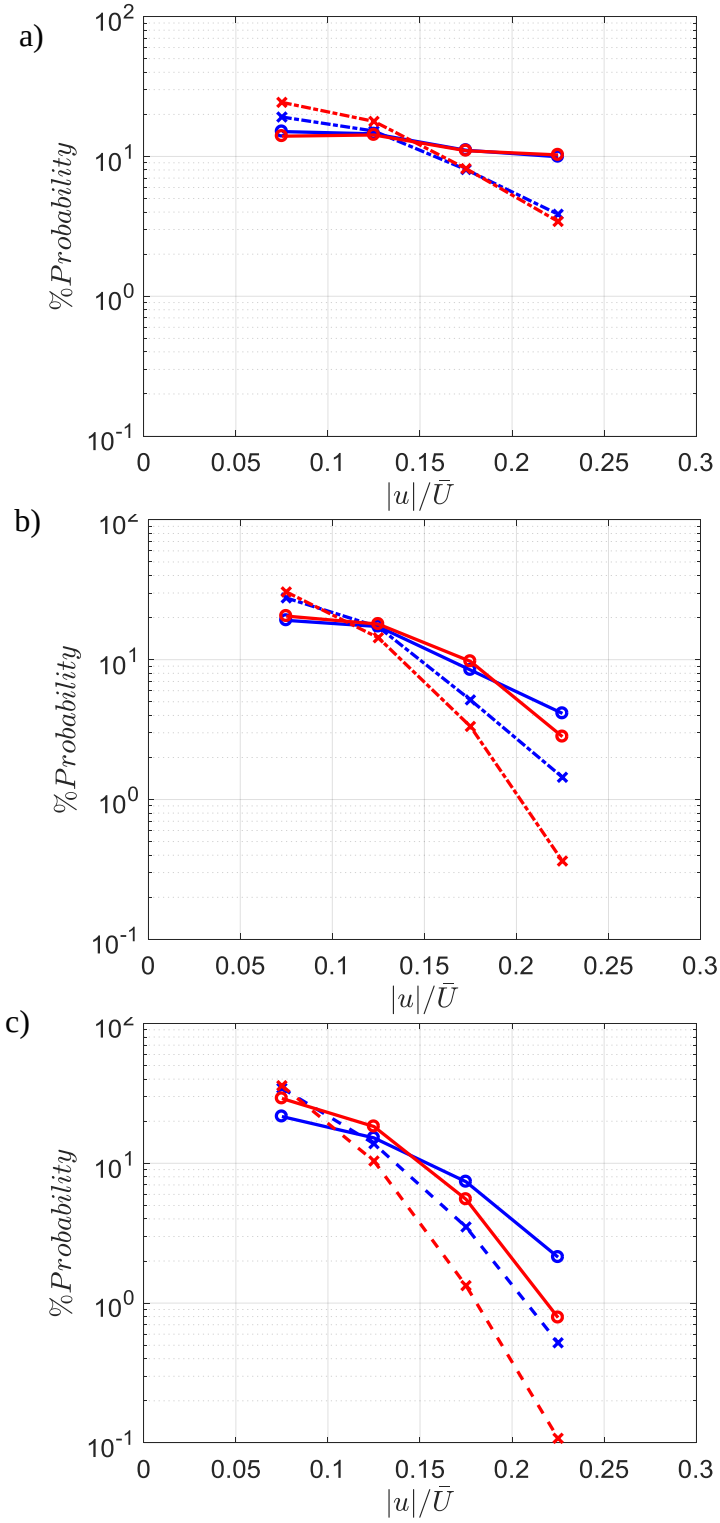

Figure 3-17: Distributions of the absolute magnitudes of the deviations away from the local mean velocity within extracted low(blue)/high(red) momentum regions at a) z^+ = 125, b) z^+ = 300 and c) z^+ = 500. Distributions separated for CMRs with $L_{ex} > 0.5\delta$ (solid) and $L_{ex} < 0.5\delta$ (dashed).

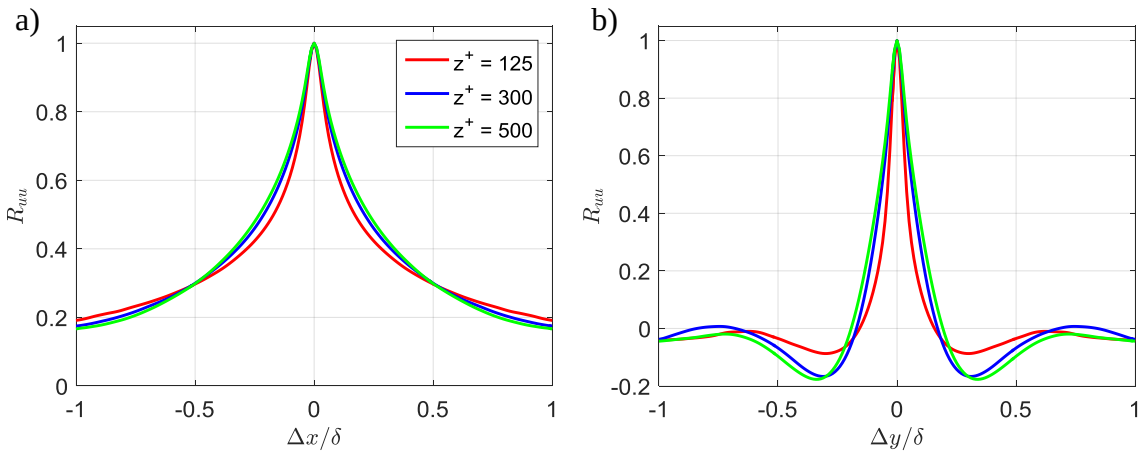

Figure 3-18: Unperturbed flow. a) Streamwise ($\Delta y/\delta = 0$) and b) spanwise ($\Delta x/\delta = 0$) autocorrelations of streamwise velocity fluctuations at $z^+ = 125$ (red), $z^+ = 300$ (blue) and $z^+ = 500$ (green).

For the $\Delta x = 0$ autocorrelations (Fig. 3-18b), the central positive lobe of the correlation becomes wider with increasing measurement height. This suggests that characteristic spanwise scales become greater with increasing measurement height, consistent with instantaneous visualizations. Also, the negative lobe adjacent to the positive central lobe shifts to greater $\Delta y/\delta$ and becomes increasingly negative with increased measurement height. The negative lobes may be interpreted as corresponding to the spanwise distance between the center line of the high momentum zones and the center line of the adjacent low momentum zones. The trends thus indicate that on average, the spanwise spacing between these zones increases with increased measurement height.

Autocorrelation trends across multiple streamwise locations are plotted in Figure 3-19 for all measurement heights. In general, correlation values for $\Delta y = 0$ autocorrelations (Figs. 3-19a-c) increased with x-location. This effect is more evident at $z^+ = 300$ and 500, compared to $z^+ = 125$. This is reasonable as the boundary layer thickness and Reynolds

number both increase as a function of x, hence the largest characteristic scales should grow as well. In comparison, only very weak trends possibly within uncertainty are present in the Δx = 0 autocorrelations (Figs 3-19d-f). The width of the positive lobe possibly increases while the position of the negative lobes shifts towards greater magnitudes with increasing x-location.

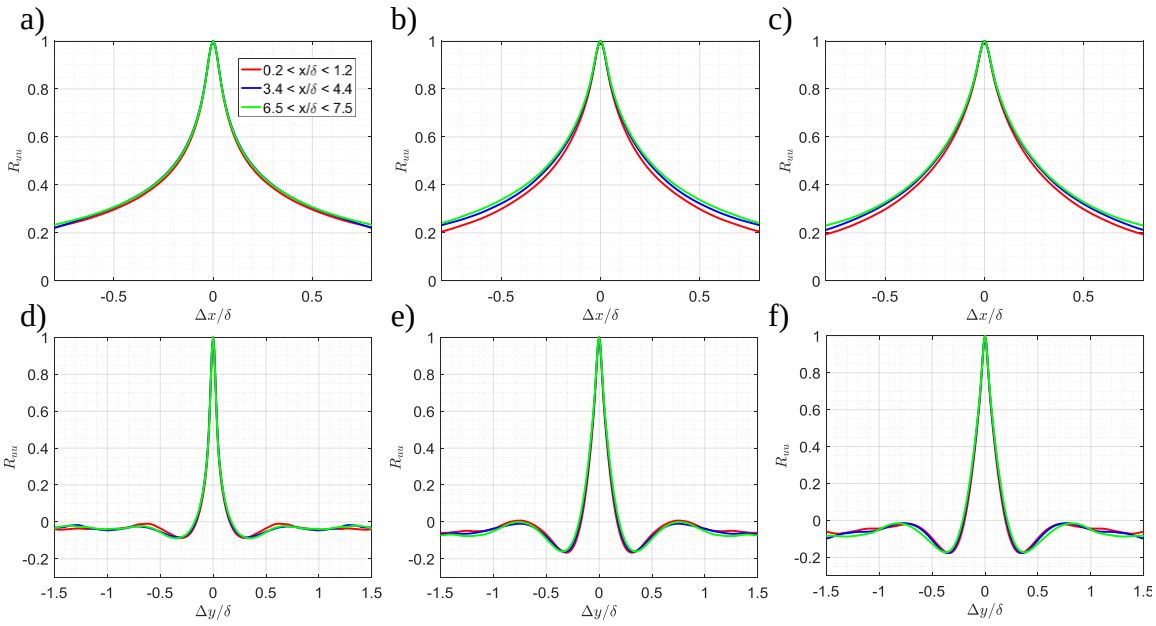

Figure 3-19: Unperturbed flow. Streamwise (Δy/δ = 0) autocorrelations for a) z^+ = 125, b) z^+ = 300 and c) z^+ = 500. Spanwise (Δx/δ = 0) autocorrelations for d) z^+ = 125, e) z^+ = 300 and f) z^+ = 500.

Autocorrelation results computed from wall parallel planes extracted from 3-D PTV volumes at z^+= 155, 300 and 465 are shown in Figure 3-20. The depth of each wall parallel plane was 60 wall units. In Figures 3-20d and 3-20e, which show streamwise and spanwise cuts with Δy = 0 and Δx = 0 respectively, two points are notable. First, the streamwise correlation at Δy = 0 is distinctly lower near the tails (|Δx| > 0.5) at z^+ = 465 than at 155 or 300 where the values are similar. This result implies that fewer long low

and high momentum regions are present. Second, the spanwise cut with $\Delta x = 0$ shows that the central positive lobe grows wider with increasing height indicative of growing spanwise length scales. The trends are consistent with the PPIV autocorrelation results, and visualizations. The trends from all autocorrelation results are also consistent with previous results in unperturbed turbulent boundary layers (Ganapathisubramani *et al.* 2005; Hutchins & Marusic 2007; Tutkun *et al.* 2009).

3.3.3 Wall-parallel cross correlations from 3-D PTV

Cross correlations of streamwise velocity from planes at different depths are shown in Figure 3-21. Values from a reference plane at $z_{ref}^+ = 155$ are correlated with values at depths of $z_c^+ = 200$ (Fig. 3-21a), 300 (Fig. 3-21b) and 465 (Fig. 3-21c) respectively. In the plots, positive values of Δx correspond with a positive offset in the streamwise location in the upper z plane compared with the streamwise location at z_{ref}^+. As would be expected, the cross correlation peak values decrease with greater separation between the reference plane and the correlated plane. This trend is most obvious in the streamwise cuts with $\Delta y = 0$ shown in Fig. 3-21d. Furthermore, the correlation peaks shift toward positive Δx as the wall-normal separation increases, and values for positive Δx drop off more slowly than those for negative Δx. This trend is consistent with previous streamwise-wall normal correlations (e.g. Dennis and Nickels 2011), and may be attributed to the presence of forward leaning structures (e.g. hairpin packets). In Fig. 3-21e, which shows the spanwise cut with $\Delta x = 0$, the central positive region became wider with increasing wall-normal separation. Interestingly, the negative lobes were very similar in all three correlations, which might suggest that many of the neighboring low

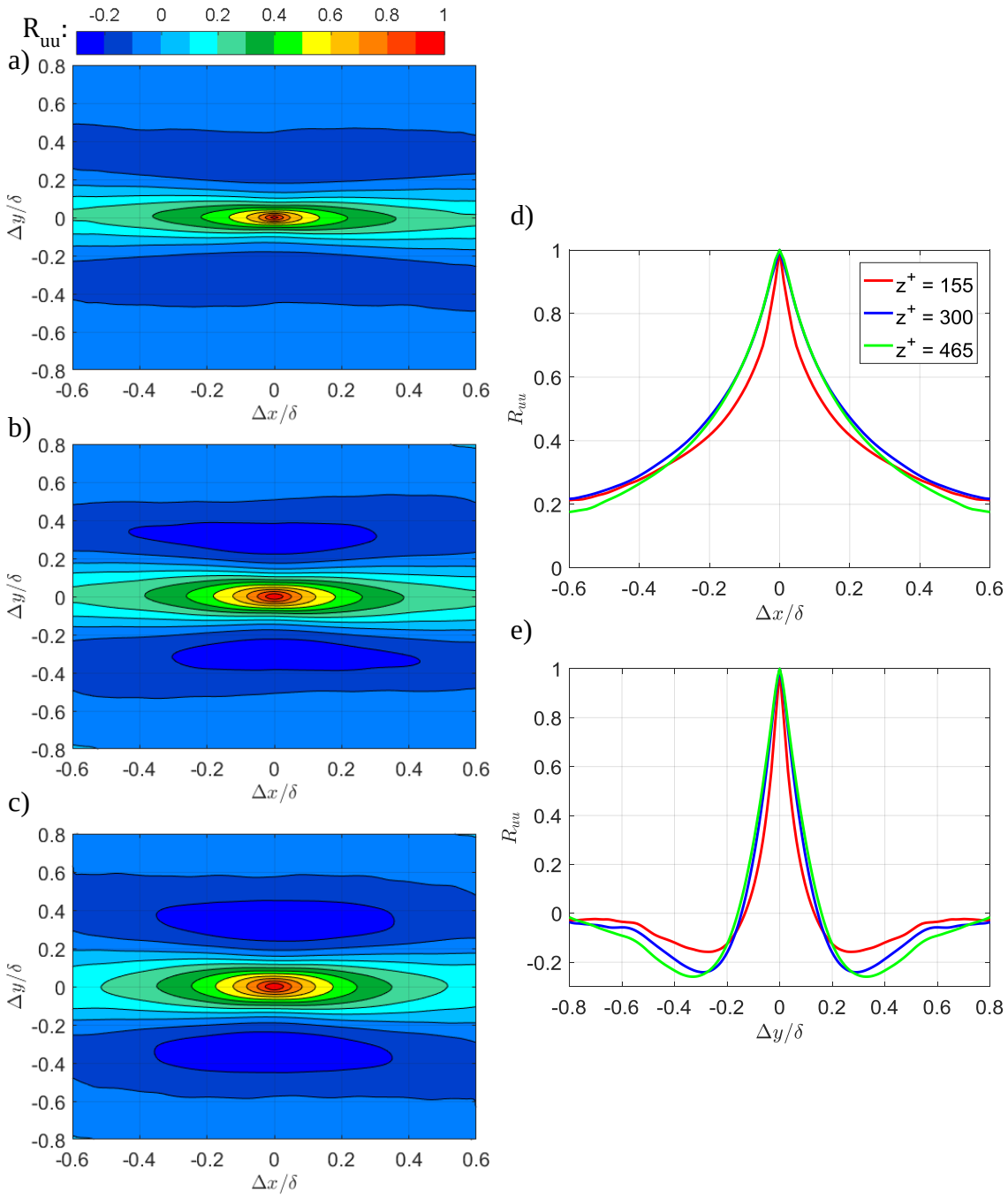

Figure 3-20: Unperturbed flow. Autocorrelations of streamwise velocity fluctuations at a) $z^+ = 155$, b) $z^+ = 300$ and c) $z^+ = 465$ from 3-D PTV measurements. Autocorrelations for aforementioned heights at d) $\Delta y/\delta = 0$ and e) $\Delta x/\delta = 0$. 500 independent fields correlated.

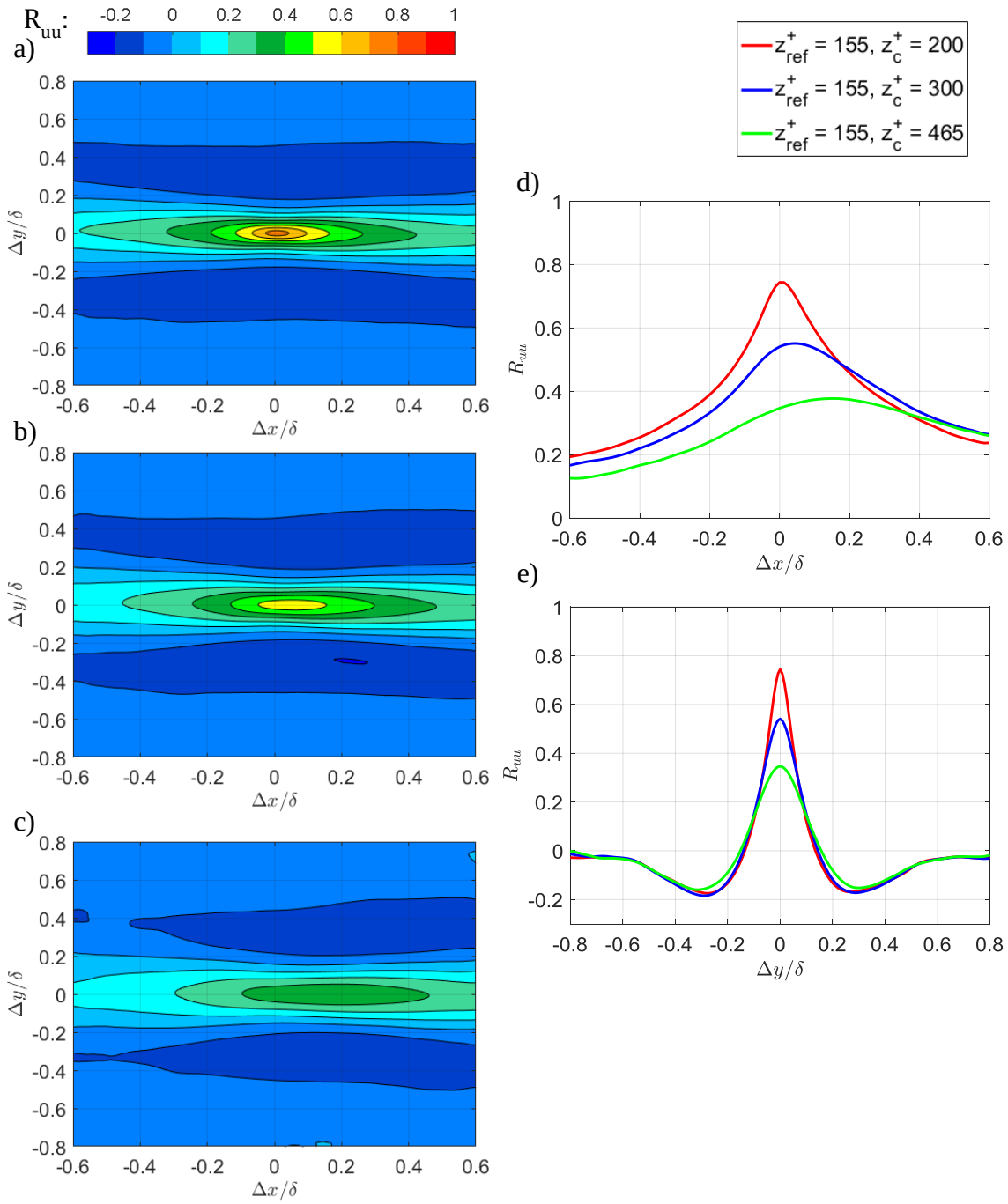

Figure 3-21: Unperturbed flow. Cross-correlation contours of streamwise velocity fluctuations from 3-D PTV measurements at z^+_{ref} = 155, with measurement plane at a) z^+ = 200, b) z^+ = 300 and c) z^+ = 465. Cross-correlations for d) $\Delta y/\delta = 0$ and e) $\Delta x/\delta = 0$ at aforementioned heights.

and high speed structures have similar spanwise spacing across the depth of the measurement domain.

3.3.4 Pre-multiplied energy spectra and dominant spanwise modes

One dimensional premultiplied energy spectra (Figure 3-22) averaged over 1000 instances were computed for streamwise velocity fluctuations along the spanwise direction from PPIV velocity fields. The dominance of the 0.6δ spanwise wavelength for all measurement planes is evident in results normalized two different ways, one by the RMS velocity squared (Figure 3-22a), and the other by friction velocity, U_τ (Figure 3-22b). The peaks in the energy spectra for all measurement heights coincides at $\lambda_y/\delta \approx 0.6$. With increasing measurement height, larger spanwise wavelengths become more energetic. Figure 3-22a shows that for $z^+ = 125$, wavelengths smaller than 0.35δ contain more energy on average compared to $z^+ = 300$ and 500 at the same wavelengths. In comparison, spanwise wavelengths greater than ~0.35δ are more energetic for $z^+ = 300$ and 500 compared to $z^+ = 125$.Similar inferences albeit at different cut-off wavelengths can be drawn with regard to Figure 3-22b. The spectra shapes and trends with increasing z^+ aligns well with results by Tomkins & Adrian (2005) in a canonical boundary layer.

Related two dimensional pre-multiplied spectra are shown in Figure 3-23. Results show that energy near spanwise modes with $\lambda_y/\delta \approx 0.6$ became increasingly important with increasing streamwise wavelength, up to $\lambda_x/\delta = \infty$, the wavelength interpreted by Tomkins & Adrian (2005) to represent contributions of all modes longer than the PIV data domain. At shorter streamwise wavelengths, the shape of the energy spectrum becomes broader with the peak shifting towards smaller spanwise modes. For $\lambda_x/\delta = 0.5$, the peaks in the spectra occurred at $\lambda_y/\delta \approx 0.2$ for $z^+= 125$ and $\lambda_y/\delta \approx 0.4$ for both $z^+ = 300$

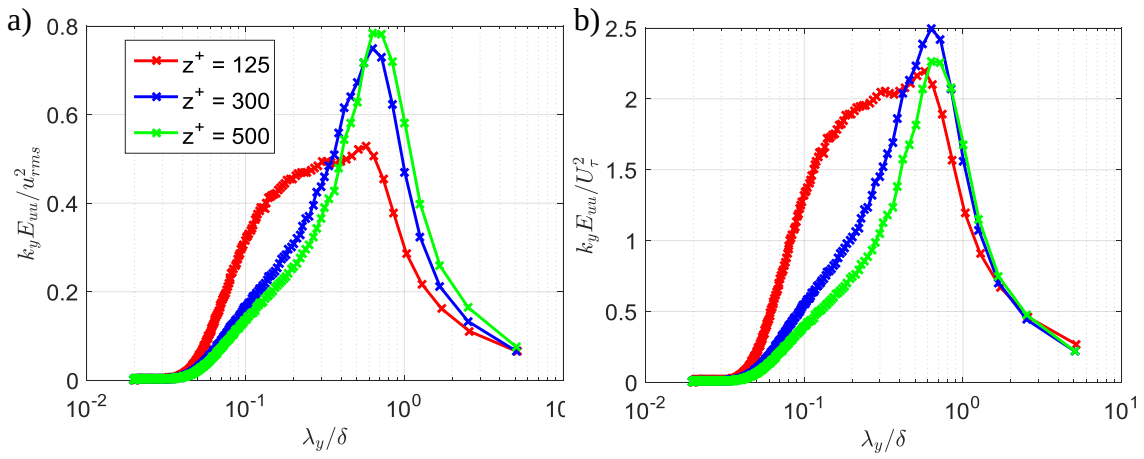

Figure 3-22: 1-D premultiplied energy spectrum of streamwise velocity fluctuations along the spanwise direction.

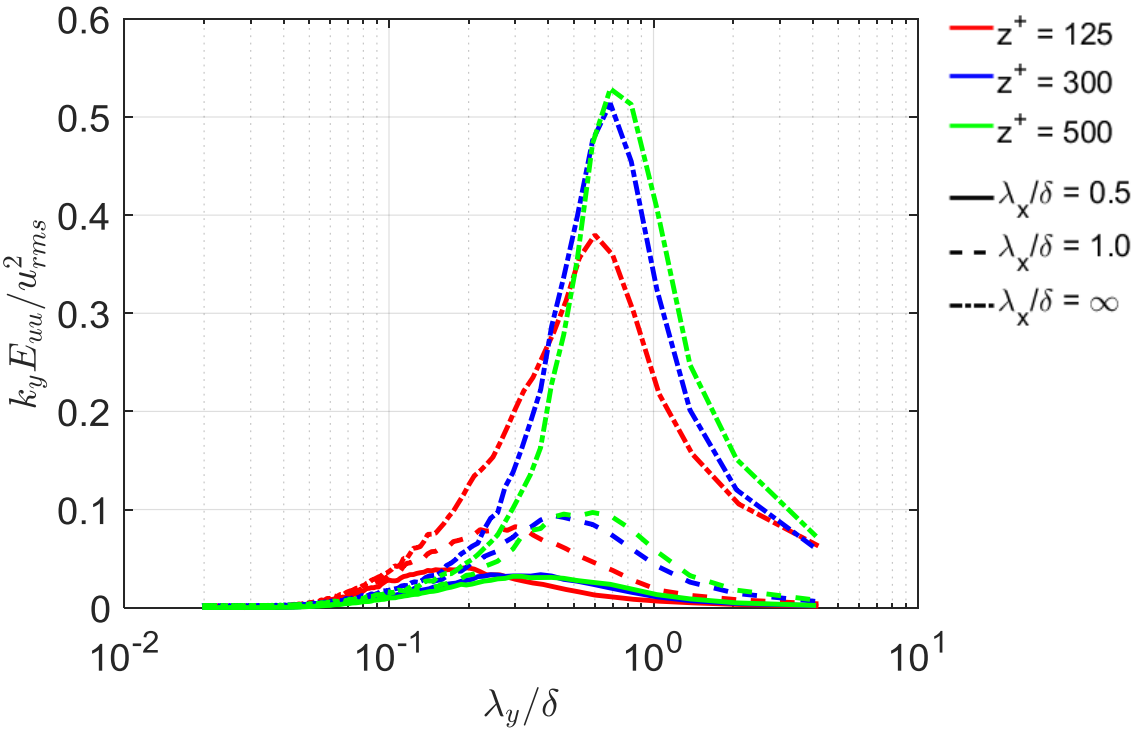

Figure 3-23: 2-D premultiplied energy spectrum of strreamwise velocity fluctuations along the spanwise direction for select streamwise wavelengths for all measurement heights.

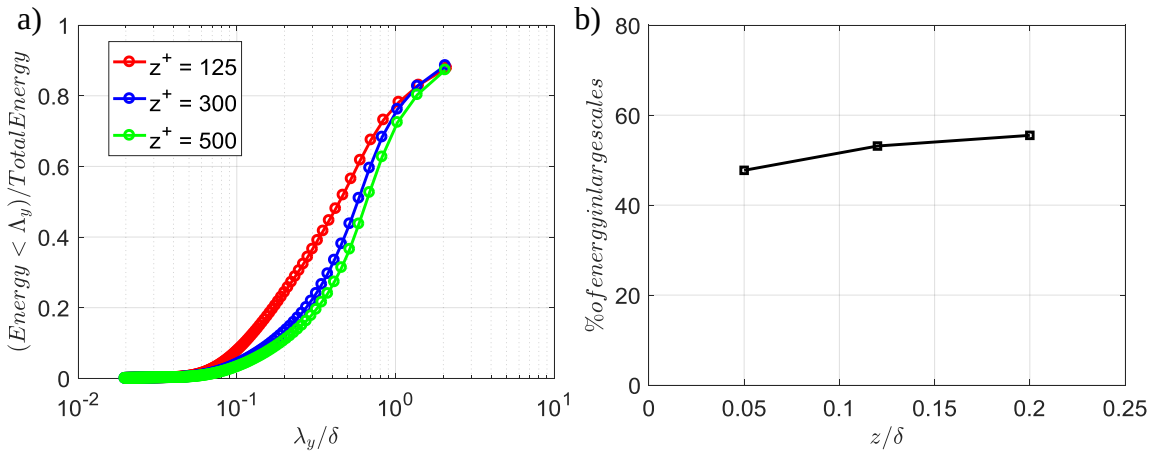

Figure 3-24: a) Cumulative spectral energy normalized by total energy versus spanwise wavelength for all measurement heights. b) Percentage of energy for $\lambda_y/\delta > 0.5$ versus wall normal location.

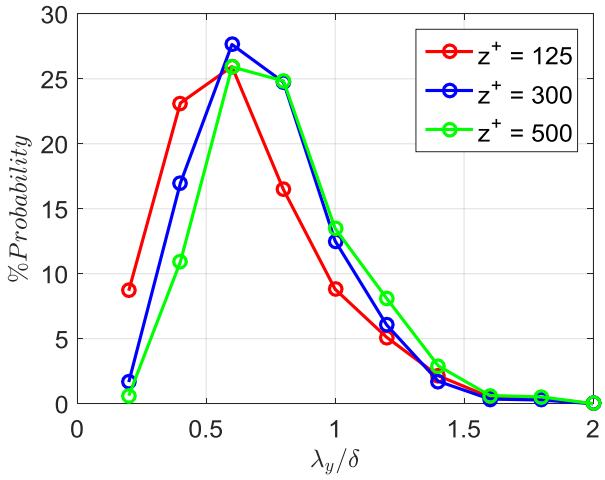

Figure 3-25: Normalized probability of dominant spanwise modes extracted from streamwise velocity fluctuations versus spanwise wavelength.

and 500. With increasing streamwise wavelength, the peaks of the spectra for all measurement heights shifts to larger spanwise wavelengths while also increasing in magnitude. For $\lambda_x/\delta = \infty$, the peaks are located at $\lambda_y/\delta \approx 0.6$ for $z^+ = 125$ and $\lambda_y/\delta \approx 0.69$ for both $z^+ = 300$ and 500.

Results showing cumulative spectral energy normalized by the total energy up to the maximum resolvable spanwise wavelength versus spanwise wavelength are shown in Figure 3-24a. The plot illustrates the energetic dominance of the larger spanwise modes. At $z^+ = 125$, close to 50% of the energy is contained in spanwise wavelengths greater than 0.5δ and this percentage increases with increasing z^+ as shown in Figure 3-24b. These trends, which are consistent with results from Tomkins & Adrian (2005), indicate that the large scale wavelengths dominate the energy throughout the logarithmic region.

The normalized probabilities of the dominant spanwise modes of streamwise velocity fluctuations are shown for all measurement heights for the field centered at $x = 0.5\delta$ (Figure 3-25). Results show the dominance of the 0.6δ spanwise mode across the logarithmic layer as indicated by the coinciding peaks of the distributions. With increasing z^+, the overall distribution shifts towards larger wavelengths, suggesting that larger spanwise modes become more energetic, consistent with spectral results.

Figure 3-26 shows the change in the dominant spanwise mode distributions with increasing x for all measurement heights. At $z^+ = 125$ (Fig. 3-26a), the 0.6δ spanwise mode dominates for all streamwise locations. The distribution also shifts towards larger wavelengths suggesting that larger spanwise modes become more energetic with increasing x, consistent with spanwise scale growth. The boundary layer thickness grows by 10% over the measurement domain thus the largest scales within the flow must

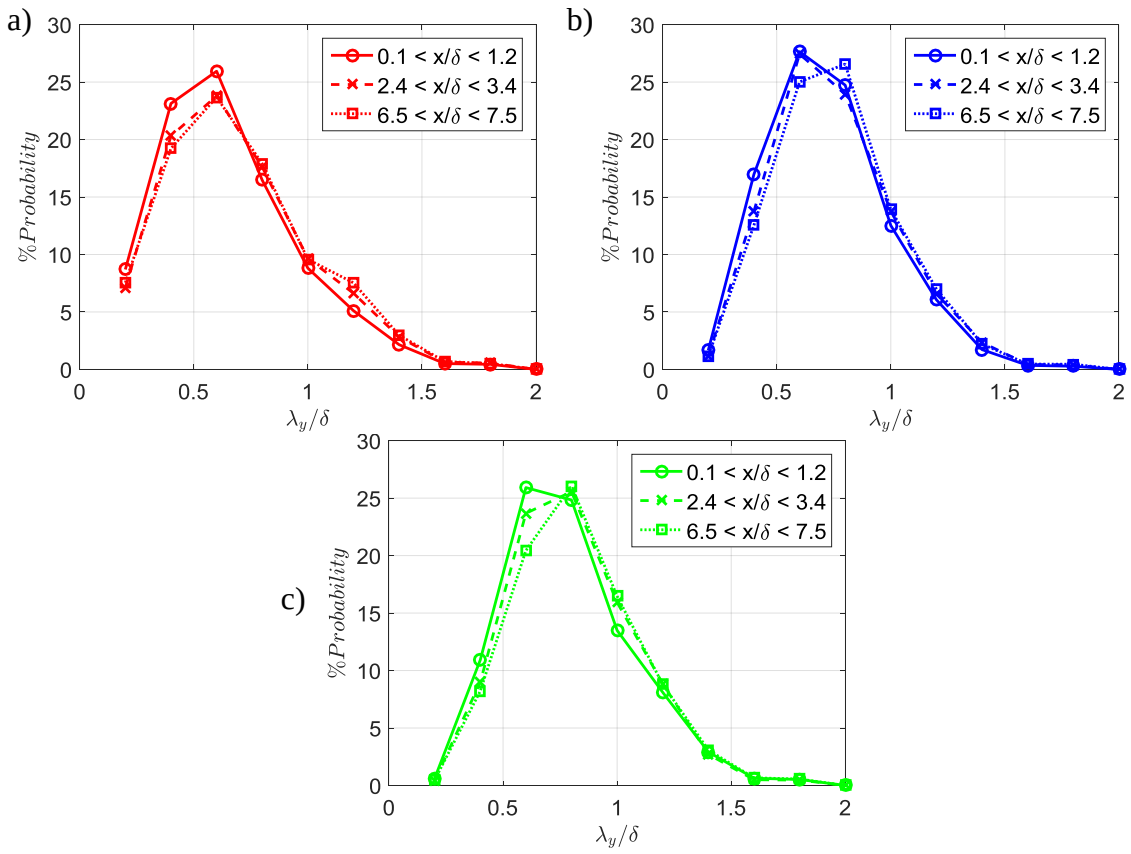

Figure 3-26: Streamwise evolution of normalized probability of dominant spanwise modes versus spanwise wavelength for a) z^+ = 125, b) z^+ = 300 and c) z^+ = 500.

increase as well. Autocorrelations show weak trends that support the aforementioned observation as well.

In comparison, with increasing x, the peaks of distributions at both z^+ = 300 and 500 (Figs. 3-26 b&c) shift towards 0.8δ, although at x = 7δ, the probabilities of the 0.6δ spanwise modes are still comparable to the 0.8δ spanwise modes. The peak locations of the dominant spanwise mode distributions across the logarithmic layer compare well with previous findings (Tomkins & Adrian 2005; Elsinga *et al.* 2011; Gao 2011; Zheng & Longmire 2014). With increasing x, both distributions at z^+ = 300 and 500 also shifts

slightly to larger spanwise modes, similar but to a lesser degree compared to the distribution at $z^+ = 125$.

3.3.5 VPIA results

The VPIA was applied to the unperturbed data (sets of 1000 fields). Results showed that the unperturbed number of individual packets per field, $N_{p/f}$ was greatest at $z^+ = 125$ (1.45/field), decreasing to 0.9/field at $z^+ = 300$ and 0.4/field at $z^+ = 500$.

The number of packets per field as a function of skeleton length is shown in Figure 3-27a. The number of packets with length greater than the field of view (FOV) is largest at $z^+ = 125$ and least at $z^+ = 500$. The normalized packet distributions (Figure 3-27c) showed similar percentages of packets longer than the FOV at $z^+ = 125$ and 300 (22%), but a smaller percentage at $z^+ = 500$ (16%). Recall at $z^+ = 125$, long and skinny packets were frequently observed (e.g. Figure 3-12a), consistent with this result.

Figure 3-27b shows the distribution of the mean widths of detected packets. With increasing wall normal distance, the distribution becomes broader with the peak shifting toward larger values. The peak values of 0.075δ at $z^+ = 125$, 0.125δ at $z^+ = 300$ and 0.15δ at $z^+ = 500$ agree well with the findings of Tomkins & Adrian (2003), and observations in instantaneous flow. Figure 3-27d shows the normalized packet distributions, where results also corroborated the aforementioned inferences.

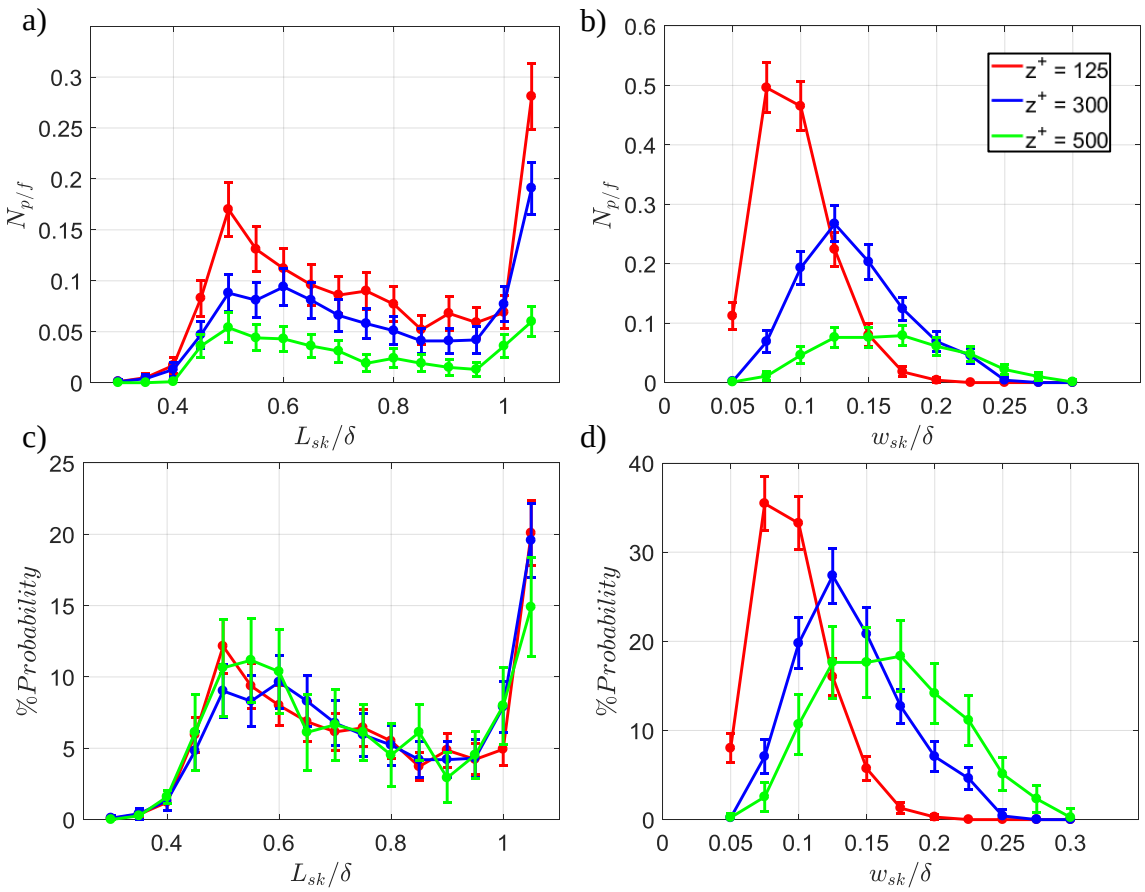

Figure 3-27: Unperturbed flow. Number of packets per field as a function of a) packet skeleton length and b) mean packet skeleton width. Normalization with total number of packets versus c) packet skeleton length, and d) mean packet skeleton width.

Chapter 4

Results & Discussion: 0.2δ spacing array, boundary layer and vortex packet recovery

In this chapter, results of the flow perturbed by the S = 0.2δ cylinder array are shown and compared with the unperturbed flow results in Chapter 3. Two array heights are considered, H = 0.2δ and H = δ. First, the results for the flow perturbed by H = 0.2δ cylinders will be presented, followed by the H = δ results. Then, results from both arrays will be summarized and discussed.

4.1 Flow perturbed by array with S = 0.2δ and H = 0.2δ

4.1.1 Time-averaged velocity results

Wakes are observed directly behind each cylinder with the local momentum deficit becoming weaker on average as the cylinder tip height, $H^+ = 500$ is approached. Average streamwise velocity contours from PPIV measurements are shown in Figure 4-1. For $z^+ =$ 125 and 300 (Fig.4-1a & b), wakes occur directly behind every cylinder compared to faster moving zones on average at $z^+ = 500$ (Fig. 4-1c). The fast moving zones may be attributed to tip structures shedding off each cylinder, directing faster moving fluid from above towards the wall on average, consistent with volumetric measurements by Ortiz-Dueñas *et al.* (2011). Our 3-D PTV results immediately behind the H = 0.2δ array agreed with the PPIV results. Figure 4-2 shows iso-surfaces (blue) of average streamwise velocity slower than 95% of the local $\overline{U}$. The iso-surfaces are elongated in the streamwise direction closest to the wall ($z^+ = 155$) and becomes shorter as the cylinder tip

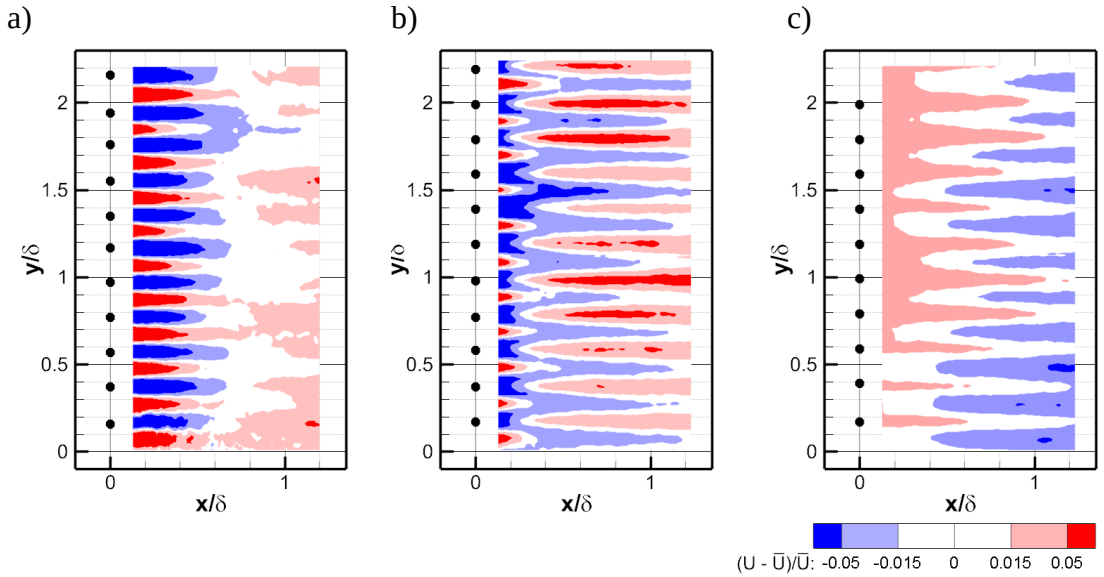

Figure 4-1: S = 0.2δ, H = 0.2δ array. Average streamwise velocity results from PPIV at measurement height a) z^+ = 125, b) z^+ = 300 and c) z^+ = 500.

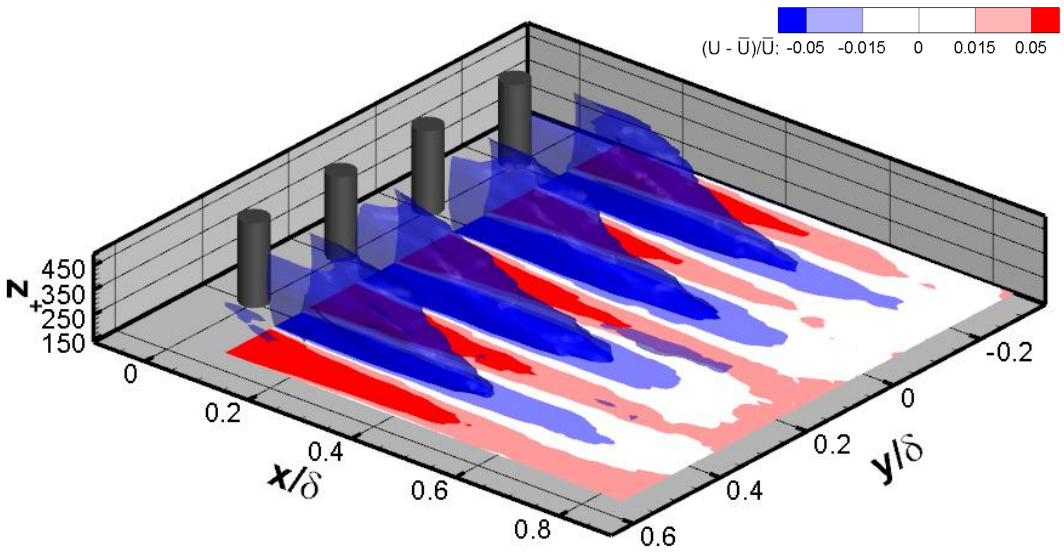

Figure 4-2: S = 0.2δ, H = 0.2δ array. Average streamwise velocity results from 3-D PTV. Colors show fractional deviation away from the local mean velocity for the plane at z^+ = 155. Iso-surfaces show regions with U < 0.95Ū.

height is approached. Furthermore, at z^+ = 300 and 465 (Figs 4-3b & c), fluid moves towards the wall on average behind every cylinder at the beginning of the measurement zone (x = 0.1δ). This effect is not observed at z^+ = 155 (Fig. 4-3a) immediately downstream of the cylinders. Instead a weak upwash effect is observed. This may relate to a base vortex generated at the junction of the cylinder and the wall, which leads to an upwash on average near the base of the cylinder (Sumner *et al.* 2004; Wang *et al.* 2006). Later, near x = 0.7δ, spots with weak downwash are seen (e.g. y/δ = 0.2). The downwash magnitude is within uncertainty, although this result still suggests that the downwash effects exist in planes below. This is confirmed by examining planes between z^+ = 155 and z^+ = 300. The z^+ = 215 plane (not shown) show obvious downwash effects starting only at x = 0.4δ, later compared to measurement planes above.

On average, at z^+ = 300 (Fig. 4-1b), the cylinder wakes are split by the downwash induced at the cylinder tips. The split wakes then merge with adjacent split wakes along the spanwise direction, forming slow moving zones aligned with spanwise locations midway between cylinders, while faster moving zones form behind the cylinders. This behavior is seen clearly in averaged streamwise velocity plots from PPIV results (Figs. 4-1b) and 3D-PTV results (Figs. 4-4b&c). Results also show the location where momentum reversal occurs shifting further downstream with decreasing measurement height. At z^+ = 500 (Fig 4-1c), fast moving zones were observed already starting x = 0.15δ behind the cylinders. In contrast, fast moving zones were seen later at x = 0.3δ at z^+ = 300 (Figs. 4-1b and 4-3b). This may be related to the increased delay in the downwash effects with decreasing z^+. Furthermore, there was no clear indication of wakes splitting and merging

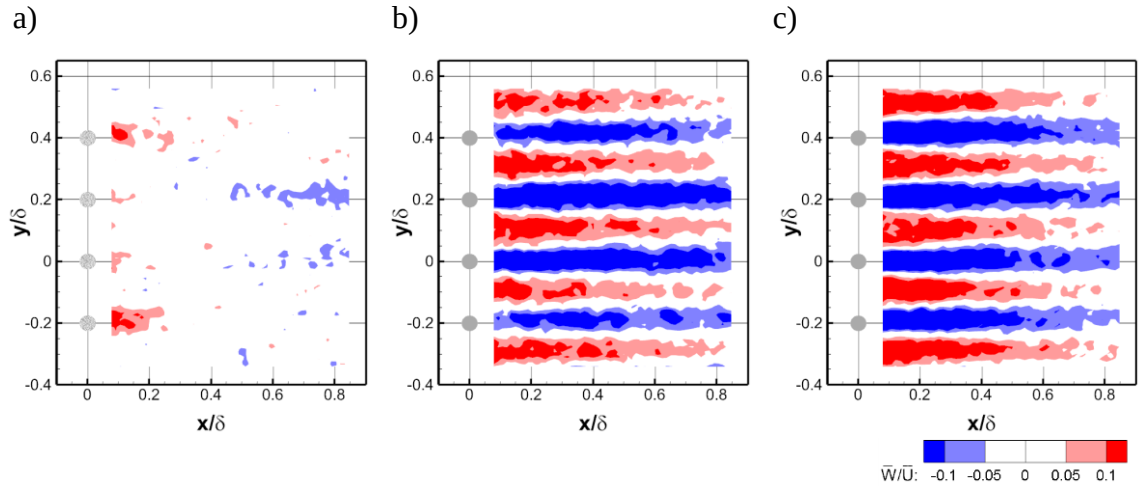

Figure 4-3: S = 0.2δ, H = 0.2δ array. Streamwise-spanwise slices of average wall-normal velocity from 3-D PTV at a) z^+ = 155, b) z^+ = 300 and c) z^+ = 465.

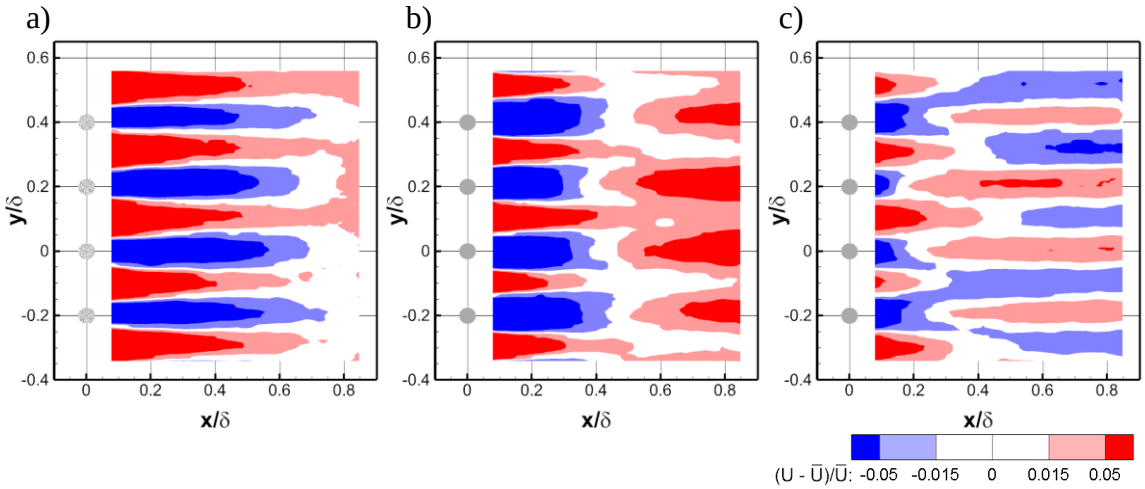

Figure 4-4: S = 0.2δ, H = 0.2δ array. Streamwise-spanwise slices of average streamwise velocity from 3-D PTV at a) z^+ = 155, b) z^+ = 300 and c) z^+ = 465.

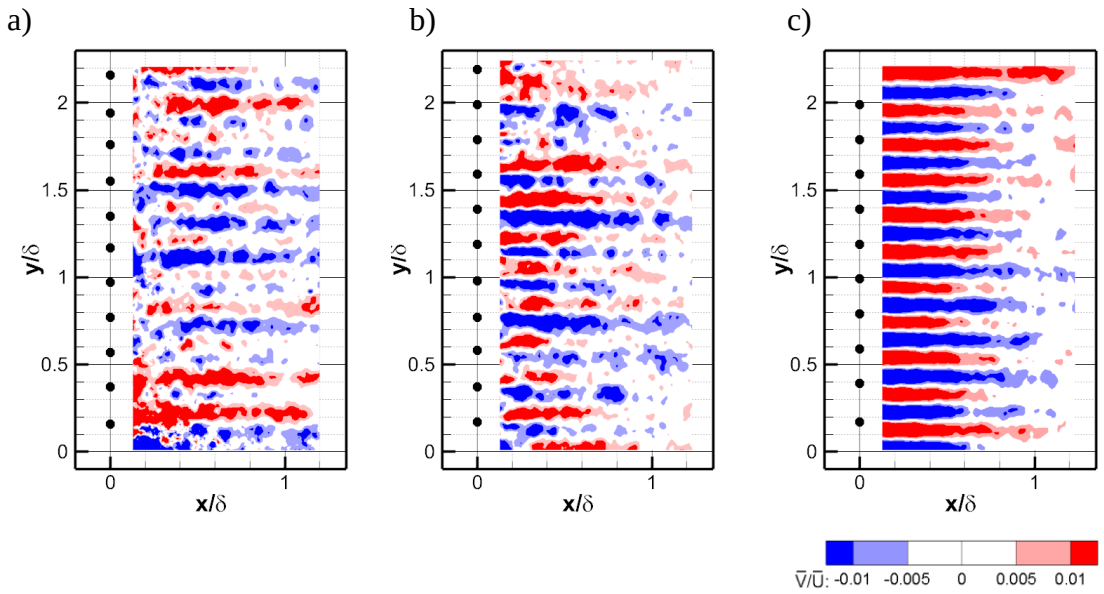

Figure 4-5: S = 0.2δ, H = 0.2δ array. Average spanwise velocity results from PPIV at measurement height a) z^+ = 125, b) z^+ = 300 and c) z^+ = 500.

at z^+ = 125 (Fig. 4-1a) and z^+ = 155 (Fig. 4-4a). This is consistent with the absence of average downwash (Fig. 4-3a) at the aforementioned planes.

In plots of spanwise velocity, regions of converging fluid were observed on average at the cylinder tips (see Fig. 4-5c) consistent with the signature of a pair of tip vortices (Sumner *et al.* 2004; Ortiz-Dueñas *et al.* 2011). With decreasing measurement height, the tip velocity pattern becomes weaker and switches signs at z^+ = 300 (see Fig. 4-5a & b). At these heights, periodic Karman-like vortices were likely dominant. The pattern points to fluid diverging behind the cylinder on average, consistent with the split cylinder wakes (Fig 4-1 & 4-4). 3-D PTV results also showed similar trends (see Fig. 4-6).

The mean and root mean square (RMS) streamwise velocity versus streamwise location for both unperturbed flow and flow downstream of the H = 0.2δ array are shown in

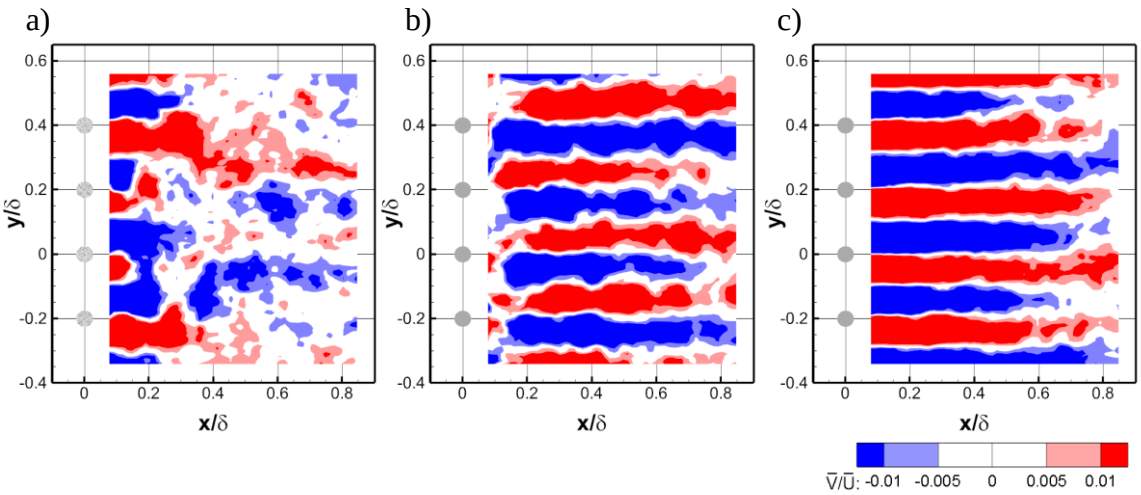

Figure 4-6: S = 0.2δ, H = 0.2δ array. Streamwise-spanwise slices of average spanwise velocity from 3-D PTV at a) z^+ = 155, b) z^+ = 300 and c) z^+ = 465.

Figure 4-7. In all cases, PPIV results were averaged over measurement fields centered on the plotted streamwise location.

Mean velocity results (Fig. 4-7a) showed that in the perturbed flow, the mean streamwise velocity was reduced compared to the unperturbed flow at all measurement heights due to the blockage posed by the H = 0.2δ array. The decrease immediately downstream of the array was significant at 10% of free-stream velocity U_∞ for both z^+ = 125 and z^+ = 300 but much smaller ($0.01U_\infty$) at z^+ = 500, the array tip height. With increasing streamwise distance, the mean velocity at z^+ = 500 first decreased towards a minimum between 2δ and 3δ before increasing gradually toward the unperturbed value. At both z^+ = 125 and 300, the mean velocity in the perturbed flow increased more rapidly towards the unperturbed value. At x = 7δ, the streamwise velocity remained suppressed by 2-3% of U_∞ at all measurement heights compared to the values in the unperturbed flow.

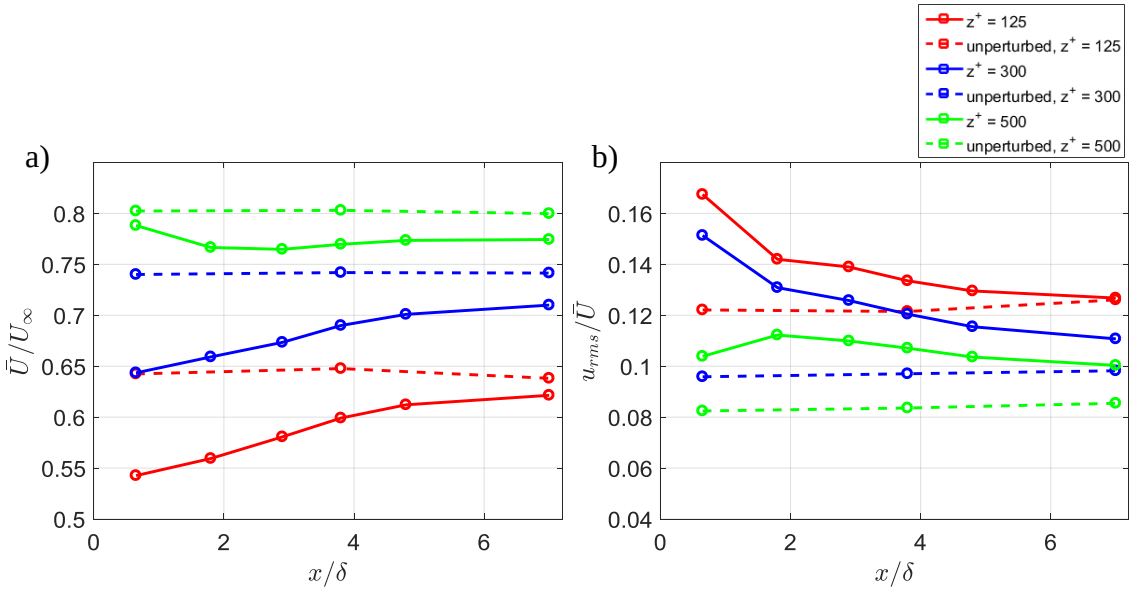

Figure 4-7: S = 0.2δ, H = 0.2δ array. Variation of a) mean streamwise velocity normalized by free-stream velocity, and b) RMS of streamwise velocity normalized with local mean velocity at measurement height, with x-location.

The RMS velocity (Fig. 4-7b) increased substantially immediately downstream of the H = 0.2δ array at all measurement heights compared to the unperturbed values. The greatest relative increase occurred at z^+ = 300 (0.05Ū), followed by 0.04Ū at z^+ = 125 and 0.02Ū at z^+ = 500, where Ū represents the mean value at the given measurement height. The RMS velocity at z^+ = 500 first increased to a maximum at x = 1.8δ before decreasing with increasing streamwise distance, while the RMS velocity decreased monotonically at the two locations closer to the wall. By x = 7δ, the relative RMS velocity had recovered to the unperturbed value at z^+ = 125, while remaining elevated by 0.01Ū at z^+ = 300 and 500. The streamwise variations of spanwise RMS velocity (not shown) exhibited trends similar to those in streamwise RMS velocity shown in Fig. 4-7b.

4.1.2 Instantaneous Results

Instantaneous realizations of perturbed flow at z^+ = 125 and 300 revealed Karman like wake structures immediately downstream of the cylinders. No obvious packets were observed. If any were present, they were difficult to distinguish from the wakes. At z^+ = 125 (Fig. 4-8a), wakes were observed at y/δ = 0.15, 0.55, and 1.95. Similarly for z^+ = 300 (Figure 4-9a), wakes were observable at y/δ = 0.15, 0.35, 0.55 and so on. Neighboring wakes often interact as seen at y/δ = 0.95 and 1.15 in Figure 4-9a for z^+ = 300, and y/δ = 1.75 and 1.95 in Fig 4-8a at z^+ = 125. In spanwise regions between the cylinders, fast moving zones were seen frequently, for example y/δ = 1.65 at z^+ = 125 (Figure 4-8a) and y/δ = 0.45 for z^+ = 300 (Figure 4-9a). Wake structures were also dominant in the fields centered at $x = 1.8\delta$ (not shown).

In contrast, at the array tip height (z^+ = 500), wakes occurred less frequently directly behind the cylinders (Fig. 4-10a). More often, regions faster than the mean velocity were found in those locations, for example at y/δ = 0.75, 1.35 and 2. These regions might be caused by vortices shed from the tips of the arrays drawing faster moving fluid from above towards the wall. Notably, in the instantaneous spanwise velocity fields, the signatures of aforementioned tip vortices/structures were difficult to detect. At z^+ = 500, packet signatures were frequently observed directly downstream of the array as at y/δ = 1.15 and 1.7 in Figure 4-10a. With increasing x, packet signatures continued to be observed, for example at $x = 2.9\delta$ (Figure 4-10b) at y/δ = 0.3 and 1.5, and at $x = 7\delta$ (Figure 4-10c) at y/δ = 0.4 and possibly 1.2 and 1.8.

At z^+ = 300, packets similar to those in the unperturbed flow were not apparent until 2.9δ downstream of the $H = 0.2\delta$ array, for example at y/δ = 1.3 and 2.1 in Figure 4-9b. With

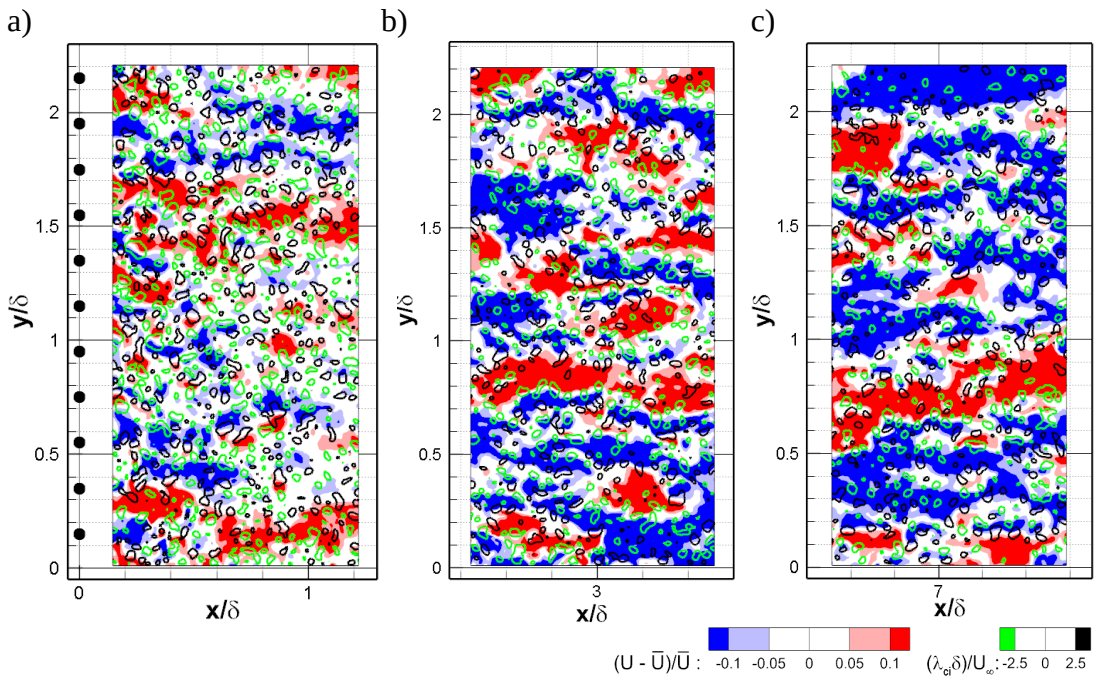

Figure 4-8: S = 0.2δ, H = 0.2δ array. Instantaneous vector fields from PPIV of perturbed flow at z^+ = 125 centered at a) x = 0.7δ, b) x = 2.9δ and c) x = 7δ.

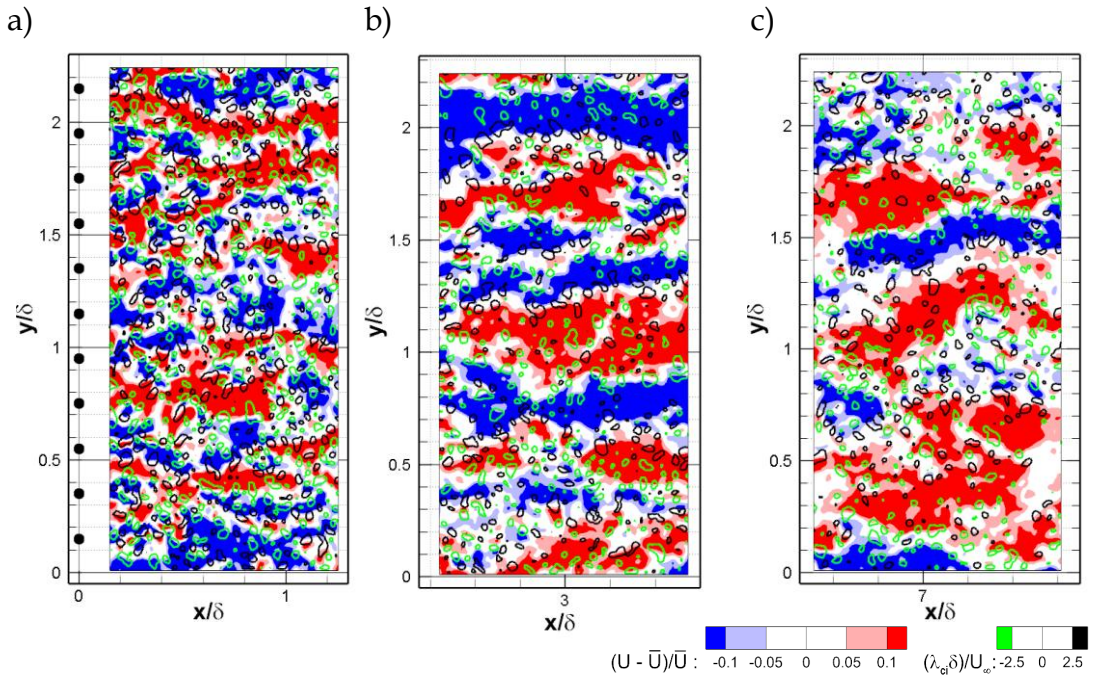

Figure 4-9: S = 0.2δ, H = 0.2δ array. Instantaneous vector fields from PPIV of perturbed flow at z^+ = 300 centered at a) x = 0.7δ, b) x = 2.9δ and c) x = 7δ.

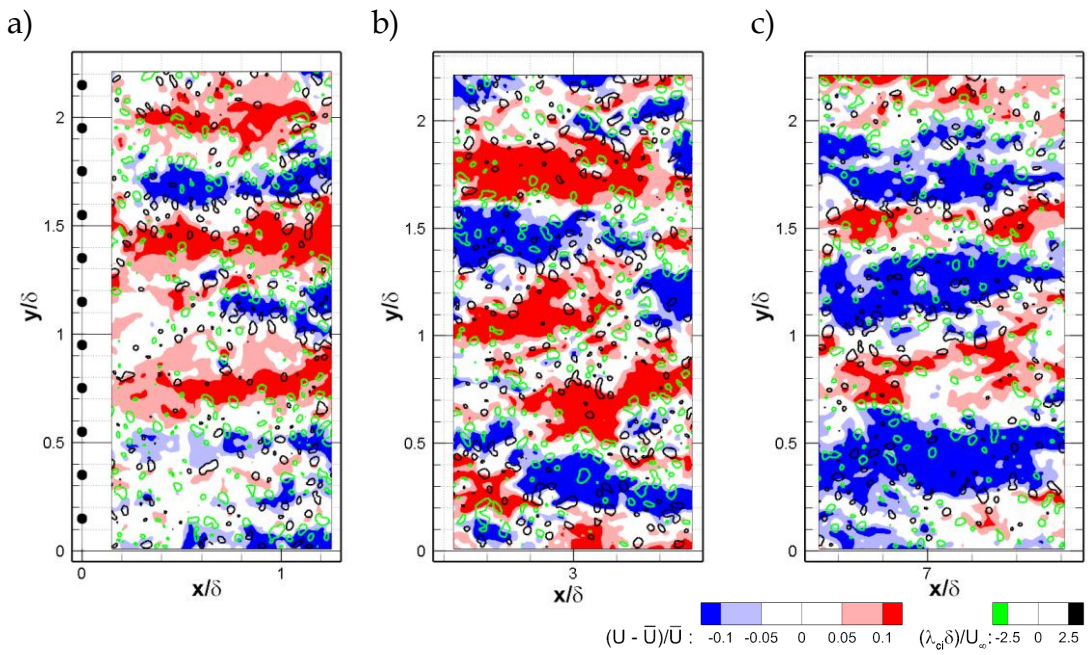

Figure 4-10: S = 0.2δ, H = 0.2δ array. Instantaneous vector fields from PPIV of perturbed flow at z^+ = 500 centered at a) x = 0.7δ, b) x = 2.9δ and c) x = 7δ.

increasing x, packets became even more like those observed in the unperturbed flow, i.e. their forms became less undulating and more similar to packets signatures seen in unperturbed flow. Examples of these are shown in Figure 4-9c at y/δ = 1.5.

At z^+ = 125, in contrast, low momentum structures at x = 2.9δ appeared wavy and unlike packet signatures in the unperturbed flow. Frequently, these wavy structures were connected to spanwise adjacent ones, as seen at y/δ = 0.3 in Figure 4-8b. Wavy low momentum structures were still observed at x/δ = 7, although they appeared less undulating compared with those at x/δ = 2.9. In addition, many spanwise merged or merging structures were still observed. Examples of wavy and merged structures can be seen at y/δ = 0.4, 1.1 and 1.6 in Figure 4-8c. Thus, the H = 0.2δ array was effective at

enhancing and sustaining spanwise interactions between adjacent coherent zones of uniform streamwise velocity at $z^+ = 125$.

FPIV runs for the H = 0.2δ array are shown in Figure 4-11. For plotting purposes, the mean velocity for each field was subtracted to obtain the velocity deviation from the mean. For the first location behind the array, this instantaneous mean was significantly less than the unperturbed mean. The mean of the field then increased with downstream distance toward the average unperturbed value. In Figure 4-11a, five incoming packets at $z^+ = 125$ are disrupted by the array. Comparing the upstream and downstream fields, the top packet signature reappeared by $x/\delta \sim 3.8$, the second packet disappeared, the third packet possibly reappeared by $x/\delta \sim 5$, the fourth disappeared, and the bottom packet reappeared by $x/\delta \sim 2.3$. Examining of additional runs showed that typically packets were disrupted by the array and remained disorganized to roughly $x/\delta \sim 3$ where packet signatures similar to the unperturbed flow re-emerged at spanwise locations aligned roughly with their previous upstream spanwise coordinates (i.e with the same phase), prior to encountering the array. Further downstream, the packet signatures were longer and less wavy. The waviness of the observed LMR is a key feature used to qualitatively differentiate between wake structures and packet signatures. Figure 4-8a illustrates the wakes generated by each cylinder at $z^+ = 125$. The individual wakes persist to about 0.6δ behind the array before either pairing with neighboring wakes or becoming unstable. Generally, the LMRs associated with these wakes look wavier than the unperturbed LMRs seen in Figure 3-10.

At $z^+ = 300$ (Figure 4-11b), two incoming packets approached the array at $y/\delta \sim 0.4$ and $y/\delta \sim 1.6$. The array disrupted the incoming organization as seen by the additional

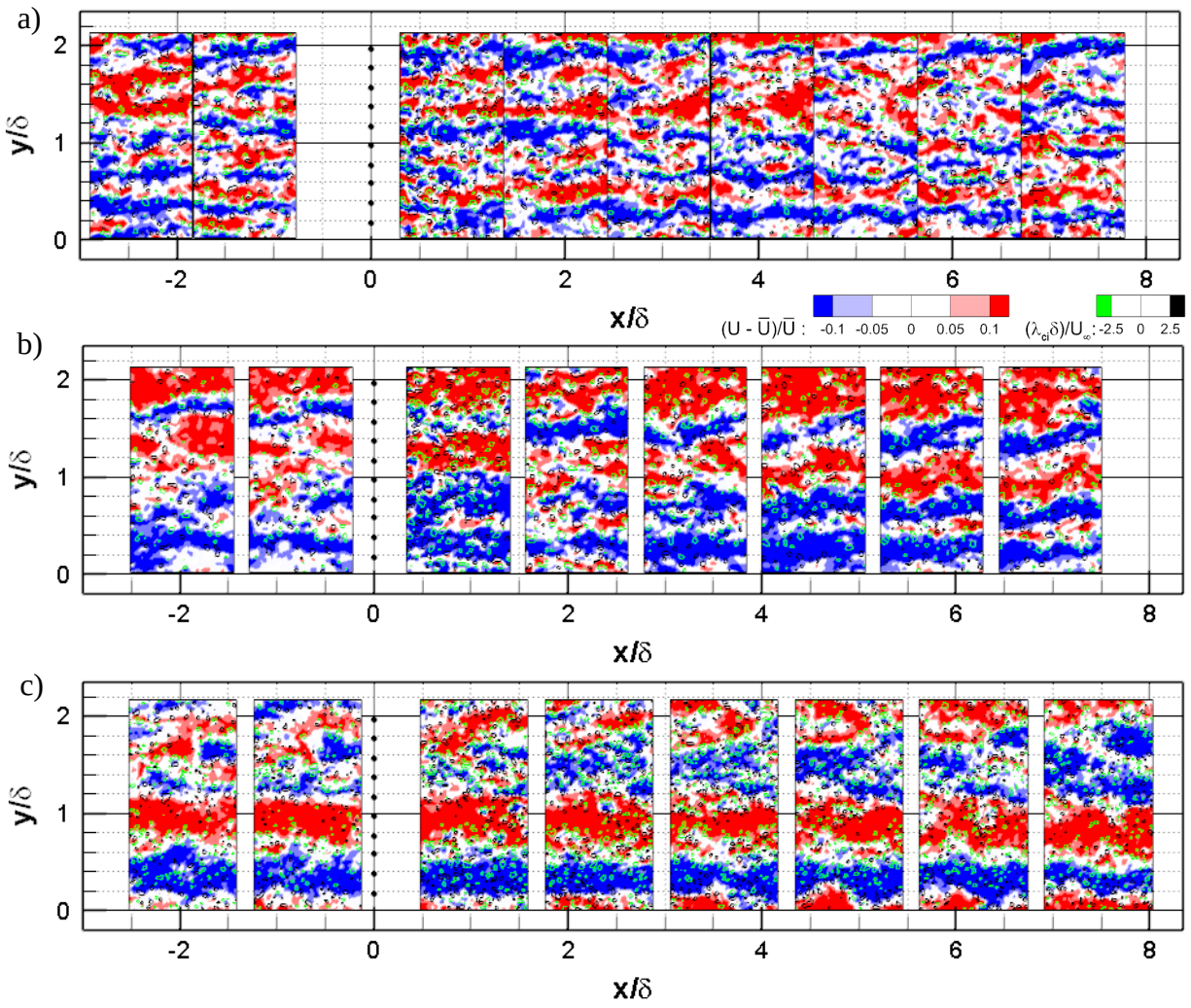

Figure 4-11: S = 0.2δ, H = 0.2δ array. FPIV runs at a) z^+ = 125, b) z^+ = 300 and c) z^+ = 500.

swirling structures and disorganized motions directly behind the array. However, the incoming packet signatures reappeared by $x/\delta \sim 2$ at roughly the same spanwise locations. With increasing downstream distance, the packets appeared less wavy and more similar to the unperturbed packets. Considering many runs as well as fixed PIV data, we generally observed signatures resembling unperturbed packets reappearing sooner at $z^+ = 300$ ($x/\delta \sim 2$) than at $z^+ = 125$ ($x/\delta \sim 3$). At $z^+ = 500$ (Figure 4-11c), which equaled the cylinder tip height, the incoming packet organization persisted through the array. In some runs, at $z^+ = 500$, the incoming packet signatures became more coherent (i.e. enhanced) immediately downstream of the array and persisted at the same spanwise location.

4.1.3 Regions of uniform streamwise momentum

Figure 4-12 illustrates the differences in the number of CMRs between the perturbed and unperturbed flow at two streamwise locations, sorted by length based on the extrema of the detected low/high speed regions, for all measurement heights. The relative differences as a percentage of the number of CMRs in the unperturbed flow are shown in Figures 4-12d-f. At $z^+ = 300$ (Fig. 4-12b & e) and 500 (Fig. 4-12c & f), $x = 2.9\delta$, the numbers of both short (bin, $L_{ex} = 0.2\delta$) and long (bin, $L_{ex} = \delta$) CMRs increased relative to the unperturbed values. In contrast, at $z^+ = 125$(Fig. 4-12a & d), the number of short CMRs decreased significantly; A larger decrease was observed for LMRs relative to HMRs. On the other hand, numbers of long CMRs remained similar to unperturbed values.

At both $z^+ = 300$ (Fig. 4-12b & e) and 500 (Fig. 4-12c & f), and $x = 7\delta$, the CMR length distributions relaxed towards the unperturbed values, although differences were still evident at $z^+ = 500$ with more long and short CMRs compared to the unperturbed flow. In

comparison, at z^+ = 125 (Fig. 4-12a & c), the significant reduction in short CMRs persisted to x = 7δ, with the number of short HMRs even smaller than at x = 2.9δ.

The mean width distributions for detected CMRs for all measurement heights in the perturbed flow are shown in Figure 4-13. The distributions show that structure widths varied little relative to the unperturbed flow at z^+ = 300 and 500 at either x = 2.9δ or x = 7δ. In comparison, at z^+ = 125, the CMRs increased at x = 2.9δ and x = 7δ. This was consistent with the instantaneous visualizations illustrating wider CMRs as a result of increased spanwise merging due to the perturbations, persisting to the field centered at x = 7δ (see Fig. 4-8). The reduction in the numbers of short CMRs at z^+ = 125 (see Fig. 4-12a & d) can be linked to the width increase.

4.1.4 Statistics on number of swirls

Figure 4-14a shows the total number of swirling structures identified downstream of the H = 0.2δ array at each measurement height where we assume that these structures represent cross sections of hairpins or other vortices intersecting the wall-parallel plane. As expected, the unperturbed swirl count was highest at z^+ = 125 and decreased with increasing measurement height. Immediately downstream of the cylinders, the number of swirls was increased at all measurement heights. At z^+ = 125 and 300, the values were similar, suggesting that identified swirling structures were likely dominated by Karman-like vortices shed from the cylinders. On the other hand, the increased number of swirls at z^+ = 500 may be attributed to the additional vortical structures generated at the tips of the cylinders.

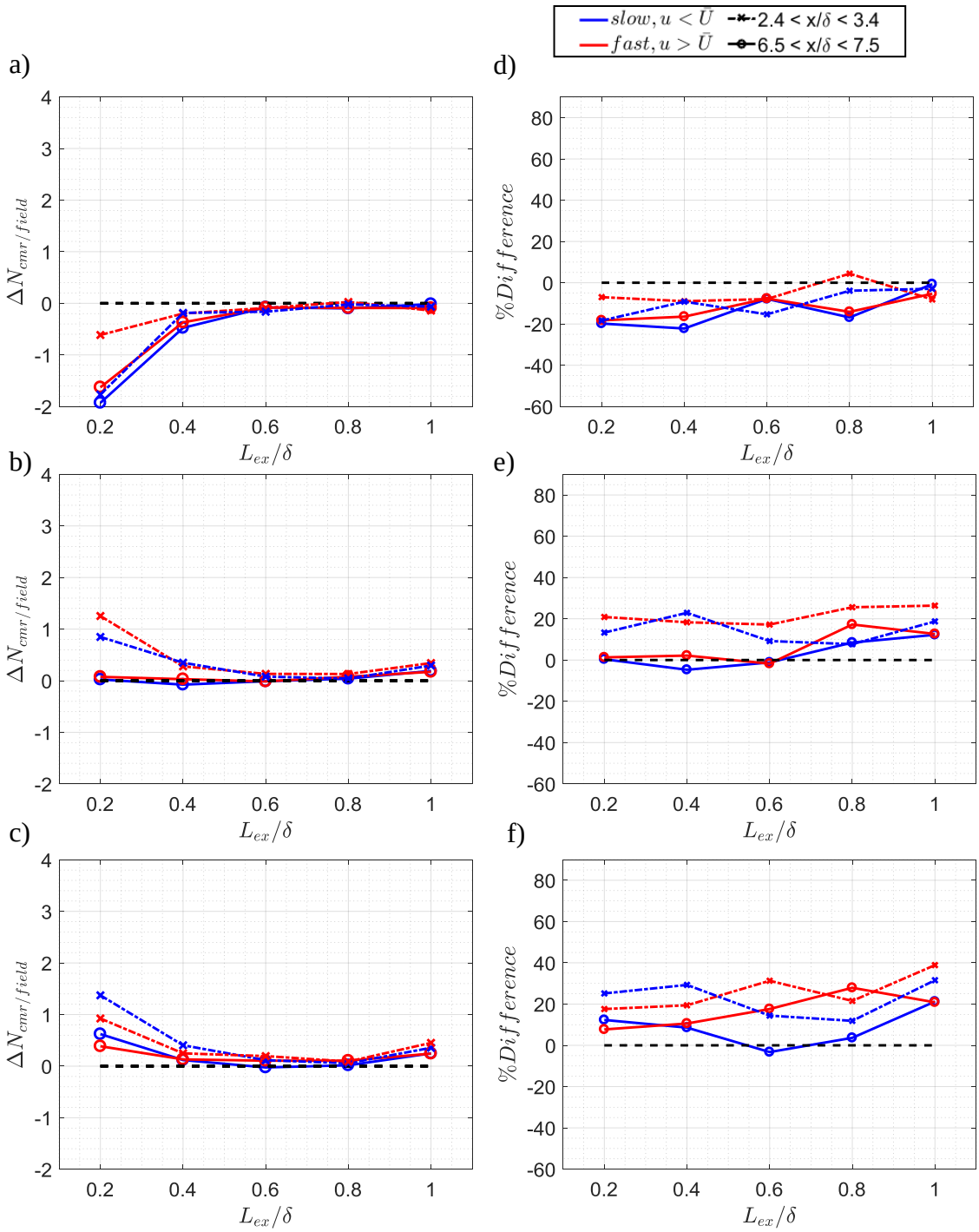

Figure 4-12: S = 0.2δ, H = 0.2δ array. Difference in number of LMRs/HMRs per field versus length between perturbed and unperturbed flow at two streamwise locations, for measurement heights a) z^+ = 125, b) z^+ = 300 and c) z^+ = 500. Bin by bin differences between length distributions of the perturbed and unperturbed flow as a percentage of the unperturbed length distribution. Bin size = 0.2δ.

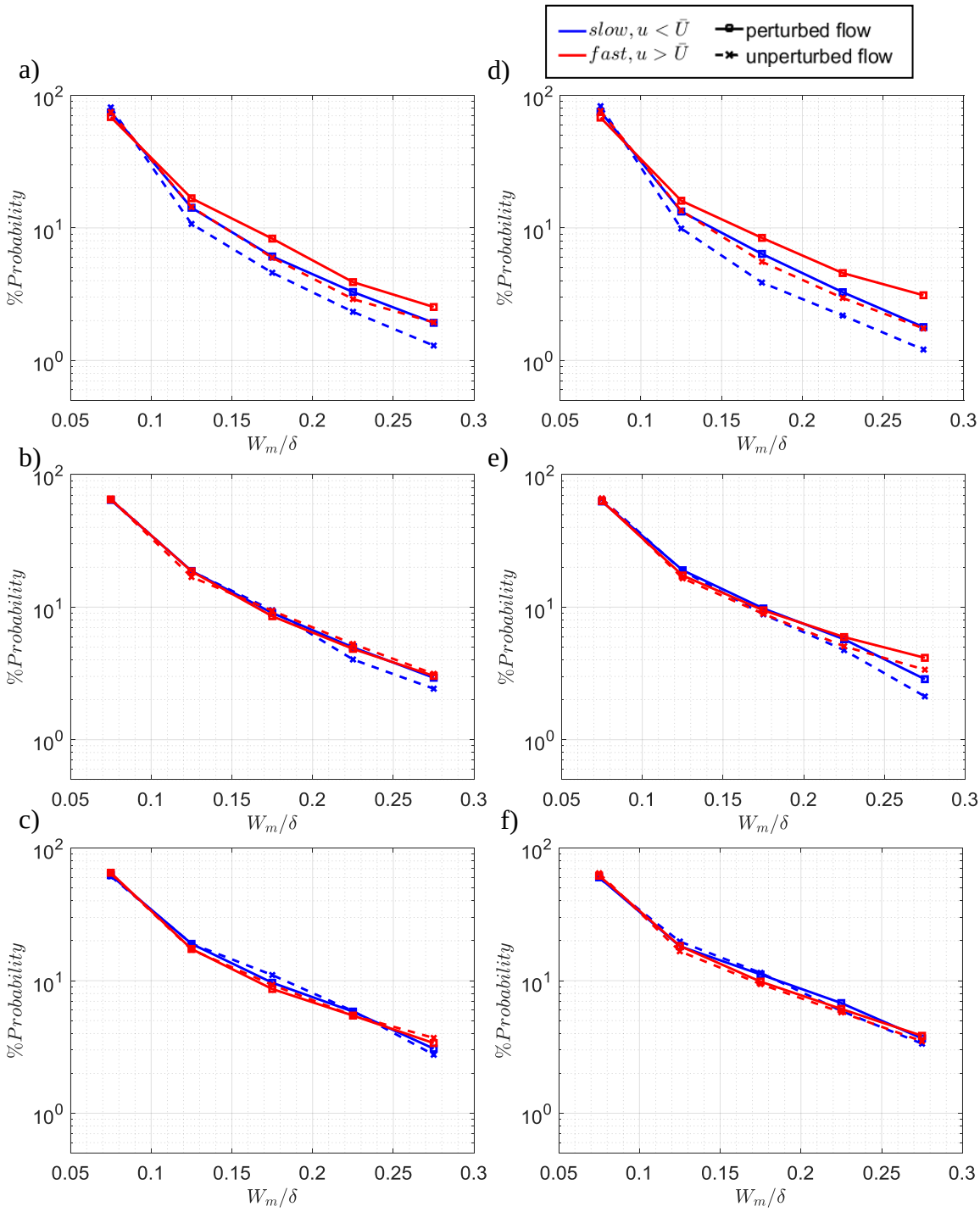

Figure 4-13: S = 0.2δ, H = 0.2δ array. Mean width histograms of detected low and high momentum regions normalized by the total number of detected low/high momentum regions respectively for 2.4 < x/δ < 3.4 at a) z^+ = 125, b) z^+ = 300 and c) z^+ = 500 and subsequently for 6.5 < x/δ < 7.5 at aforementioned measurement heights in d, e, and f.

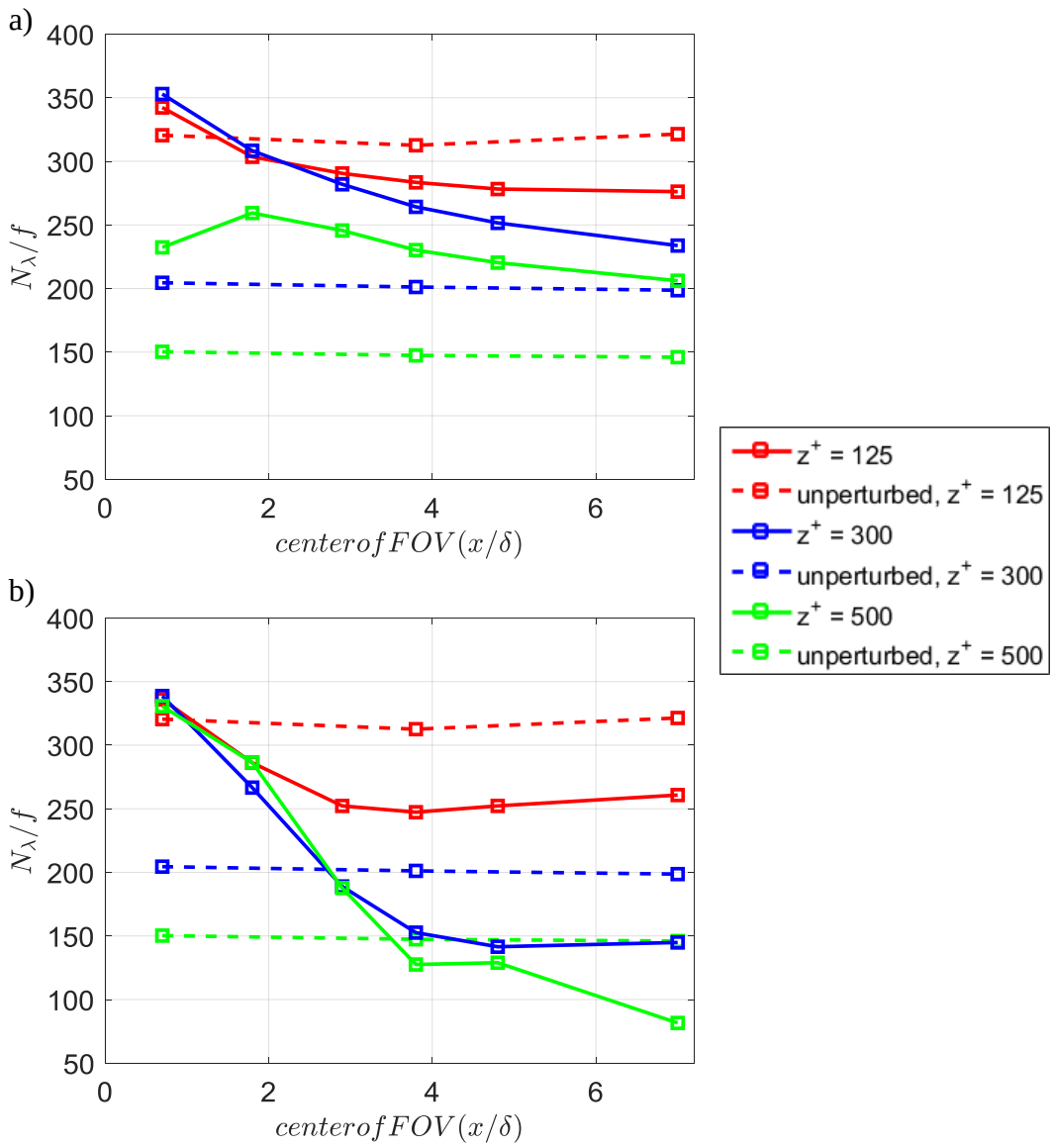

Figure 4-14: Number of swirling structures per field downstream of S = 0.2δ arrays with a) H = 0.2δ and b) H = δ.

For z^+ = 300 and 500 in the perturbed flow, the trends in number of swirling structures (Fig. 4-14a) were very similar to those for RMS velocity in Figure 4-7b. At z^+ = 300, the number of swirls first sharply increased before declining toward the unperturbed value. At z^+ = 500, the number of swirls also increased significantly and peaked at x = 1.8δ before declining toward the unperturbed value as x continued to increase. Some of the

increase may be due to the upward extension of the Karman vortices forming below the tip height. At $z^+ = 125$, however, the number of swirling structures decreased below the unperturbed value already at $x = 1.8\delta$ and continued to decrease until $x = 7\delta$ where the value was 85% of the unperturbed value. At the same time, the RMS velocity never dropped below the unperturbed level. The decrease in number of swirls may be due to stretching or re-orientation of pre-existing vortices, resulting in smaller swirl cross-sections. Furthermore, existing vortices may be weakened or eventually dissipated through interactions with surrounding structures. If the swirling cross sections are reduced, a number of vortices may still produce measurable velocity variations while becoming undetectable by the swirl identification algorithm. For a given PIV interrogation window, the attenuation in velocity gradients will be greater compared to velocity measurements (Saikrishnan *et al.* 2006).

In comparison, at $z^+ = 300$ and 500, the relative increases in number of swirls compared to the unperturbed flow at $x = 7\delta$ were 17% and 40% respectively. The increased swirl counts were consistent with the result of Jacobi & McKeon (2011) in a streamwise wall-normal plane, where additional swirling structures were observed at the top of the log layer, a distance 4δ downstream of a shorter perturbation ($H/\delta = 0.06$).

4.1.5 Autocorrelations of streamwise velocity

Autocorrelations of streamwise velocity fluctuations (Figure 4-15) immediately downstream of the array were strongly perturbed compared to the unperturbed autocorrelations. For all measurement heights, $\Delta y = 0$ autocorrelations (Figs. 4-15a-c) were strongly reduced in magnitude. Notably, the magnitude of reduction was greatest at $z^+ = 125$ (Fig. 4-15a), followed by $z^+ = 300$ (Fig. 4-15b) and $z^+ = 500$ (Fig. 4-15c). This

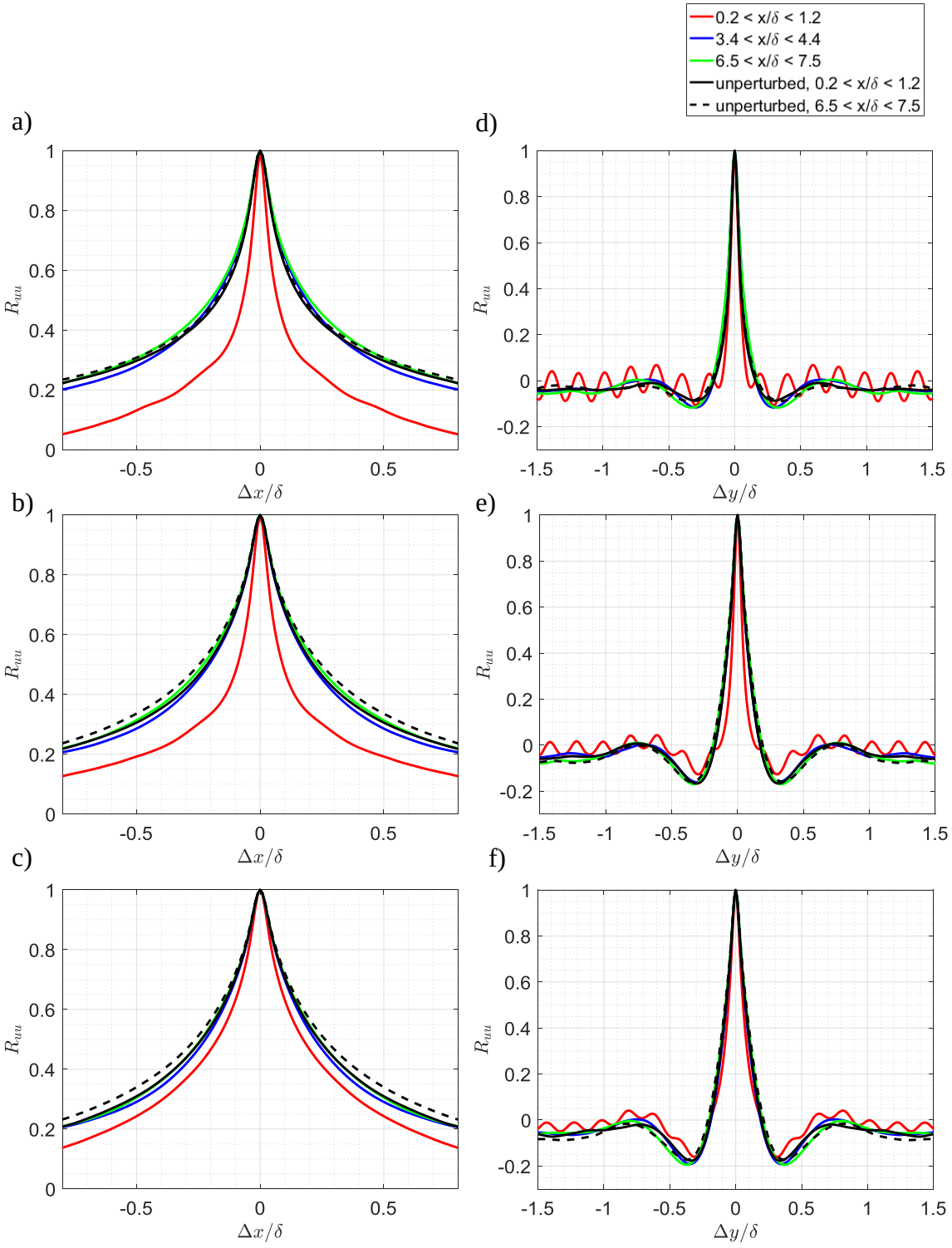

Figure 4-15: S = 0.2δ, H = 0.2δ array. Autocorrelations of streamwise velocity. Δy = 0 cuts are shown for measurement heights a) z^+ = 125, b) z^+ = 300 and c) z^+ = 500. Δx = 0 cuts are shown for measurement heights d) z^+ = 125, e) z^+ = 300 and f) z^+ = 500.

suggests that the array strongly shortened existing flow structures, with the effect diminishing as the tip of the cylinder is approached.

On the other hand, $\Delta x = 0$ autocorrelations (Figs. 4-15d-f) immediately downstream of the array showed spanwise periodicities manifesting as peaks adjacent to the central positive lobe. Peak magnitudes were strongest at $z^+ = 125$ (Fig. 4-15d) and weakest at $z^+ = 500$ (Fig. 4-15f). These peaks are associated with the cylinder wakes at 0.2δ. Furthermore, for all measurement heights, the correlation magnitudes near $\Delta y = 0$ were reduced. The spanwise range of reduction was largest at $z^+ = 300$ (Fig. 4-15e). This may relate to perturbation effects being strongest at 2/3 of the $H = 0.2\delta$ cylinders (Ryan *et al.* 2011).

For all measurement heights, as x increased, both the shapes and magnitudes of $\Delta y = 0$ autocorrelations recovered substantially towards unperturbed values. For the streamwise correlations ($\Delta y = 0$), in general, recovery to the unperturbed state occurred first for smaller Δx then later for larger Δx at all measurement heights. This physically makes sense as longer structures are typically associated with larger time scales (Smits & Wood 1985), hence it would take a longer time for the longer structures to re-organize. At $x = 1.8\delta$, $z^+ = 125$(not shown), the correlation magnitudes for $|\Delta x| < 0.1\delta$ had already recovered to the unperturbed values, in contrast to $z^+ = 300$ and 500, which is consistent with the shorter response times closer to the wall (Smits & Wood 1985). Further downstream, at $x = 3.9\delta$, at $z^+ = 125$, the correlation values exceeded the unperturbed values, suggesting more content with length scales less than 0.3δ on average, which did not occur for $z^+ = 300$ or 500. Finally, at $x = 7\delta$, correlations showed recovery to unperturbed values at $z^+ = 125$ (Fig. 4-15a), with slight enhancement for $0.1\delta < |\Delta x| <$

0.3δ, although this effect was within the uncertainty. In contrast, at z^+ = 300 and 500, correlation values remained suppressed for $|\Delta x| > 0.2\delta$, suggesting fewer long structures in the perturbed versus unperturbed flow.

In spanwise correlations ($\Delta x = 0$, Figs. 4-15d-f), values recovered to the unperturbed values more quickly at all measurement heights. The spanwise periodicities induced by the array had already dissipated in the field centered at $x = 1.8\delta$ for all measurement heights. By $x = 3.9\delta$, all curves have largely relaxed to the unperturbed state, except for z^+ = 125, where the negative lobe adjacent to the central positive lobe remained suppressed. This suggests that the natural spanwise periodicity of alternating low and high speed zones remained altered compared to the unperturbed state. Nevertheless, by $x = 7\delta$, all $\Delta x = 0$ curves recovered to the unperturbed state, while $\Delta y = 0$ slices remained altered compared to unperturbed correlations at z^+ = 300 and 500.

4.1.6 Wall-parallel cross correlations from 3-D PTV data

Streamwise velocity cross correlations between reference plane of z^+_{ref} = 155 and z^+_c = 200, 300 and 465 are shown in Figure 4-16. The resulting line plots for $\Delta y = 0$ are shown in Figures 4-16a-c. Immediately behind the array, all three cross correlations (z_c^+ = 200, 300 & 465) were strongly suppressed compared to the values in the unperturbed flow. The correlations exhibited increasing streamwise asymmetry with increasing z separation between correlated planes. Although all peaks for all three correlations occurred at $\Delta x = 0$, the values decreased faster for positive Δx and even became negative for $\Delta x > 0.4$ for both z_c^+= 300 and 465. The negative values can be attributed to the streamwise inversion in streamwise velocity deviation shown in (Figs 4-1b and c). Further downstream, at $x/\delta = 2.4$ and $x/\delta = 3.7$, the correlation curves overlapped for the perturbed and unperturbed

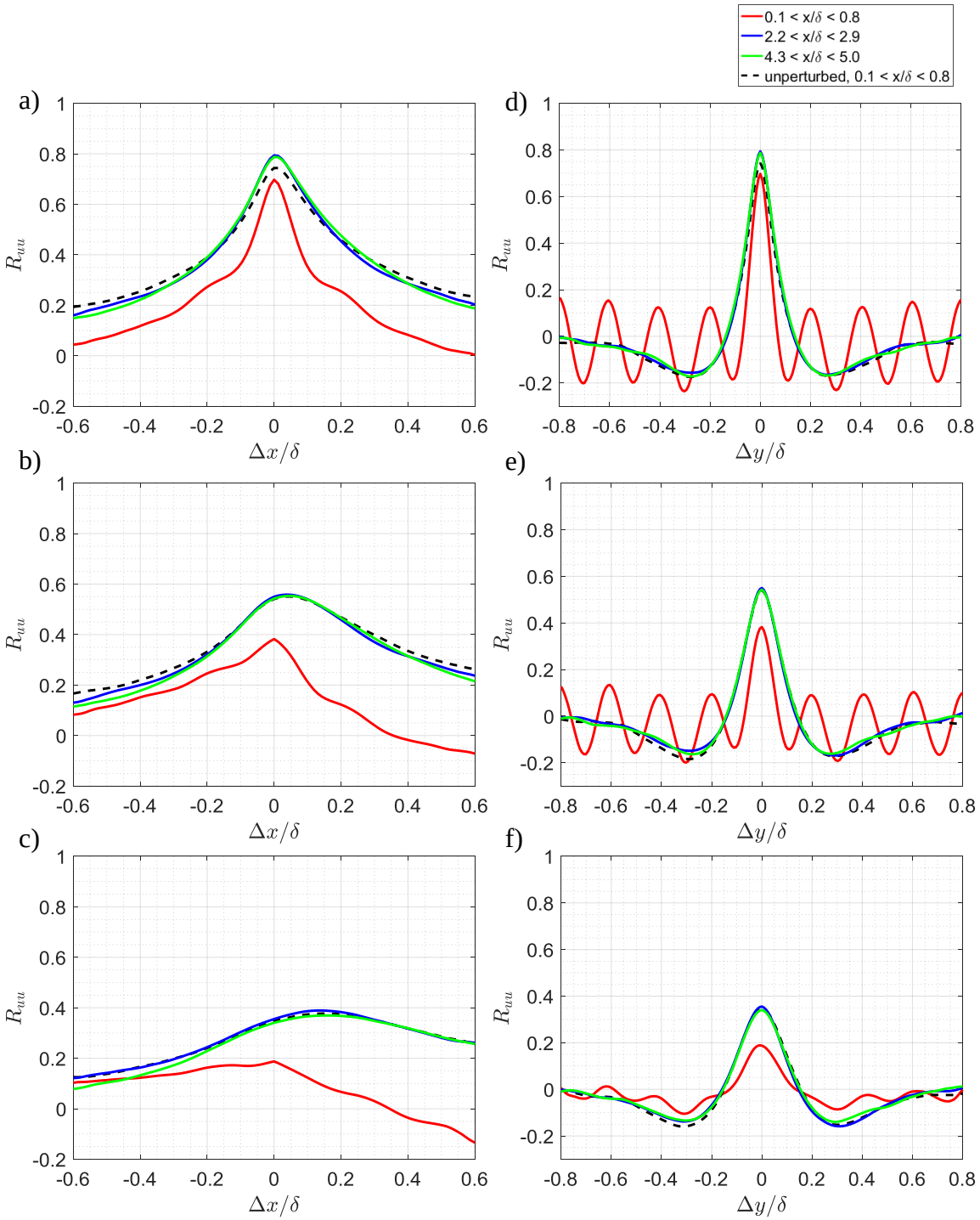

Figure 4-16: S = 0.2δ, H = 0.2δ array. Streamwise velocity cross correlations averaged over 500 fields. Cross correlations at Δy = 0, where the planes at z_{ref}^{+} = 155 were correlated with a) z_c^{+} = 200, b) z_c^{+} = 300, & c) z_c^{+} = 465. Δx = 0 cross-correlations for the aforementioned correlated planes shown in d, e & f.

flow. This result is consistent with the instantaneous observations where features of LMRs at these locations were similar to those in unperturbed flow (see Fig. 4-9 and 4-10, and Zheng & Longmire, 2014).

Spanwise cross correlations ($\Delta x = 0$) are plotted in Figure 4-16d-f. Immediately behind the array, the correlations showed strong periodicity, and suppressed correlation values near $\Delta y = 0$. The strongest suppression in peak magnitude relative to the unperturbed values occurred for the largest z separation, suggesting de-correlation between tip structures near $z^+ = 465$ and cylinder wakes at $z^+ = 155$. This also manifested in weaker peaks associated with spanwise periodicity. As x increased, the correlations recovered substantially to the unperturbed values. Notably the negative lobes were slightly weaker for the perturbed flow, perhaps owing to a persistent alteration of the spanwise organization of flow structures, although this effect was likely within uncertainty.

Wall-normal velocity cross correlations between reference plane of $z^+_{ref} = 155$ and $z^+_c = 200$, 300 and 465 are shown in Figure 4-17. At both $z^+_c = 200$ and 300, $\Delta y = 0$ line plots (Figs. 4-17a-b) immediately behind the array showed increased correlation magnitudes compared to the unperturbed flow. Furthermore, $z^+_c = 300$ and 465 correlations were evidently asymmetric, owing to the downwash effect felt first at the cylinder tip, and later (and weaker) in planes closer to the wall. This may have contributed to the reduced correlation magnitudes for $z^+_c = 465$ correlations. As x increased, the correlations remained enhanced for both $z^+_c = 200$ and 300, although with decreased correlation peaks. For $z^+_c = 465$, however the correlation recovers to the unperturbed value. At $x = 3.5\delta$, all correlations were enhanced with respect to the unperturbed flow. This suggests increased flow interactions across the measured depth. In terms of the initial perturbation

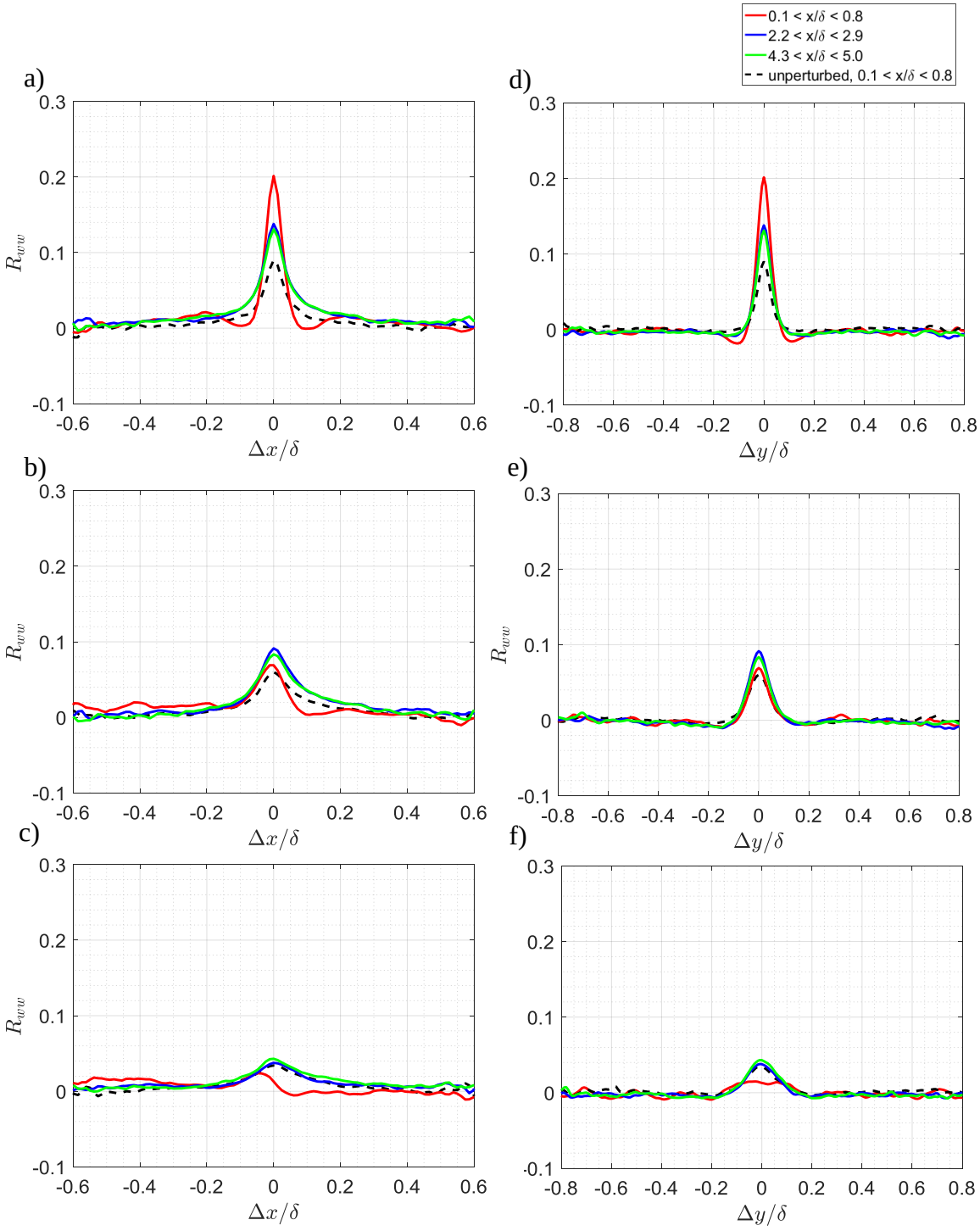

Figure 4-17: S = 0.2δ, H = 0.2δ array. Wall-normal velocity cross correlations averaged over 500 fields. Cross correlations at Δy = 0, where the planes at z_{ref}^{+} = 155 were correlated with a) z_c^{+} = 200, b) z_c^{+} = 300, & c) z_c^{+} = 465. Δx = 0 cross-correlations for the aforementioned correlated planes shown in d, e & f.

and subsequent recovery, $\Delta x = 0$ line plots for the wall-normal velocity cross correlations (Fig. 4-17d-f) illustrate similar trends compared to the $\Delta y = 0$ line plots.

4.1.7 Pre-multiplied energy spectra and dominant spanwise modes

Immediately downstream of the array, results from one dimensional pre-multiplied spectra of spanwise variations in streamwise velocity (Figs 4-18a-c) showed an initial shift in energy towards smaller scales for all measurement heights. In addition, a peak at 0.2δ corresponding to the cylinder spacing was present. The peak magnitudes were comparable for both $z^+ = 125$ and 300, while smaller at $z^+ = 500$. Also a secondary peak at 0.1δ was observed at $z^+ = 300$, owing to the splitting of the wakes (see Fig. 4-1b).

As x increased, the spectra at both $z^+ = 300$ and 500 (Figs. 4-18b & c) recovered quickly towards unperturbed shapes, first for scales smaller than $\lambda_y < 0.1\delta$, later for the larger scales. At $x = 7\delta$, both spectra had approximately recovered to the unperturbed values. In contrast, at $z^+ = 125$, as x increased, the energy in the small scales decreased below the unperturbed values, while the energy contained in the large scales ($0.4 < \lambda_y/\delta < 1$) increased beyond the unperturbed values, starting at $x = 1.8\delta$. Remarkably, at $x = 7\delta$, the shape of this spectrum was very similar to the shapes of the spectra at $z^+ = 300$ and 500, although energy contained in the smaller scales was slightly greater at $z^+ = 125$. This seems consistent with the modulation effects of fluid motions close to the wall by structures further out (Hutchins & Marusic 2007b).

Histograms from the dominant spanwise mode analysis (Figure 4-19) computed from a dataset of 1000 independent samples showed the resilience of the 0.6δ spanwise mode to array perturbation. Interestingly, at both $z^+ = 300$ and 500 (Figs. 4-19 b & c), the peak of

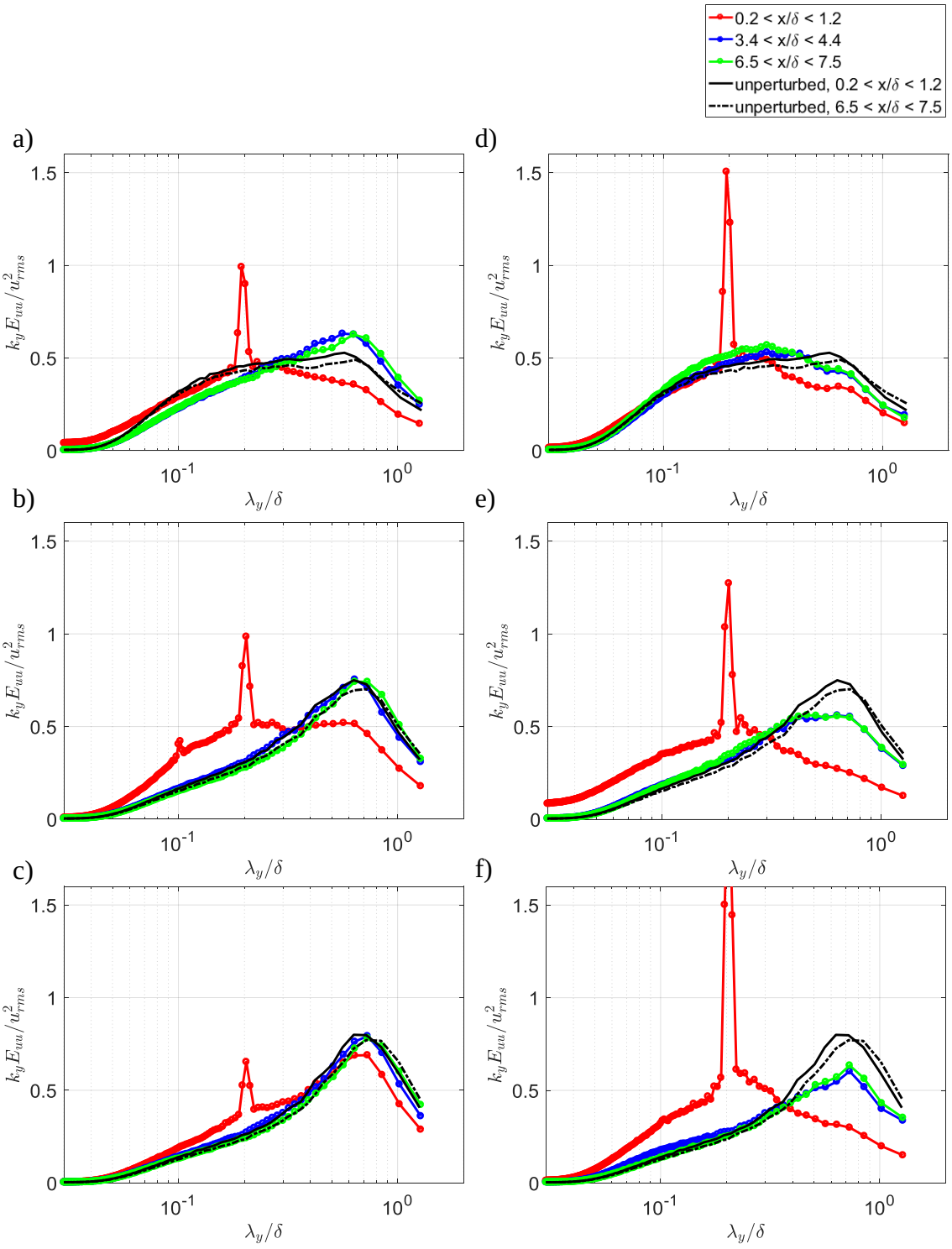

Figure 4-18: 1-D pre-multiplied spectra for flow downstream of S = 0.2δ, H = 0.2δ for measurement height at a) z^+ = 125, b) z^+ = 300 and c) z^+ = 500, and flow downstream of H = δ, S = 0.2δ array with d) z^+ = 125, e) z^+ = 300 and f) z^+ = 500.

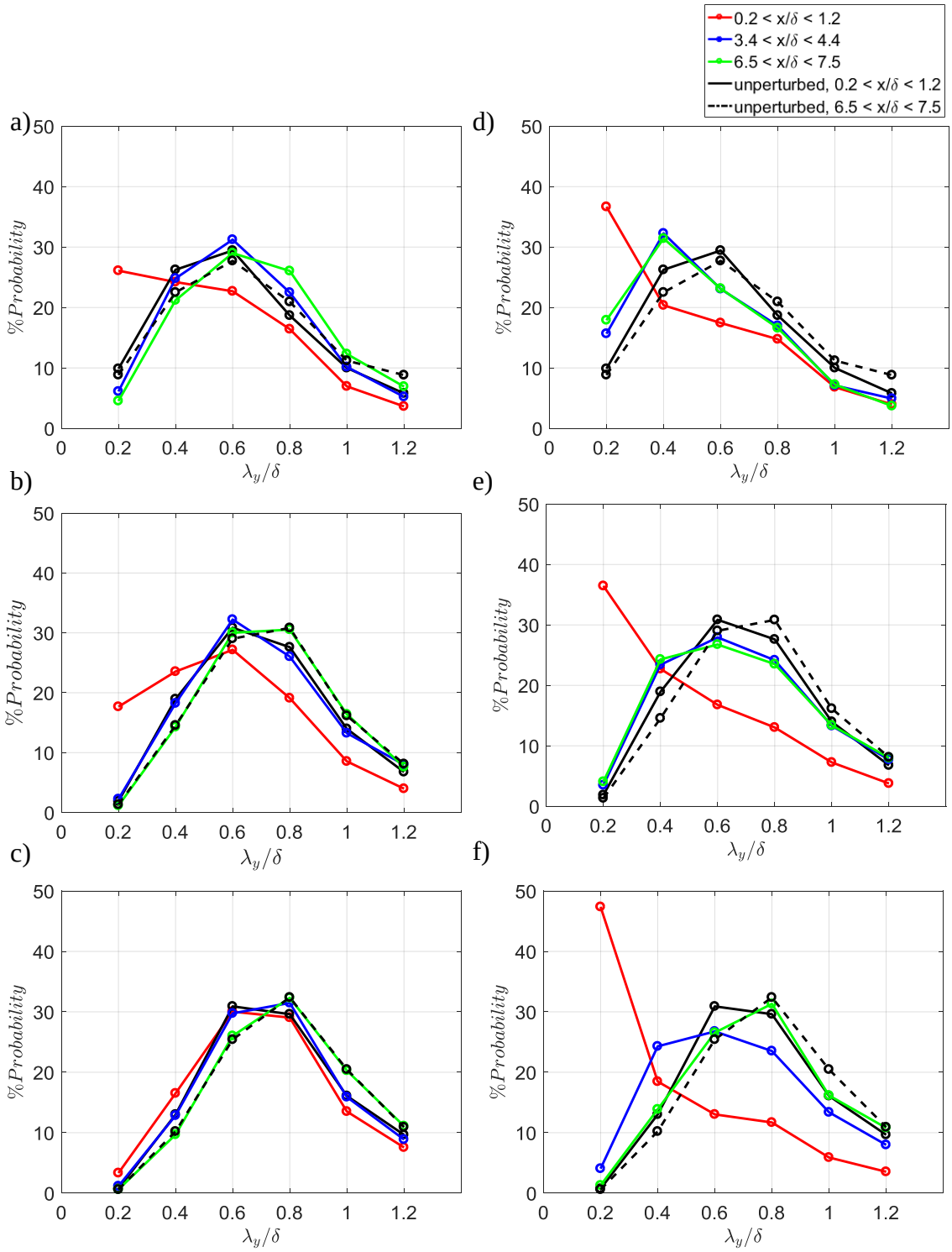

Figure 4-19: Dominant spanwise mode histograms for flow downstream of S = 0.2δ, H = 0.2δ for measurement height at a) z^+ = 125, b) z^+ = 300 and c) z^+ = 500, and flow downstream of H = δ, S = 0.2δ array with d) z^+ = 125, e) z^+ = 300 and f) z^+ = 500. Histogram bin size = 0.2δ.

the histogram still occurred at 0.6δ, even in the field immediately after the array. In comparison, although the 0.2δ mode was the most dominant at z^+ = 125, the 0.6δ spanwise mode quickly recovers to become the most dominant in the next field at x = 1.8δ, then persists downstream. At x = 7δ, the peaks in the distribution occur at 0.6δ at z^+ = 125 and 0.8δ for both z^+ = 300 and z^+ = 500 respectively. The shift towards the 0.8δ mode for both z^+ = 300 and 500 occurred for the natural case too and may be attributed to natural spanwise scale growth due to growth of the boundary layer thickness (Adrian & Tomkins 2003).

4.1.8 VPIA results

The number of packets per field identified by the VPIA as a function of streamwise location is shown in Figure 4-20a. For flow downstream of the H = 0.2δ array, the VPIA was not applied at the first two streamwise locations where wake structures were dominant (as in Figs 4-8a & 4-9a). At z^+ = 125, the number of packets were reduced at all streamwise locations examined up to x/δ = 7. Over this streamwise range, the number per field was reduced by 20% of the unperturbed value, where the reduction may stem from the increased number of merging/merged structures that were excluded by the VPIA. At z^+ = 500, by contrast, the packet count first increased, then relaxed toward the unperturbed value with increasing streamwise distance. The relative increase was 40% compared with the unperturbed packet count at z^+ = 500. On the other hand, the packet counts at z^+ = 300 matched the unperturbed packet count to within uncertainty. The reason for the increase at z^+ = 500 was difficult to determine from the instantaneous fields. Additional low momentum zones may be generated at the tips of the cylinders, which were spaced at scales smaller than the dominant spanwise scale between low

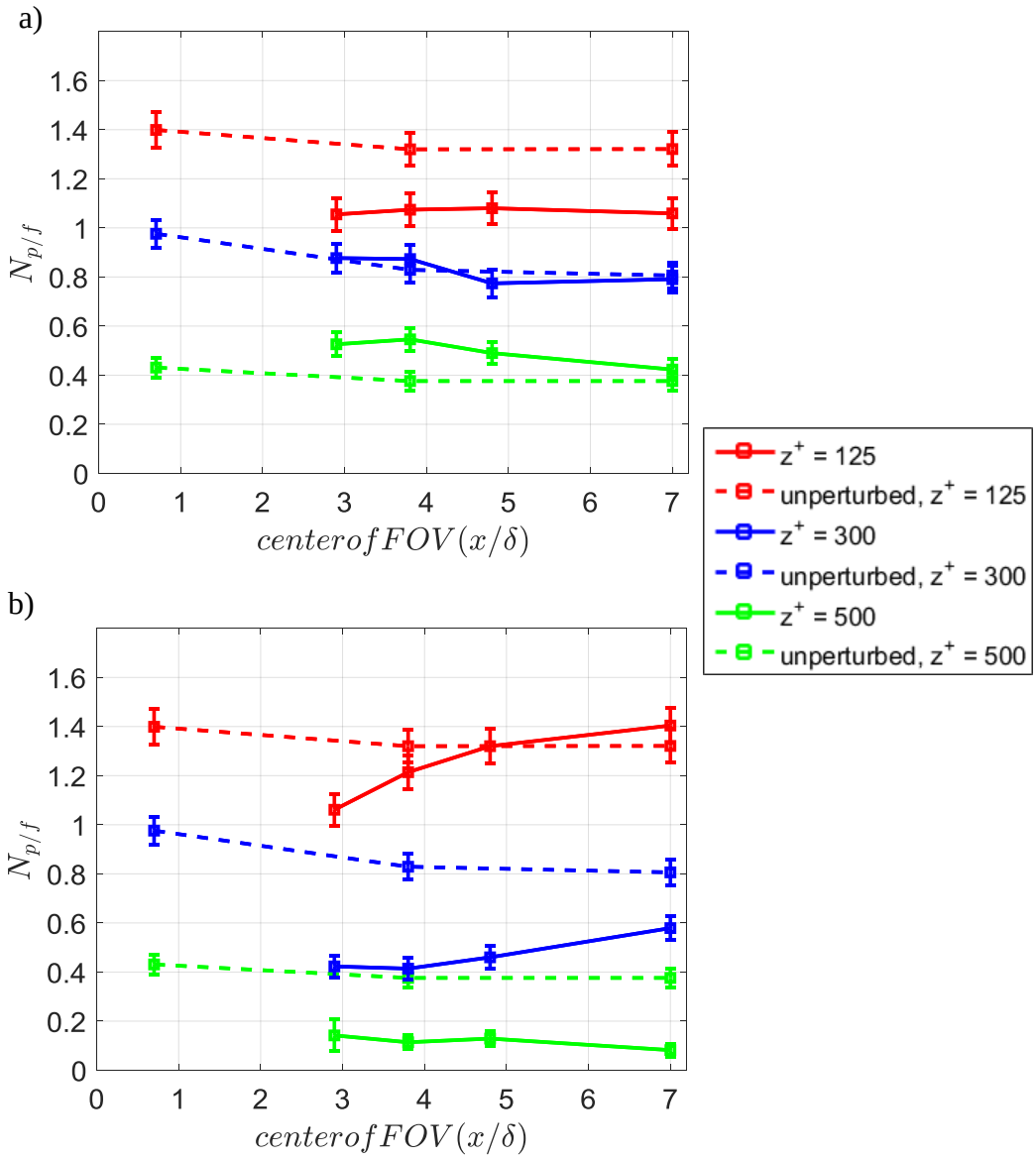

Figure 4-20: Number of individual packets per field, $N_{p/f}$ versus x-location across three measurement heights for S = 0.2δ arrays with a) H = 0.2δ and b) H = δ. The unperturbed counts are shown in dashed lines.

momentum regions in unperturbed flow (see Zheng & Longmire 2014), thereby increasing the LMR density per span.

Packet skeleton length distributions for flow downstream of the H = 0.2δ array are plotted in Figure 4-21a-c and compared against the unperturbed distributions. At z^+ = 125 (Fig. 4-21a), the number of packets for all length scales were reduced initially and remained lower relative to unperturbed values until the last measurement location. In contrast, at both z^+ = 300 (Fig. 4-21b) and z^+ = 500 (Fig. 4-21c), the number of shorter packets increased initially. This trend is also evident in packet length distribution plots normalized by the total number of detected packets shown in Figures 4-21e & f. As x increased, the distributions for both z^+ = 300 and 500 reverted towards the unperturbed distribution shape and values.

Packet skeleton width histograms are shown in Figure 4-22a-f, illustrating the H = 0.2δ arrays effect at enhancing the packet widths for z^+ = 125. In comparison, number of packets with narrower widths increased at z^+ = 500. The normalized packet distributions shown in Figure 4-22d-f corroborated the aforementioned trends, showing a shift towards larger widths for z^+ = 125, and a shift towards smaller widths for z^+ = 500. The distribution at z^+ = 300 remained similar to the unperturbed flow at both x = 2.9δ and 7δ.

4.2 Flow perturbed by array with S = 0.2δ and H = δ

4.2.1 Time-averaged results

Compared with the H = 0.2δ case, substantial differences were observed in the average flow pattern downstream of the taller H = δ array (Fig. 4-23). Although mean velocities generally decreased in both the H = 0.2δ and H = δ cases, both the initial pattern and the

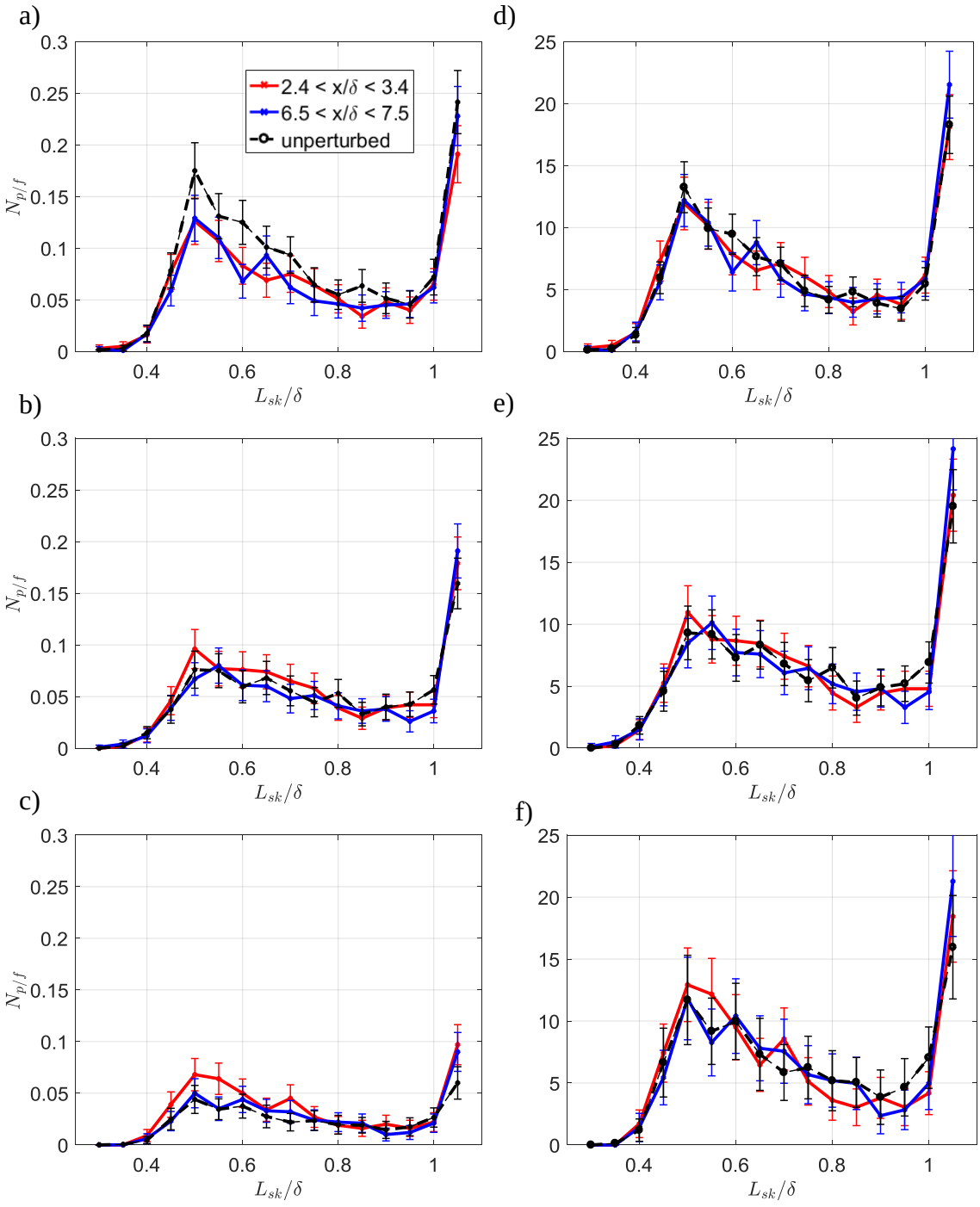

Figure 4-21: Packet skeleton length histograms for flow downstream of S = 0.2δ with H = 0.2δ at a) z^+ = 125, b) z^+ = 300 and c) z^+ = 500 and histograms normalized by total number of packets at d) z^+ = 125, e) z^+ = 300 and z^+ = 500. Histogram bin size = 0.05δ.

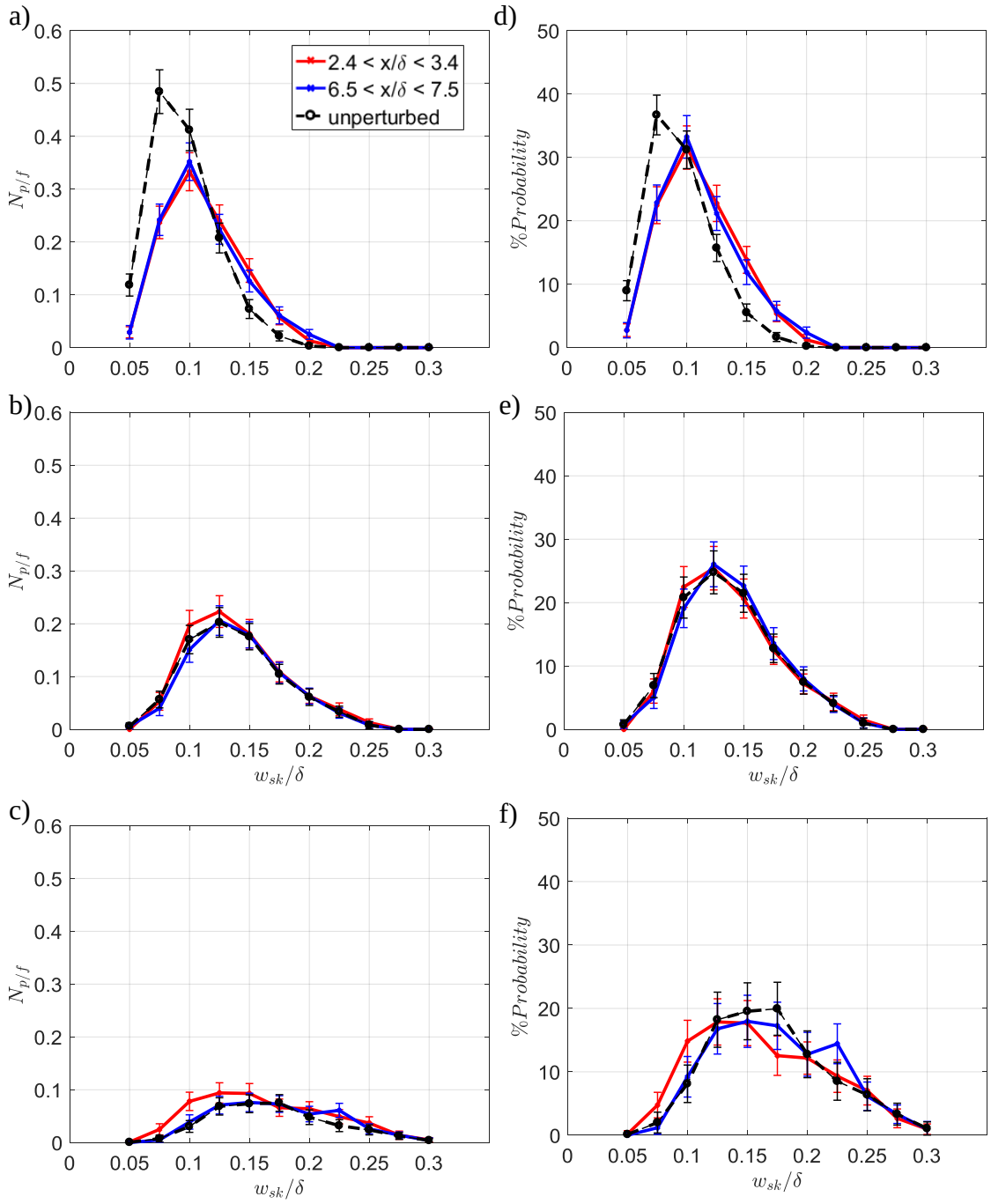

Figure 4-22: Packet skeleton width histograms for flow downstream of S = 0.2δ with H = 0.2δ at a) z^+ = 125, b) z^+ = 300 and c) z^+ = 500 and histograms normalized by total number of packets at d) z^+ = 125, e) z^+ = 300 and z^+ = 500. Histogram bin size = 0.05δ.

streamwise evolution were different. For all measurement heights (Fig. 4-23) and throughout the 3-D PTV measurement volume (Fig. 4-24), wakes occurred downstream of each cylinder and persisted at the same spanwise location. This behavior was different than the H = 0.2δ case at z^+ = 300 where averaged wakes would split and merge with adjacent wakes (see Fig. 4-1b), and at the tip (z^+ = 500, Fig. 4-1c) where faster moving fluid on average was observed. The average spanwise velocity variations downstream (not shown) also differed from those in the H = 0.2δ case, such that the effect of the tips were absent at z^+ = 500. Average wall-normal velocity variations from both SPIV (not shown) and 3D-PTV (Fig. 4-25) show average upward movement behind the H = δ cylinders, with downward moving fluid in the region in between, opposite of the H = 0.2δ case. This affected the entire depth of the measurement volume.

Mean streamwise velocity averaged over each planar field versus streamwise location downstream of the H = δ array is shown in Figure 4-26a. The mean streamwise velocities immediately downstream of the H = δ array decreased at z^+ = 300 and 500 due to the blockage from the array. Curiously, the mean velocity at z^+ = 125 matched the unperturbed value initially, different from the H = 0.2δ case. This was caused by weaker average velocity deficits immediately behind the H = δ cylinders at z^+ = 125 compared to the H = 0.2δ case, while the strength of the bleed flow (region between cylinders) through both arrays were comparable. Most importantly, as x increased, for all measurement heights, the mean velocities did not recover towards the equilibrium value. In fact, at z^+ = 125, the mean velocity increasingly diverged from the unperturbed value. Volumetric and SPIV results indicate net upwash on average throughout the logarithmic region at this location. The net upwash may be a continuity effect resulting from upstream fluid

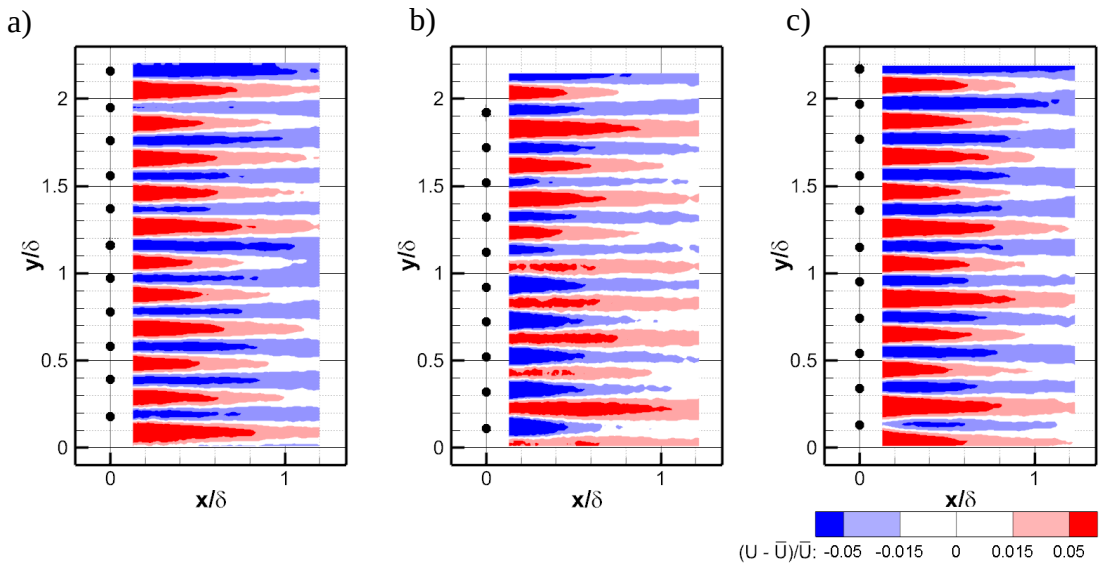

Figure 4-23: S = 0.2δ, H = δ array. Average streamwise velocity results from PPIV at measurement height a) z^+ = 125, b) z^+ = 300 and c) z^+ = 500.

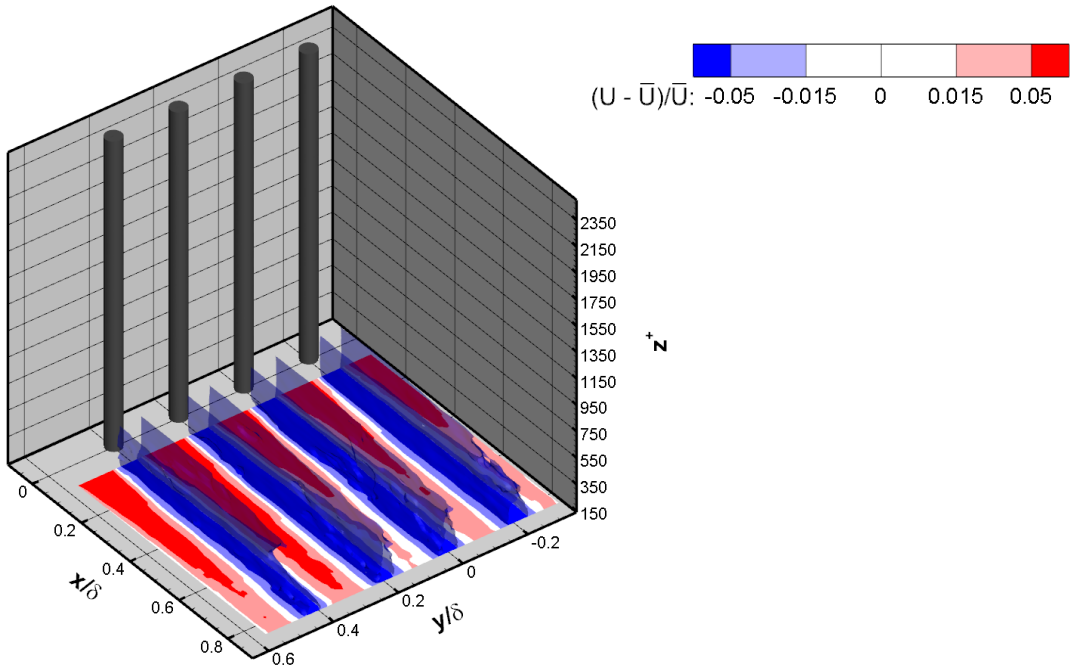

Figure 4-24: S = 0.2δ, H = δ array. Average streamwise velocity results from 3-D PTV. Colors show fractional deviation away from the local mean velocity for the plane at z^+ = 155. Iso-surfaces show regions with $U < 0.95\bar{U}$.

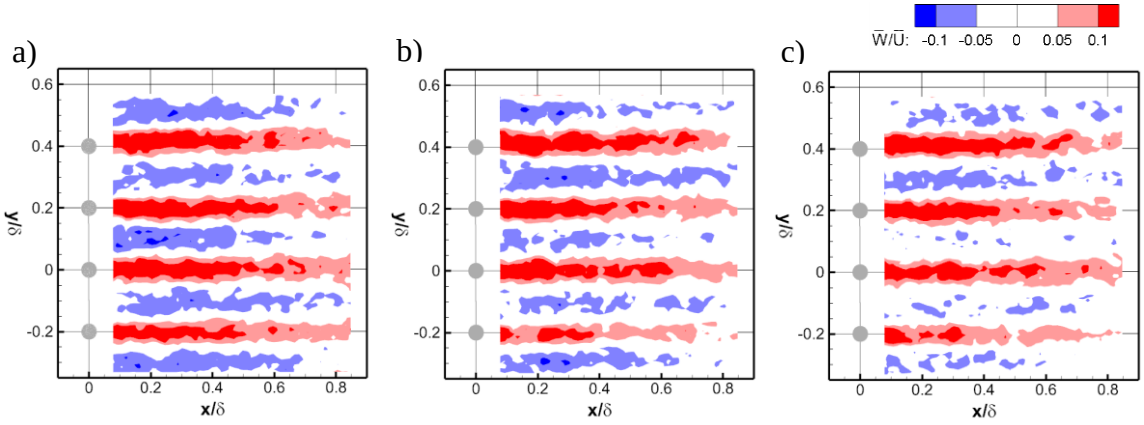

Figure 4-25: S = 0.2δ, H = δ array. Average streamwise velocity results from 3-D PTV at measurement height a) z^+ = 155, b) z^+ = 300 and c) z^+ = 465.

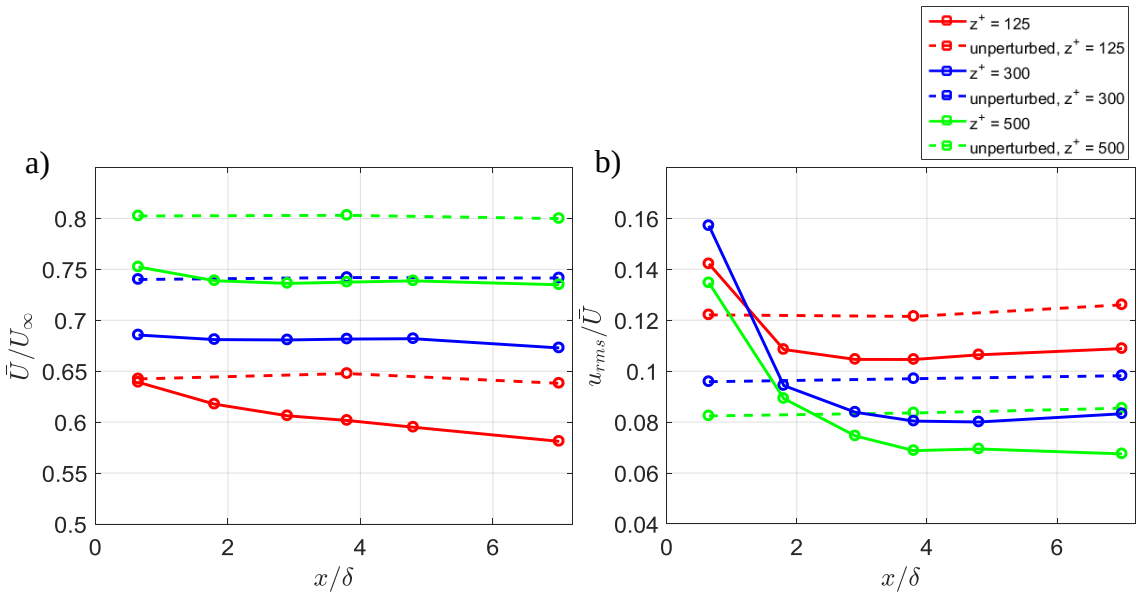

Figure 4-26: Variation of a) mean streamwise velocity normalized by free-stream velocity, and b) RMS of streamwise velocity normalized with local mean velocity at measurement height, with x-location, downstream of the S = 0.2δ and H = δ array.

displaced above the array, thus fluid below must move upwards to compensate. The net upwash can also result in streamline curvature leading to an increasingly adverse streamwise pressure gradient locally, acting to decelerate the flow at $z^+ = 125$.

At $z^+ = 125$, $x = 7\delta$, the mean velocity was reduced by $0.06\bar{U}$ compared to the unperturbed flow. On the other hand, at $z^+ = 300$ and 500, 7δ downstream of the $H = \delta$ array, the mean streamwise velocity was reduced by $0.05\bar{U}$ compared to the unperturbed value. Thus, the $H = \delta$ array had a sustained effect on the mean velocity over a long distance. This was consistent with previous work by Corke *et al.* (1981) and Lee *et al.* (1999), albeit with perturbations different from the present study. Their results showed reduction of mean streamwise velocity within the log region compared to the equilibrium values at locations up to 9.3δ and 7.5δ downstream of their perturbations respectively.

Streamwise RMS velocity trends downstream of the two arrays were also different. Initially, the normalized RMS velocity downstream of the $H = \delta$ array (Fig. 4-26b) was increased at all measurement heights, similar to the $H = 0.2\delta$ case (see Fig. 4-7b). In contrast, for the $H = \delta$ case, the relative increase was strongest at $z^+ = 500$ and weakest at $z^+ = 125$. Moreover, different from the $H = 0.2\delta$ case, the initially increased RMS velocities downstream of the $H = \delta$ array decayed rapidly to levels below the unperturbed values, even when normalized by the reduced local mean velocities. The RMS velocity leveled off first at $z^+ = 125$ ($x/\delta = 2.9$), followed by $z^+ = 300$ and 500 at $x/\delta = 3.8$ and remained lower by $0.01\bar{U}$, 7δ downstream. A similar reduction in streamwise RMS velocity was observed by Boiko & Kornilov (2009), Hutchins and Choi (2002) and Corke *et al.* (1981) within the log region of their perturbed boundary layers.

4.2.2 Instantaneous results

Instantaneous fields also revealed key differences between the flows downstream of the two arrays. For all three measurement heights, undulating wake structures were a dominant feature in the vicinity behind the H = δ array. At z^+ = 125 and 300, the wake structures were qualitatively similar to those observed downstream of the H = 0.2δ array even though the mean streamwise velocity statistics differed. The low momentum zones corresponding to wake structures often appeared short and very wavy. A few examples can be seen at z^+ = 125 (Fig. 4-27a), y/δ = 1.35, at z^+ = 300 (Fig. 4-28a), y/δ = 0.3 and z^+ = 500 (Fig. 4-29a), y/δ = 0.15. Often, individual wakes would interact with adjacent ones, for example at z^+ = 125, y/δ = 1.35 and 1.55, z^+ = 300, y/δ = 1.1 and 1.3, and z^+ = 500, y/δ = 1.35 and 1.55.

Remarkably, at z^+ = 125 and x/δ = 2.9, the flow structures downstream of the H = δ array were relatively similar to those in unperturbed flow, and unlike the structures observed at the same location downstream of the H = 0.2δ array (compare Figs. 4-27b & 4-8b to unperturbed flow in Figure 3-13a). This similarity occurred in spite of the reduced mean velocity downstream of the H = δ array. For the H = δ case, packets similar to those in the unperturbed flow were observed beginning at this streamwise location, as in Figure 4-27b at y/δ = 0.15, 0.3, 1.0 and 2.0. As x increased, the packet signatures became more similar to the packets in the unperturbed flow, such that they became less wavy and frequently longer than packet signatures upstream, for example in Figure 4-27c at y/δ = 0.3, 0.5, 1.0 and 1.3.

At z^+ = 300 and 500, in contrast, packet signatures were hardly ever observed 2.9δ downstream of the H = δ array. The low momentum zones there often appeared

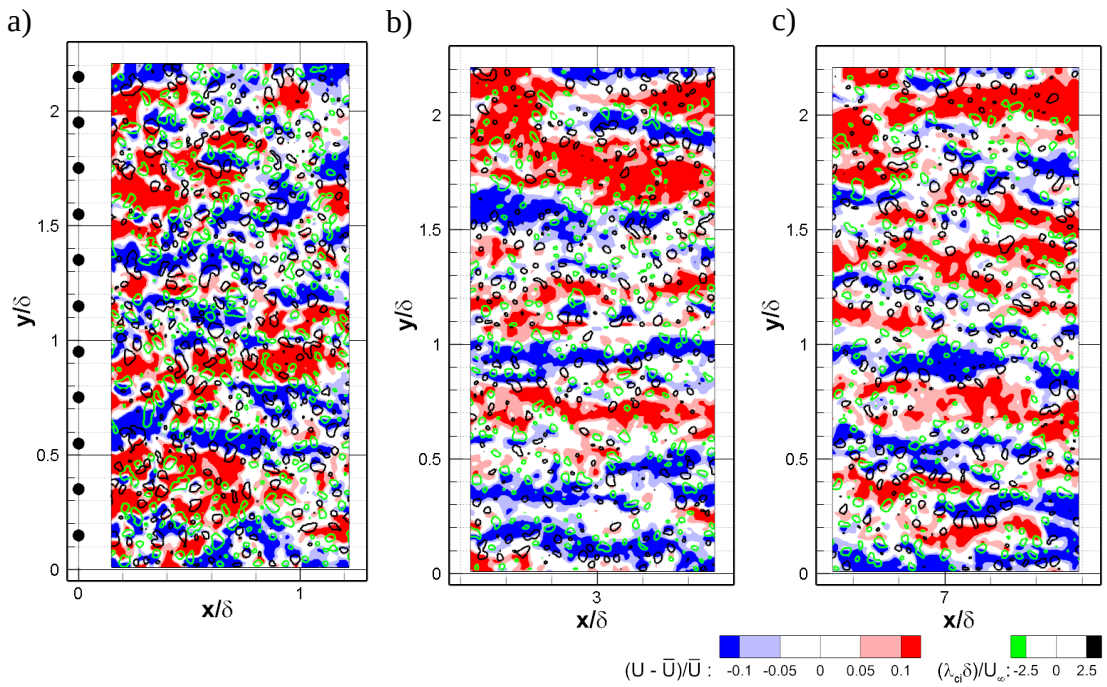

Figure 4-27: S = 0.2δ, H = δ array. Instantaneous vector fields from PPIV of perturbed flow at z^+ = 125 centered at a) x = 0.7δ, b) x = 2.9δ and c) x = 7δ.

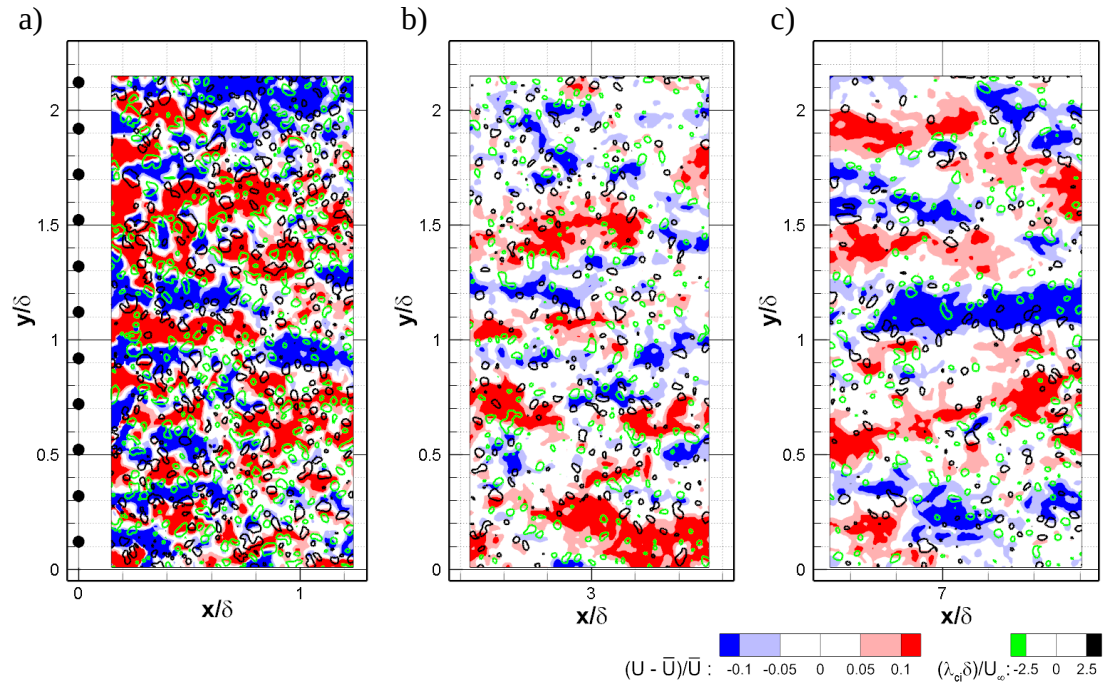

Figure 4-28: S = 0.2δ, H = δ array. Instantaneous vector fields from PPIV of perturbed flow at z^+ = 300 centered at a) x = 0.7δ, b) x = 2.9δ and c) x = 7δ.

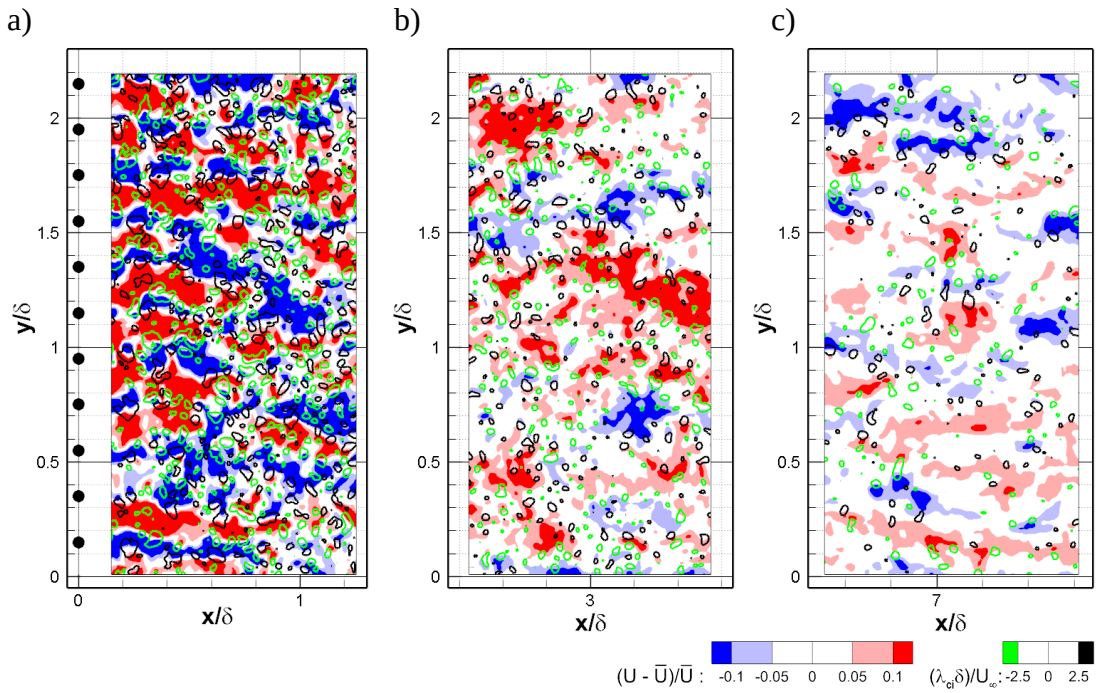

Figure 4-29: S = 0.2δ, H = δ array. Instantaneous vector fields from PPIV of perturbed flow at z^+ = 500 centered at a) x = 0.7δ, b) x = 2.9δ and c) x = 7δ.

disorganized, wavy, and short. Moreover, they were patchy with a dearth of obvious counter rotating swirls. Examples at z^+ = 300 (Fig. 4-28b, y/δ = 0.7, 1.2 and 1.8) and at z^+ = 500 (Fig. 4-29b, y/δ = 0.7 and 1.5) reflect this. At x/ δ = 7 and z^+ = 300, some packets similar to those in unperturbed flow were observable (e.g. at y/δ = 1.1 in Fig. 4-28c). In comparison, at z^+ = 500, packets similar to those in the unperturbed flow were hardly ever observed. Any packet-like structures tended to look narrower and shorter than those in the unperturbed flow. Examples can be seen in Figure 4-29c at y/δ = 1.9 and possibly 2.0. The flow organization here was substantially different from the flow downstream of the H = 0.2δ array (Fig. 4-10c).

Visualizations of instantaneous volumetric fields 4.3δ downstream of the H = δ array revealed that LMRs at z^+ = 155 frequently did not extend to z^+ = 465, in contrast to the

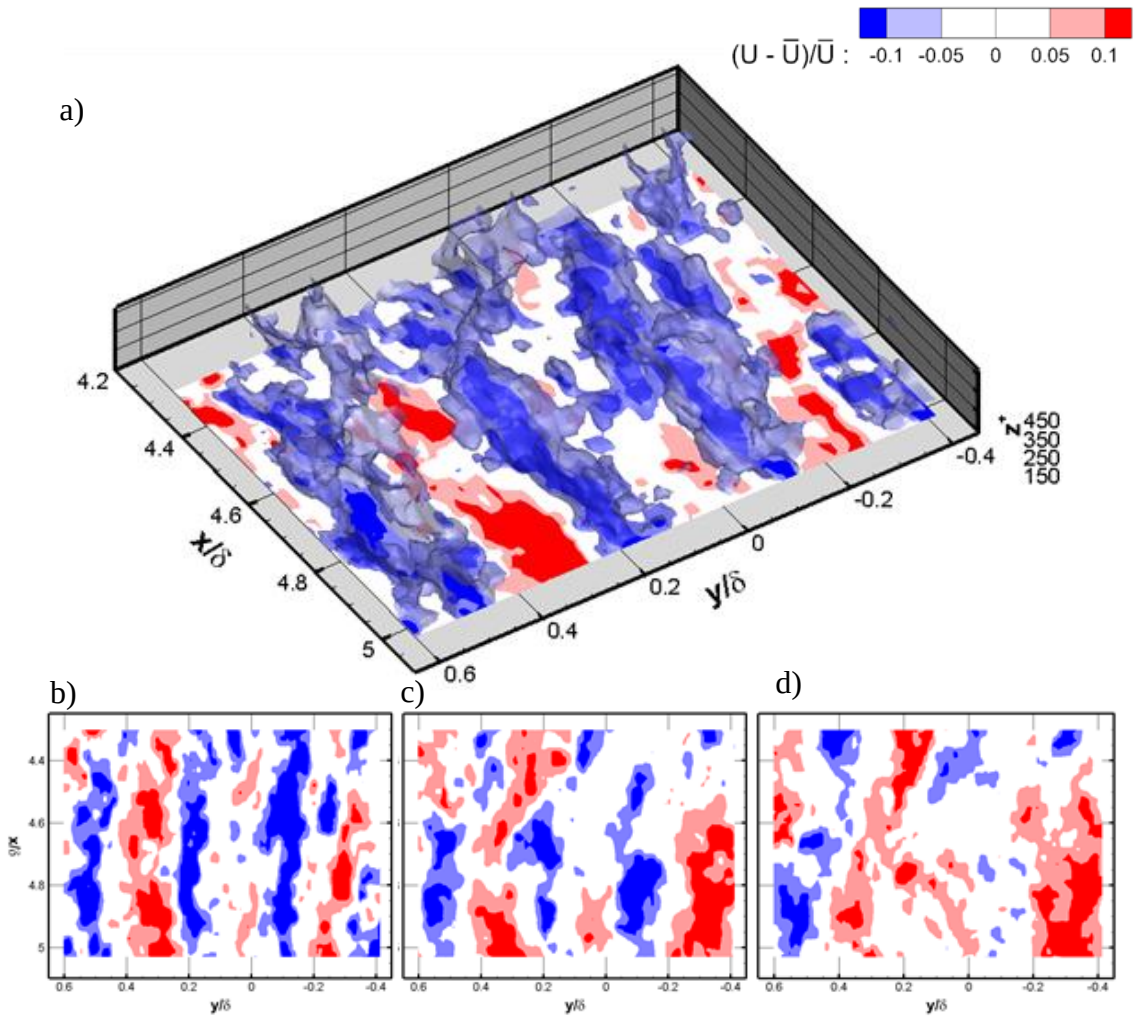

Figure 4-30: a) Instantaneous volume showing streamwise velocity at starting at $x/\delta = 4.3$ behind $H = \delta$ array. Iso-surfaces of $U < 0.95\bar{U}$ are shown, with the streamwise-spanwise contour of streamwise velocity at $z^+ = 155$. Z-planes at b) $z^+ = 155$, c) $z^+ = 300$ and d) $z^+ = 465$ of streamwise velocity deviation away from $\bar{U}$.

structure observed in unperturbed flow where LMRs frequently extended through the volume in the z direction. Figure 4-30 shows a representative example of such a scenario at $x/\delta = 4.6$, where isosurfaces of the LMRs at $y/\delta = 0.2$ and -0.1 are limited in their extension across the depth. Beginning at $z^+ = 155$ and toggling through streamwise-spanwise slices for increasing z, the LMRs observed at the aforementioned spanwise

locations weaken with increasing height until they are hardly visible at $z^+ = 465$ (Figs. 4-30 b-d).

The FPIV runs for the H = δ array are shown in Figure 4-31. At $z^+ = 125$ (Fig. 4-31a), two incoming packets encounter the array. A packet at $y/\delta \sim 0.3$ was disrupted and does not reappear. A packet at $y/\delta \sim 1$ was disrupted, but possibly reappeared in the second data field at $x/\delta = 2.5$, $y/\delta = 0.9$, then continued downstream. Beginning at $x/\delta \sim 2.5$, another packet signature appeared at $y/\delta \sim 1.8$ and then persisted up to $x = 7\delta$. At $z^+ = 300$ (Fig. 4-31b), the packet at $y/\delta \sim 1.3$ appeared at $x/\delta = 3.5$ and persisted till $x/\delta = 6$. A second packet near $y/\delta = 0.3$ was disrupted but possibly reappeared in the last data field ($x/\delta \sim 7$). A packet also appeared starting at $y/\delta = 1.9$ starting $x/\delta = 3$, and persisted. On the other hand at $z^+ = 500$, no packet signatures appeared downstream of the array until $x/\delta \sim 7.5$ (one signature at $y/\delta = 0.3$ in Fig. 4-31c). Generally, incoming packets were disrupted by the array at all measurement heights. On average, packet signatures were observed earliest downstream at $z^+ = 125$ followed by $z^+ = 300$ and latest at $z^+ = 500$. This trend was clearly different to that found downstream of the medium array whereby coherent packets were frequently observed sooner at $z^+ = 300$ than at $z^+ = 125$.

4.2.3 Regions of uniform streamwise momentum

For all measurement heights, at $x = 2.9\delta$ downstream of the H = δ array, more short CMRs ($L_{ex} = 0.2\delta$) were present (Fig. 4-32) compared to the unperturbed flow, while the number of long CMRs ($L_{ex} = \delta$) decreased. The trend at $z^+ = 125$ was opposite from the $H = 0.2\delta$ case at the same location, where the numbers of short CMRs went down relative to the unperturbed flow (see Fig. 4-12a). Notably, the deviations away from the unperturbed values are larger for the short LMRs compared to short HMRs in both plots (compare Fig

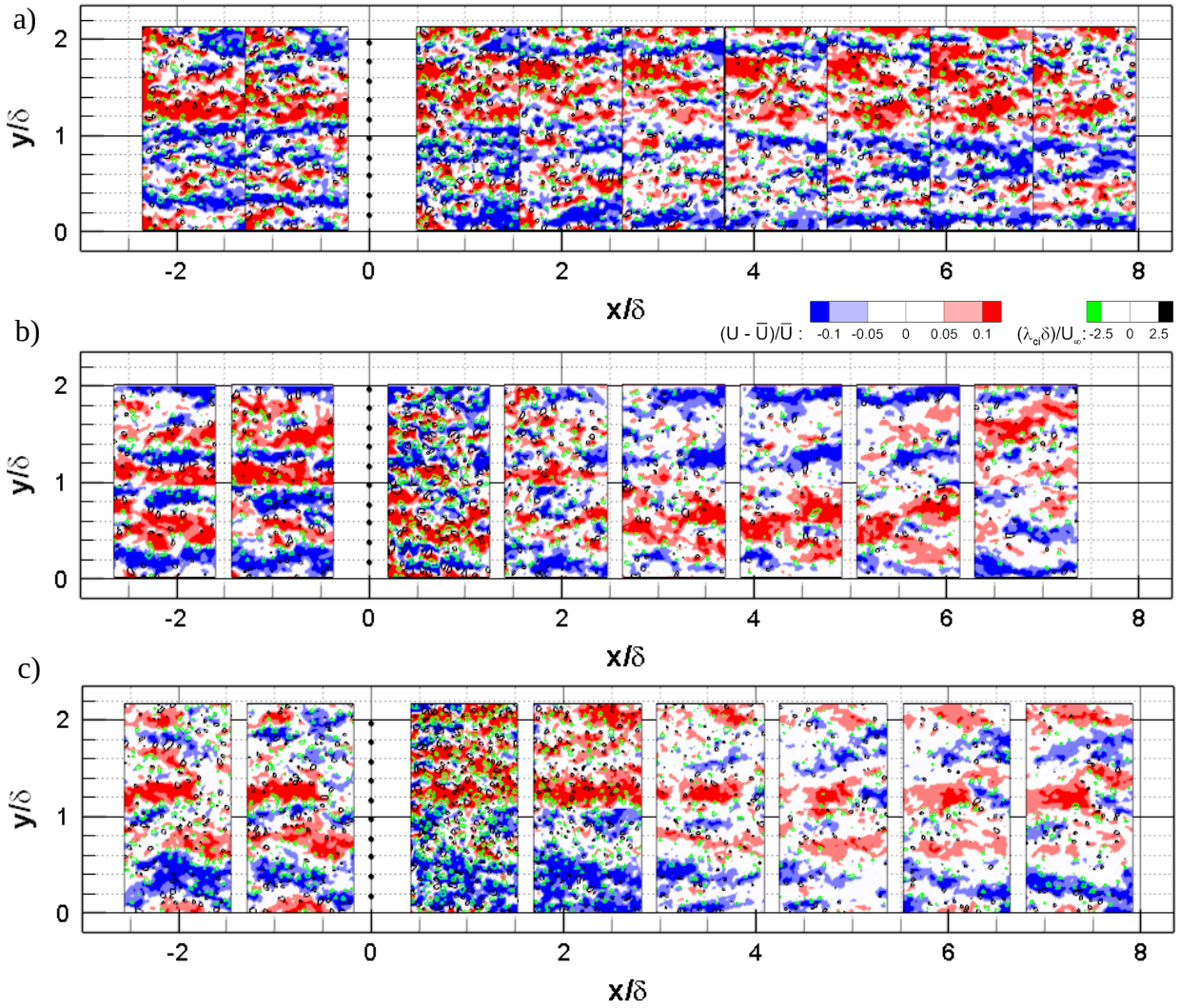

Figure 4-31: S = 0.2δ, H = δ array. FPIV runs at a) z^+ = 125, b) z^+ = 300 and c) z^+ = 500.

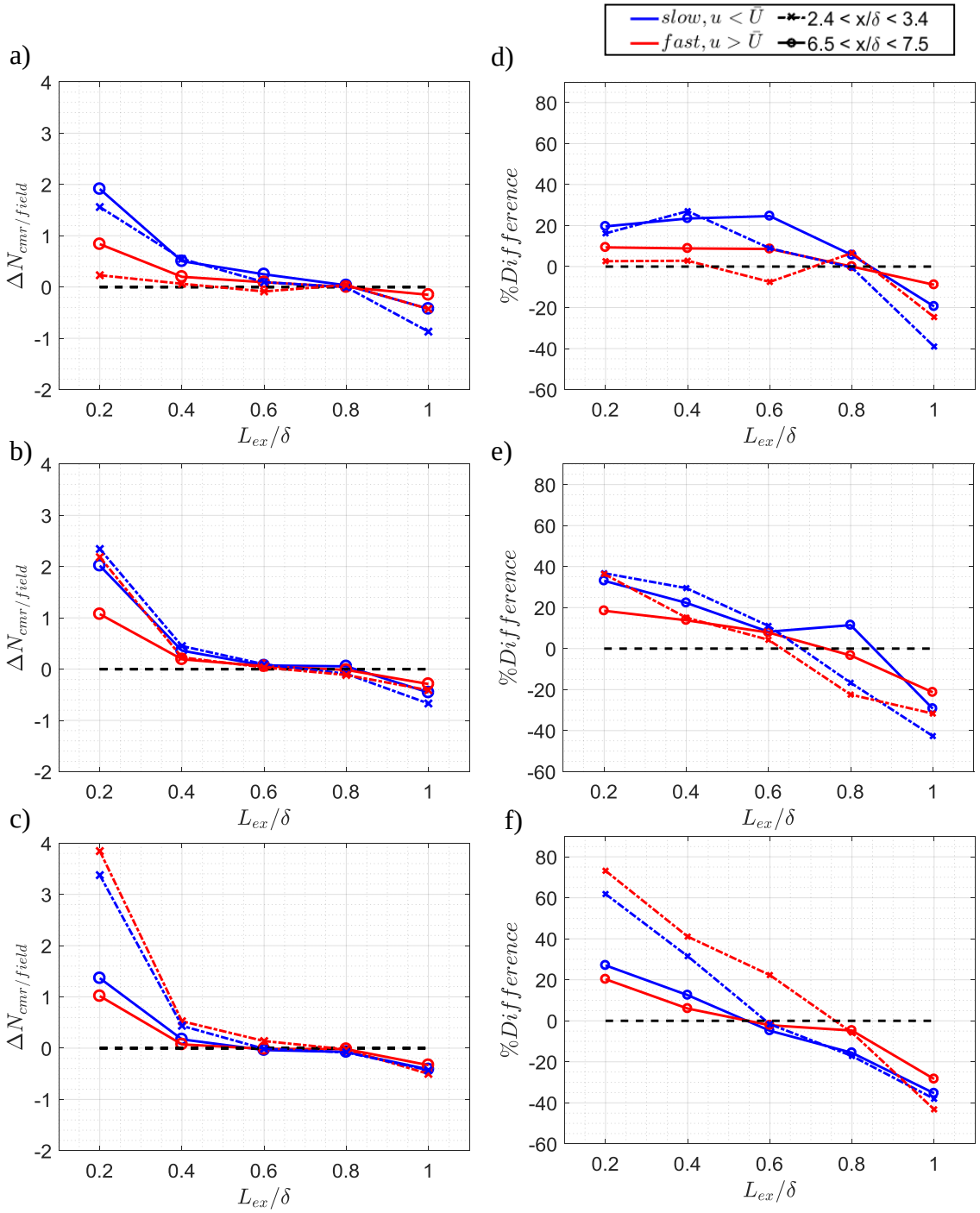

Figure 4-32: S = 0.2δ, H = δ array. Difference in number of LMRs and HMRs per field versus length between perturbed and unperturbed flow at two streamwise locations, for measurement heights a) z^+ = 125, b) z^+ = 300 and c) z^+ = 500. Bin by bin differences between length distributions of the perturbed and unperturbed flow as a percentage of the unperturbed length distribution for aforementioned heights (d,e,f). Bin size = 0.2δ.

4-12a and Fig. 4-32a). The numbers of long CMRs (bin, $L_{ex} = \delta$) decreased significantly in the flow downstream of the H = δ array at x = 2.9δ for all measurement heights, relative to the unperturbed flow. This is also different from the H = 0.2δ case. The largest decrease occurred for $z^+ = 125$ (0.9/field) followed by $z^+ = 300$ (0.6/field) and least at $z^+ = 500$ (0.4/field). On the other hand, more short CMRs were detected for all measurement heights at x = 2.9δ, relative to the unperturbed flow. The greatest increase occurs at $z^+ = 500$, followed by $z^+ = 300$ then $z^+ = 125$.

At x = 7δ, the numbers of long LMRs increased towards the unperturbed values for $z^+ = 125$ and 300 compared to the upstream location, with a larger increase at $z^+ = 125$ (-0.9/field to -0.4/field), compared to $z^+ = 300$ (-0.6/field to -0.45/field). Counter to these trends, the numbers hardly increased at $z^+ = 500$, consistent with observations of shorter LMRs at that location in the perturbed flow (see Fig. 4-29c). Similar trends were observed in the plots where the distributions are normalized by the unperturbed values of the respective LMRs and HMRs (Figs. 4-32d-f). Notably, at x = 7δ, the percentage decrease of the long LMRs is the least at, $z^+ = 125$ (-20%), larger at $z^+ = 300$ (-29%) and largest at (-39%) for $z^+ = 500$.

For all measurement heights, the width distributions show fewer wide CMRs at x = 2.9δ relative to the unperturbed distribution (Fig. 4-33a-c). This was different from the H = 0.2δ case where widths of CMRs were affected minimally at $z^+ = 300$ and 500, while greater numbers of wide CMRs were detected at $z^+ = 125$. Interestingly at $z^+ = 125$, x = 2.9δ, downstream of the H = δ array, the HMR width distribution was more similar to the unperturbed flow, compared to the LMR width distribution. This suggests that the array affects LMR widths more strongly than HMR widths at $z^+ = 125$. Although numbers of

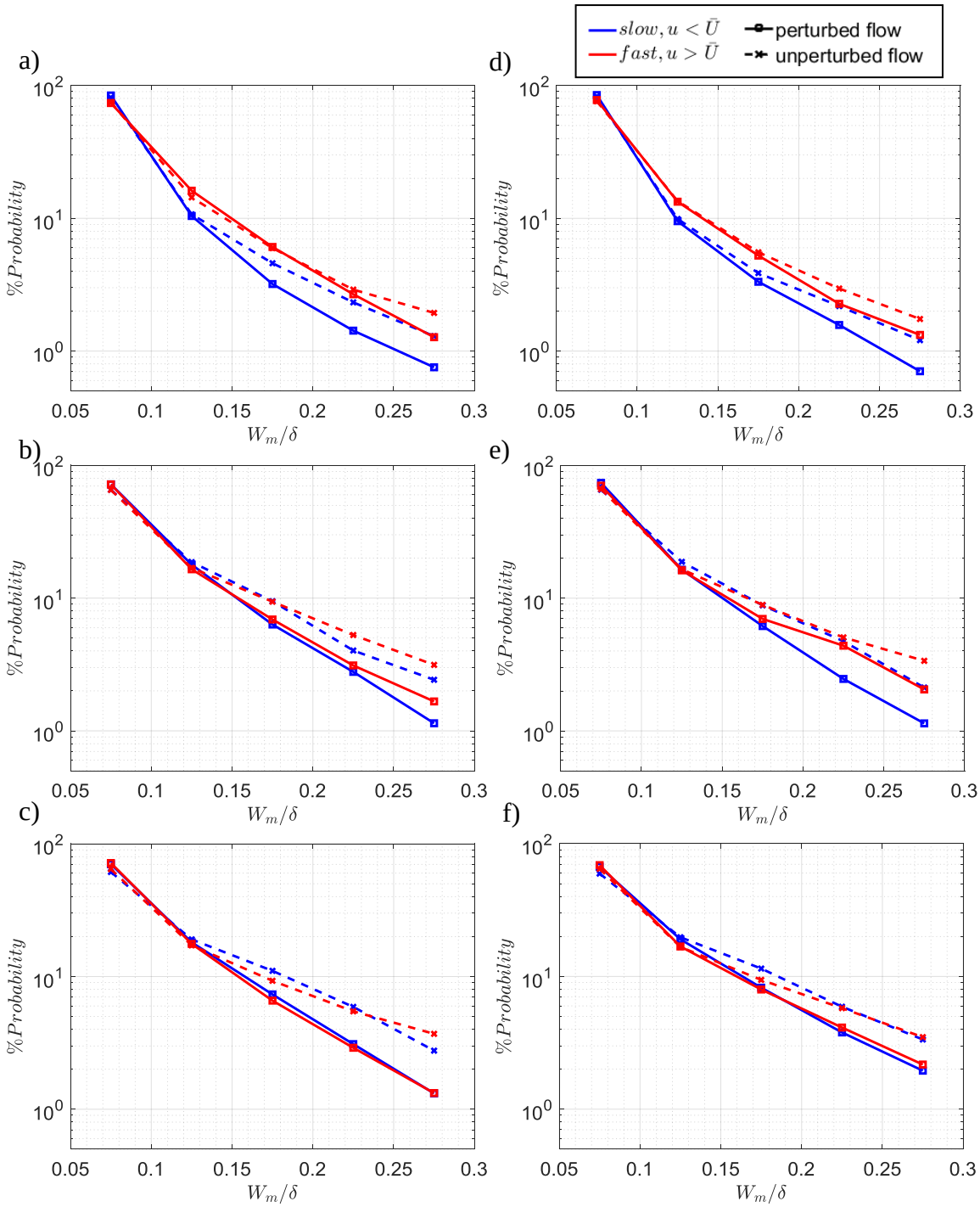

Figure 4-33: S = 0.2δ, H = δ array. Mean width histograms of detected low and high momentum regions normalized by the total number of detected low/high momentum regions respectively for 2.4 < x/δ < 3.4 at a) z^+ = 125, b) z^+ = 300 and c) z^+ = 500 and subsequently for 6.5 < x/δ < 7.5 at aforementioned measurement heights in d, e, and f.

wide CMRs did increase slightly at x = 7δ towards the unperturbed distribution values, the number of wide CMRs remained lower relative to unperturbed values (Figs. 4-33a-c).

4.2.4 Statistics on number of swirls

The total number of swirls downstream of the H = δ array is shown in Figure 4-14b. Immediately downstream of the array, the swirl counts increased at all measurement heights compared to the unperturbed values. The number of swirls at all three measurement heights was comparable to the numbers at z^+ = 125 and 300 for H = 0.2δ (see Fig. 4-14a). Again, this collapse suggests that the number counts were dominated by swirls related to 2-D vortex shedding in the near wake of each cylinder.

Notably, the relative increase in number of swirls at z^+ = 500 was much greater at 2.2 times the unperturbed value compared to immediately downstream of the H = 0.2δ array (1.5 times unperturbed value in Fig. 4-14a). This comparison suggests that, although additional vortices were initiated at the tips of the H = 0.2δ array, the number was comparatively fewer than the number generated in the more two-dimensional wakes below the cylinder tips. Interestingly, the streamwise variations in swirl count downstream of the H = δ array (Fig. 4-14b) were similar to the trends in RMS velocity for all measurement heights (Fig. 4-26b), as was also true for z^+ = 300 and 500 in the H = 0.2δ array case.

As x increased, the number of swirls downstream of the H = δ array decreased rapidly to levels below the equilibrium values at all measurement heights as occurred at z^+ = 125 for the H = 0.2δ case. Downstream of the H = δ array, the curve for z^+ = 125 encountered a minimum at x = 3.8δ before slightly increasing towards the unperturbed value with a

shallow slope. At x = 7δ, the number of swirls for z^+ = 125 was 80% of the unperturbed value. In contrast, at z^+ = 300 and 500, the number of swirls decreased continuously with increasing streamwise location. The curve at z^+ = 300 possibly encountered a minimum near x = 4.8δ and remained relatively flat until x = 7δ. On the other hand, the curve for z^+ = 500 continued to decrease until x = 7δ. At the final measurement location, the number of swirls measured was 72% and 54% of the unperturbed values at z^+ = 300 and 500 respectively.

4.2.5 Autocorrelations of streamwise velocity

Autocorrelations of streamwise velocity fluctuations downstream of the H = δ array showed some striking differences compared to the H = 0.2δ case. The streamwise autocorrelations (Δy = 0) are shown in Figures 4-34a-c for all measurement heights. Immediately downstream of the H = δ array, correlation magnitudes were reduced relative to the unperturbed flow, at all measurement heights, similar to the H = 0.2δ case at z^+ = 125 and z^+ = 300 (see Fig. 4-15 a & b). This was reasonable as the array now extends further up, thus the effects previously seen at z^+ = 125 and z^+ = 300 for the H = 0.2δ case were now observed for all measurement heights. Different from the H = 0.2δ case, an evident change in the slope of the correlation curve was seen for all three measurement heights with peaks occurring at Δx = 0.23δ. This suggests that there were more flow structures with this characteristic length which may be related to the Karman-like vortices, now occurring at all measurement heights due to the cylinder height. The Reynolds number based on the cylinder diameter varied from 2100 to 2600 across the logarithmic layer, corresponding to a roughly constant Strouhal number, St ~ 0.2. This gives characteristic vortex shedding frequencies, f_s of 10.4 Hz and 13Hz at z^+ = 125 and

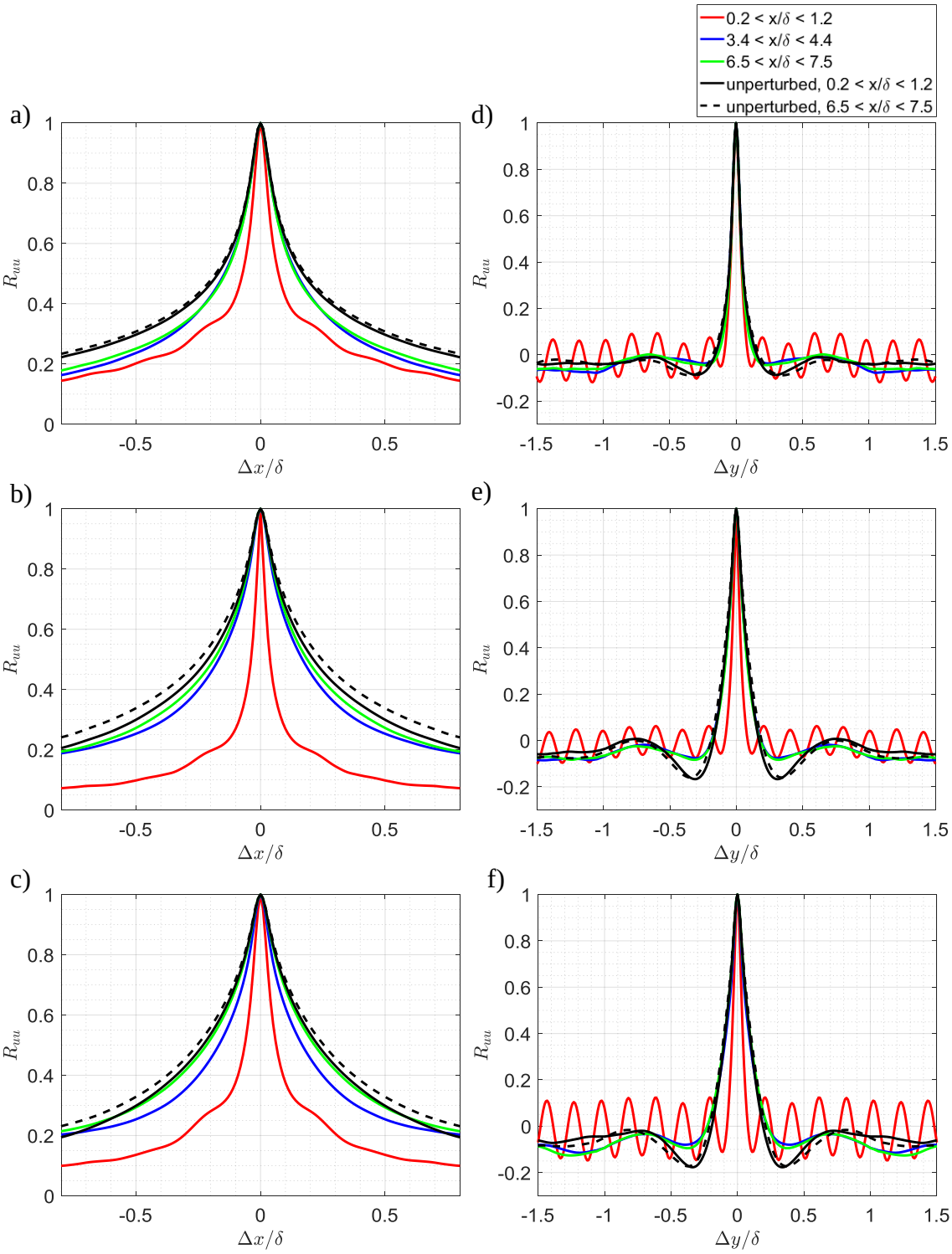

Figure 4-34: S = 0.2δ, H = δ array. Autocorrelations of streamwise velocity. Δy = 0 cuts are shown for measurement heights a) z^+ = 125, b) z^+ = 300 and c) z^+ = 500. Δx = 0 cuts are shown for measurement heights d) z^+ = 125, e) z^+ = 300 and f) z^+ = 500.

500 respectively. Assuming that the wake vortices convect at the reduced local mean velocities immediately downstream of the H = δ array (see Figure 4-26a), a length scale corresponding to f_s can be estimated, equal to 0.25δ and 0.23δ for z^+ = 125 and z^+ = 500 respectively, roughly corresponding to the peak location. This phenomenon was not evident in the H = 0.2δ case, which may indicate that the cylinder tip structures disrupted or weakened the vortex shedding signatures in the planes below.

As x increased, all correlation curves recovered towards the shape seen in the unperturbed flow, while approaching the unperturbed correlation values. However, at x = 7δ, correlation magnitudes remained lower relative to unperturbed values at all measurement heights, different from the H = 0.2δ case. Notably, at both z^+ = 125 and 300, correlation values were reduced more compared to z^+ = 500. This was fairly surprising considering that the instantaneous visualizations at x = 7δ showed similar structures to the unperturbed flow at z^+ = 125 (see Fig.4-29a), while hardly any were observed at z^+ = 500 (see Fig.4-29c), where regions of uniform streamwise momentum appear much shorter. This may suggest that there were still fewer long structures relative to the unperturbed flow at z^+ = 125. On the other hand, the trend at z^+ = 500 could very well be from uncertainty, as values for smaller Δx shifts remain lower relative to unperturbed values, except near the tail.

Spanwise autocorrelations (Δx = 0) are shown in Figures 4-34 d-f. In the field immediately downstream of the H = δ array, spanwise periodicities were present for all measurement heights, in contrast to the H = 0.2δ case, where the spanwise periodicity effect was diminished as the tip of the cylinder is approached. Furthermore, the negative lobes adjacent to the central positive region for all measurement heights shifted towards

0.1δ, as opposed to only occurring at $z^+ = 125$, for the H = 0.2δ case (see Fig. 4-15d). This shift can be related to the wakes behind the cylinders and faster moving fluid between them (see Fig. 4-21). Moreover, the steeper negative slope for the correlation curves at all measurement heights near Δy = 0 indicate fewer wide flow structures, relative to the unperturbed flow. As x increased, the central positive lobe recovers to the unperturbed correlations for all measurement heights, suggesting again that shorter relaxation times apply to spanwise scales compared to streamwise scales, similar to the H = 0.2δ array. However, at x = 7δ, different from the H = 0.2δ case, the magnitude of the negative lobes at all measurement heights remained lower relative to unperturbed values. This may be indicative of a persistent alteration to the spanwise organization of flow structures, despite the recovery of smaller spanwise scales.

4.2.6. Wall parallel cross correlations from 3-D PTV data

Cross-correlations of streamwise velocity across wall parallel planes for the flow downstream of the H = δ array indicate reduced streamwise coherence compared to the unperturbed flow (Figure 4-35). This effect can be seen clearly in streamwise cross-correlations (Δy = 0) in Figures 4-35a-c. Immediately downstream of the cylinders (red curves), cross correlations also exhibited periodic oscillations similar to those in autocorrelations of PPIV data (see Fig. 4-34). This can be attributed to the regular spanwise oscillations in wake position downstream of the cylinder, related to the Karman shedding. The regularity of oscillations in all cross correlations suggests that wakes were two-dimensional across the logarithmic layer. This was clearly different from the H = 0.2δ case, where the effect was less pronounced, occurring only at $z^+ = 125$.

The peak values for all correlations were smaller than those in the unperturbed flow. At $x/\delta = 2.6$ and 4.6, the reduction in peak correlation value was minimal for $z_c^+ = 200$, but increasingly significant for larger z separations (e.g., $z_c^+ = 300$ and $z_c^+ = 465$). In addition, correlation values were suppressed everywhere along the Δx direction compared to the unperturbed flow. At the two larger wall-normal separations corresponding with $z_c^+ = 300$ and $z_c^+ = 465$, the skewness of the cross-correlations were reduced significantly compared with the results in unperturbed flow, possibly suggesting fewer flow structures with forward inclination across the measurement volume on average.

When comparing the results at $x/\delta = 2.6$ and 4.6, all correlations indicated some recovery towards the unperturbed condition, although the correlations for $z_c^+ = 465$ exhibited the least amount of recovery. These trends were consistent with observation in the PPIV fields at different heights, where packet organization seems to recover initially closer to the wall.

The spanwise cross correlation ($\Delta x = 0$) are plotted in Figures 4-35d-f. Immediately behind the array, all correlations showed strong periodicity associated with alternating wakes behind cylinders, and faster moving zones between them. The magnitudes of the peaks and valleys adjacent to the central positive lobe were similar for all cross correlations, also suggesting that the wakes aligned across the thickness of the volume. This was clearly different from the $H = 0.2\delta$ case where the periodicity diminishes as the cylinder tip height is approached. Also at this streamwise location, for the $H = \delta$ array, all cross correlations indicate strong suppression of the width of the central positive lobe compared to the unperturbed flow. This can be explained by the shift towards smaller spanwise scales induced by the narrowly-spaced array. Further downstream, the width of

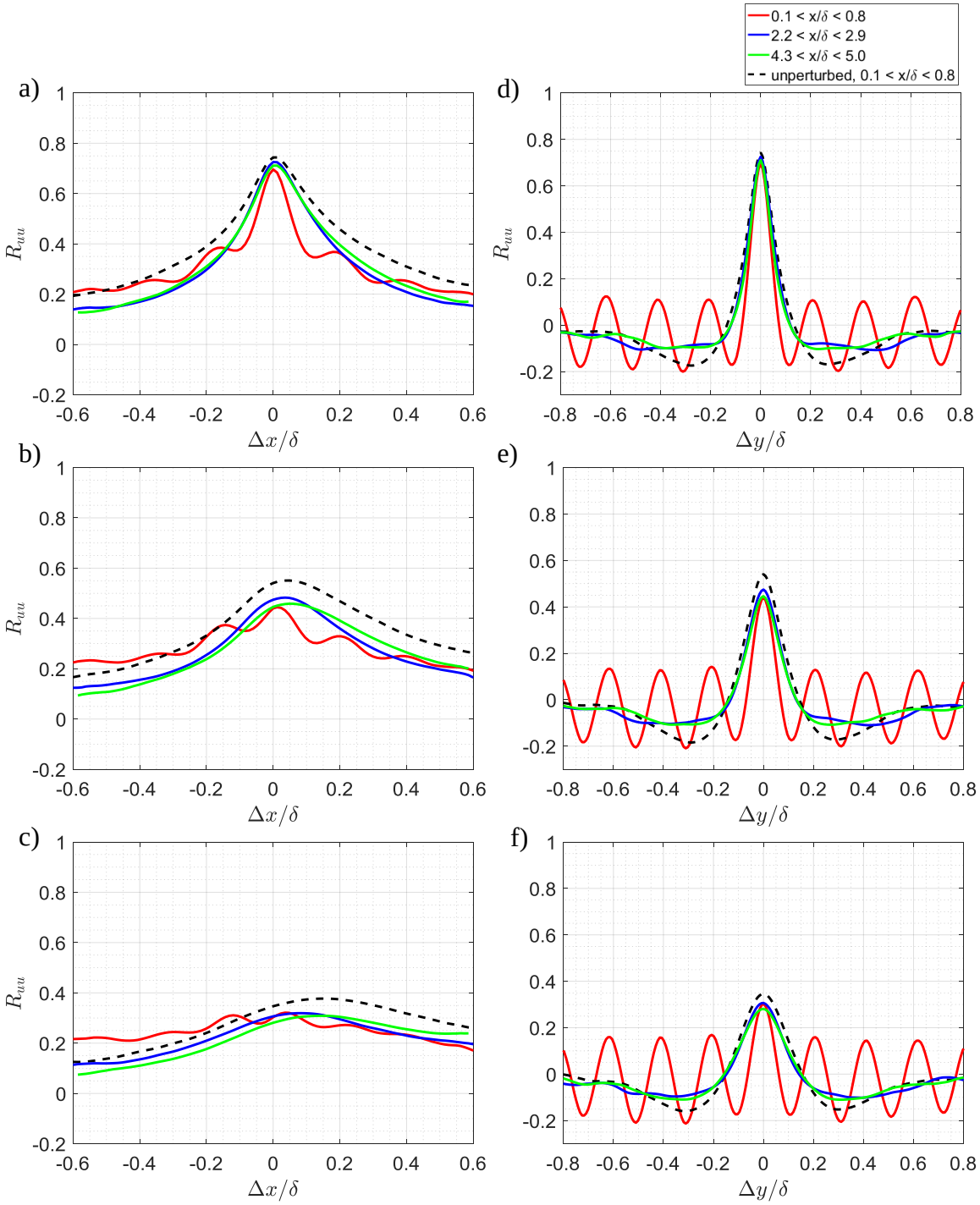

Figure 4-35: S = 0.2δ, H = δ array. Streamwise velocity cross correlation slices averaged over 500 fields at Δy = 0, where the planes at z_{ref}^+ = 155 were correlated with a) z_c^+ = 200, b) z_c^+ = 300, & c) z_c^+ = 465. Cross-correlations at Δx = 0 for the aforementioned correlated planes shown in d, e & f.

the central positive lobe increased, but remained slightly narrower compared to the unperturbed width in all three correlations. At $x/\delta = 2.6$ and 4.6, the adjoining negative lobes were clearly damped compared with the results in unperturbed flow, indicating persistent alterations of the spanwise organization.

Wall-normal velocity cross correlations immediately downstream of the $H = \delta$ array indicate increased correlation of wall normal fluctuations across the depth of the measurement volume along the Δx direction ($\Delta y = 0$), relative to the unperturbed flow (Figure 4-36a-c). With increasing x, this effect diminished for all correlations. At $x = 7\delta$, correlations at $z_c^+ = 300$ and $z_c^+ = 465$ were reduced with respect to the unperturbed correlation values, while the $z_c^+ = 155$ correlation seemed to relax to the unperturbed flow. This was opposite from the $H = 0.2\delta$ array where correlation magnitudes were enhanced at $x = 7\delta$.

Strong spanwise periodicities associated with alternating zones of fluid moving away and toward the wall were seen for all $\Delta x = 0$ correlations (Figs. 4-36d-f), immediately behind the $H = \delta$ array, different compared to the $H = 0.2\delta$ array. This suggests initial alignment of wall-normal fluctuations across the measurement volume relative to the unperturbed flow. With increasing x, this effect diminished and at $x = 7\delta$, the peaks of the correlations for all measurement heights were suppressed relative to the unperturbed correlation.

4.2.7 Pre-multiplied energy spectra and dominant spanwise modes

For all measurement heights, immediately downstream of the $H = \delta$ array, one dimensional pre-multiplied spectra (Figs. 4-18d-f) showed reductions in energy contained within spanwise wavelengths greater than ~0.3δ, relative to the unperturbed spectrum.

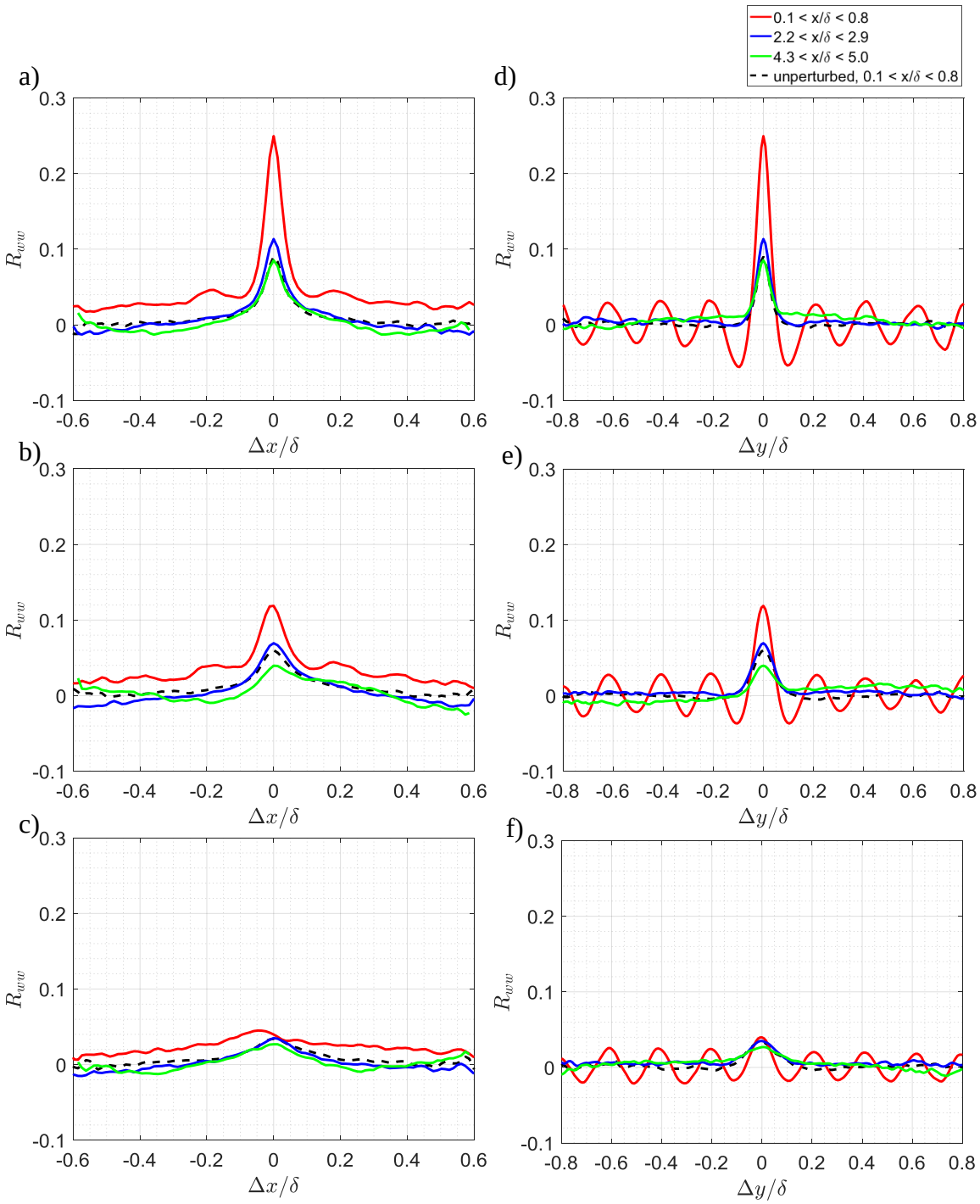

Figure 4-36: S = 0.2δ, H = δ array. Wall-normal velocity cross correlations averaged over 500 fields. Cross correlations at Δy = 0, where the planes at z_{ref}^{+} = 155 were correlated with a) z_c^{+} = 200, b) z_c^{+} = 300, & c) z_c^{+} = 465. Δx = 0 cross-correlations for the aforementioned correlated planes shown in d, e & f.

This occurred also immediately downstream of the H = 0.2δ array for all measurement heights, although the magnitudes of reduction were much stronger for H = δ at z^+ = 300 and 500 (compare Fig 4-18b & c). Also, dominant peaks in energy at λ_y = 0.2δ were observed at all measurement heights for the H = δ case with the strongest at z^+ = 500 followed by z^+ = 125 then 300. Notably, at z^+ = 125, and different from the H = 0.2δ case, the energy contained in the smaller spanwise wavelengths did not increase relative to the unperturbed flow. It did increase however for z^+ = 300 and 500, similar to the H = 0.2δ case.

As x increased, for z^+ = 300 and 500 (Figs. 4-18e & f), the H = δ spectra did not recover to the unperturbed spectra, even at x = 7δ, different from the H = 0.2δ case. Energy contained within spanwise wavelengths greater than 0.4δ remained lower relative to the unperturbed spectra. The initially increased energy in smaller spanwise wavelengths did relax to the unperturbed energy levels with increasing x at those heights. In contrast, at z^+ = 125 (Figs. 4-18d), the spectra tended towards the unperturbed energy levels as x increased for all spanwise wavelengths. At x = 7δ, energy levels for $0.1\delta < \lambda_y < 0.5\delta$ remained above the unperturbed values while spanwise wavelengths greater than 0.5δ were slightly less energetic compared to the unperturbed flow. Nevertheless, the shape of the spectra at this height resembled the unperturbed spectra, unlike the H = 0.2δ case, whose shape appeared more similar to spectra at z^+ = 300.

The dominant spanwise modes immediately downstream of the H = δ array also revealed differences relative to the H = 0.2δ case. For all measurement heights, immediately downstream of the H = δ array (Figs. 4-19 d-f), the most probable spanwise mode was 0.2δ, consistent with the spectra results. In contrast, the 0.6δ spanwise mode remained

dominant for both $z^+ = 300$ and possibly 500 for the $H = 0.2\delta$ case, although the related spectra showed an energy peak at $\lambda_y = 0.2\delta$ (see Figure 4-18b & c). This suggests a more persistent 0.2δ spanwise mode for the flow immediately downstream of the $H = \delta$ array compared to the $H = 0.2\delta$ case. The probability of 0.2δ as the dominant spanwise mode was greatest at $z^+ = 500$ (48%), and comparable for $z^+ = 125$ and 300 (both 38%).

With increasing x, the shapes of the distributions tended towards the unperturbed distribution for $z^+ = 300$ and 500, while alterations persisted at $z^+ = 125$. This result was different from the $H = 0.2\delta$ case where all distributions relaxed toward the unperturbed values. For $z^+ = 125$, $H = \delta$ and $x = 3.8\delta$, probabilities for the 0.2δ and 0.4δ modes remained larger while probability values for spanwise modes greater than 0.4δ were reduced relative to the unperturbed flow. The peak probability occurs at the 0.4δ mode (32%). At $x = 7\delta$, the distribution hardly changed. For $z^+ = 300$ and $x = 3.8\delta$ the 0.4δ mode value was greater than in the unperturbed flow, while modes larger than that were suppressed, except 1.2δ. The peak for the distribution occurs at 0.6δ instead of 0.8δ seen in the unperturbed flow, and remained so even at $x = 7\delta$, with the distribution hardly changing compared to $x = 3.8\delta$. Interestingly, the distribution at $x = 7\delta$ for $z^+ = 500$ resembled the unperturbed distribution. This suggests that although instantaneous visualizations show that flow structures at $z^+ = 500$ hardly resembled ones in the unperturbed flow (compare Fig. 4-29c and Fig. 3-13), the distributions of low and high speed zones along the spanwise direction can be similar between the perturbed and unperturbed flow. This was not obvious from the instantaneous visualizations.

4.2.8 VPIA results

The number of packets downstream of the array with H = δ is plotted in Figure 4-20b. The packet counts were reduced initially at all three measurement heights. This was different from the H = 0.2δ case, where the numbers increased initially at z^+ = 500 (see Fig. 4-20a). At z^+ = 125, the number of packets in the flow perturbed by the H = δ array was 78% of the number in the unperturbed flow. With increasing x, the number of packets increased, matching the unperturbed packet count at x = 4.8δ and remaining greater than the unperturbed value at x = 7δ (1.4 compared to 1.3) although this was within uncertainty. This was also different from the trend downstream of the H = 0.2δ array, where the packet count was suppressed at z^+ = 125 for all streamwise locations.

For H = δ, the packet counts at z^+ = 300 and 500 were 51% and 37% of the unperturbed values respectively at x = 2.9δ. With increasing x, the number of packets at z^+ = 300 decreased slightly to a minimum at x = 3.8δ, then increased towards the unperturbed value with a shallower slope than the curve at z^+ = 125. In contrast, the number of packets at z^+ = 500 remained lower at all downstream locations with no indication of recovery. Packet counts at z^+ = 300 and 500 did not recover to the unperturbed value by x = 7δ, remaining at 72% of the unperturbed packet count at z^+ = 300 and 22% at z^+ = 500.

Packet skeleton length histograms shown in Figures 4-37a-f indicate the effectiveness of the H = δ array at disrupting long packets, defined as packets with skeleton lengths greater than the field of view (1.05δ). At x = 2.9δ, the decrease in the number of long packets as a percentage of the unperturbed value was greatest at z^+ = 500 (90%), followed by z^+ = 300 (82%) and z^+ = 125 (60%). This effect was particularly evident in packet length histograms normalized by the respective number of packets detected at each

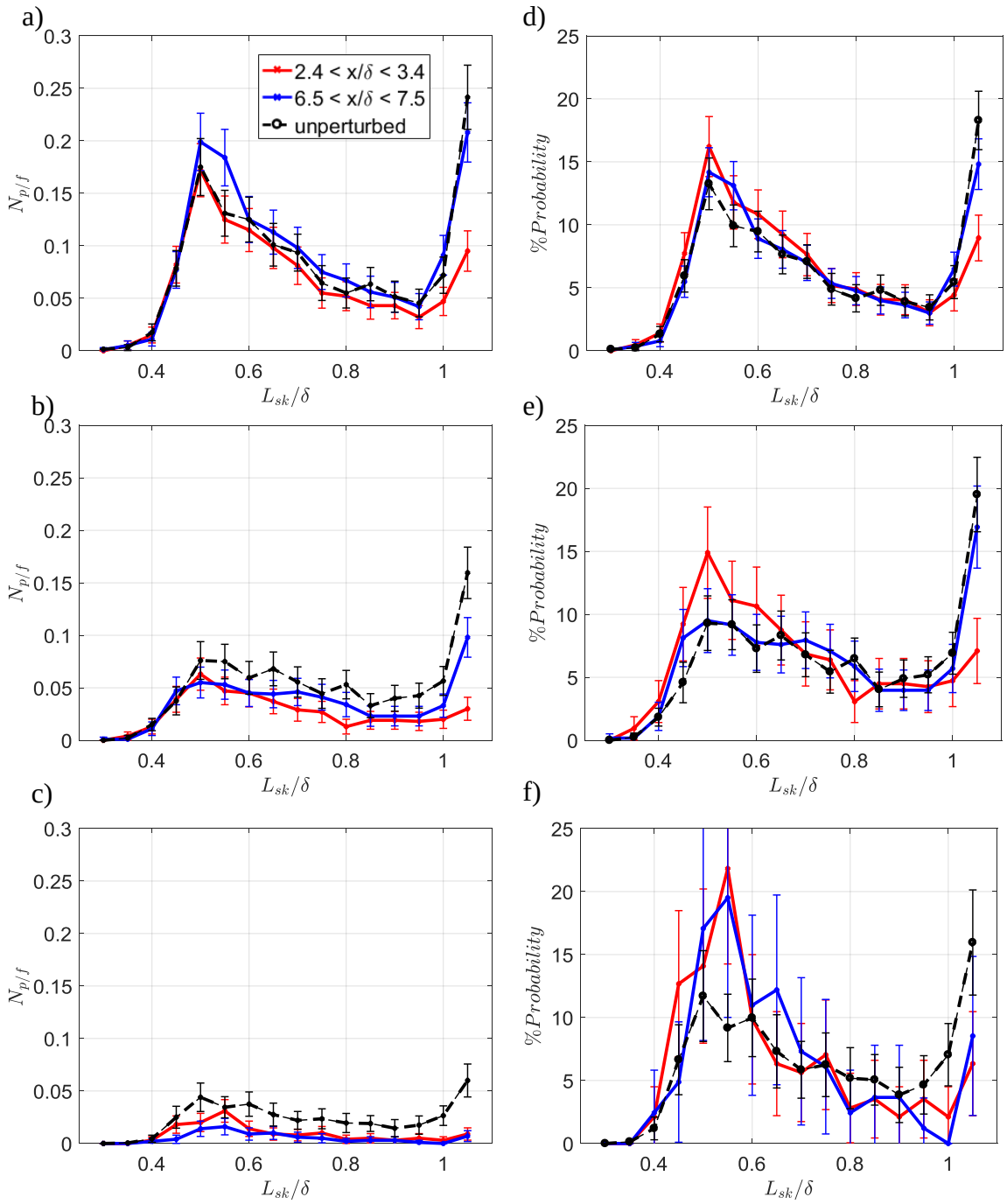

Figure 4-37: S = 0.2δ, H = δ array. Packet skeleton length histograms at two streamwise locations and at a) z^+ = 125, b) z^+ = 300 and c) z^+ = 500 and histograms normalized by total number of packets at d) z^+ = 125, e) z^+ = 300 and z^+ = 500. Histogram bin size = 0.05δ.

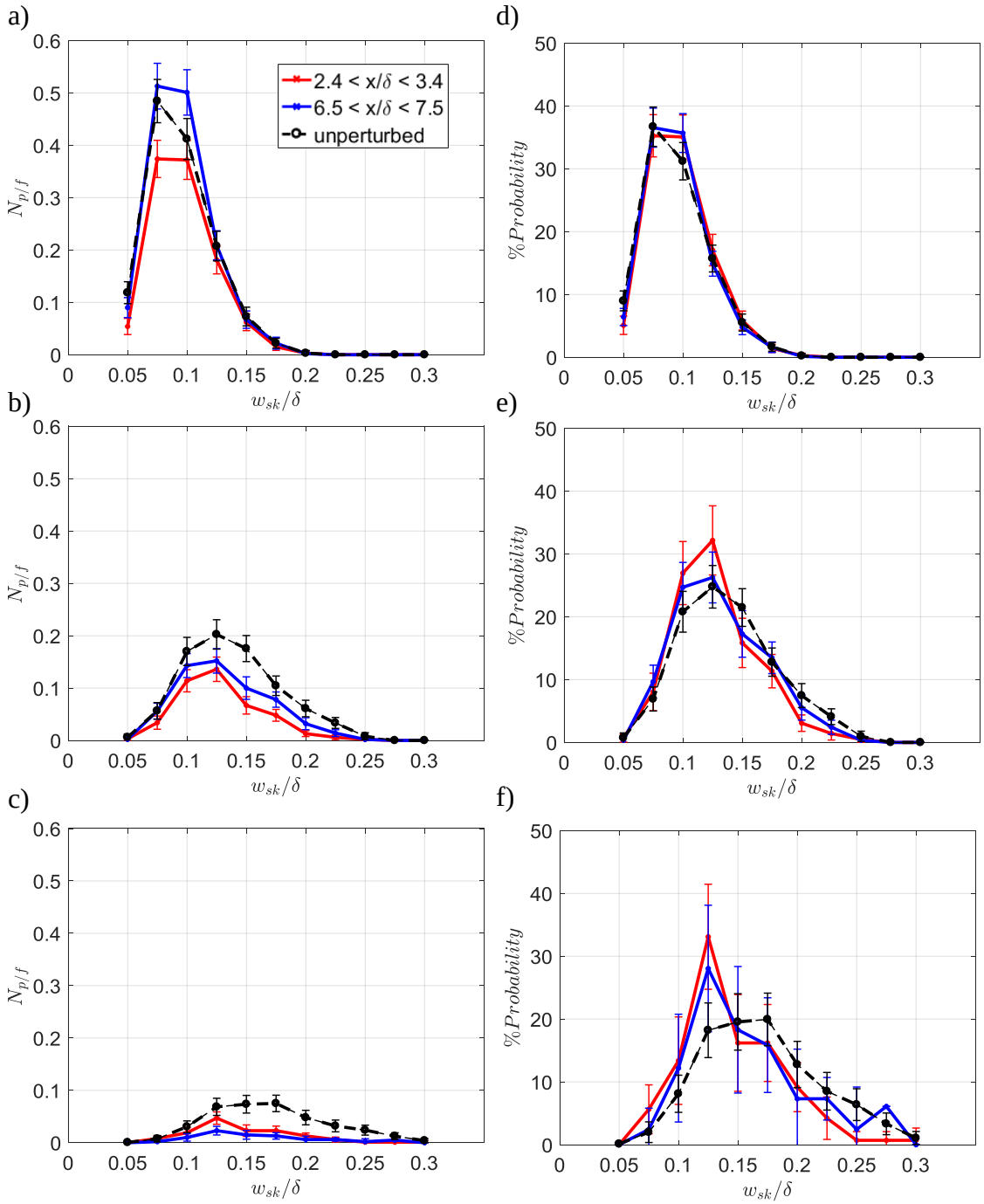

Figure 4-38: S = 0.2δ, H = δ array. Packet skeleton width histograms at two streamwise locations and at a) z^+ = 125, b) z^+ = 300 and c) z^+ = 500 and histograms normalized by total number of packets at d) z^+ = 125, e) z^+ = 300 and z^+ = 500. Histogram bin size = 0.05δ.

measurement height (Figs 4-37d-f). Normalized packet length distributions shifted towards shorter packets at all measurement heights at both x = 2.9δ and 7δ. However, the number of long packets increased substantially between 2.9δ and 7δ at both z^+ = 125 (Fig. 4-37a) and 300 (Fig. 4-37b) but only minimally at z^+ = 500 (Fig. 4-37c).

Packet skeleton width histograms in Figure 4-38 show that the H = δ array reduced the width of packets at z^+ = 300 and 500. In comparison, the packet width distributions at z^+ = 125 (Fig. 4-38a) remained similar to the unperturbed flow. Normalized packet width distributions showed a shift towards narrower packets for both z^+ = 300 (Fig.4-38e) and 500 (Fig.4-38f) at both x = 2.9 and 7δ, although for z^+ = 300, the distribution seemed to relax towards the unperturbed distribution at x = 7δ.

4.3 Summary of results and discussion

The results highlight major differences in boundary layer and packet organization recovery downstream of the two arrays. The H = δ array generated profound perturbations across the entire boundary layer thickness. The blockage posed by this array led to significant upwash in the mean flow, and consequently mean velocity deficits throughout the logarithmic region that lasted beyond the end of the measurement domain, 7δ downstream of the perturbation. Although relative RMS velocities rose immediately downstream of the cylinders, they decreased rapidly with downstream distance, falling below unperturbed levels by x = 2δ and remaining suppressed until at least x = 7δ.

Strong velocity deficits were prevalent behind all cylinders, in addition to prominent wavy, Karman like wake patterns, ultimately obscuring any packet organization. Starting at x = 2.9δ, however, in spite of the strong perturbations to the mean and RMS velocity

statistics, instantaneous velocity fields and FPIV runs revealed flow structures and packet signatures resembling those in the unperturbed flow at $z^+ = 125$, the measurement location closest to the wall. At this wall normal distance, the number of packet signatures identified by the algorithm increased with downstream distance, exceeding the unperturbed value at $x = 4.8\delta$ and continued to increase until the end of the measurement domain. Furthermore, numbers in both long CMRs and packet signatures increased substantially towards unperturbed values, corroborating the trends in the visualizations.

In contrast, at $z^+ = 300$, packet signatures and flow structures resembling those in the unperturbed flow first became apparent further downstream than at $z^+ = 125$, with the number of packet signatures beginning to increase after a minimum at $x = 3.8\delta$. At $z^+ = 500$, however, flow structures and packet signatures like those in unperturbed flow were hardly ever observed, even at 7δ downstream of the perturbation, where the number of packets remained much lower relative to the unperturbed values. The numbers of long CMRs and packet signatures were also strongly reduced at this location.

It is interesting that, at $z^+ = 125$ and $x = 7\delta$, the number of identified packet signatures exceeded the unperturbed value even though the relative RMS velocity and number of identified swirling structures remained below the unperturbed values. These opposing trends indicate clearly that other boundary layer features not related to individual packet signatures have not recovered to the unperturbed state. This was supported by the suppressed magnitudes of the streamwise autocorrelations ($\Delta y = 0$) of streamwise velocity at $z^+ = 125$, $x = 7\delta$. Nevertheless, the minimum in swirl count at $x = 2.9\delta$ corresponded directly to the streamwise location where packet signatures like those in the unperturbed flow were first observed and thus may be an indicator for initiation of

recovery at this location. At $z^+ = 300$, a similar minimum occurred near $x/\delta = 4.8$, consistent with the location where packet signatures like those in the unperturbed flow were first observed. No minimum in swirl count was observed at $z^+ = 500$ as the number continuously decreased to the end of our measurement domain.

The aforementioned trends seem to fit a bottom up recovery model, where flow first reorganizes near the wall, then later above. This seems reasonable as characteristic scales of eddies close to the wall are smaller than those of eddies further away from the wall, therefore, it must take a longer distance for larger eddies away from the wall to develop and interact in order to return to the equilibrium state. Furthermore, initial streamwise growth (Adrian 2000; Zhou *et al.* 1996 & 1999; Kim,Sung Adrian 2008; Jodai & Elsinga 2016) and subsequent spanwise pairing mechanisms (Wark & Nagib 1989; Tomkins & Adrian 2003) for scale growth have been previously proposed and could have contributed significantly to the recovery process.

Generally, correlations, structural analyses and VPIA results showed that the $H = \delta$ array significantly reduced streamwise length scales throughout the logarithmic layer immediately downstream. Autocorrelations indicate streamwise periodicities at $\Delta x = 0.23\delta$ representing the prominence of Karman like vortex shedding from the cylinders. Substantial spanwise periodicities at the cylinder spacing were also introduced across the log layer, with a substantial increase in energy at the 0.2δ spanwise wavelength. Subsequently, energy decreased for the 0.6δ spanwise wavelength typically associated with the spanwise distribution of vortex packets in unperturbed flow (Hutchins *et al.* 2005; Zheng & Longmire 2014). The decrease signified the disruption of the natural spanwise scaling, or possibly the disruption of the packets themselves.

Autocorrelation results were used to evaluate the relaxation of characteristic scales on average within the flow. Both streamwise ($\Delta y = 0$) and spanwise ($\Delta x = 0$) autocorrelations relaxed substantially towards unperturbed values with increasing x, even though mean and RMS velocity statistics remained altered relative to the unperturbed flow. Surprisingly, at $x = 7\delta$, streamwise autocorrelations at $z^+ = 500$ deviated the least from unperturbed correlations, despite hardly any sign of recovery in large-scale flow features, while correlation values at $z^+ = 125$ deviated by a larger amount, where the large-scale flow organization resembled unperturbed flow. Notably, autocorrelations were normalized by streamwise RMS velocity, which decreased significantly at $z^+ = 500$ at this location, while instantaneous visualizations were performed at a fixed threshold scaling with the local mean velocity, held as a constant between perturbed and unperturbed flows. Further examination at a lower threshold did reveal large-scale flow organization of alternating low and high momentum zones longer than ones visualized at the larger threshold. These weaker structures could contribute to the recovered correlation magnitudes, as the correlation values were normalized by the reduced RMS velocities, resulting in correlation values that could be similar to those in unperturbed flow. Generally, the structures visualized at the lower threshold were quite different relative to those in unperturbed flow, where they had more small-scale variations, and were substantially wavier. Thus, recovery trends in the characteristic scales from autocorrelations should be interpreted carefully, as flow features can still deviate substantially from those in unperturbed flow, despite correlation values closely matching unperturbed levels.

Spanwise autocorrelations ($\Delta x = 0$) relaxed much quicker with increasing x–location than streamwise autocorrelations ($\Delta y = 0$) downstream of the $H = \delta$ array. Characteristic widths seemed to recover first at $z^+ = 125$ by $x = 1.8\delta$, then later at both $z^+ = 300$ and 500 at $x = 3.8\delta$. On the other hand, alterations to the spanwise distribution of alternating low and high momentum zones persisted to $x = 7\delta$ at all measurement heights. This trend was corroborated by the dominant spanwise mode analysis at both $z^+ = 125$ and 300, $x = 7\delta$, with distributions favoring smaller spanwise wavelengths.

Immediately downstream of the cylinders, streamwise cross-correlations ($\Delta y = 0$) of streamwise velocity showed periodicities associated with Karman shedding for all z separations. In addition, correlation magnitudes and skewness were reduced, which may indicate fewer forward inclined structures and reduced wall-normal extent of coherent low and high momentum zones in the streamwise direction. As x increased, correlation values remained lower for all z separations relative to the unperturbed flow. The correlation shapes did revert towards the unperturbed shapes, although with reduced skewness, even at $x = 7\delta$ downstream of the $H = \delta$ array. These trends were consistent with the limited z-extent of low momentum regions observed in instantaneous visualizations.

Periodicities at the cylinder spacing were initially prominent also in the spanwise coordinate of the cross correlations ($\Delta x = 0$) across the logarithmic layer. As x increased, the spanwise periodicities disappeared for all Δz, while the central positive lobes recovered towards unperturbed values. On the other hand, the magnitude of the negative lobes remained lower up to $x = 7\delta$ downstream of the array, indicative of a persistent alteration of alternating low and high momentum zones throughout the logarithmic layer,

consistent with autocorrelations from planar PIV. This was also consistent with the decreased energy contained in the 0.6δ spanwise mode in spectra and dominant spanwise mode analysis. This trend suggests that the array profoundly altered the spanwise distribution of flow structures across the logarithmic layer downstream.

Wall-normal velocity cross correlations also showed periodicities along the spanwise direction associated with upwash downstream of the cylinders and downwash in regions between them as shown in averaged velocity statistics. Correlation peak magnitudes increased in the field immediately downstream of the array compared to the unperturbed flow. Then, as x increased, the values decreased below the unperturbed value at $x = 4.6\delta$ for the largest z separation. This decrease may be a consequence of the disruption of large-scale organization across the boundary layer, similar to the results of flow downstream of LEBU devices extending significantly into the boundary layer (Corke *et al.* 1981; Boiko & Kornilov; Hutchins and Choi 2002). Furthermore, this could also signify decreased wall-normal transport across the logarithmic layer, as a result of the reduced alignment of movement away and toward the wall.

The flow in the logarithmic region downstream of the $H = 0.2\delta$ ($H^+ = 500$) array revealed some significant differences in averaged statistics and flow structure recovery. The shorter cylinders also initially induced average velocity deficits immediately downstream, but the deficits decreased rapidly with downstream distance, implying subsequent mean downwash that was confirmed in measurements of wall-normal velocity. In the measurement planes below the cylinder tip height, the relative RMS velocities first rose strongly, as in the $H = \delta$ case. At $z^+ = 500$, RMS values also increased although less strongly. Unlike the $H = \delta$ case, however, the RMS values decreased more slowly with

increasing streamwise distance and remained elevated throughout the measurement domain except at $z^+ = 125$ and $x = 7\delta$ where values recovered to unperturbed levels.

Although visualizations and trends in packet counts suggested a top down approach to an equilibrium state as hypothesized by Zheng & Longmire (2014), the overall picture was not so clear, as the flow structures in the region closest to the wall remained altered beyond the measurement domain. At $z^+ = 500$, which was the cylinder tip height, flow structures and packet signatures like those in the unperturbed flow existed throughout the streamwise domain as might be expected. At $z^+ = 300$, incoming flow structures and packet signatures were disrupted initially, replaced by wakes and spanwise interactions of the wakes thereafter. Packet signatures reappeared starting near $x = 2.9\delta$. The number of packet signatures identified here remained similar to the unperturbed flow up to $x = 7\delta$.

Interestingly, perturbations to the packet signatures and flow structures at $z^+ = 125$ appeared to last longer than in the $H = \delta$ case, even though streamwise velocity statistics (e.g. mean, RMS, autocorrelations, cross-correlations) seemed to nearly recover to the unperturbed values. The number of packet signatures identified at $x = 2.9\delta$ was 27% less than in unperturbed flow through the end of the measurement domain. Instantaneous visualizations showed that the large-scale flow organization at $x = 7\delta$ continued to differ from that in the unperturbed flow, such that LMRs and HMRs were wider. Both the CMR width histograms and packet signature width distributions corroborated this observation at $z^+ = 125$, while both analyses showed width distributions resembling those in unperturbed flow at $z^+ = 300$ and 500. Therefore, the reason behind the reduced number of packet signatures at $z^+ = 125$ likely resulted from fewer 'single width packets' that the algorithm was designed to identify.

The highly three-dimensional wake structures induced by the shorter cylinder array likely had a significant effect on the downstream flow and packet evolution. Averaged volumetric results by Ortiz-Dueñas *et al.* (2011) showed streamwise rollers immediately downstream of a similar array, thought to be initiated at the cylinder tips. Coherent vortical structures (see illustration in Fig. 1-12) were likely initiated at the tips, and was supported by the increased number of swirls seen at $z^+ = 500$, in the region immediately behind the cylinders. The tip structures act to induce flow towards the wall directly behind each cylinder and away from the wall in regions in between on average. Average wall-normal velocities were significant over the range $z^+ = 200$ to 500, with the effect persisting beyond their measurement volume which extended to $x = \delta$. The wall-normal velocity cross correlations support the increase in wall-normal movement, as correlation values were elevated compared to unperturbed flow. SPIV measurements also indicate increases in wall-normal RMS velocity throughout the logarithmic region in the perturbed versus unperturbed flow which lasted up to $x = 7\delta$. The aforementioned trends all suggest increased vertical movement across the log layer, possibly leading to stronger outer-inner interactions, such that the modulation of near wall fluctuations by large-scale outer structures (Hutchins & Marusic 2007b; Mathis *et al.* 2011) were enhanced. The stronger outer-inner interactions may have had an influence on the pre-multiplied energy spectrum for streamwise velocity at $z^+ = 125$ and $x = 7\delta$, where energy was shifted from smaller to larger spanwise wavelengths compared with the unperturbed spectrum. Moreover, the shape of the spectrum resembled those in measurement planes further away from the wall.

Ultimately, the stronger influence of the outer layer structures could have impeded the relaxation behavior near the wall, consistent with the findings of Alving & Fernholz (1996) and Rodríguez-López *et al.* (2016a & 2016b) who examined a reattached boundary layer downstream of a separation and a boundary layer developing downstream of a wall-mounted sawtooth fence respectively. In these studies, strong wall-normal interactions from recirculating fluid downstream of the separation and the obstacles resulted in slow relaxation of the flow within the logarithmic layer and the near wall region. Alving & Fernholz (1996) observed sustained perturbations to wall-normal and Reynold stress profiles throughout their logarithmic layer up to 28δ downstream. On the other hand, Rodríguez-López *et al.* (2016a) noted deviations in spanwise correlation coefficients within their logarithmic layer at a streamwise location 64 times their initial perturbed boundary layer thickness, which they ascribed to be an indication for altered spanwise eddy organization.

By contrast, downstream of two rows of relatively high aspect ratio cylinders more resemblant of our H = δ array, Rodríguez-López *et al.* (2016a) observed a weaker influence from the outer layer on the near wall region resulting in faster relaxation of the averaged near-wall flow statistics towards a canonical state, consistent with the trends observed downstream of our H = δ array. Rodríguez-López *et al.* (2016a, 2016b) attributed the differences in boundary layer development between their two cases to wake-driven (sawtooth) and wall-driven (cylinders) mechanisms respectively. Although the sawtooth fence had relatively larger blockage close to the wall and measurable separation downstream, unlike the current H = 0.2δ case, the sawtooth geometry implies that it must nevertheless initiate significant average streamwise vorticity in the near-wall

region as occurs in the H = 0.2δ case. Therefore, even though the current H = 0.2δ and H = δ arrays present similar blockage and geometries beneath z^+ = 500, the enhanced outer/inner interactions initiated near the tips of the shorter cylinders are sufficient to cause long-lasting disruptions to the vortex packet organization closer to the wall. Another conclusion drawn is that the bottom-up relaxation of flow downstream of the H = δ array may be promoted by the weaker outer/inner interaction in the perturbed flow.

Chapter 5

Results & Discussion: 0.6δ spacing array, perturbing natural spanwise modes

In this chapter, results of the flow perturbed by the S = 0.6δ cylinder array are shown and compared with results from the unperturbed flow. Two array heights are considered, H = 0.2δ and H = 0.05δ. First the results for both the flow perturbed by the H = 0.2δ and H = 0.05δ arrays are presented. Then, a summary and discussion for both cases follows.

5.1 Flow perturbed by S = 0.6δ, H = 0.2δ and H = 0.05δ arrays

5.1.1 Time-averaged results

Average streamwise velocity contours from PPIV measurements for the flow downstream of the S = 0.6δ, H = 0.2δ array are shown in Figure 5-1. Similar to the S = 0.2δ case, velocity deficits were evident directly behind each cylinder on average with fast moving zones between them at both z^+ = 125(Fig. 5-1a) and 300(Fig. 5-1b). In contrast, at z^+ = 500(Fig. 5-1c), the effects of the cylinders were much weaker, with possibly weak fast moving zones occurring behind the cylinders on average. This may be attributed to the average downwash effect at the cylinder tips, shown in Figure 5-2a. Also, the averaged spanwise velocity patterns indicated converging fluid at the tips of the cylinders (Fig. 5-3c). These results are consistent with previous measurements of flow over wall mounted finite cylinders where the aforementioned average patterns at the tip suggests the existence of a pair of tip vortices (Sumner *et al.* 2004; Pattenden *et al.* 2005; Park & Lee 2002;Ortiz-Duenas *et al.* 2007; Ryan 2011;). In contrast, at z^+ = 300(Fig. 5-3b), strong average patterns in spanwise velocity were seen very close to the cylinder, but starting at

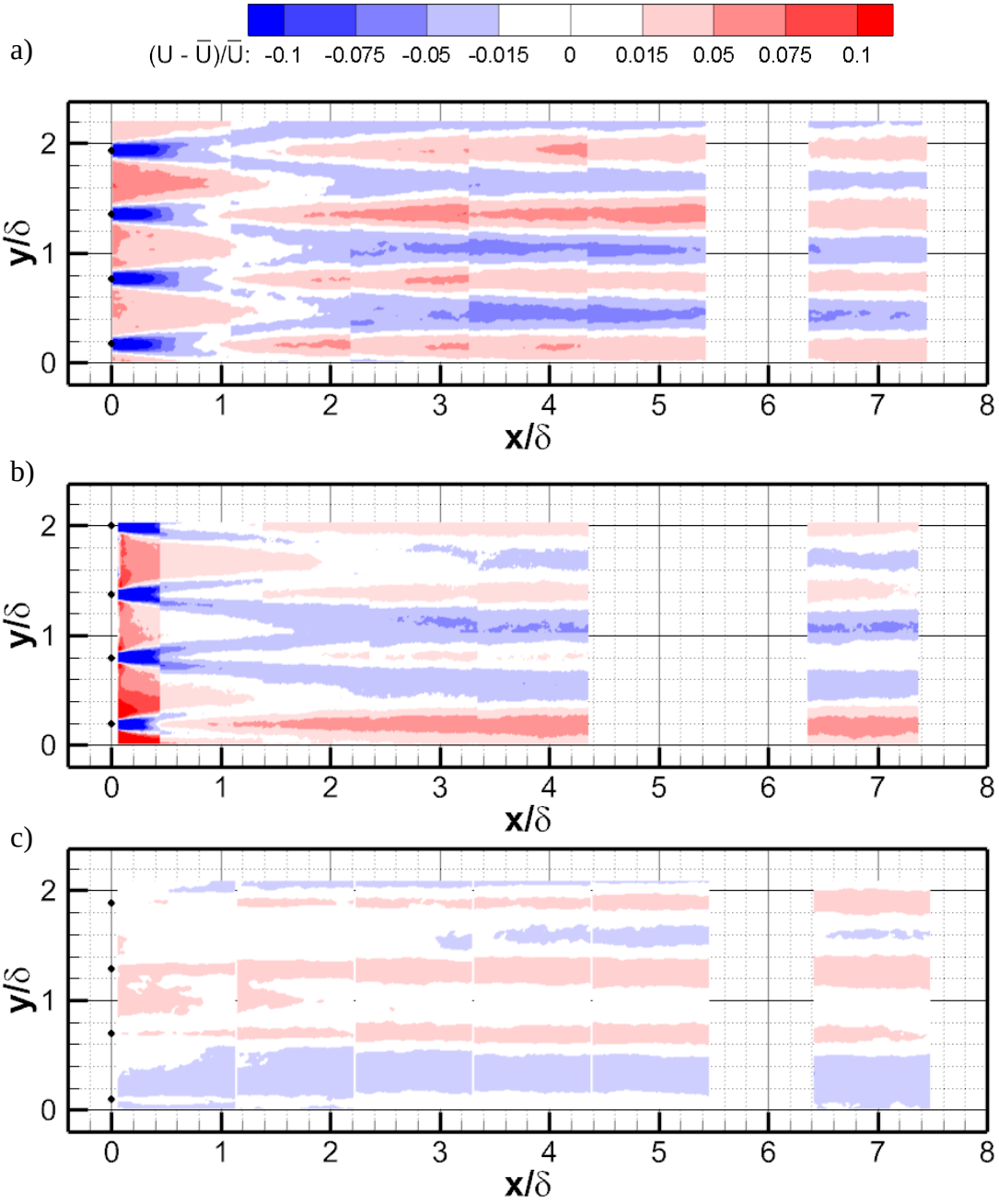

Figure 5-1: S = 0.6δ, H = 0.2δ array. Average streamwise velocity results from PPIV at measurement heights, a) z^+ = 125, b) z^+ = 300 and c) z^+ = 500. Note z^+ = 300 data reproduced from Zheng & Longmire (2014).

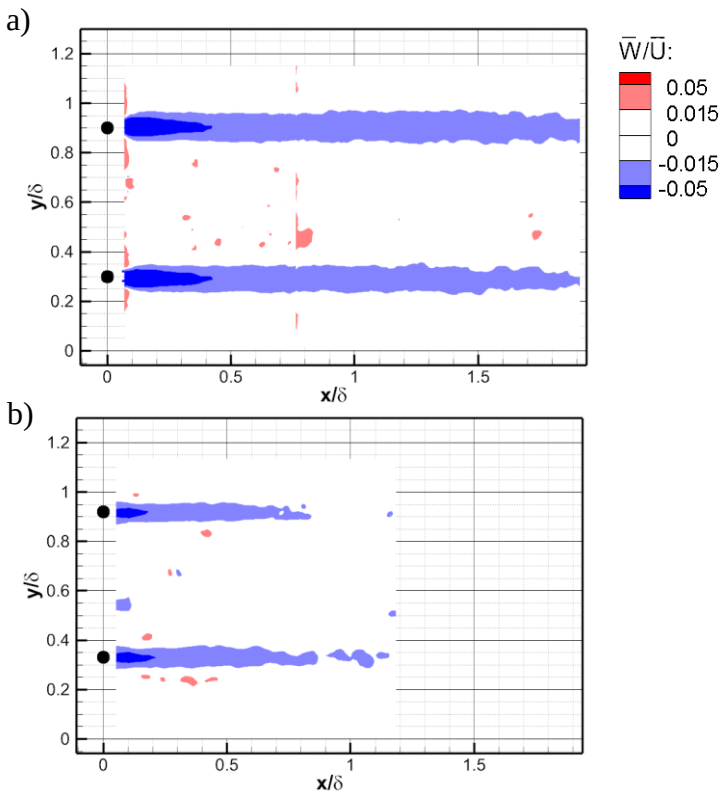

Figure 5-2: Average wall-normal velocity results from SPIV at measurement height, a) z^+ = 500, downstream of the S = 0.6δ, H = 0.2δ array and for flow downstream of b) S = 0.6δ, H = 0.05δ array at z^+ = 125.

x = 0.1δ, this pattern dissapeared. The disappearance is consistent with unsteady shedding of Karman-like vortices, resulting in the spanwise velocity trace of the vortices to average out. In the plane closest to the wall (Fig. 5-3a), fluid diverged directly behind the cylinders on average, opposite compared to the array tips. This is consistent with a base vortex structure, which has an opposite sense of rotation compared to the tip structures (Ortiz-Duenas *et al.* 2011; Sumner *et al.* 2004). Notably, the average streamwise velocity patterns were not symmetric across the span, i.e. there appears to be a systematic variation with increasing y-location. This can be related to the expansion of the laser sheet through the measurement region (discussed in Chapter 2, section 2.2).

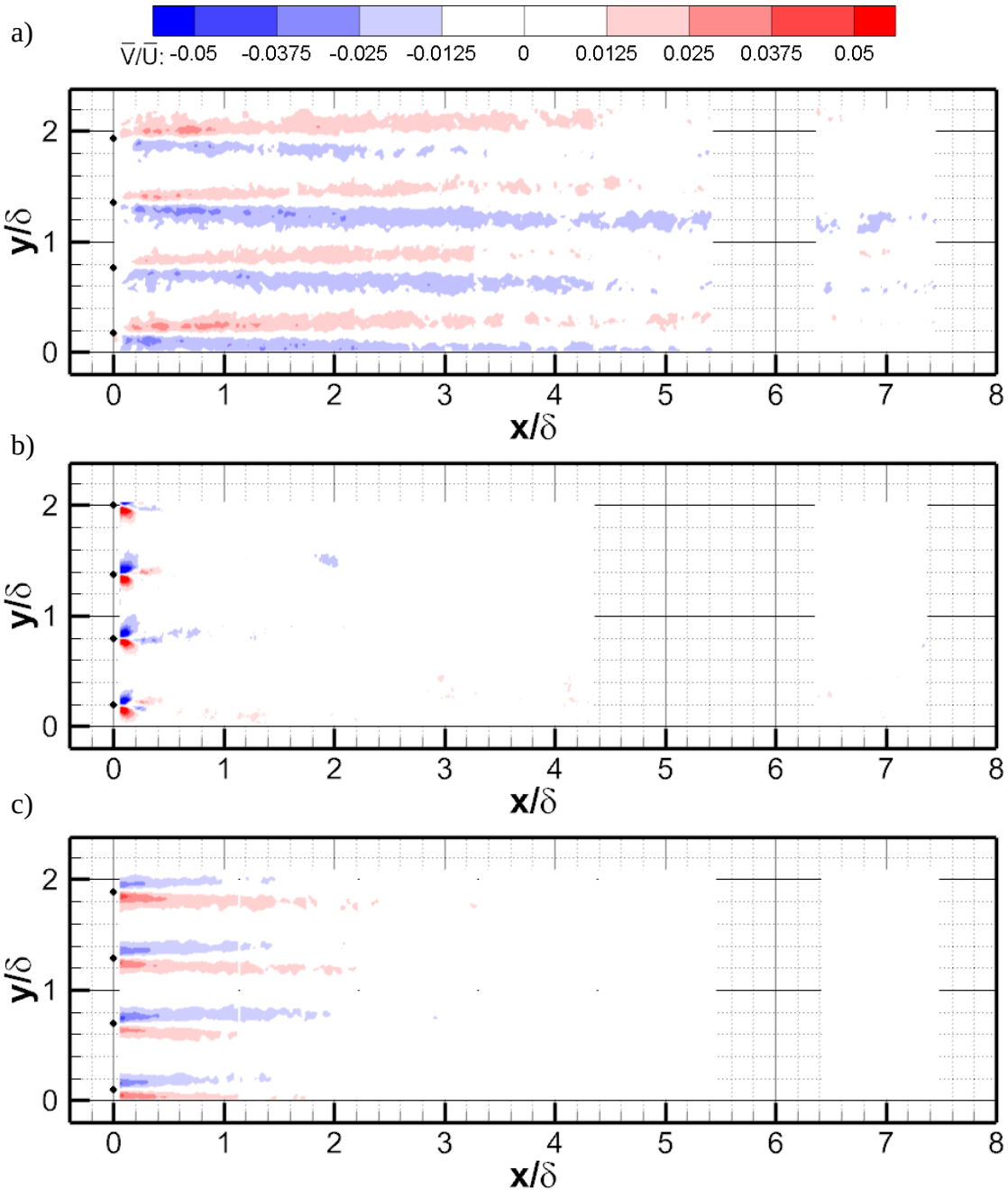

Figure 5-3: S = 0.6δ, H = 0.2δ array. Average spanwise velocity results from PPIV at measurement heights, a) z^+ = 125, b) z^+ = 300 and c) z^+ = 500.

At z^+ = 300 (Fig. 5-1b), the averaged streamwise velocities showed cylinder wakes splitting starting at x = 0.4δ, with the slow moving zones migrating to the regions between the cylinders, then merging with spanwise adjacent split wakes on average(Zheng & Longmire 2014). The pattern of alternating fast and slow moving regions persisted to x = 7δ. A similar pattern was observed at z^+ = 125 (Fig. 5-1a), but the location where the wakes start to split was further downstream at x = δ. The location where the split wakes merged on average coincided at x ~ 1.8δ for both z^+ = 125 and 300. This occurred much later compared to the S = 0.2δ, H = 0.2δ case at similar heights (see Fig. 4-1a & b) where merging occurs by x ~ 0.4δ. When the wake splits, there must be a fast moving zone directly behind the cylinders, forming as a result of the downwash initiated at the array tips (e.g Ortiz-Duenas *et al.* 2007; Zheng & Longmire 2014; Sumner *et al.* 2004). This was similar to the S = 0.2δ, H = 0.2δ array at z^+ = 300. Interestingly, the flow at the tip height, z^+ = 500 (Fig. 5-1c) was persistently altered up to x = 7δ, with fast moving zones aligning with upstream cylinder locations.

The averaged velocity fields for all velocity components immediately downstream of the H = 0.05δ (H^+ = 125) cylinder tips (Fig. 5-2b, 5-4 and 5-5) also showed patterns consistent with tip structures. The wakes split almost immediately behind the cylinder (Fig.5-4a). Again, the formation of the fast moving zones can be attributed to the downwash effect induced by the cylinder tips. Surprisingly, these effects were much more apparent at the H = 0.05δ cylinder height (Fig. 5-4a), compared to z^+ = 500 downstream of the H = 0.2δ array (Fig. 5-1c). This may be due to the increased influence of the tip structures on average, due to the smaller AR of the H = 0.05δ cylinders, where Karman like shedding was unlikely to occur. This was consistent with results from

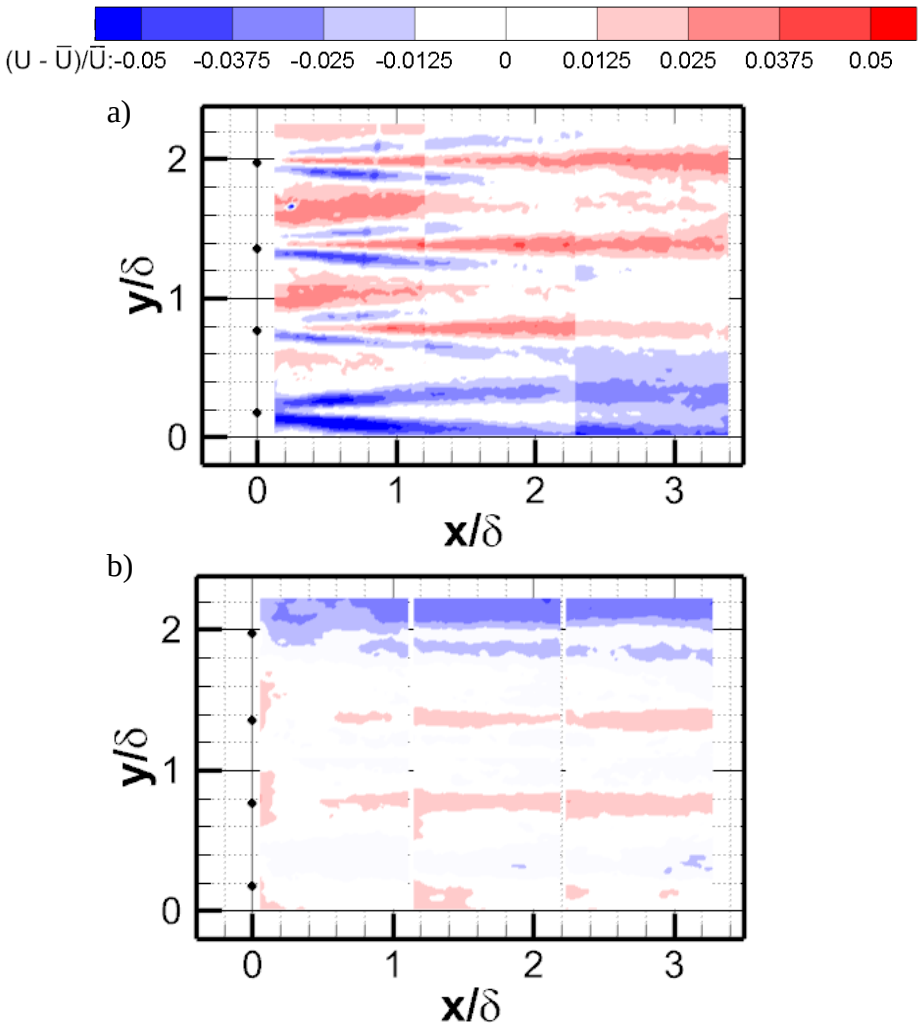

Figure 5-4: S = 0.6δ, H = 0.05δ array. Average streamwise velocity results from PPIV at measurement heights, a) z^+ = 125 and b) z^+ = 300.

Sumner *et al.* (2004), showing stronger tip vortices on average with decreasing cylinder aspect ratio. Furthermore, the cores of the time averaged streamwise vortices associated with the tip structures moved closer to the cylinder tip height from below. Additionally, the more apparent wakes at z^+ = 125 downstream of the H = 0.05δ array could possibly be due to the increased turbulence intensity of the incoming flow at z^+ = 125.

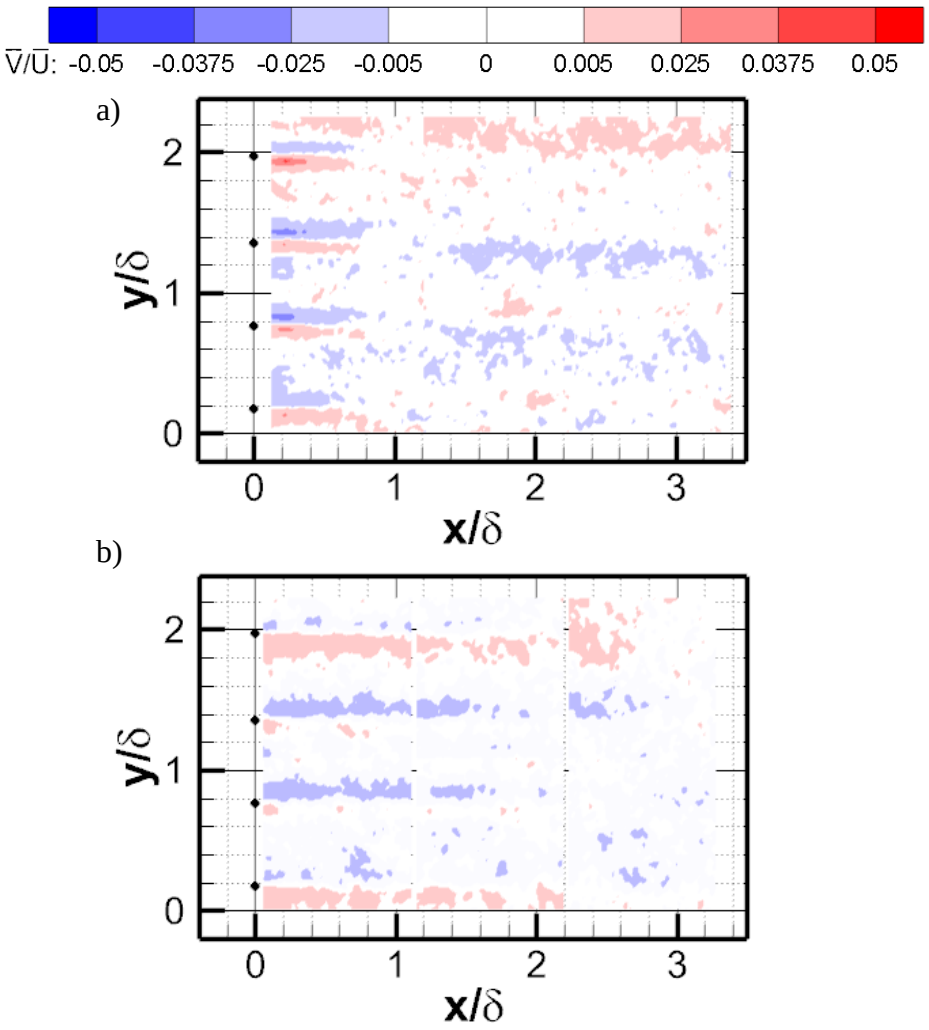

Figure 5-5: S = 0.6δ, H = 0.05δ array. Average spanwise velocity results from PPIV at measurement heights, a) z^+ = 125 and b) z^+ = 300.

Average spanwise velocity fields downstream of the H =0.05δ cylinder tips (Fig. 5-5a) were similar to those downstream of the H = 0.2δ cylinder tips. On average, fluid converged immediately behind the cylinders, and was directed towards the wall as indicated by the average wall normal velocity fields (Fig. 5-2b). The downwash was weaker and less persistent with increasing x for the H = 0.05δ case, compared to H = 0.2δ (Fig. 5-2a), which may be due to the shorter array's proximity to the wall.

Beyond the H = 0.05δ cylinder height, at z^+ = 300, some average perturbations were also observable. Signatures of average fast moving zones lining up with the cylinder locations were seen in Figure 5-4b starting at x = 0.6δ. In addition, average spanwise velocity (Fig. 5-5b) fields at z^+ = 300 indicated converging fluid on average behind the cylinders. Thus, effects of the array extended beyond its height, consistent with previous results by Tomkins (2001) of hemispheres with similar heights where the effects of additional swirling structures and reduced streamwise length scales extend to ~2H.

No effects were observed in the average velocity fields at z^+ = 500 (z/δ = 0.2), four times the height of the short array (H = 0.05δ). This was not surprising as at z^+ = 300, the effects were already weak, suggesting that this height was close to the upper limit of the array's influence. As x increased, the aforementioned effects for z^+ = 125 and 300 downstream of the H = 0.05δ array decayed. At x= 7δ (not shown), weak effects below the values of our uncertainties were observed (<0.01$\bar{U}$), where weak fast moving zones were aligned with the upstream cylinder locations, with slower moving regions between them.

Mean velocity results averaged over measurement planes centered on the plotted streamwise location are shown in Figure 5-6a for flow downstream of the H = 0.2δ array. Immediately downstream of the array, the mean streamwise velocity was reduced for both z^+ = 125 and 300 compared to the unperturbed flow, due to the blockage posed by the array (1.7% of the frontal area of the incoming BL). The reductions were 5.5% and 3% of U_∞ respectively, lower compared to S = 0.2δ, H = 0.2δ at similar heights. This was reasonable considering the blockage was larger for the S = 0.2δ, H = 0.2δ array (5%), compared to the S = 0.6δ, H = 0.2δ array (1.7%). Interestingly, no initial reduction was

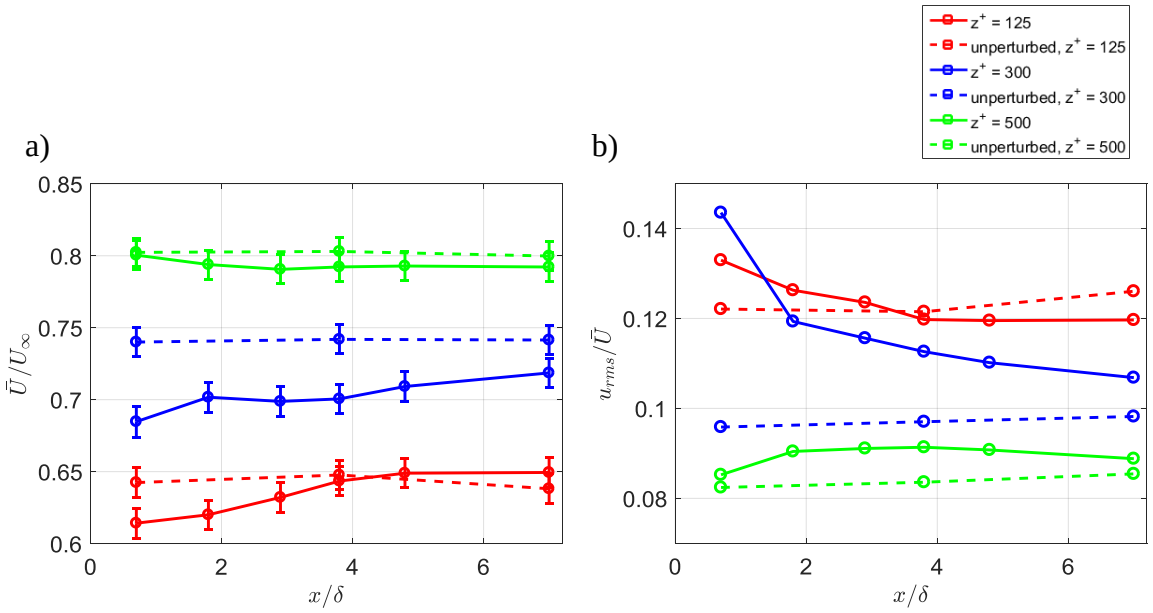

Figure 5-6: S = 0.6δ, H = 0.2δ. Variation of a) mean streamwise velocity normalized by free-stream velocity, and b) RMS of streamwise velocity normalized with local mean velocity at measurement height, with x-location.

observed at z^+ = 500. As x increased, however, the streamwise velocity at z^+ = 500 decreased relative to the unperturbed value. The reductions were small and at the limit of the uncertainty. At both z^+ = 125 and 300, the mean streamwise velocity increased toward the unperturbed values, first recovering at z^+ = 125, x = 3.8δ. Interestingly, at z^+ = 300, the average speed remained 3% below the unperturbed value, although it appeared to be increasing slowly. The mean velocities for the S = 0.6δ, H = 0.2δ array relaxed quicker towards unperturbed values compared to the S = 0.2δ, H = 0.2δ case. This makes sense as the strength of the perturbation (i.e. blockage) was greater in the S = 0.2δ case.

The RMS velocity (Fig. 5-6b) increased for all measurement heights immediately downstream of the array. The largest increase occurred at z^+ = 300 (0.05$\bar{U}$), followed by z^+ = 125 (0.01$\bar{U}$) and z^+ = 500 (0.003$\bar{U}$). The RMS values at both z^+ = 125 and 300

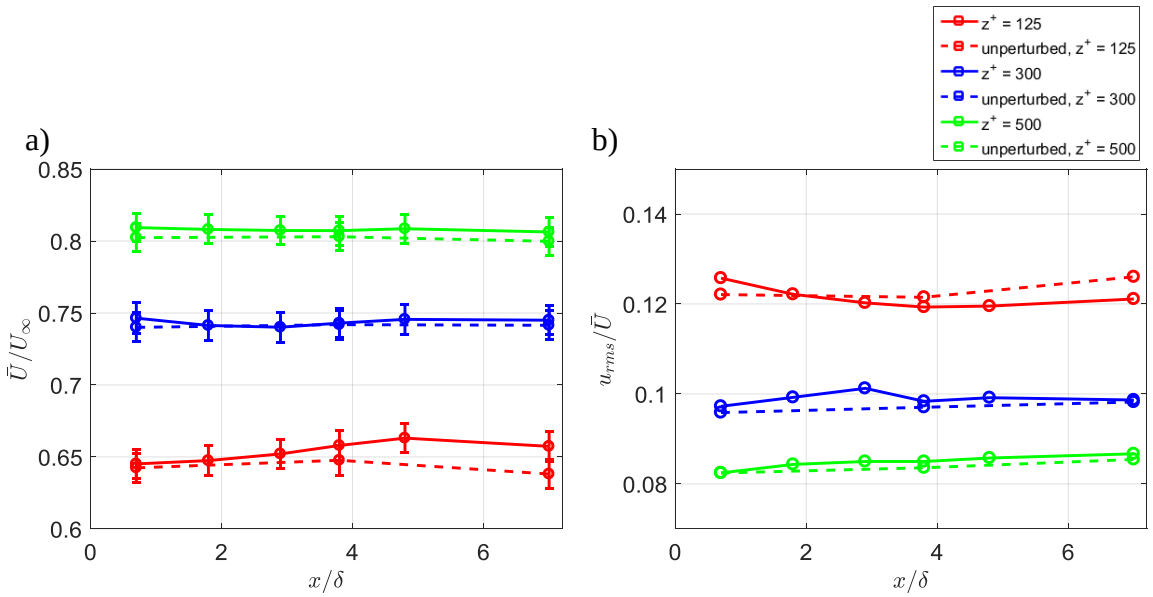

Figure 5-7: S = 0.6δ, H = 0.05δ. Variation of a) mean streamwise velocity normalized by free-stream velocity, and b) RMS of streamwise velocity normalized with local mean velocity at measurement height, with x-location.

decayed monotonically as x increased. The value at z^+ = 125 dipped below the unperturbed value starting at x = 3.8δ, and remained lower at x = 7δ by 0.005$\bar{U}$ relative to the unperturbed flow. In comparison, although the RMS value decreased at z^+ = 300 with increasing x, it still remained larger at x = 7δ relative to the unperturbed value by 0.01$\bar{U}$. Conversely, at z^+ = 500, the RMS value increased to a maximum that was sustained from x = 1.8δ to x = 3.8δ before decreasing towards the unperturbed value.

Mean and RMS velocity plots (Figure 5-7) for the flow downstream of the H = 0.05δ array show minimal changes relative to the unperturbed values, especially at z^+ = 300 and 500. No mean velocity deficits were observed even at z^+ = 125, where wakes were evident (Fig. 5-7a). At z^+ = 125, streamwise velocity increased starting at x = 4.8δ and remained slightly larger than the unperturbed value by 0.02$\bar{U}$ at x = 7δ. This may be related to the downwash at the tips of the cylinders, drawing fast moving fluid towards

the wall, although at x = 4.8δ, no discernible wall-normal movement larger than uncertainty was observed.

The RMS velocity plots (Figure 5-7b) on the other hand show slightly larger streamwise RMS values immediately downstream of the array for both z^+ = 125 and 300, although this effect may be within uncertainty. Notably, with increasing x, the RMS values at z^+ = 300 increased continuously to a maximum at x = 2.9δ. This may be the effect of the perturbation propagating upwards which was previously reported by Jacobi & McKeon (2011) and Tan (2014), although notably, the rate of upward propagation of the perturbation peak in RMS was slower compared to the previous studies. Conversely, the RMS values at z^+ = 125 decreased below the unperturbed levels, and remained so till x = 7δ. No perturbation effects were observed at z^+ = 500.

5.1.2 Instantaneous PPIV Results

Wake structures were apparent at both z^+ = 125 and 300 immediately downstream of the S = 0.6δ, H = 0.2δ array. At z^+ = 125 (Fig. 5-8a), wakes were observed at y/δ = 0.15, 0.75, 1.35 and 1.95. Frequently, the wakes looked wavy as at y/δ = 0.75, which can be due to Karman-like vortex shedding. Signatures of the Karman-like vortex shedding were apparent in the instantaneous spanwise velocity fields shown in Figure 5-9a. Alternating positive and negative regions of spanwise velocity were seen immediately downstream of the cylinders. Similarly, for z^+ = 300 (Fig. 5-8b), wakes were observed directly behind every cylinder. Notably, for both z^+ = 125 and 300, fast moving zones frequently occurred in the region between the cylinders. Occasionally, LMRs possibly associated with upstream packets were seen in the region between the cylinders as well, for example at y/δ = 1.2 at z^+ = 300 (Fig. 5-8b). Spanwise velocity patterns indicative of Karman-like

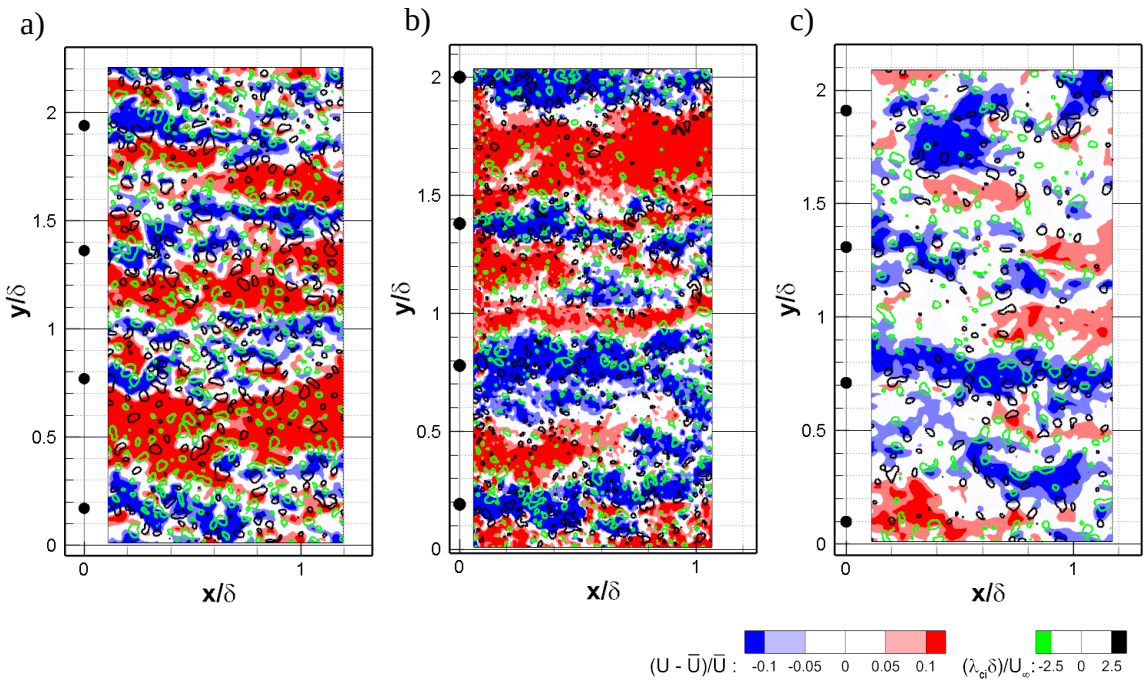

Figure 5-8: S = 0.6δ, H = 0.2δ. Instantaneous streamwise velocity fields from PPIV centered at x ~ 0.6δ at a) z^+ = 125, b) z^+ = 300 and c) z^+ = 500.

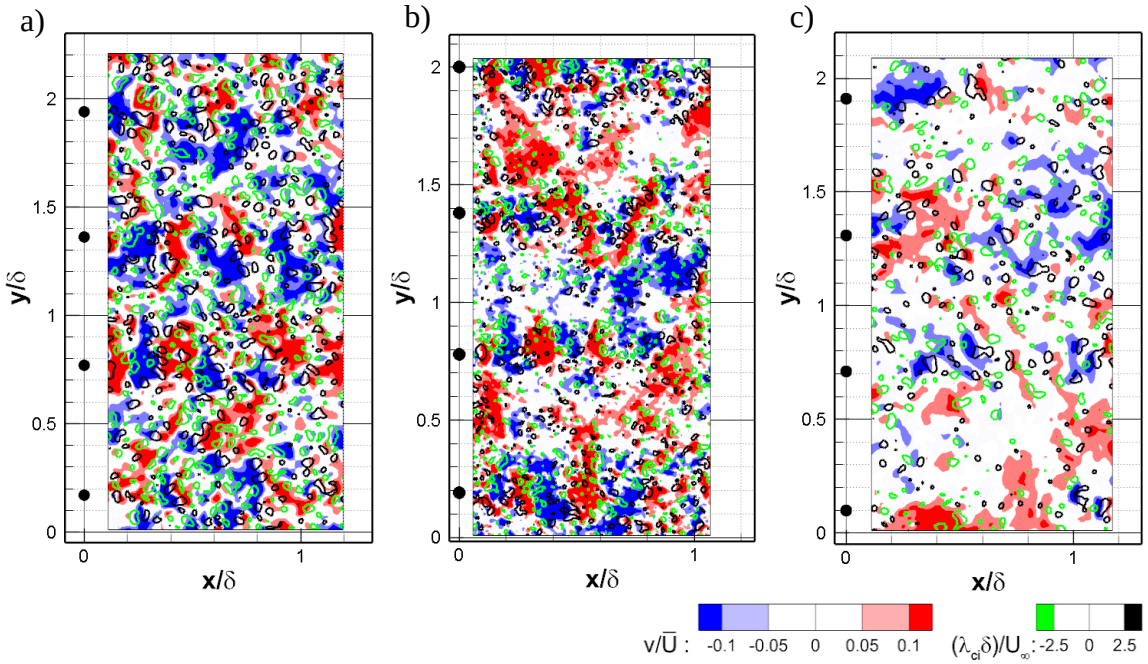

Figure 5-9: S = 0.6δ, H = 0.2δ. Instantaneous spanwise velocity fields from PPIV centered at x ~ 0.6δ at a) z^+ = 125, b) z^+ = 300 and c) z^+ = 500.

vortex shedding were present as well (Fig. 5-9b), similar to $z^+ = 125$. Different from the S = 0.2δ array, the wakes behind the S = 0.6δ array rarely interacted with spanwise adjacent wakes in the first data field, as the cylinders were spaced further apart.

Directly downstream of the array tips, wakes occurred much less frequently. More often, fast moving zones were observed immediately downstream of the cylinders (e.g y/δ = 0.1, Fig. 5-8c). If wakes were observed, they typically did not persist downstream, as in $y/\delta = 1.3$. In light of this, the long slow region seen at $y/\delta = 0.85$ was very likely an upstream packet, as its location was not aligned with the cylinder location. Instantaneous fields showing spanwise velocity (Fig. 5-9c) did not exhibit strong variations, in contrast to the flow at $z^+ = 125$ and 300. Sometimes, at the cylinder tips, patterns consistent with a tip vortex structure were seen, as at $y/\delta = 1.3$ (Fig. 5-9c). These variations were not likely to be strong as the axis of the tip vortices were predominantly aligned with the streamwise direction.

At $z^+ = 125$, wake structures were observed immediately downstream of the H = 0.05δ array, although more frequently, fast moving zones were seen (e.g. Figure 5-10a, y/δ = 0.2, 1.35 and 2). Any observed wakes typically did not persist downstream (e.g. Figure 5-10b, $y/\delta = 0.8$ and 1.35). Instantaneous spanwise velocity fields (e.g. Figure 5-10c) indicate increased spanwise velocity fluctuations immediately downstream of the array. In some instances, spanwise velocity signatures consistent with tip structures were observed immediately downstream of the cylinders (e.g. Figure 5-10c, y/δ = 0.2, 0.8, 1.35 and 2), supporting their existence. At $z^+ = 300$, beyond the array height, any perturbation effects were hard to decipher from instantaneous streamwise velocity fields. The flow features appeared similar to those in the unperturbed flow. On the other hand,

visualizations of instantaneous spanwise velocity fields (Figs 5-11a &b) showed increased activity, with increased numbers of larger positive and negative coherent regions relative to the unperturbed flow (e.g. Figure 5-11c). This may be a subtle manifestation of the effects from the cylinders below on the flow at $z^+ = 300$, possibly driven by the downwash effect at the array tips.

5.1.3 Instantaneous FPIV Results

FPIV visualizations were useful because the instantaneous flow fields downstream of a given array were highly dependent on the incoming flow structures (Zheng & Longmire 2014). We characterized the in-flow conditions based on the categories proposed by Zheng and Longmire (2014) for the flow downstream of the $S = 0.6\delta$ and $H = 0.2\delta$ array. In the first scenario, no distinct CMRs were observed in the incoming flow. In such a case, typically individual cylinder wakes merged and pair into new LMRs at spanwise locations midway between the cylinders. In the second scenario, CMRs moved downstream through the region between the cylinders. The third scenario consists of direct impingement of the incoming CMRs on the cylinders.

Tables 5-1 and 5-2 show the probabilities of occurrence of the aforementioned scenarios grouped by low/high momentum regions at all measurement heights for the $S = 0.6\delta$, $H = 0.2\delta$ array. Three cells were defined as in Figure 5-12 for the aforementioned analysis, where 20 runs were evaluated and characterized, giving a total of 60 samples for every case considered. Incoming LMRs and HMRs were characterized as scenario III (direct impingement) when part of it contacts the cylinder. Given the sparseness of the cylinders, we expect that scenario II (mid-region) occurred more frequently. On the other hand, as the dominant spacing between flow structures in the unperturbed flow was 0.6δ, it seems

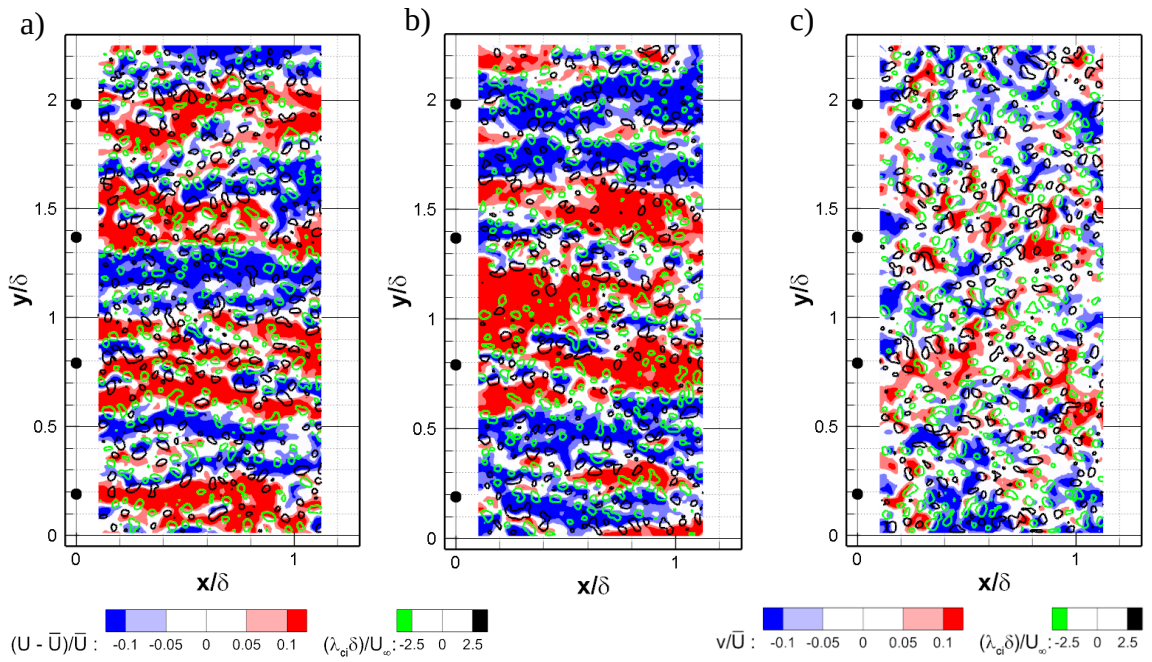

Figure 5-10: S = 0.6δ, H = 0.05δ, z^+ = 125. Instantaneous streamwise (a, b) and c) spanwise velocity fields from PPIV measurements.

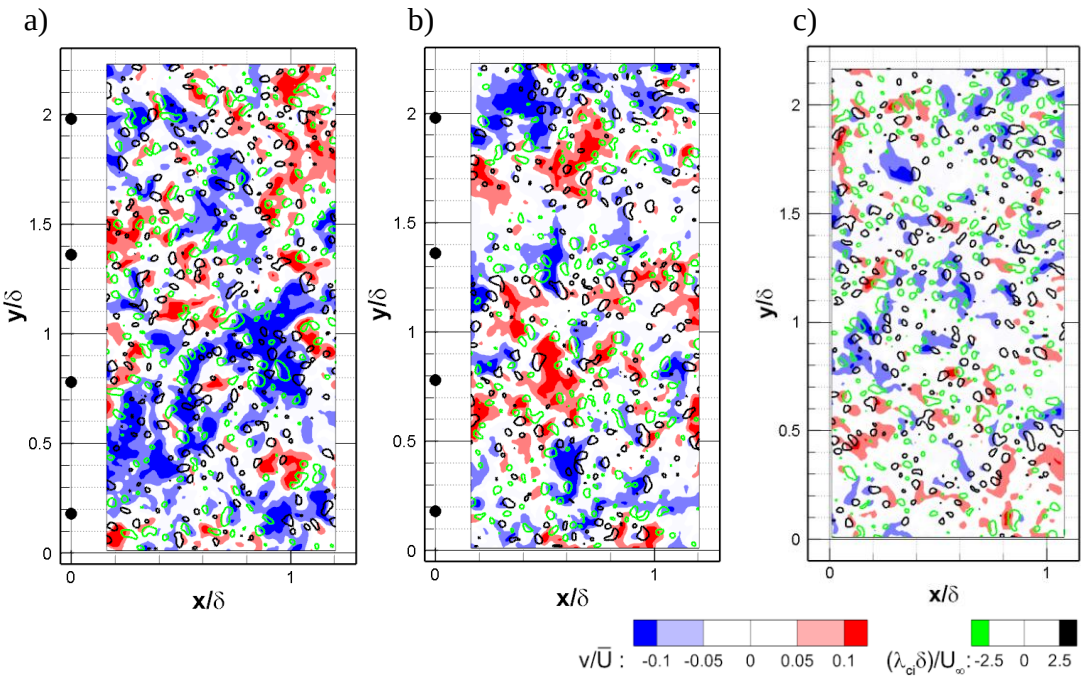

Figure 5-11: S = 0.6δ, H = 0.05δ, z^+ = 300. Instantaneous spanwise velocity fields from perturbed flow (a,b). Sample of instantaneous spanwise velocity field for c) unperturbed flow at z^+ = 300 for comparison.

Table 5-1: S = 0.6δ, H = 0.2δ array. Occurrence probabilities of different scenarios for low momentum regions, extracted from visualizations of FPIV measurements.

LMR	Scenario I	Scenario II	Scenario III	Scenario II & III
$z^+ = 125$	3.2%	20.7%	36.5%	39.7%
$z^+ = 300$	17.5%	46.0%	28.6%	7.9%
$z^+ = 500$	15.9%	41.3%	31.8%	11.1%

Table 5-2: S = 0.6δ, H = 0.2δ array. Occurrence probabilities of different scenarios for high momentum regions, extracted from visualizations of FPIV measurements.

HMR	Scenario I	Scenario II	Scenario III	Scenario II & III
$z^+ = 125$	4.8%	50.8%	38.1%	6.4%
$z^+ = 300$	9.5%	54.0%	31.8%	4.8%
$z^+ = 500$	14.3%	38.1%	33.3%	14.3%

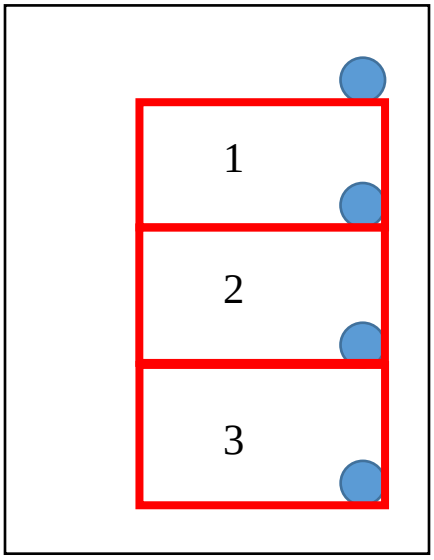

Figure 5-12: Cell definition evaluation of occurrence probabilities (Tables 5-1&2) for the S = 0.6δ, H = 0.2δ array. Diagram not to scale.

likely that whenever either a LMR/HMR impinged on a cylinder in one cell, the same scenario would likely occur for the remaining cells as well. Finally, the outcomes would vary with z^+ as well since smaller scales were more prominent at $z^+ = 125$ in the unperturbed flow versus $z^+ = 300$ and 500 (see Fig. 3-25 in Chapter 3). Therefore, the increased likelihood of CMRs being spaced closer together will result in a higher chance for both scenario II and III occurring at $z^+ = 125$.

Both tables showed that for all measurement heights, except for LMRs at $z^+ = 125$, scenario II was more likely to occur relative to scenario III. This seems consistent considering the available cross section for scenario II to occur was larger by ten times relative to scenario III. Notably, if partial contact was not considered as direct impingement (scenario III), the differences in the probabilities between scenario II and III would be greater. At $z^+ = 125$, the opposite occurred where incoming LMRs were more likely to contact the cylinders rather than pass between them. This was largely due to the LMRs being narrower to begin with at $z^+ = 125$, therefore, allowing more of them to exist given the same available cross section, in addition, they could be spaced much closer to one another. This explanation was consistent with the larger probabilities of scenario III and both scenario II and III versus scenario II only. On the other hand, HMRs at $z^+ = 125$ in the unperturbed flow tended to be wider relative to the LMRs (see Fig. 3-16b), consistent with the reduced probability of both scenario II and III occurring. Moreover, since LMRs at $z^+ = 125$ were more likely to encounter the cylinders, HMRs must then be found more frequently between the cylinders, as reflected in Table 5-2.

FPIV runs downstream of the $S = 0.6\delta$, $H = 0.2\delta$ array highlight the response and evolution of incoming flow structures downstream of the perturbations. In comparison to

the S = 0.2δ array, incoming flow structures were less disrupted. Instead, the S = 0.6δ array frequently enhanced LMRs passing between the cylinders at both z^+ = 125 and 300 (Scenario II). In addition, meandering behavior for LMRs in scenario II was reduced. Enhancement includes increased coherence, stronger magnitudes of high or low velocities within the affected LMR or HMR, or increased alignment with respect to the streamwise direction. In most cases, one or more of the aforementioned features were observed. These effects were weaker at the array tip height (z^+ = 500). For Scenario III, the dominant effect was not obvious and depended substantially on flow conditions surrounding the LMRs. Possible outcomes include LMRs being enhanced while gradually migrating to the mid-span location as x increased. While in other instances, LMRs were weakened (i.e less coherent/increased meandering/break-up) as x increased while also migrating to the mid-span. The aforementioned outcomes could relate to the z-extension of the LMRs beyond the array height, such that LMRs that do extend substantially above were able to sustain themselves downstream of the cylinders (through downward communication) while LMRs that do not may be prone to being weakened.

Figure 5-13 shows two representative runs at z^+ = 125 for the flow perturbed by the H = 0.2δ array. For Figure 5-13a, three LMRs at y/δ = 0.4, 0.9 and 1.5 moved through the region between the cylinders (Scenario II). The LMRs were enhanced, and meandered minimally with increasing x persisting to x = 7δ. On the other hand, incoming LMRs (y/δ

= 0.2, 0.8, 1.4, and 2) impinged almost directly on every cylinder in Figure 5-13b. The LMR at $y/\delta = 0.8$ and 1.4 both got weaker, with the $y/\delta = 0.8$ LMR moving towards the mid span location. By $x = 7\delta$, both LMR signatures appeared weaker compared to upstream of the array. In contrast, the LMR at $y/\delta = 0.2$ was enhanced immediately downstream of the array. With increasing x, the LMR migrated gradually towards the mid span location. The migration effect can be explained by the formation of the fast moving zones due to the downwash at the cylinder tips (Zheng & Longmire 2014). Any net downwash would act to displace the existing fluid or structure, either downwards or to the side. This example seemed to indicate that downwash effects do extend to $z^+ = 125$, in contrast to average measurements.

In comparison, HMRs impinging directly on the cylinders at $z^+ = 125$ (Scenario III) were clearly enhanced, also likely owing to the tip downwash effect. Examples are shown in Figure 5-13a for the incoming HMRs at $y/\delta = 0.6$, 1.2 and 1.8. Immediately behind the array, wakes were observed as in $y/\delta = 0.2$, 0.8 and 2, however as x increased, the wakes were quickly washed out or displaced while a strong HMR persists usually to $x = 7\delta$. In some cases, the velocity magnitudes within become increasingly stronger and the HMRs became more coherent with increasing x (e.g Figure 5-13a, $y/\delta = 1.2$). On the contrary, the dominant effect for scenario II HMRs was unclear. In some cases, they may be enhanced, such as the example given in Figure 5-13b, $y/\delta = 0.4$, and would migrate towards the region aligned with upstream cylinder locations as x increased. Other cases show weaker HMRs with increasing x, such as the example at $y/\delta = 1.2$ (Fig. 5-13b). In this specific case, the spanwise adjacent LMR at $y/\delta = 0.9$ migrated to the mid span,

which may have contributed to the weakening of the LMR while also obscuring the HMR.

The perturbation effects on LMRs for scenario III were clearer at $z^+ = 300$ than at $z^+ = 125$. LMRs contacting the cylinder were enhanced and migrated to the mid span location (Zheng & Longmire 2014). Figure 5-14a shows incoming LMRs roughly aligned with cylinder locations. The LMR at $y/\delta = 1.4$ was enhanced, and directed to the mid span, where a clear packet signature was later observed at $x = 5\delta$ and $x = 7\delta$. On the other hand, no obvious LMR was observed at $y/\delta = 2$ for $x < 0$, but later downstream, an LMR seemed to form starting at $x = \delta$ which then appeared to migrate towards the mid span and persisted to $x = 7\delta$, at $y/\delta = 1.4$. Finally, LMRs on the bottom half of the field ($y/\delta = 0.2$ and 0.5) were both disrupted initially, but later reformed beginning $x = 5\delta$, and seemed to be in the process of merging. This suggests that although LMRs may be initially disrupted, they can later re-develop. Figure 5-14b shows another example where HMRs are enhanced when impinging directly on the cylinder ($y/\delta = 1.4$), while LMRs that pass between the cylinders are enhanced ($y/\delta = 1$). Interestingly, the LMR at $y/\delta = 0.4$ seemed to be increasingly aligned with the streamwise direction as x increased.

At the tip height ($z^+ = 500$, Fig. 5-15), the array's effects were weaker. LMRs impinging directly on the cylinders (scenario III) were more likely to be weakened, while those in regions between the cylinders (scenario II) were enhanced. In contrast, HMRs for scenario II were weakened more frequently than at $z^+ = 125$ and 300, while HMRs for scenario III were enhanced. Figure 5-15 a and b show representative examples of these effects. For example, the HMR at $y/\delta = 0.8$ was strongly enhanced downstream, while being weakened when passing through the region between the cylinders in Figure 5-15b

at $y/\delta = 0.4$ and 0.9. Incoming LMRs for scenario II were enhanced, as in seen in Figure 5-15a, $y/\delta = 0.4$ and 1.2 while possibly weaker when coming into direct contact with the cylinder, such as $y/\delta = 0.7$ in Figure 5-15b.

The effects of the $H = 0.05\delta$ array on incoming CMRs at $z^+ = 125$, the shorter array tip height were similar to the effects observed at the $H = 0.2\delta$ array tips, $z^+ = 500$. A key difference here was that the incoming CMRs were narrower than in planes above. Generally, incoming LMRs for scenario II were also enhanced, while HMRs become weaker. The effects for scenario III can vary for the LMRs, such that the more dominant effect was stronger LMRs downstream of the cylinder, although in several instances, LMRs did become weaker. On the other hand, HMRs for scenario III were usually enhanced. Figure 5-16 shows two representative runs for the flow perturbed by the $H = 0.05\delta$ array. In the first example (Figure 5-16a), incoming HMRs at $y/\delta = 0.2$ and 1.4 become stronger downstream of the array. LMRs passing through the region between the cylinders ($y/\delta = 0.4$ and 1.2) were enhanced and persisted to $x = 7\delta$. The LMR at $y/\delta = 1.2$ was seen migrating to the mid span with increasing x. Conversely, LMRs impinging directly on the cylinders (Figure 5-16b) were shown at $y/\delta = 0.2$, 0.8, 1.4 and 2. The LMRs were generally weakened immediately downstream of the cylinders, except for $y/\delta = 0.2$, while it was unclear whether the LMR at y/δ shifted spanwise or merged with the LMR adjacent to it. As x increased, the LMRs at $y/\delta = 1.4$ and 2 shifted substantially in the spanwise while merging. LMRs at $y/\delta = 0.2$ and 0.8 appeared stronger with increasing x, and migrated towards one another. Both LMRs persisted till $x = 7\delta$. On the contrary, incoming HMRs through the region between the cylinders were weakened initially ($y/\delta = 0.4$, 1.0, 1.4 and 1.8). Typically their signatures at $x = 7\delta$ were much weaker relative to

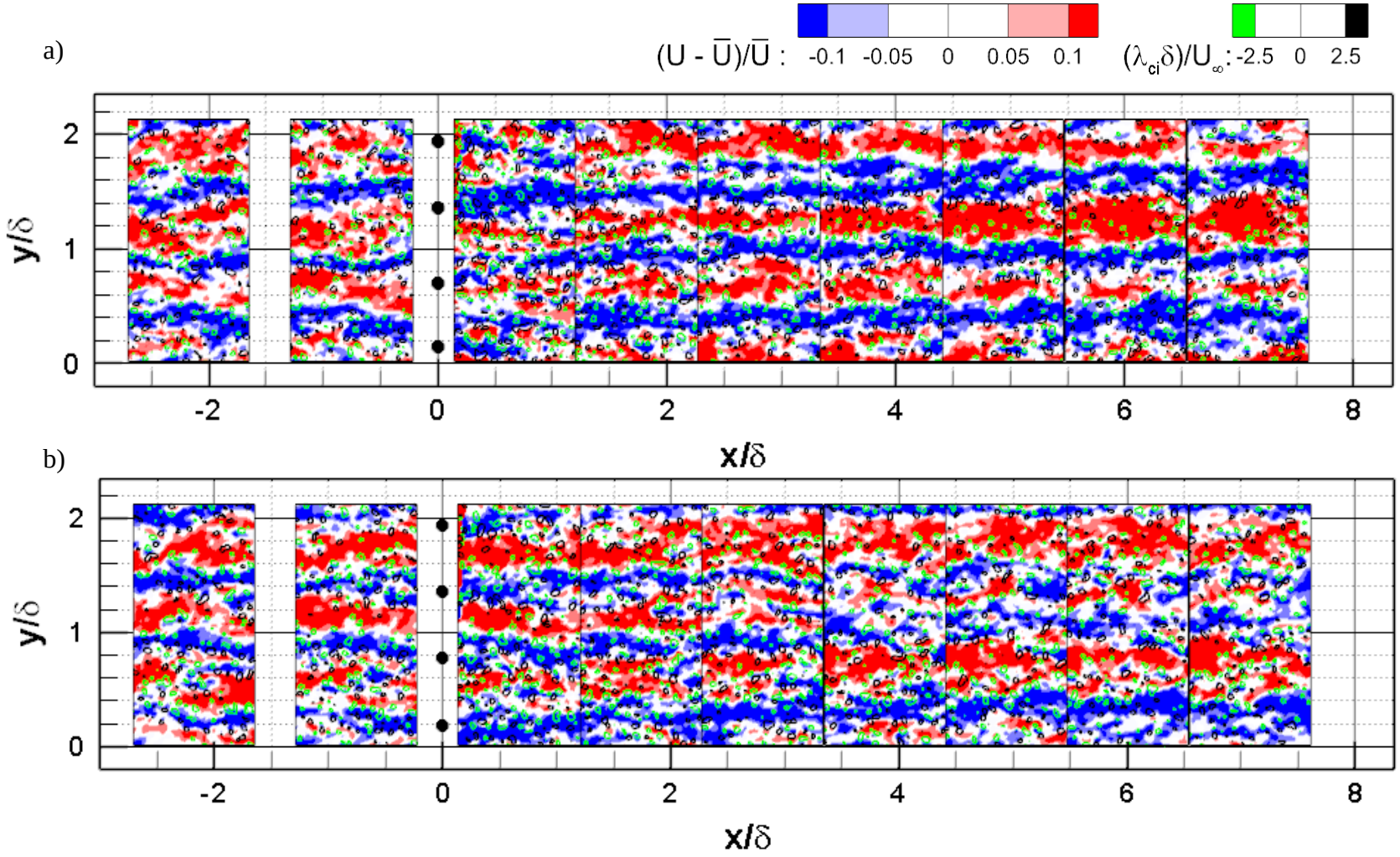

Figure 5-13: S = 0.6δ, H = 0.2δ. Two examples of FPIV runs at z^+ = 125. Cylinders in array (diameter not to scale) located at x = 0.

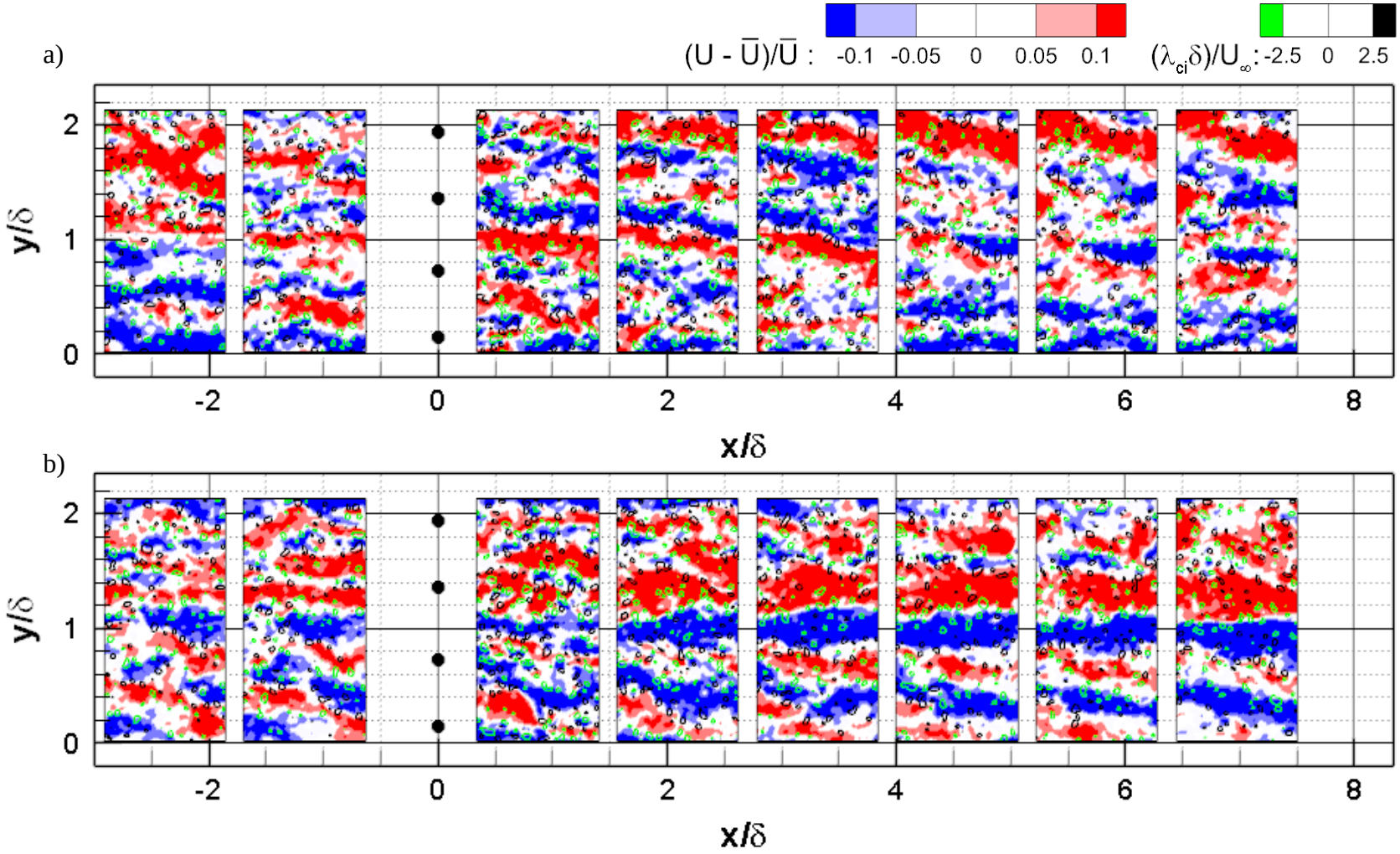

Figure 5-14: S = 0.6δ, H = 0.2δ. Two examples of FPIV runs at z^+ = 300. Cylinder array (diameter not to scale) located at x = 0.

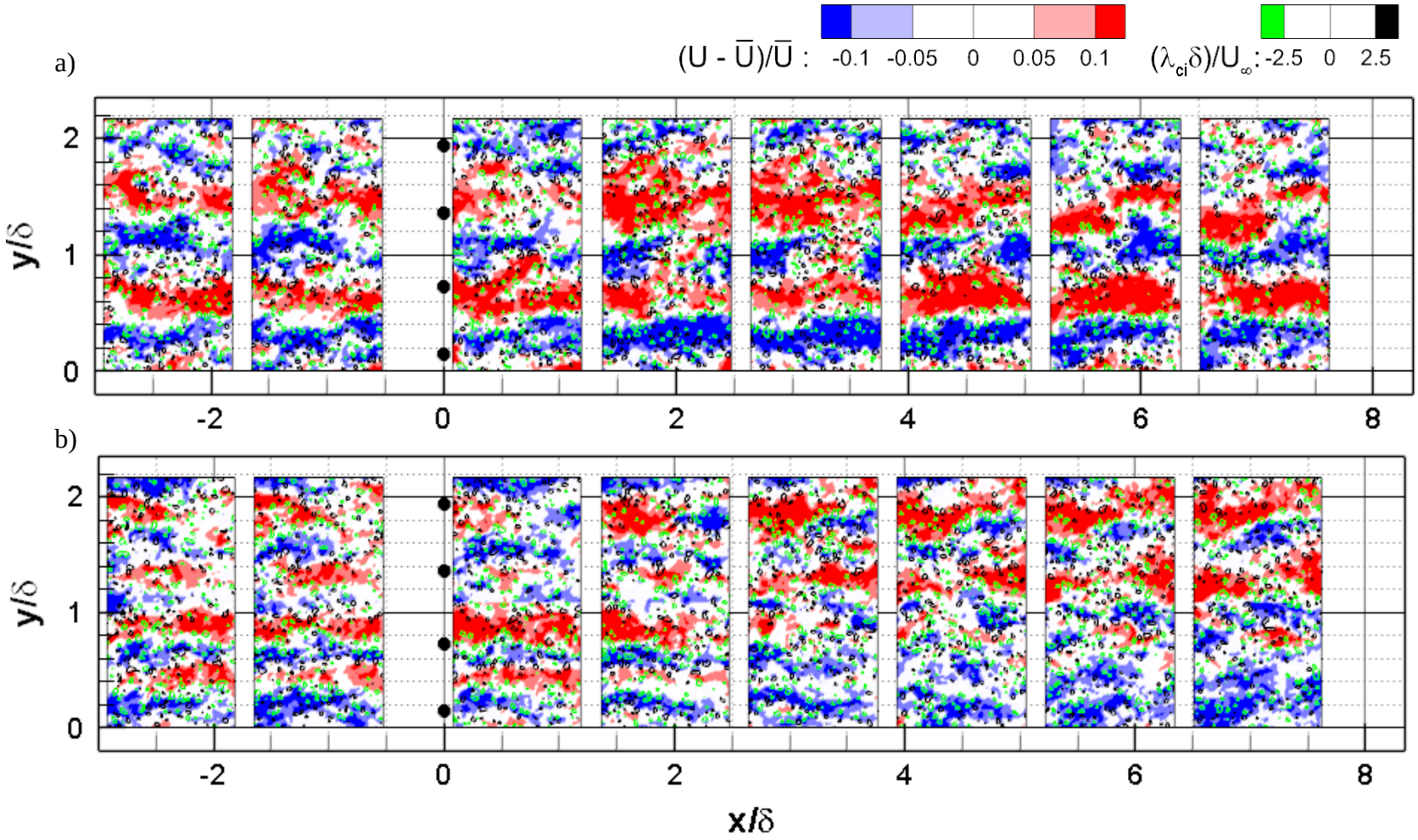

Figure 5-15: S = 0.6δ, H = 0.2δ. Two examples of FPIV runs at z^+ = 500. Cylinder array (diameter not to scale) located at x = 0.

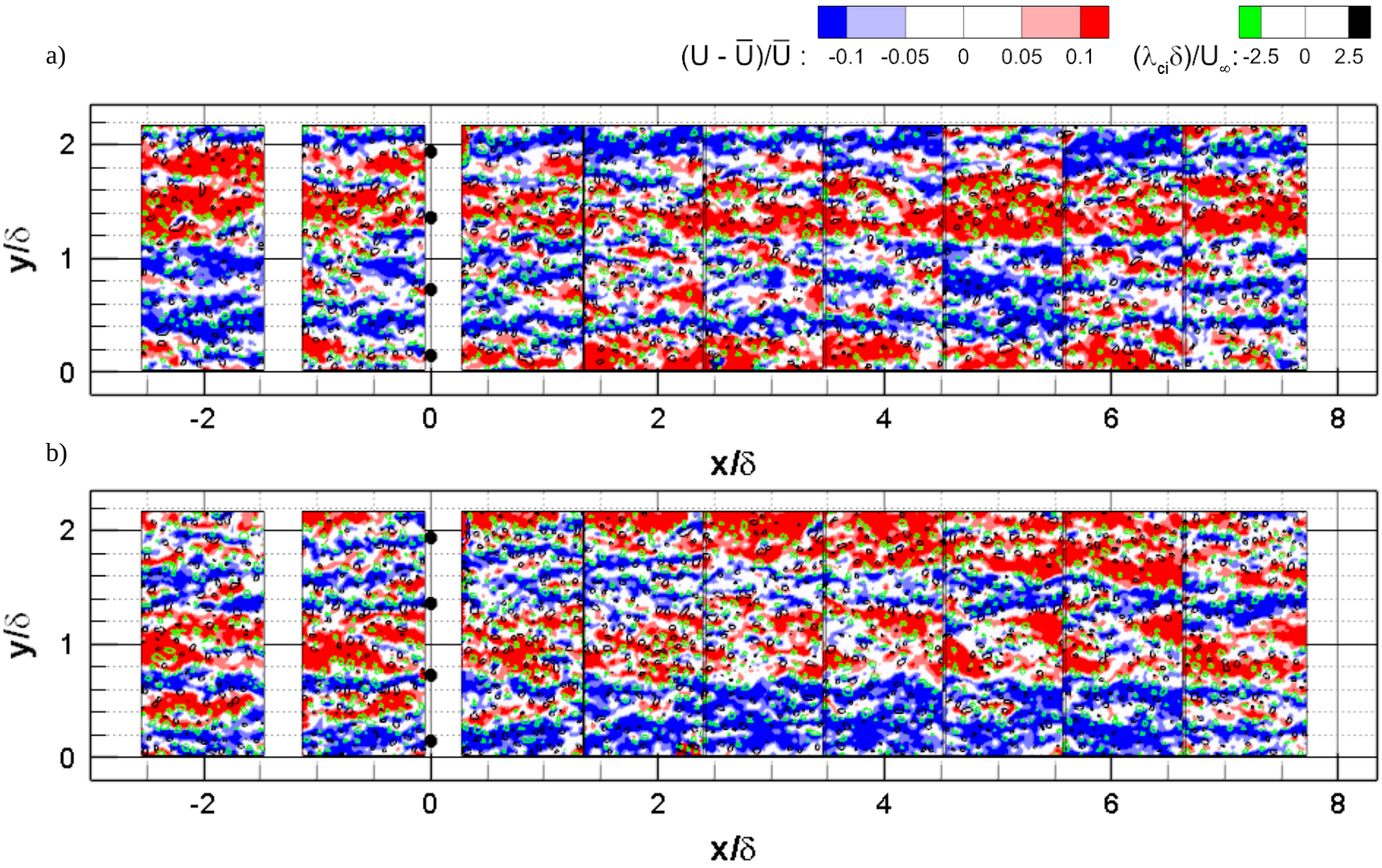

Figure 5-16: S = 0.6δ, H = 0.05δ. Two examples of FPIV runs at z^+ = 125. Cylinder array (diameter not to scale) located at x = 0.

upstream locations (e.g. HMR at $y/\delta = 0.4$), but in certain cases, their strength may be comparable (e.g. HMR at $y/\delta = 1.0$). The enhancement of HMRs and the weakening and shifting of LMRs to the mid span directly behind the cylinders can also be attributed to the downwash at the tips. In comparison, the $H = 0.05\delta$ array did not affect incoming CMRs at $z^+ = 300$, beyond the array height. Examination of many runs show that flow structures simply propagate downstream as they would in the unperturbed flow.

5.1.4 Regions of uniform streamwise momentum

The differences in length and width distributions of extracted CMRs between the flow perturbed by the $H = 0.2\delta$ array and the unperturbed flow throughout the logarithmic layer are shown in Figures 5-17, 18 & 19. Plots show fewer long LMRs (bin, $L_{ex} = \delta$) in the field immediately downstream of the array for all measurement heights, relative to the unperturbed flow. In comparison, more long HMRs were present in the perturbed flow for $z^+ = 125$ (Fig. 5-17a) and 300 (Fig. 5-18a). The largest difference occurred at $z^+ = 300$, with 21% fewer LMRs and 48% greater HMRs. In contrast, the reductions for long LMRs at both $z^+ = 125$ and $z^+ = 500$ (Fig. 5-19a) were 10%, which was only slightly greater than the estimated uncertainties. In contrast, the HMR increase at $z^+ = 125$ was smaller, at 5% greater than the values in unperturbed flow, while no increase was seen at $z^+ = 500$ (Fig. 5-19a). The reduction in long LMRs was consistent with frequent observations of the disruption of LMRs upon directly impinging on cylinders (see Figure 5-13a) and from interactions with the wakes from the cylinders. On the other hand, the increase in long HMRs may stem from the occasional enhancement of HMRs passing through the region between the cylinders, as seen in the FPIV run at $z^+ = 125$ (Figure 5-

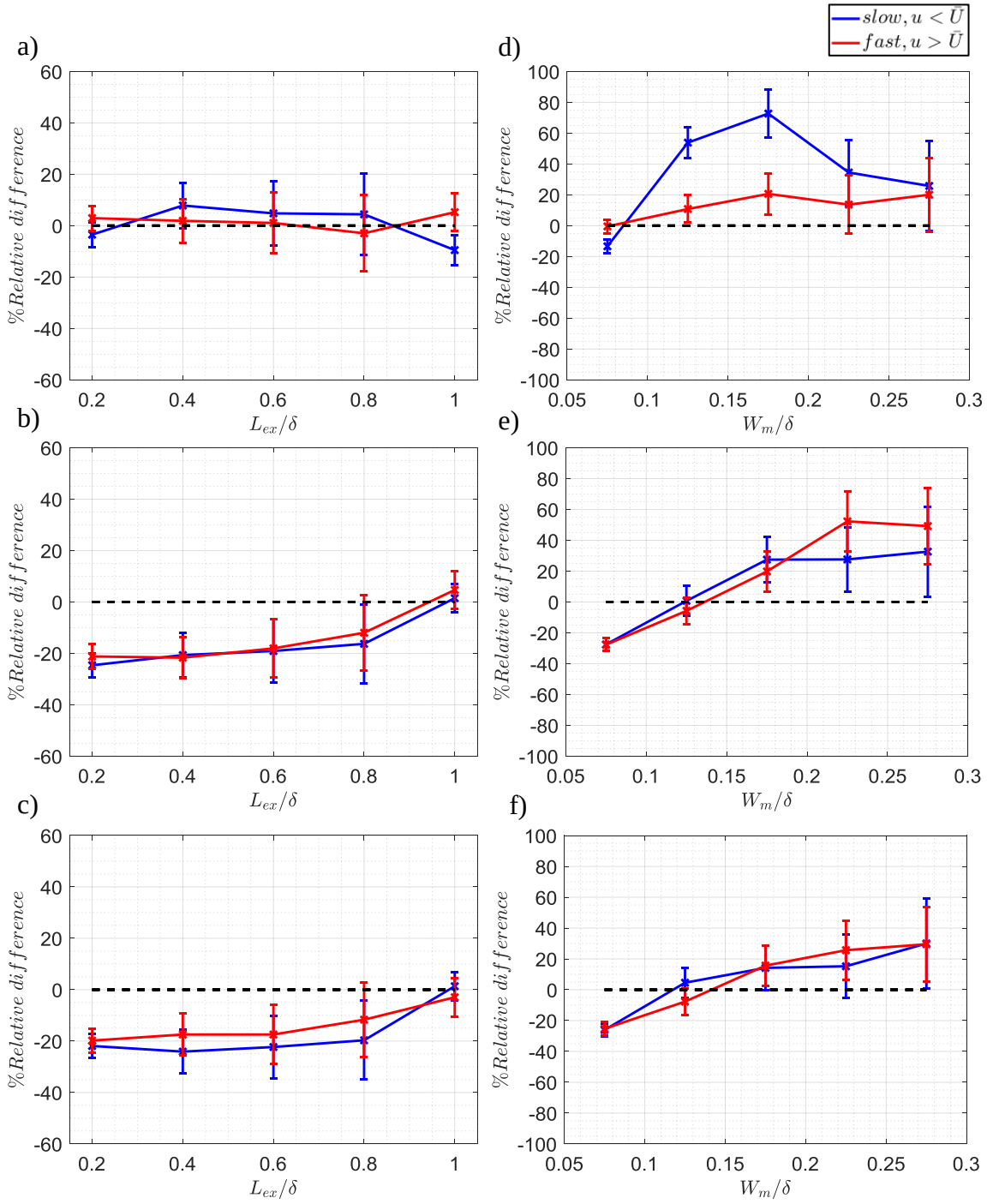

Figure 5-17: S = 0.6δ, H = 0.2δ, z^+ = 125. Extrema length differences between perturbed and unperturbed flow as a percentage of the unperturbed distribution of regions with uniform streamwise momentum at streamwise locations centered at a) x = 0.7δ, b) x = 2.9δ and c) x = 7δ. Differences in mean width at aforementioned locations shown in d,e,f. Bin sizes are 0.2δ and 0.05δ respectively.

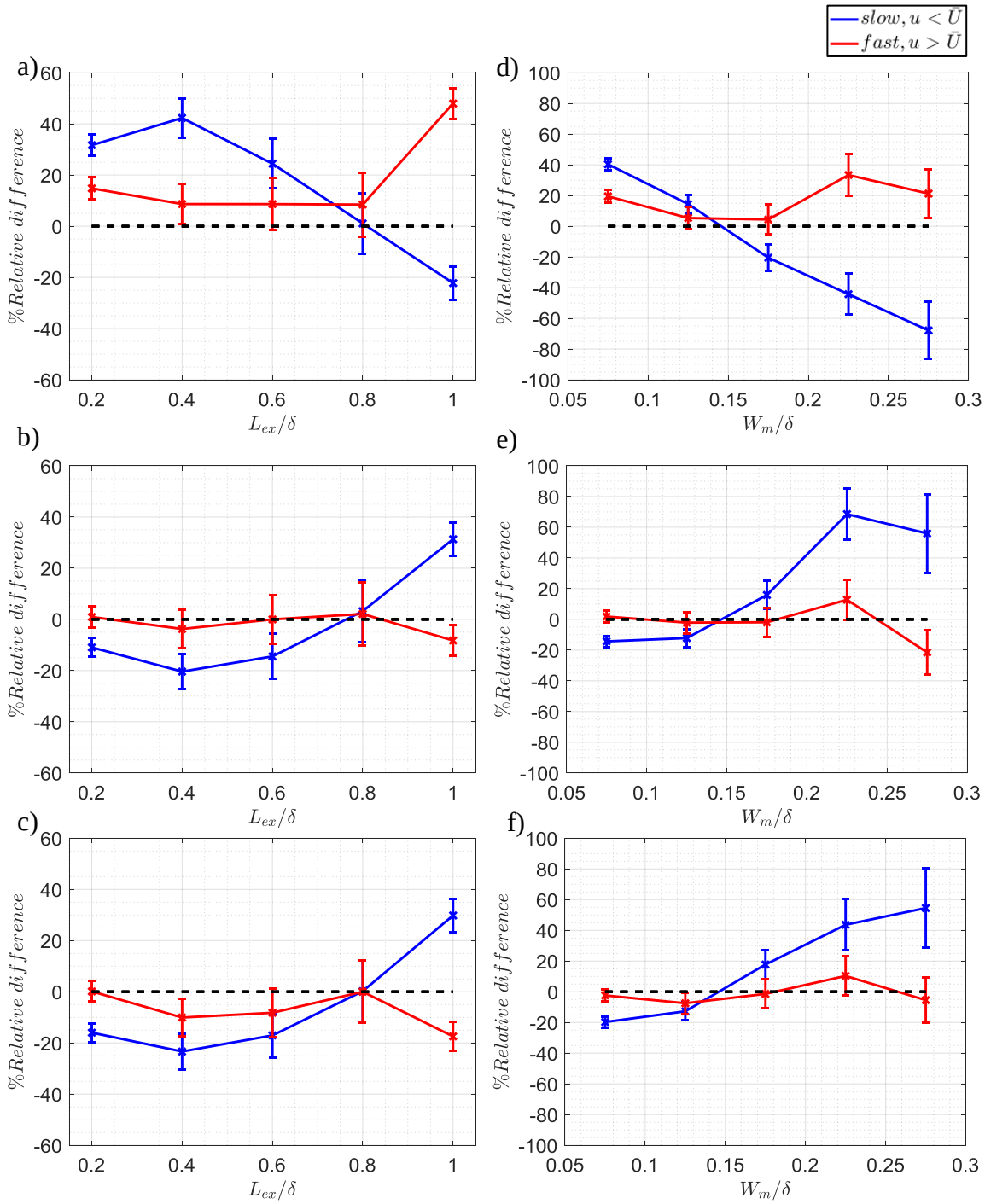

Figure 5-18: S = 0.6δ, H = 0.2δ, z^+ = 300. Extrema length differences between perturbed and unperturbed flow as a percentage of the unperturbed distribution of regions with uniform streamwise momentum at streamwise locations centered at a) x = 0.7δ, b) x = 2.9δ and c) x = 7δ. Differences in mean width at aforementioned locations shown in d,e,f. Bin sizes are 0.2δ and 0.05δ respectively.

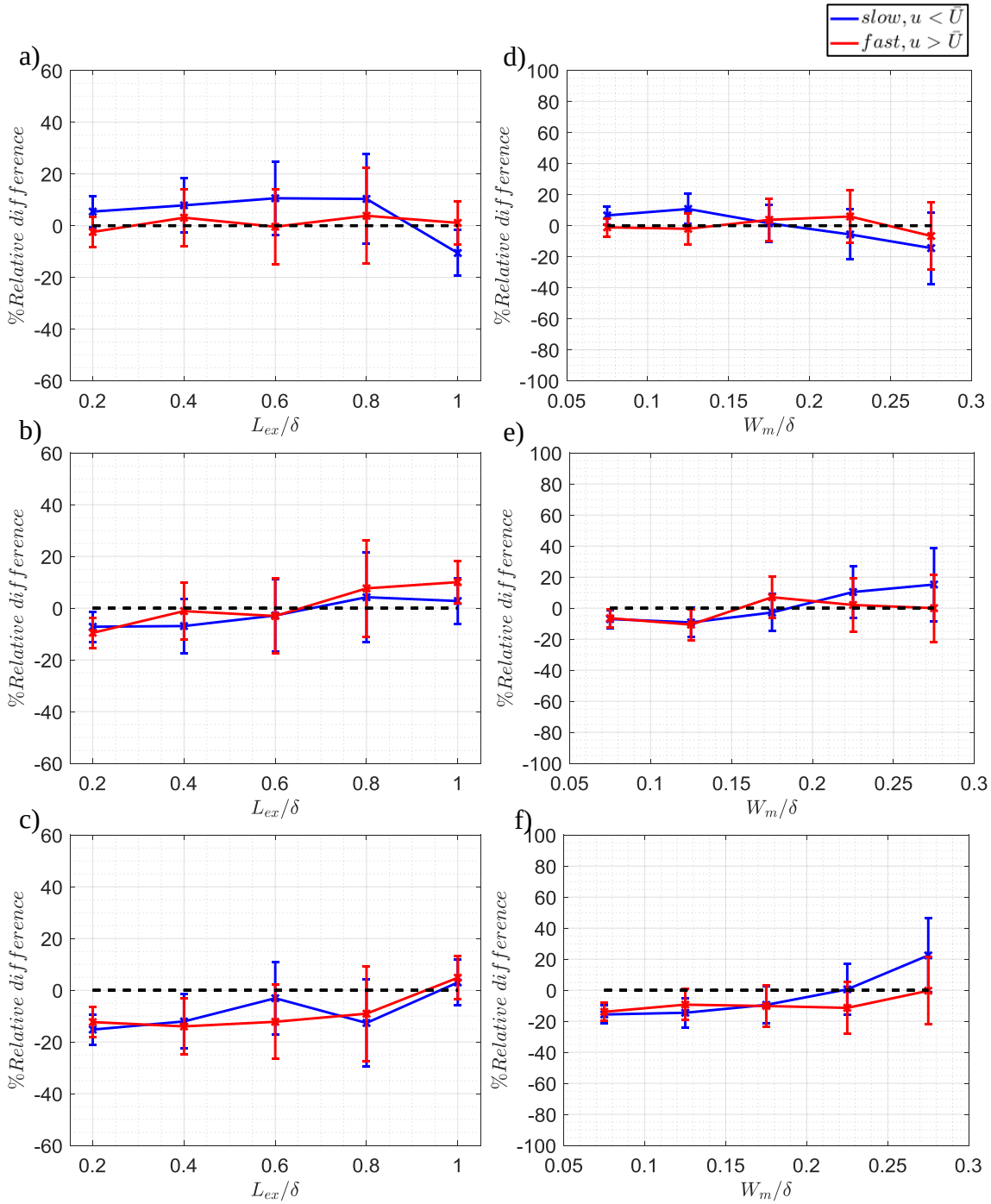

Figure 5-19: S = 0.6δ, H = 0.2δ, z^+ = 500. Extrema length differences between perturbed and unperturbed flow as a percentage of the unperturbed distribution of regions with uniform streamwise momentum at streamwise locations centered at a) x = 0.7δ, b) x = 2.9δ and c) x = 7δ. Differences in mean width at aforementioned locations shown in d,e,f. Bin sizes are 0.2δ and 0.05δ respectively.

13a, $y/\delta = 1.2$) and possible enhancement from the downwash induced at the cylinder tips when impinging directly on the cylinder.

As x increased, the number of short LMRs ($L_{ex} = 0.2\delta$) decreased relative to unperturbed values for all measurement heights, with reductions persisting to $x = 7\delta$. The reductions at $x = 7\delta$ were larger at both $z^+ = 125$(Fig. 5-17c) and 300(Fig. 5-18c) compared to $z^+ = 500$(Fig. 5-19c). The reductions may result from increased spanwise interactions between LMRs from LMRs migrating to the mid-span due to the wakes from the cylinders, thereby possibly leading to increased merging of shorter LMRs amongst themselves, and with longer LMRs.

At $z^+ = 125$ the number of long LMRs and HMRs relaxed to the unperturbed values starting at $x = 3.8\delta$ (Fig. 5-17b), and remained so till $x = 7\delta$ (Fig. 5-17c). In contrast, there were more long LMRs but fewer HMRs at $z^+ = 300$ (Fig. 5-18b), persisting till $x = 7\delta$. Effects with increasing x at the cylinder tip height were weak and at the limits of the estimated uncertainties. HMRs possibly increased at $x = 3.8\delta$ (Fig. 5-19b) but the increase diminished at $x = 7\delta$. The increase in long HMRs may be caused by enhancement upon directly impinging on a cylinder due to the downwash at the cylinder tips (see Fig. 5-15a).

Plots for the width differences between perturbed and unperturbed flow showed an increase in the number of wide CMRs ($W_m = 0.275\delta$) at $z^+ = 125$ immediately downstream of the array (Fig. 5-17d), with a larger effect on LMRs. The number of wide HMRs increased also at $z^+ = 300$(Fig. 5-18d). In comparison, at $x = 0.7\delta$, $z^+ = 300$(Fig. 5-18d) and 500(Fig. 5-19d), reductions in wide LMRs were observed, while the number of narrower LMRs increased.

As x increased, the number of wide LMRs increased at all measurement heights and persisted to x = 7δ, with the largest increase at z^+ = 300 (Fig. 5-19d-f). In contrast, only plots at z^+ = 125 show sustained effects on HMRs with increasing x, where more wide HMRs were observed at both x = 3.8δ(Fig. 5-17e) and x = 7δ(Fig. 5-17f). The increase in the number of wide CMRs can be due to the increased frequency of merging between smaller and larger CMRs, and between CMRs and wakes, consistent with instantaneous results (see Fig. 5-13,14,15).

Immediately downstream of the tips of the H = 0.05δ array (z^+ =125, Figure 5-20a), the number of short CMRs also increased, similar to at the tips of the H = 0.2δ array (compare Fig. 5-19a). The increase was larger downstream of the H = 0.05δ array. The number of long HMRs increased as well, different from the H = 0.2δ case. CMR widths also differed with more narrow LMRs and wide HMRs at x = 0.7δ, although the increase in wide HMRs was within uncertainty. As x increased, the aforementioned effects diminished. At x = 7δ (Fig. 5-20f), plots show fewer short CMRs, similar to the effect at the H = 0.2δ array tips (Fig. 5-19f).

In contrast, at x = 0.7δ, z^+ = 300 above the H = 0.05δ array (Fig. 5-21a & d), no discernible effects for both length and widths of CMRs larger than the uncertainty were observed. As x increased, the number of short CMRs decreases (Fig. 5-21b) with the effects persisting to x = 7δ (Fig 5-21c). Strangely, at x = 3.8δ, the magnitude of reduction in short CMRs was greater at z^+ = 300 compared to z^+ = 125. This may relate to the initial increase in short CMRs at z^+ = 125 and x = 0.7δ (see Fig. 5-21a). At x = 7δ (Fig 5-21c), the number of short CMRs decreased more relative to x = 3.8δ. Separately CMR widths did not change at x = 0.7δ (Fig. 5-21a). As x increased, the numbers of narrow CMRs

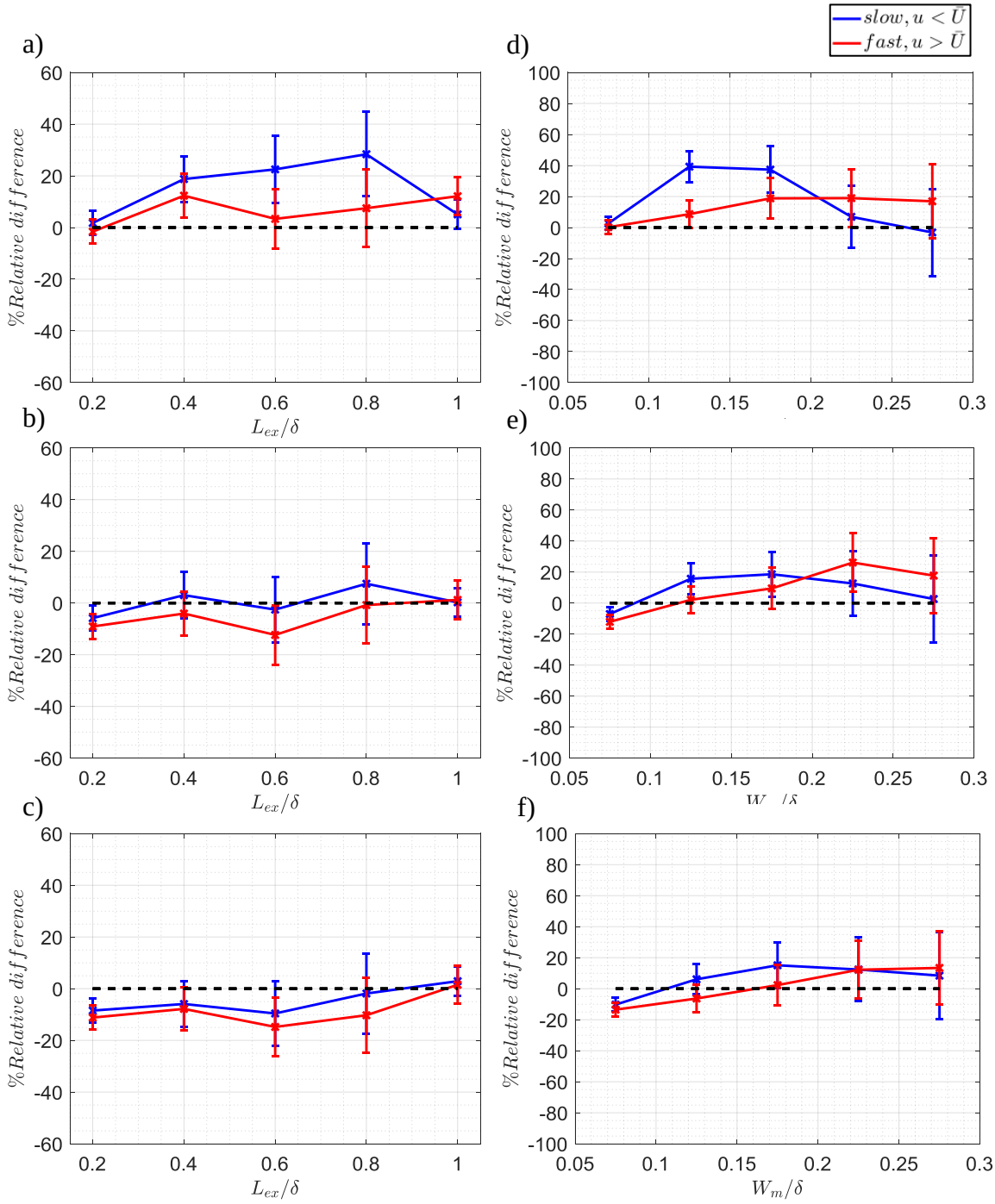

Figure 5-20: S = 0.6δ, H = 0.05δ, z^+ = 125. Extrema length differences between perturbed and unperturbed flow as a percentage of the unperturbed distribution of regions with uniform streamwise momentum at streamwise locations centered at a) x = 0.7δ, b) x = 2.9δ and c) x = 7δ. Differences in mean width at aforementioned locations shown in d,e,f. Bin sizes are 0.2δ and 0.05δ respectively.

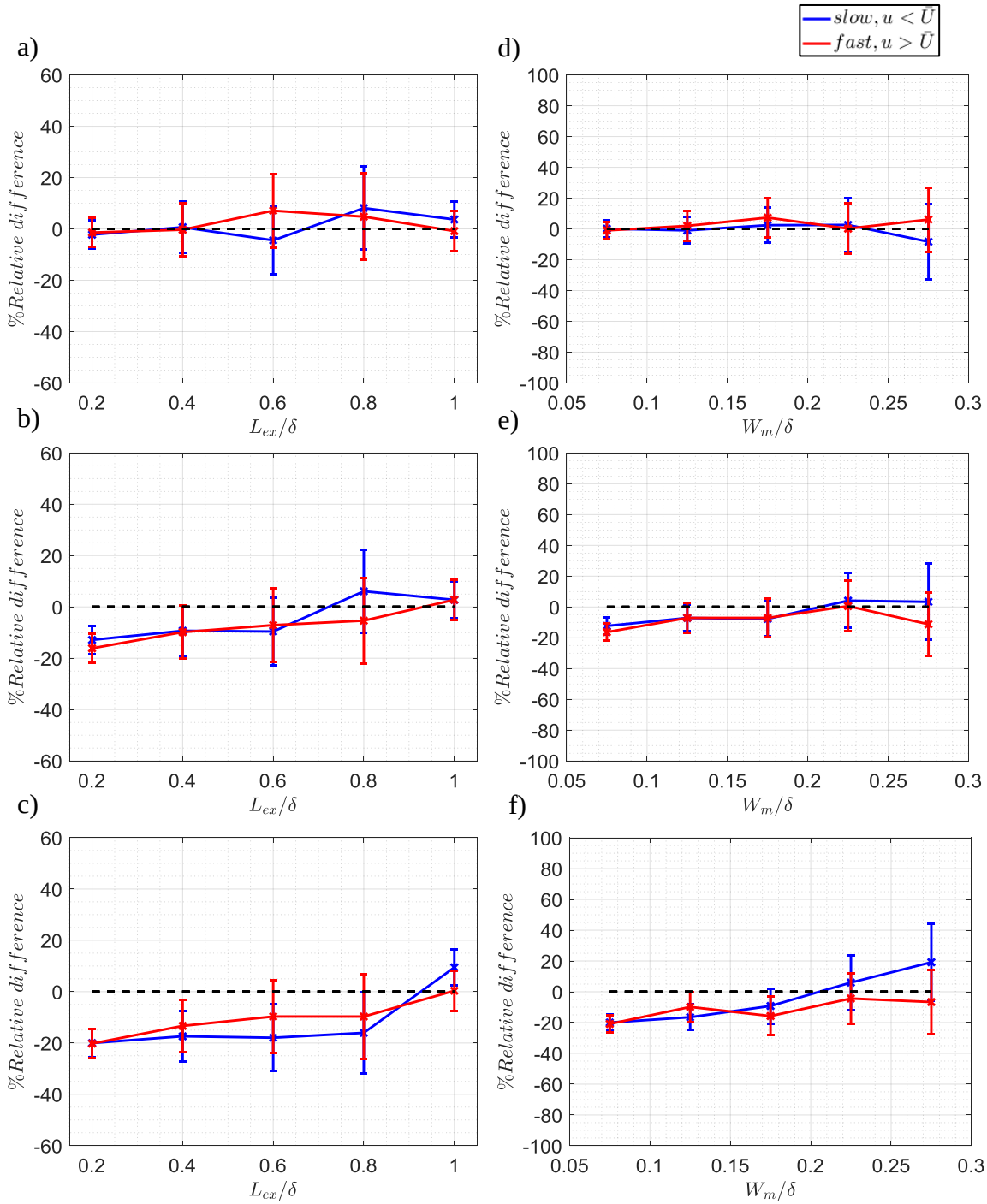

Figure 5-21: S = 0.6δ, H = 0.05δ, z^+ = 300. Extrema length differences between perturbed and unperturbed flow as a percentage of the unperturbed distribution of regions with uniform streamwise momentum at streamwise locations centered at a) x = 0.7δ, b) x = 2.9δ and c) x = 7δ. Differences in mean width at aforementioned locations shown in d,e,f. Bin sizes are 0.2δ and 0.05δ respectively.

decreased while numbers of wide LMRs seem to increase, although this effect may be within uncertainty. At x = 7δ, there were fewer short CMRs relative to the unperturbed flow (Fig. 5-21c). The aforementioned trends in CMR lengths and width suggest that the array's effects extend above to $z^+ = 300$.

The centroids of CMRs longer than $L_{ex} > 0.5\delta$ downstream of both arrays were extracted along the spanwise direction. Their distributions are shown in Figure 5-22. Immediately downstream of the array, at both $z^+ = 125$ (Fig. 5-22a) and 300 (Fig. 5-22b), LMRs were more aligned with cylinder locations, while HMRs were found aligned more with regions in between the cylinders. In contrast, no preferential alignment was observed at $z^+ = 500$. As x increased, the distribution of the centroids of the CMRs was altered throughout the logarithmic layer. LMRs were more aligned with regions between the cylinders while HMRs became more aligned with cylinder locations (Figs. 5-22d,e,f). Notably, trends at $z^+ = 500$(Fig. 5-22f) were observed also where HMRs were more aligned with cylinder locations while LMRs were more frequently aligned with regions between them. The preceding trends were much weaker when conditioned on CMRs with $L_{ex} < 0.5\delta$, suggesting that the array had a greater effect on long CMRs. These trends support FPIV runs showing the migration of LMRs to the mid-span due to the cylinder wakes. In comparison, the distribution of the spanwise centers of CMRs longer than $L_{ex} > 0.5\delta$ downstream of the H = 0.05δ showed no spanwise variations.

Figure 5-23 shows the percentage difference between the perturbed and unperturbed distribution of the magnitude of streamwise velocity deviations away from the local mean velocity within CMRs longer than 0.5δ. Immediately downstream of the array, deviations were evident for both LMRs and HMRs at $z^+ = 125$ (Fig. 5-23a) and 300 (Fig. 5-23b) due

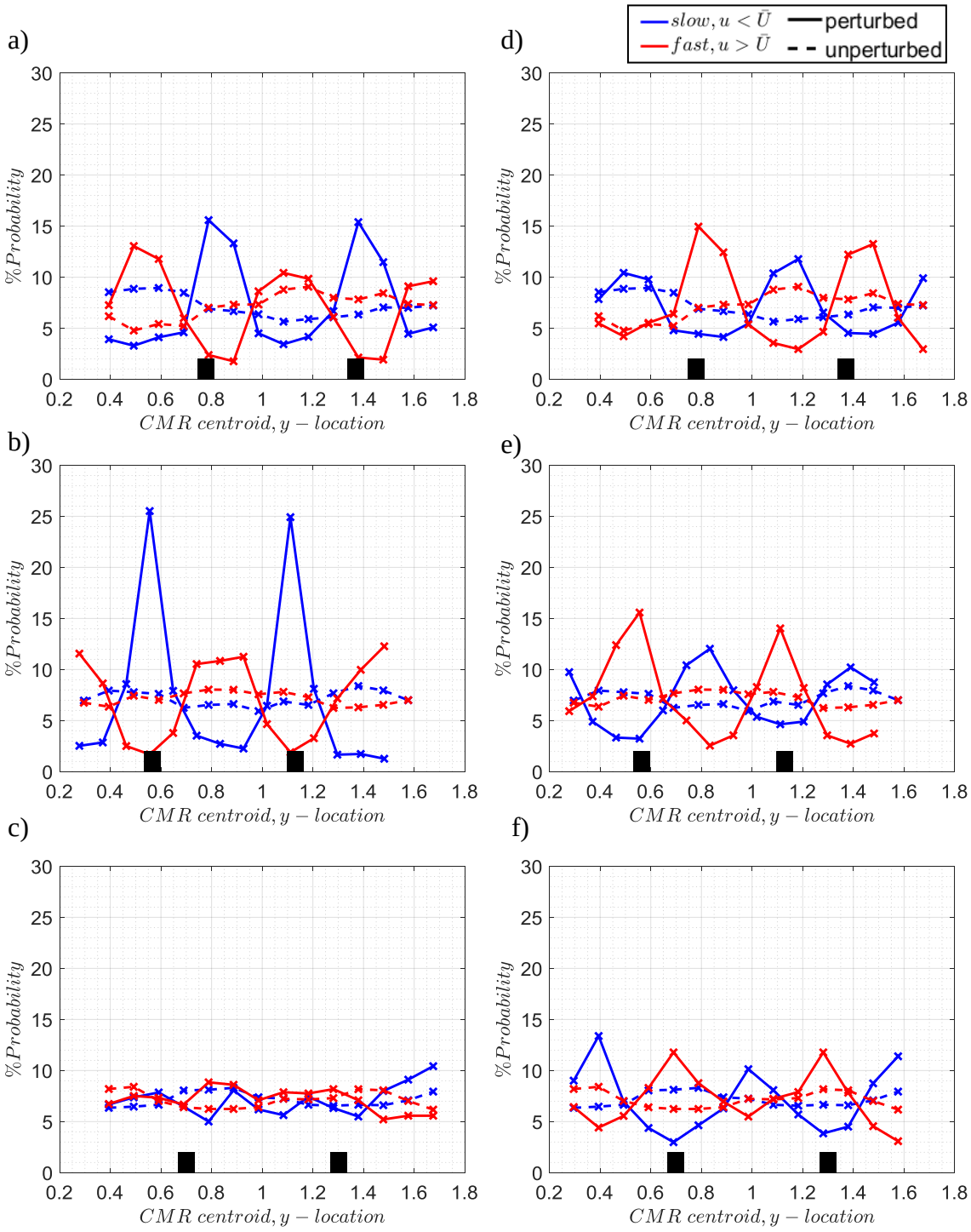

Figure 5-22: S = 0.6δ, H = 0.2δ. Distribution of the spanwise centroids of LMRs and HMRs along the spanwise direction at x = 0.7δ, for a) z^+ = 125, b) z^+ = 300 and c) z^+ = 500 and x = 7δ for d) z^+ = 125, e) z^+ = 300 and f) z^+ = 500.

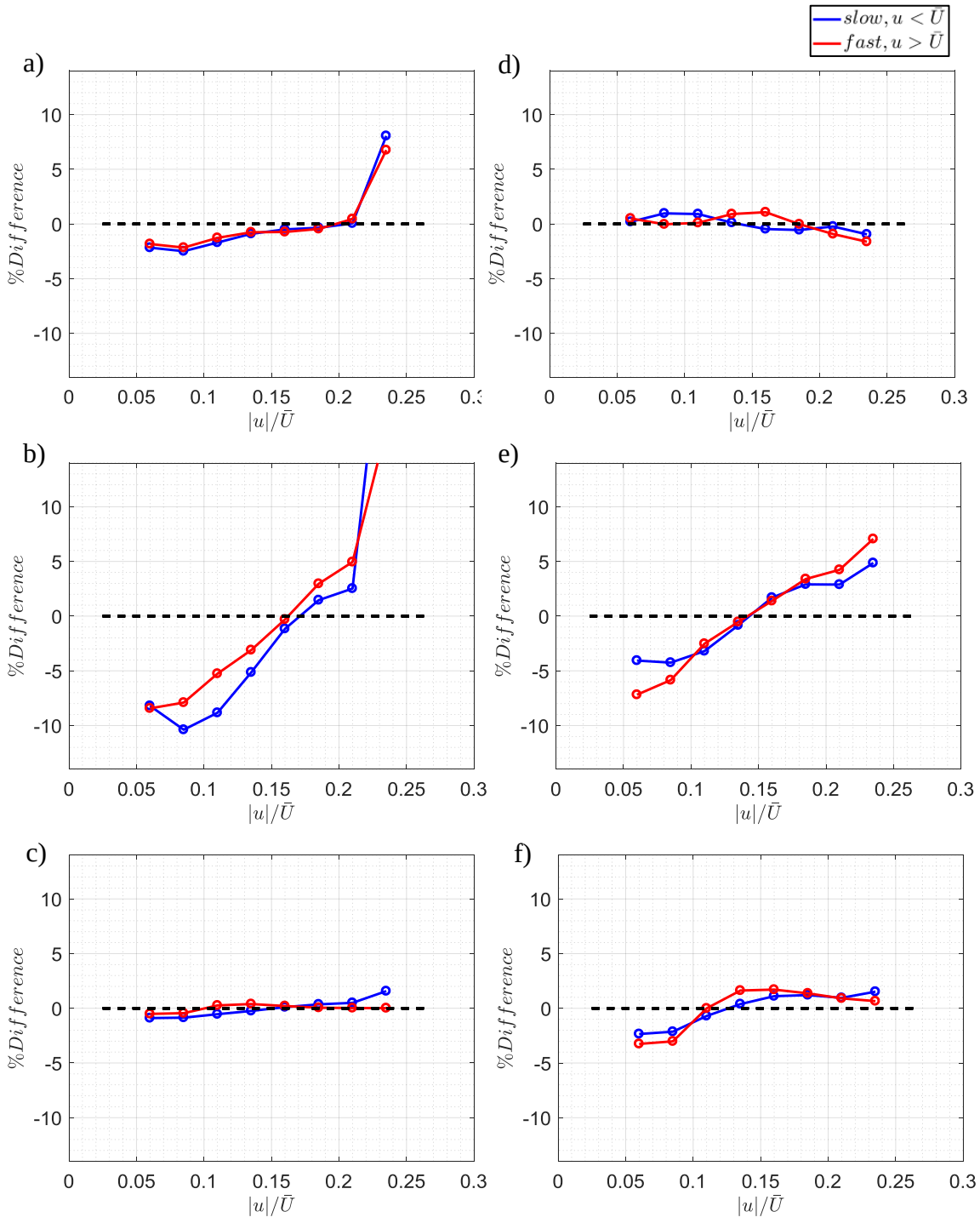

Figure 5-23: S = 0.6δ, H = 0.2δ. Percentage difference between perturbed and unperturbed distributions of the magnitude of streamwise velocity deviations away from the local mean velocity within CMRS longer than $L_{ex} > 0.5\delta$ at measurement heights, a) $z^+ = 125$, b) $z^+ = 300$ and $z^+ = 500$ at x = 0.7δ. Same plots at aforementioned heights at streamwise location x = 7δ shown in d,e,f. PDFs normalized by its respective counts before subtraction. Histogram bin size = 0.025.

to the cylinder wakes. Both HMRs and LMRs showed more frequent extreme velocity fluctuations, while fluctuations with smaller magnitudes were less frequent. In comparison, at z^+ = 500(Fig. 5-23c), effects were weak with a slight increase in the frequency of extreme velocity fluctuations in LMRs. As x increased, effects diminished at z^+ = 125 (Fig. 5-23a), remained apparent at z^+ = 300 while becoming even more apparent at z^+ = 500. At x = 7δ, deviations were minimal at z^+ = 125(Fig. 5-23d). In comparison, at z^+ = 300 (Fig. 5-23e), extreme values were still more frequent while smaller values less frequent. While, at z^+ = 500 (Fig. 5-23f), larger deviations away from the local mean occurred more frequently, while smaller deviations were suppressed, with the effect being more pronounced relative to x = 0.7δ. The sustained deviations at z^+ = 300 at x = 7δ may relate to the initial perturbations being strongest at z^+ = 300, 2/3 the cylinder height (Ryan *et al.* 2011). On the other hand, CMRs at x = 7δ, z^+ = 500, may experience larger deviations from interaction with cylinder wakes, possibly by enhancement through fluid drawn in by the downwash at the cylinder tips for the HMRs, or the ingestion of cylinder wakes or merging with adjacent structures for the LMRs. The aforementioned trends were consistent with the observed behavior of LMRs and HMRs downstream of array. In comparison, no effects larger than uncertainty were apparent downstream of the H = 0.05δ array at either z^+ = 125 or 300, hence the velocity distributions were not shown.

5.1.5 Autocorrelations of streamwise velocity

Immediately downstream of the H = 0.2δ array, Δy = 0 autocorrelations (Fig. 5-24) show reduced correlation values for all measurement heights. The largest reduction occurs at z^+ = 300 (Fig. 5-24b), and the least at z^+ = 500(Fig. 5-24c). This was consistent with the

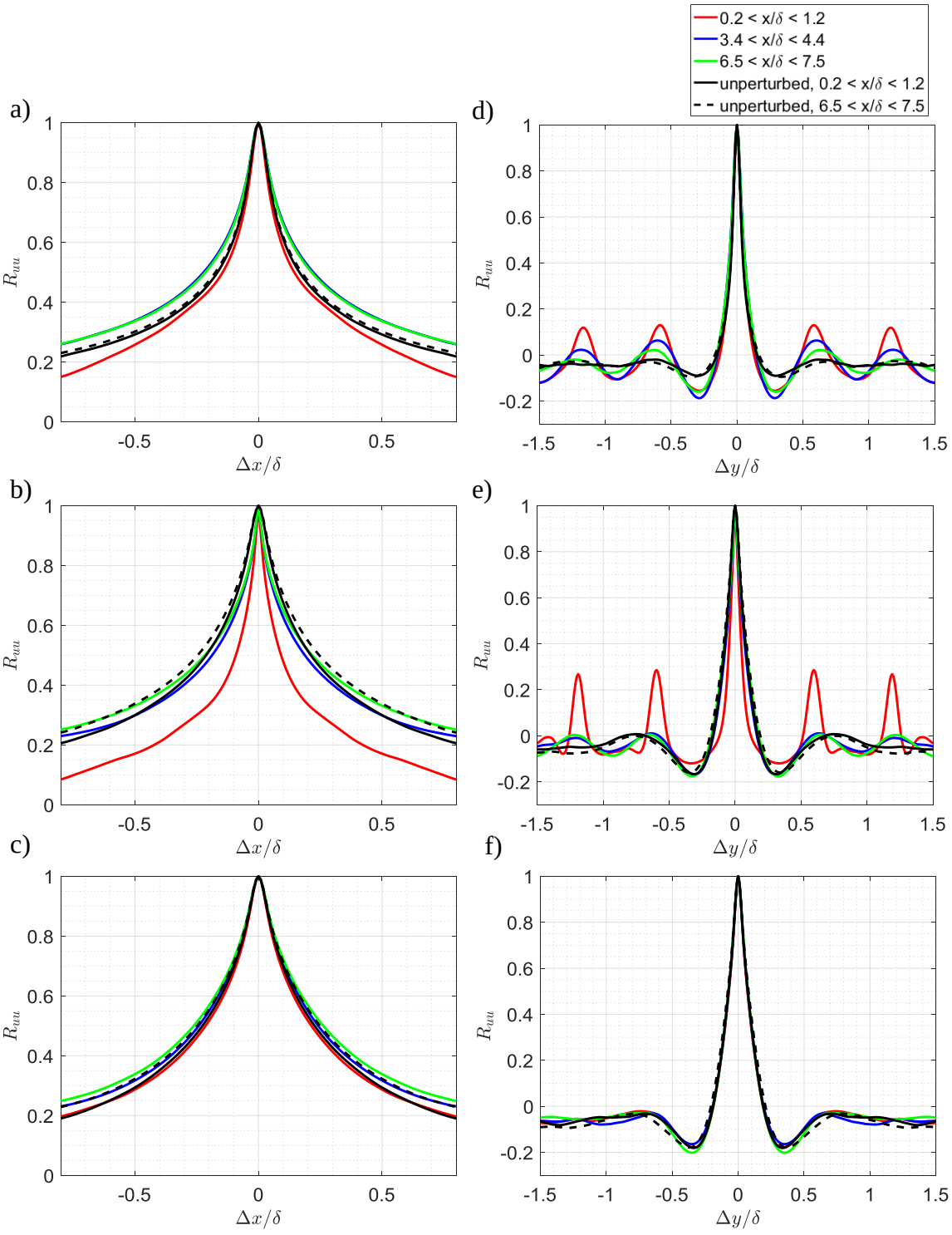

Figure 5-24: S = 0.6δ, H = 0.2δ. Δy = 0 autocorrelations shown for measurement heights a) z^+ = 125, b) z^+ = 300 and c) z^+ = 500. Δx = 0 autocorrelations are shown for measurement heights d) z^+ = 125, e) z^+ + 300 and f) z^+ = 500.

hot-wire measurements of Ryan *et al.* (2011) showing the strongest perturbation effects at 2/3 their cylinder height, where the peak of streamwise RMS velocity occurs, therefore, in our measurements, the strongest effects should correspond to that. On the other hand, visualizations of the data at the cylinder tip heights and average velocity measurements (Fig. 5-1c) showed minimal deviations relative to the unperturbed flow, thus the reduction should be the least. The reduction in $\Delta y = 0$ autocorrelation values can be related to the disruptive effect of the cylinders, breaking up existing long flow structures directly, or via the cylinder wakes.

As x increased, the correlation magnitudes generally reverted towards unperturbed values for all measurement heights. At $x = 1.8\delta$, the correlation at $z^+ = 125$ (Fig. 5-24a) has recovered while the correlations in planes above that remained suppressed. At $x = 3.8\delta$, and $z^+ = 125$, the autocorrelations increased above unperturbed values and remained so to $x = 7\delta$. This could either suggest an increase in the number of structures with characteristic lengths of $\Delta x > 0.1\delta$ or increased alignment of structures along the streamwise direction. The latter option was more likely as the numbers of long CMRs remained similar to unperturbed values (see Fig. 5-17c). By contrast, at $z^+ = 300$ and $x = 7\delta$, values for $\Delta x > 0.5\delta$ matched unperturbed values while values for $\Delta x < 0.5\delta$ were reduced. This may relate to the reductions in short LMRs shown in Figure 5-18c. Previously, Figure 5-18c also indicated increased numbers of long LMRs here, but autocorrelations values did not increase near the tails, which may relate to also a subsequent decrease in long HMRs seen in Figure 5-18c. Separately, the correlation values at the tip height (Fig. 5-24c) reverted to unperturbed values by $x = 3.8\delta$ and remained so till $x = 7\delta$. Notably, the values near the tails at $x = 7\delta$ were larger than the

unperturbed flow, and may be due to increased alignment of CMRs along the streamwise direction as the numbers of long LMRs did not increase there (see Fig. 5-19c).

Spanwise autocorrelations ($\Delta x = 0$) show periodicities matching the array spacing at both $z^+ = 125$ (Fig. 5-24d) and 300(Fig. 5-24e) in the field immediately downstream of the $H = 0.2\delta$ array. The magnitudes in the additional peaks were stronger at $z^+ = 300$. As x increased, the magnitudes of the additional peaks at $z^+ = 125$ (Fig. 5-24d) increasingly diminished, although the peaks were still apparent at $x = 7\delta$. The aforementioned trends also applied at $z^+ = 300$ (Fig. 5-24e) as x increased, with comparable peak magnitudes at $x = 7\delta$, relative to $z^+ = 125$. The persistent spanwise periodicities at the aforementioned heights was likely due to the preferential alignment of long LMRs and HMRs downstream as shown in Figure 5-22. At $z^+ = 500$ (Fig. 5-24f), no trend was observed.

Any effects of the $H = 0.05\delta$ array on the streamwise velocity autocorrelations were much weaker. In the region immediately behind the array, at the array tip height of $z^+ = 125$ (Fig. 5-25a), streamwise autocorrelations ($\Delta y = 0$) were slightly reduced. In comparison, at $z^+ = 300$(Fig. 5-25b), correlation values slightly increased near the tails of the correlations, although this effect may be within uncertainty. At $z^+ = 500$(Fig. 5-25c), plots show no discernible trends. As x increased, plots show slight increases in correlations values at $z^+ = 125$ and 300 at $x = 7\delta$, which may again be within uncertainty. The effect of increased correlation values seemed more apparent at $z^+ = 125$ compared to $z^+ = 300$, and appeared similar to the effect at the tips of the $H = 0.2\delta$ array tips (see Fig. 5-24c). Again, as long CMRs did not increase in number at $x = 7\delta$ at both these heights (see Fig. 5-20c and 5-21c), the increased correlation values was likely due to increased streamwise alignment of existing structures. Spanwise autocorrelation ($\Delta x = 0$) remained

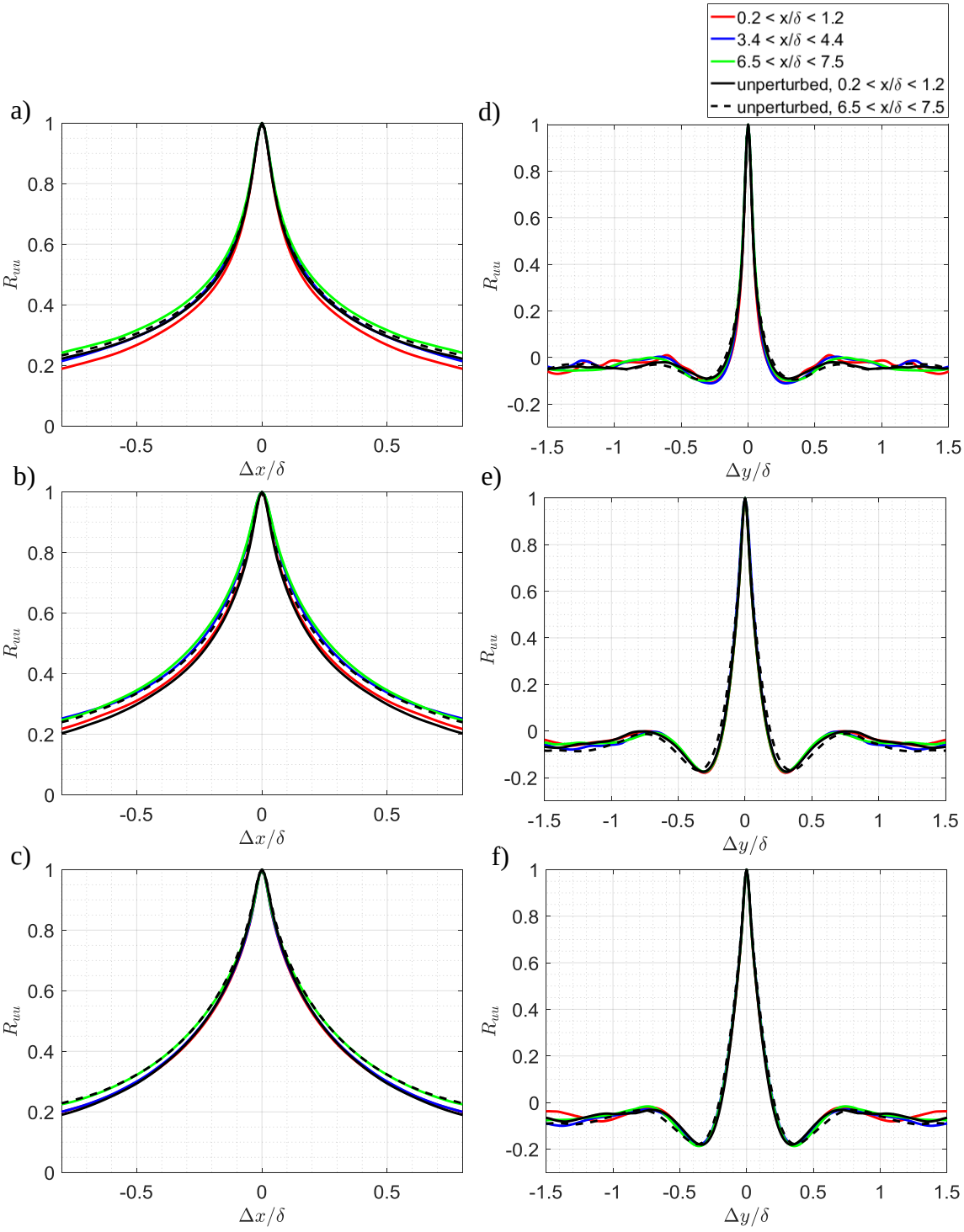

Figure 5-25: S = 0.6δ, H = 0.05δ. Δy = 0 autocorrelations shown for measurement heights a) z^+ = 125, b) z^+ = 300 and c) z^+ = 500. Δx = 0 autocorrelations are shown for measurement heights d) z^+ = 125, e) z^+ + 300 and f) z^+ = 500.

unchanged relative to the unperturbed flow throughout the logarithmic layer for all measurement heights.

5.1.6 Pre-multiplied energy spectra and dominant spanwise modes

Streamwise velocity energy spectra downstream of the H = 0.2δ array showed substantial variation at both z^+= 125 and 300 relative to the unperturbed flow. At both locations, the strongest peak in energy occurred at $\lambda_y = 0.6\delta$, matching the cylinder spacing. Additional peaks at $\lambda_y = 0.2$ and 0.3 were evident at both $z^+ = 125$ (Fig. 5-26a) and 300 (Fig. 5-26b), while the spectrum at $z^+ = 300$ also showed another peak at $\lambda_y = 0.15$. The peak at 0.3δ can be related to the splitting of the wakes at both measurement planes. For example, the average streamwise velocity fields (Figs 5-1a,b) showed that the spacing between the fast moving zones directly behind the cylinders with ones in the mid-span region were roughly 0.3δ apart in the first data field. On the other hand, the additional peak at 0.2δ and 0.15δ likely relate to the small-scale structures generated from the wakes of the cylinders (see Fig. 5-8a and b). Besides that, energy contained in small spanwise wavelengths $\lambda_y < 0.2\delta$ at $z^+ = 125$ were suppressed relative to the unperturbed spectra. On the other hand, the energy for $\lambda_y < 0.35\delta$ increased slightly at the cylinder tip height, $z^+ = 500$ (Fig. 5-26c), while no initial increase was observed at $\lambda_y = 0.6\delta$.

The peaks in spectra at $\lambda_y = 0.6\delta$ remained prominent for $z^+ = 125$ (Figure 5-26a) and z^+= 300 (Figure 5-26b), until x = 7δ. The magnitude of the peak at 0.6δ $z^+ = 125$ decayed as x increased, while increasing at $z^+ = 300$. The energy for $\lambda_y = 0.6\delta$ at $z^+ = 500$ also increased with x, with the peak at $\lambda_y = 0.6\delta$ lasting up to x = 7δ. The delay in the increase of energy at the 0.6δ spanwise wavelength at $z^+ = 500$ suggests that the array's effect was felt later at $z^+ = 500$ compared to planes below.

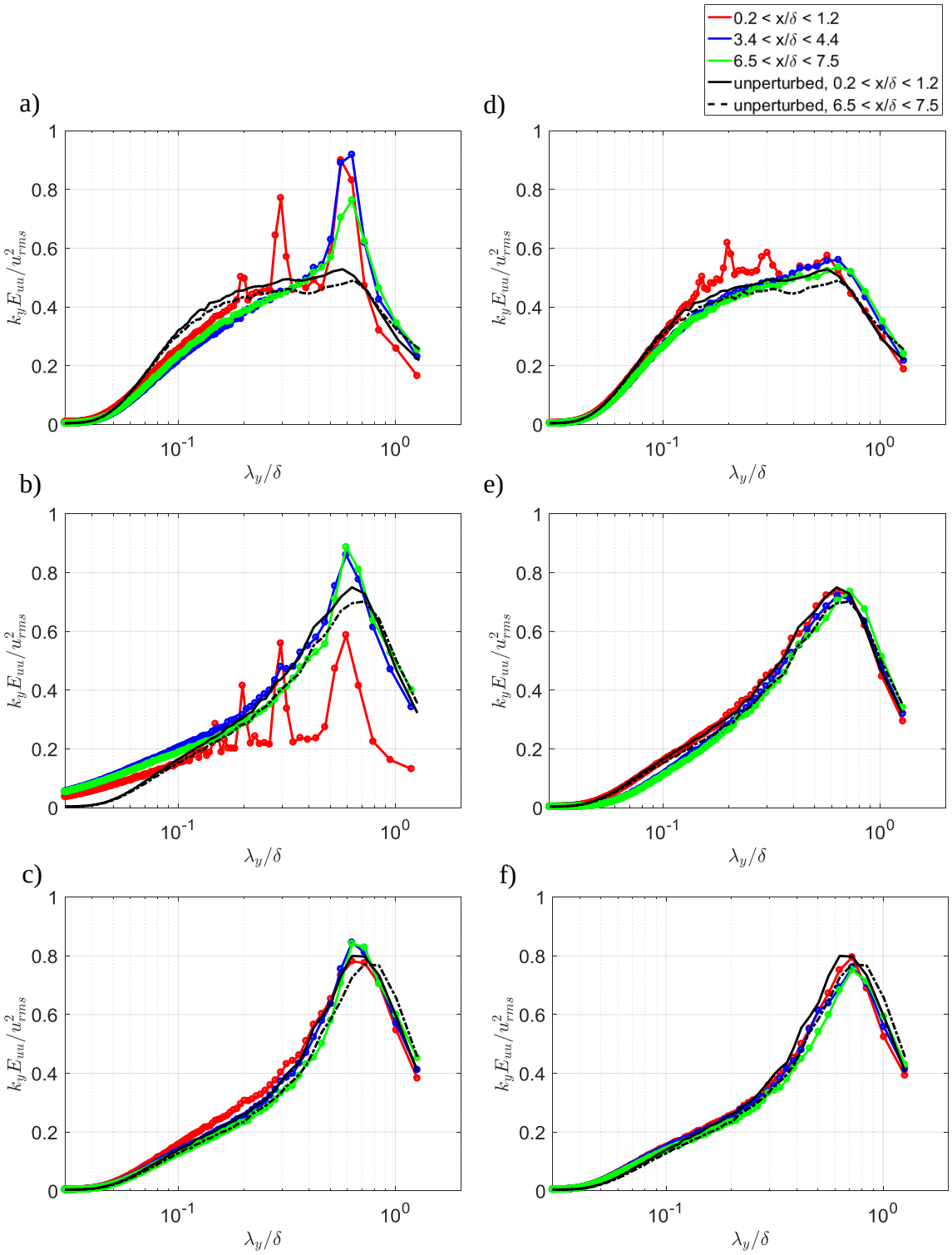

Figure 5-26: 1-D pre-multiplied spectra of streamwise velocity for flow downstream of S = 0.6δ, H = 0.2δ for measurement height at a) z^+ = 125, b) z^+ = 300 and c) z^+ = 500, and flow downstream of S = 0.6δ, H = 0.05δ array with d) z^+ = 125, e) z^+ = 300 and f) z^+ = 500.

In comparison, the spectra for the flow downstream of the H = 0.05δ were different only at z^+ = 125 (Fig. 5-26d) and 300(Fig. 5-26e). Although there were slight differences between spectra at z^+ = 500(Fig. 5-26f) versus the unperturbed spectra, it was unclear if these differences were real, since visualizations and various statistical analyses showed no obvious variations relative to the unperturbed flow. This may suggest that the array's effects were limited to a height a little beyond z^+ = 300(Fig. 5-26f). Plots at the tips of the H = 0.05δ array, z^+ = 125(Fig 5-26d) show evident peaks at λ_y = 0.2δ, and additional smaller peaks for 0.6δ, 0.3δ and 0.15δ. The peaks at 0.6δ and 0.3δ relate to the cylinder spacing and wake splitting. On the other hand, the cause of the additional peaks at 0.15δ and 0.2δ were harder to deduce and were not obvious from instantaneous visualizations. Possibly, these wavelengths could relate to the relative spacing of incoming structures passing through the region between the cylinders with respect to wakes structures generated at the tips of the cylinders, when wakes do occur. On the other hand, at z^+ = 125, width distributions of individual LMRs in the unperturbed flow was roughly ~ 0.1δ (see Fig. 3-27), therefore, smaller spacings of 0.1δ between the structures could occur in the case where the LMRs impinged directly on the cylinder, with the incoming LMRs split into two equal halves downstream, such that their widths were 0.05δ. The additional peaks were not seen in the spectra at the tips of the H = 0.2δ array (Fig. 5-26c), while the averaged velocity fields there (Fig. 5-1c) also did not show wake splitting. Therefore, this seems to suggest that the additional peaks, at least for 0.3δ and 0.6δ were related to the split wakes.

As x increased, at z^+ = 125, energy was reduced for wavelengths less than 0.25δ at z^+ = 125 while increasing for wavelengths larger than the aforementioned value, relative to the

unperturbed spectra. This suggests that the H = 0.05δ array may have shifted energy from the small spanwise scales to larger spanwise scales. These effects were sustained at x = 7δ.

The spectra at z^+ = 300 (Fig. 5-26d) did not change initially relative to the unperturbed spectrum. Starting at x = 3.8δ, energy was reduced in smaller spanwise wavelengths (λ_y < 0.15δ) and remained so till x = 7δ. Also, increases for larger spanwise wavelengths were observed at x = 7δ, and may indicate that the array's effects did extend above to regions beyond the array height.

The dominant spanwise mode histograms (Fig. 5-27) downstream of the S = 0.6δ, H = 0.2δ array are shown in Fig. 5-27a-c. The plots show that the 0.6δ mode was the most likely to be dominant energetically at all measurement heights and streamwise locations. This shows that the S = 0.6δ, H = 0.2δ array energized the 0.6δ spanwise mode throughout the boundary layer and downstream, such that the low and high speed zones were more frequently spaced at 0.6δ apart, relative to the unperturbed distribution. In the first field, the peak probability was strongest at z^+ = 300 (50%, Fig. 5-27b) and the least at z^+ = 500 (30%, Fig. 5-27c). As a result of the increase at 0.6δ, the probabilities of spanwise modes larger than 0.6δ were reduced for all measurement heights for the field centered at x = 0.7δ. As x increased, the peak probabilities decreased at z^+ = 125 and 300 with values being comparable at 40%, at x = 7δ. On the other hand, the peak probability did not decrease at z^+ = 500 and remained at 30% up to x = 7δ.

In contrast, changes in the dominant spanwise mode distributions downstream of the H = 0.05δ array were much weaker for all measurement heights. At z^+ = 125 (Fig. 5-27d), plots show minimal differences in the region immediately downstream of array. As x

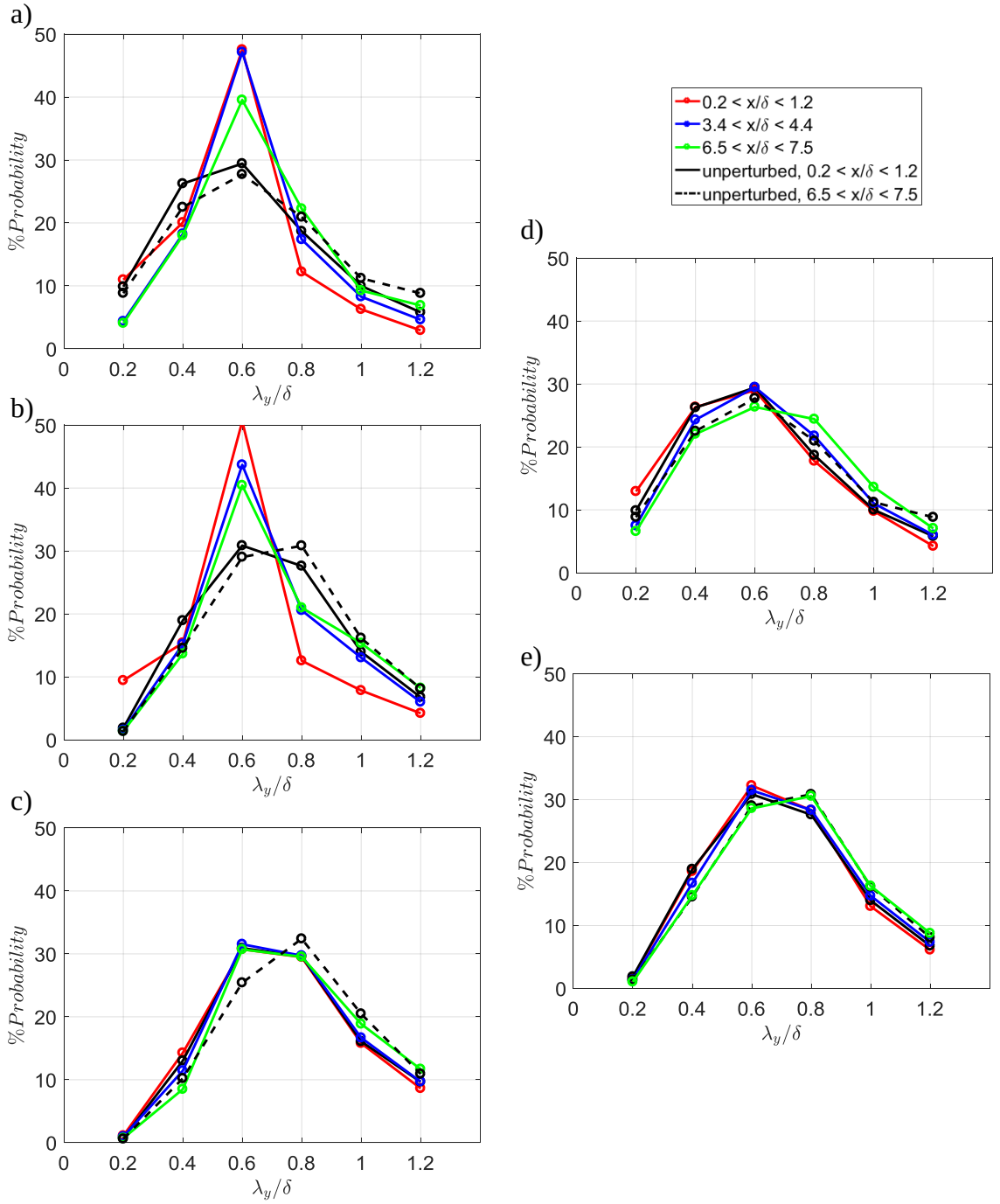

Figure 5-27: Dominant spanwise mode histograms from streamwise velocity in flow downstream of S = 0.6δ, H = 0.2δ for measurement height at a) z^+ = 125, b) z^+ = 300 and c) z^+ = 500, and flow downstream of S = 0.6δ, H = 0.05δ array with d) z^+ = 125 and e) z^+ = 300. Histogram bin size = 0.2δ.

increased, the distribution at z^+ = 125 increasingly shifted towards larger spanwise modes, with the probabilities for the 0.8δ and 1.0δ mode being larger relative to the unperturbed distribution at x = 7δ. By comparison, at z^+ = 300 (Fig. 5-27e), no significant changes were observed.

5.2 Summary of results and discussion

The results indicate substantial structural and statistical changes to the flow downstream of the S = 0.6δ, H = 0.2δ array at all measurement heights. In contrast, the changes downstream of the H = 0.05δ array were much weaker and subtle. At z^+ = 125 and 300 the S = 0.6δ, H = 0.05δ array did reduce mean streamwise velocities and increased streamwise RMS velocities immediately downstream, although to a much lesser degree compared to the S = 0.2δ, H = 0.2δ array, as the frontal blockage posed was much lower (1.7% vs. 5%). As x increased, mean and RMS streamwise velocities downstream of the H = 0.2δ array relaxed substantially towards the unperturbed values, recovering by x = 7δ at z^+ = 125. As for z^+ = 300, mean values were slightly lower at x = 7δ while RMS values remained slightly larger. This was reasonable as initial perturbation effects were strongest at this height (Ortiz-Duenas *et al.* 2007; Ryan *et al.* 2011). Effects at the array tip height (z^+ = 500) were weaker, and evolved differently with x-location. The mean streamwise velocity was initially matched with the unperturbed value, then decreased to a minimum at x = 2.9δ before reverting towards the unperturbed value at x = 7δ. On the other hand, streamwise RMS values first rose to a maximum at x = 2.9δ before reverting to the unperturbed value at x = 7δ.

Wakes were prevalent behind the cylinders at z^+ = 125 and 300, with notable waviness likely associated with Karman like shedding. The wakes typically lasted up to x = 0.8δ

and often beyond the end of the first field. In contrast, the S = 0.2δ, H = 0.2δ wakes were far less coherent, generally breaking up or interacting with adjacent wakes by x = 0.4δ. Wake signatures were less prominent at the array tip height, z^+ =500 while incoming structures seemed less perturbed downstream, relative to measurement planes below. Nevertheless, the S = 0.2δ, H = 0.2δ array generated profound and lasting effects on the downstream flow organization, despite the relatively small blockage posed.

Instantaneous visualizations and structural analyses showed that long HMRs and LMRs shifted preferentially to spanwise locations aligned with cylinder locations and the regions between them respectively. Short HMRs and LMRs were also affected but to a lesser degree. In addition, the coherence of long CMRs was altered depending on whether they impinged directly or passed between the cylinders. Both of these effects were driven by the cylinder wakes.

Generally, long LMRs that impinged directly on the cylinders were driven to spanwise locations aligned to the region between the cylinders, while occasionally becoming stronger likely through wake-ingestion. Some instances showed two spanwise adjacent long LMRs being re-directed towards the mid-span such that they converged and merged into a single wider LMR. On the other hand, long LMRs that passed through the region between the cylinders were frequently enhanced through wake ingestion and persisted downstream. These long LMRs tend to be better aligned along the streamwise direction downstream of the H = 0.2δ array, with respect to ones in the unperturbed flow. This suggests weaker meandering behavior.

Long HMRs on the other hand showed some trends that were opposite to the long LMRs. HMRs encountering the cylinders were more likely to be enhanced then persisting

downstream. On the other hand, HMRs that passed between the cylinders were occasionally re-directed to regions roughly aligned with cylinder locations, and sometimes enhanced. Two HMRs could also be re-directed such that they converge to align with spanwise coordinates corresponding to cylinder locations.

The preferential re-alignment of long structures increased the energy at the 0.6δ spanwise wavelength in streamwise velocity spectra throughout the logarithmic region, which was already dominant to begin with. The 0.6δ spanwise mode was dominant more frequently than in the unperturbed flow at all measurement heights up to x = 7δ. The preferential spanwise shifting promoted interactions between coherent momentum zones and the small scale flow structures generated by the cylinders, which either merged or were annihilated by incoming coherent momentum zones. This was consistent with reduced numbers of short CMRs (L_{ex} = 0.2δ) while the numbers of wide CMRs (W_m = 0.275δ) increased compared to unperturbed flow. This seems to indicate growth in characteristic spanwise scales, but autocorrelations along the spanwise coordinate did not show this, as the effect may be obscured by other small-scale features, or may be too weak for the autocorrelations to pick up.

Interestingly, streamwise autocorrelations (Δy = 0) at both z^+ = 125 and z^+ = 500, x = 7δ indicated more content for Δx > 0.5δ although structural analyses showed no discernible increases in the numbers of long CMRs (L_{ex} > 0.5δ) larger than the uncertainty at those locations. Therefore, long CMRs must have been better aligned in the streamwise direction, as evidenced in instantaneous FPIV runs where their tendency to meander in the spanwise direction was reduced.

The H = 0.05δ (H^+ = 125) array yielded much weaker effects on velocity statistics in the flow downstream. This was expected since the strength of the perturbation was reduced, with blockage decreasing from 1.7% (H = 0.2δ) to 0.4% (H = 0.05δ) of the frontal area of the oncoming boundary layer. At z^+ = 125, average velocity fields showed patterns consistent with tip structures immediately downstream of the cylinders. Cylinder wakes split as fast moving zones formed on average. These patterns were more apparent than downstream of the H = 0.2δ cylinder tips, which may relate to the increased influence of the tip structures due to the reduced aspect ratio of the H = 0.05δ cylinders (Sumner *et al.* 2004). Turbulence levels were also greater at z^+ = 125 compared to z^+ = 500, and could have contributed to the aforementioned difference. Interestingly, streamwise velocity averaged over the entire planar field was initially unchanged, but then increased starting at x = 3.8δ, and remained so until x = 7δ. This may relate to increased wall-normal transport. Although, these effects in the planar PIV results were only slightly larger than uncertainty, SPIV results (not shown) also exhibited similar trends. Streamwise RMS values also increased at z^+ = 125 immediately downstream of the H = 0.05δ array, similar to but weaker than the H = 0.2δ case, before decreasing below unperturbed values at x = 3.8δ.

Interestingly, the H = 0.05δ array also affected flow at z^+ = 300 (2.4H), although very weakly. Average streamwise velocity patterns indicate weak fast moving zones aligned with cylinder locations starting at x = 0.6δ. The most apparent effect manifested in increased streamwise RMS velocities beginning immediately downstream of the H = 0.05δ cylinders, and reaching a maximum at x = 2.9δ before reverting to the unperturbed value. The initial increase was larger than at z^+ = 125. The increase in RMS velocity

appears similar to results reported by Jacobi & McKeon (2011) and Tan (2014) where the peak perturbation to the streamwise RMS velocity profile propagated upwards beyond the obstacle height as x increased. These results were also consistent with Tomkins (2001) who noticed additional swirling structures and reduced streamwise length scales downstream of a hemisphere (H = 0.05δ) at heights up to 2H.

No discernible effects in velocity statistics or structural analyses were observed at z^+ = 500(4H), up to 7δ downstream of the H = 0.05δ array. According to Tan (2014), in the flow perturbed by a S = 0.5δ, H = 0.13δ cylinder array, the peak of the perturbation to the streamwise RMS velocity profile propagated upwards till 2.6H at x = 7δ, corresponding to the extent of their measurement domain. Therefore, it may be possible that effects would be observed at z^+ = 500 at a streamwise location further downstream than 7δ, but we suspect that the effects would be even weaker, and harder to measure.

Effects of the H = 0.05δ array in instantaneous visualizations were generally weak as well, although at z^+ = 125, FPIV runs did show some preferential re-alignment of incoming CMRs similar to that occurring at the tips of the H = 0.2δ array. These events were less frequent than in the H = 0.2δ case as the distribution of the centroids along the spanwise direction of long CMRs at x = 7δ did not exhibit preferential alignment behavior, although average streamwise velocity patterns did show obvious wake splitting effects.

Streamwise autocorrelations (Δy = 0) at z^+ = 125 showed initially reduced correlation magnitudes that later increased slightly relative to the unperturbed correlation at x = 7δ. This may indicate increased stream-wise alignment of flow structures, or weaker spanwise meandering behavior. Nevertheless, the aforementioned increase was likely

within uncertainty and should be interpreted with caution. At $z^+ = 125$ and $x = 7\delta$, the number of short CMRs ($L_{ex} = 0.2\delta$) also decreased while number of wide CMRs ($W_m = 0.275\delta$) increased, similar to the $H = 0.2\delta$ case.

Surprisingly, the aforementioned trends for short CMRs was also observed at $z^+ = 300$, despite FPIV runs showing little effect on incoming CMRs. Streamwise autocorrelations ($\Delta y = 0$) at $z^+ = 300$ also showed a slight increase in correlation values for $\Delta x > 0.5\delta$ at $x = 7\delta$ downstream of the $H = 0.05\delta$ array, but the increase was within uncertainty. The increase again may be related to increased streamwise alignment of flow structures. This may be caused by the downwash effect induced at the cylinder tips, such that faster moving fluid was drawn in on average from planes above, therefore, possibly affecting flow structures there.

Spanwise scales were affected minimally by the $H = 0.05\delta$ array, different from the $H = 0.2\delta$ case. Spanwise autocorrelations hardly showed any effects of the perturbation. Although the dominant spanwise mode distribution at $x = 7\delta$ and $z^+ = 125$ did shift towards larger spanwise wavelengths. This seems to indicate increased spanwise scales compared to the unperturbed flow, which may relate to the preferential shifting of incoming CMRs. No effects were observed at $z^+ = 300$. Therefore, the $S = 0.6\delta$ and $H = 0.05\delta$ array was less effective at manipulating spanwise scales. We suspect that this may relate to the difference in spanwise scaling of structures closer to the wall, such that smaller scales were more frequently dominant (see Chapter 3, Fig. 3-25). Therefore, to increase the $H = 0.05\delta$ array's effectiveness on spanwise scales, it may help to reduce the cylinder spacing, for example, $S = 0.4\delta$ or 0.5δ spaced arrays could be more effective at

$z^+ = 125$, based on the distribution of dominant spanwise modes there in the unperturbed flow.

Chapter 6

Summary, conclusions and future work

The objective of this dissertation was to further understanding on perturbation effects by a spanwise array of cylinders on the large-scale flow organization within the logarithmic region. The novelty of the present work lies in the multipronged approach of leveraging the latest flow measurement technology and analyses analysis tools to pursue the aforementioned objective. Multiple PIV acquisition methodologies were used to achieve the aforementioned objective. Stereoscopic PIV data enabled capturing the out-of plane motion at the three discrete measurement planes heights downstream of the cylinder arrays. Wide field planar PIV data supported characterization of long coherent low/high speed zones along the spanwise dimension. The volumetric PTV data allowed for analyses of the correlation between structures across the logarithmic layer. Finally, flying PIV data enabled analyses of the time evolution of the large-scale flow organization, before and after encountering the cylinder array.

Various analyses methodologies were applied to analyze the acquired data. Analyses These included observations derived from instantaneous measurements, statistical comparisons of the mean and rms of velocity fields, and characteristics of flow structures from two point spatial correlations and Fourier analyses. Separately, a feature extraction algorithm was developed to extract statistics relevant to the large-scale flow organization within the logarithmic region (e.g. vortex packets).

6.1 Flow perturbed by array with S = 0.2δ

For S = 0.2δ, both H = 0.2δ and H = δ arrays profoundly affected velocity statistics and structural characteristics of uniform momentum regions downstream throughout the logarithmic layer.

Large-scale flow structures throughout the boundary layer were either disrupted or weakened by the H = δ array, while structures above the logarithmic layer persisted through the H = 0.2δ array. Furthermore, tip structures significantly influenced the flow within the logarithmic layer downstream of the H = 0.2δ array, while having no influence downstream of the H = δ array. The aforementioned differences resulted in different relaxation behavior downstream of the two arrays, where flow features recover from the bottom up downstream of the H = δ array, while possibly following a top down mechanism in the H = 0.2δ case.

Data generated from the feature extraction algorithm successfully captured the differences in recovery trends, lending support to observations derived from visualization of the instantaneous velocity fields. Notably, results generated from the algorithm showed that the number of packet signatures like those in the unperturbed flow recovered first at $z^+ = 125$, downstream of the H = δ array. In contrast, for the H = 0.2δ case, fewer packet signatures like ones in the unperturbed flow were seen until x = 7δ at $z^+ = 125$. The latter result is consistent with previous work (Alving & Fernholz 1996; Rodriguez *et al.* 2016). The lack of recovery downstream of the H = 0.2δ cylinders was likely due to the surviving outer-layer structures, whose influence on the flow close to the wall may have increased due to increased wall-normal interactions generated by the H = 0.2δ

cylinders. Furthermore, the shape of the energy spectrum at $z^+ = 125$ and $x = 7\delta$ resembled shapes of spectra in planes above, also supporting the aforementioned hypothesis.

For the $H = \delta$ case, the bottom-up flow recovery may have been enabled by the weakening and disruption of large outer layer structures, such that outer-inner interactions were weakened. On average, the strength of wall-normal fluctuations downstream of the $H = \delta$ array were reduced. In addition, cross-correlation magnitudes of wall-normal velocity fluctuations across the logarithmic layer were also reduced from unperturbed values which may suggest weaker alignment of movement to and away from the wall. Both effects indicate reduced wall-normal transport, which could have contributed to the weaker influence of the flow in the outer layer.

The bottom up flow recovery mechanism makes physical sense when considering differences between characteristic length and time scales of eddies close to the wall versus the planes above. Eddy scales are smaller with shorter time scales (Smits & Wood 1985) close to the wall. Therefore, they should recover first in the absence of large-scale outer layer influence. Larger scale structures above then must form later through streamwise and spanwise growth mechanisms such as auto-generation, streamwise merging of structures (e.g. Adrian 2000; Zhou 1996 & 1999; Kim, Sung, Adrian 2008; Jodai & Elsinga 2016), and spanwise merging (e.g. Wark & Nagib 1989; Tomkins & Adrian 2003; Gao 2011; Lee & Sung 2011).

Nevertheless, although flow features resembling those in unperturbed flow were observed close to the wall starting at $x = 1.8\delta$ at $z^+ = 125$, then later at $z^+ = 300$ starting at $x = 3.8\delta$, characteristic streamwise and spanwise scales remained altered up to $x = 7\delta$ throughout

the logarithmic layer. Streamwise length scales were reduced, and the energy contained in the 0.6δ spanwise mode was decreased. Furthermore, the spanwise distribution of alternating high and low momentum zones remained altered up to x = 7δ downstream of the H = δ array.

6.2 Flow perturbed by array with S = 0.6δ

Changes to velocity statistics and flow features downstream of the S = 0.6δ arrays were smaller than in the S = 0.2δ cases, as the blockage was reduced significantly. In spite of this, the flow organization downstream of the S = 0.6δ, H = 0.2δ array was profoundly affected up to 7δ downstream. In contrast, the effects of the H = 0.05δ array were quite limited due to the further reduction in blockage.

The wakes of the H = 0.2δ cylinders re-aligned incoming high and low speed zones into specific spanwise locations, in addition to possibly reducing the tendency of low and high speed zones to meander along the spanwise dimension downstream. Downstream of the H = 0.2δ array, high and low speed zones were re-aligned with cylinder locations and regions between them respectively. This phenomenon affected long coherent momentum regions (CMRs) ($L_{ex} > 0.5\delta$) more than short CMRs ($L_{ex} < 0.5\delta$), as demonstrated statistically through a modified version of the feature extraction algorithm. As a result of the re-alignment, the energy in the 0.6δ spanwise mode corresponding to the dominant spanwise mode in the logarithmic layer of the unperturbed flow (Hutchins *et al.* 2005; Zheng & Longmire 2014) was increased throughout the log layer, lasting up to 7δ downstream and likely beyond. Furthermore, streamwise autocorrelations magnitudes were increased in the range $\Delta x > 0.5\delta$, although feature extraction counts showed no

increase in structures longer than $L_{ex} > 0.5\delta$. Therefore, the increased autocorrelation values must be from existing flow structures being better aligned along the streamwise direction.

Measurable effects downstream of the $S = 0.6\delta$, $H = 0.05\delta$ array, although considerably weaker did extend above the array height to $z^+ = 300$. The average wake splitting at $z^+ = 125$ at the $H = 0.05\delta$ cylinder tips was more apparent than at $z^+ = 500$ downstream of the $H = 0.2\delta$ array tips, likely due to the increased influence of the tip structures from a reduction in the cylinder aspect ratio (Sumner *et al.* 2004). Moreover, the larger turbulence intensity levels to begin with at $z^+ = 125$, could have led to increased wall-normal transport, which may contribute to the aforementioned difference.

At $z^+ = 300$, RMS values initially increased to a maximum at $x = 2.9\delta$, then decayed to the unperturbed value. Beginning $x = 3.8\delta$, averaged streamwise velocities slightly increased and remained so to $x = 7\delta$. Long CMRs ($L_{ex} > 0.5\delta$) were also observed to align preferentially downstream of the $H = 0.05\delta$ array tips ($z^+ = 125$), similar to the $H = 0.2\delta$ case. Although, structural analyses did not show a statistically significant effect. These results suggested that the mechanism driving enhancement of the natural spanwise mode in the $S = 0.6\delta$, $H = 0.2\delta$ array still persisted, although its effects were weaker. No obvious changes to the characteristic spanwise scales were observed anywhere downstream. On the other hand, characteristic streamwise scales were decreased immediately downstream of the array at $z^+ = 125$, before becoming slightly increased at $x = 7\delta$, again possibly due to enhanced streamwise alignment.

6.3 Future work

As with many turbulent flow studies, analysis of the data generated from the present study raises more questions than the dataset provides answers for.

For the S = 0.2δ array, results showed two distinct recovery mechanisms between the H = δ and H = 0.2δ cylinders. Downstream of the H = δ cylinders, measurements can be acquired beyond 7δ to better capture the upward propagation of the relaxation of boundary layer structure to the top of the logarithmic layer. The effects of relaxation within the logarithmic layer appear to propagate upwards at an angle of 1.2° (based on minimum location of the number of swirls). This suggests that relaxation ought to be observed by 9δ at z^+ = 500. Results of Rodríguez-López *et al.* (2016) corroborated the aforementioned estimate, when scaling their reported streamwise location where canonical properties of their perturbed boundary layer were recovered downstream of their high AR cylinders, with the boundary layer thickness in the region immediately downstream of their perturbation.

Separately, it would be interesting to consider a case where the S = 0.2δ cylinder tips are located in the outer layer, but not all the way to the top of the boundary layer thickness. In such a case, the tip effects should be felt much later close to the wall. How would the flow at z^+ = 125 respond to this array? Would the recovery still be suppressed? Or would it recover from bottom up? Another alternative to modifying the tip structures would be to alter the geometry of the obstacles, for example, rounding off the tips of the cylinders, or using conical spikes/tapered cylinders to minimize tip effects.

As for the S = 0.6δ array, it would be interesting to acquire volumetric measurements including the flow above the H = 0.2δ cylinders. Volumetric measurements showed that LMRs extended across the logarithmic layer in unperturbed flow. In instances where LMRs were preferential re-aligned, what happens to structures that extend significantly away from the wall and above the array? Do they also respond with a similar migration following the movement of structures in planes below? Or do they get disconnected?

Furthermore, a significant gap remains in the literature concerning the nature of the cylinder tip structures, especially in the case where the cylinder is fully immersed in a turbulent boundary layer. Moreover, the instantaneous characteristics of these tip structures, including their formation, propagation and interaction with the Karman-vortices, base vortices, and the surrounding flow are presently lacking. Therefore, volumetric measurements of the near-field, possibly including the entire cylinder structure would be very insightful in quantifying the aforementioned effects.

For the shorter S = 0.6δ array, present results suggest that the perturbations were weak, therefore, adding an additional row of cylinders with the same height could increase the perturbation effects downstream, or perhaps extend its influence on the flow above.

Bibliography

Acarlar MS, Smith CR (1987) A study of hairpin vortices in a laminar boundary layer. Part 1. Hairpin vortices generated by a hemisphere protuberance. *J. Fluid Mech*. 175: 1-41

Adrian RJ (2007) Hairpin vortex organization in wall turbulence. *Physics of Fluids*. 19: 041301

Adrian RJ, Balachandar S, Lin ZC (2001) Spanwise growth of vortex structure in wall turbulence. *KSME Int. Journal* 15: 1741-1749

Adrian RJ, Meinhart CD, Tomkins CD (2000) Vortex organization in the outer region of the turbulent boundary layer. *J. Fluid Mech*. 422: 1-54

Agostini L, Leschziner MA (2014) On the influence of outer large-scale structures on near-wall turbulence in channel flow. *Physics of Fluids* 26: 075107

Alving AE, Fernholz HH (1996) Turbulence measurements around a mild separation bubble and downstream of reattachment. *J. Fluid Mech*. 322: 297 – 328

Baars WJ, Hutchins N, Marusic I (2017) Reynolds number trend of hierarchies and scale interactions in turbulent boundary layers. *Philosophical Transactions of the Royal Society A.* 375:20160077

Bechert DW, Bruse M, Hage W, Meyer R (2000) Fluid mechanics of biological surfaces and their technological application. *Naturwissenschaften* 87:157-171

Bechert DW, Bruse M, Hage W, Van Der Hoeven JGT, Hoppe G (1997) Experiments on drag-reducing surfaces and their optimization with an adjustable geometry. *J. Fluid Mech.* 338:59 – 87

Belcher SE, Jerram N, Hunt JCR (2003) Adjustment of a turbulent boundary layer to a canopy of roughness elements. *J. Fluid Mech*. 488: 369 – 398

Bernardini M, Pirozzoli S (2011) Inner/outer layer interactions in turbulent boundary layers: A refined measure for the large scale amplitude modulation mechanism. *Physics of Fluids*. 23(6)

Bogard DG, Tiederman WG (1986) Burst detection with single-point velocity measurements. *J. Fluid Mech*., 162: 389-413

Boiko AV, Kornilov VI (2009) On the vertical large eddy breakup device capability to decrease the turbulent drag. *Thermophysics and Aeromechanics* 16(4)

Castro IP, Cheng H, Reynolds R (2006) Turbulence over urban-type roughness: deductions from wind tunnel measurements. *Boundary-Layer Meteorology* 118:109-131

Castro IP, Epik E(1998) Boundary layer development after a separated region. *J. Fluid Mech.* 374: 91-116

Christensen KT, Adrian RJ (2001) Statistical evidence of hairpin vortex packets in wall turbulence. *J. Fluid Mech.* 431: 433–443

Clauser FH (1954) Turbulent boundary layers in adverse pressure gradients. *J. Aero Sci.* 21: 91-108

Coceal O, Dobre A, Thomas TG, Belcher SE (2007) Structure of turbulent flow over regular arrays of cubical roughness. *J. Fluid Mech.* 589: 375-409

Corino ER, Brodkey RS (1969) A visual investigation of the wall region in turbulent flow. *J. Fluid Mech*., 37:1-30

Corke TC, Guezennec Y, Nagib HM, (1981) Modification in drag of turbulent boundary layers resulting from manipulation of large- scale structures. *NASA CR* – 3444

De Silva CM, Woodcock JD, Hutchins N, Marusic I (2016) Influence of spatial exclusion on the statistical behavior of attached eddies. *Physical Review Fluids* (1): 022401

Dennis DJC, Nickels TB, (2011) Experimental measurement of large-scale three-dimensional structures in a turbulent boundary layer. Part 1. vortex packets. J. *Fluid Mech.* 673:180 – 219

Einian M, Bergstrom DJ, Sumner D (2010) Numerical simulation of the flow around a surface-mounted square cylinder. In: *Proceedings of the ASME 2010 3rd Joint US-European Fluids Engineering Summer Meeting and 8th International Conference of Nanochannels, Microchannels, and Minichannels (FEDSM2010-ICNMM2010),* August 1-5, Montreal QC, Canada. 30394

Elsinga GE, Adrian RJ, van Oudheusden BW, Scarano F (2010) Three-dimensional vortex organization in a high-Reynolds number supersonic turbulent boundary layer. *J. Fluid Mech*. 644: 35-60

Elsinga GE, Kuik DJ, van Oudheusden BW, Scarano F (2007) Investigation of the three-dimensional coherent structures in a turbulent boundary layer with Tomographic-PIV. In: *45th AIAA Aerospace Sciences Meeting and Exhibit*, Reno, Nevada.

Falco RE (1977) Coherent motions in the outer region of turbulent boundary layers. *Physics of Fluids*, 20, S124

Flack KA, Schultz MP (2014) Roughness effects on wall-bounded turbulent flows. *Physics of Fluids* 26(10)

Flack KA, Schultz MP, Shapiro TA (2005) Experimental support for Townsend's Reynolds number similarity hypothesis on rough walls. *Physics of Fluids*. 17(3)

Ganapathisubramani B, Hutchins N, Hambleton WT, Longmire EK, Marusic I (2005) Investigation of large-scale coherence in a turbulent boundary layer using two-point correlations. *J. Fluid Mech.*, 524:57-80

Ganapathisubramani B, Hutchins N, Monty JP, Chung D, Marusic I (2012) Amplitude and frequency modulation in wall turbulence. *J. Fluid Mech.* 712:61-91

Ganapathisubramani B, Longmire EK, Marusic I (2003) Characteristics of vortex packets in turbulent boundary layers. *J. Fluid Mech.* 478: 35-46

Gao Q (2011) Evolution of eddies and packets in turbulent boundary layers. *PhD Thesis* University of Minnesota

Gao Q, Ortiz-Dueñas C, Longmire EK (2011) Analysis of vortex populations in turbulent wall-bounded flows. *J. Fluid Mech.* 678:87–123.

Gao Q, Ortiz-Dueñas C, Longmire EK (2013) Evolution of coherent structures in turbulent boundary layers based on moving Tomographic PIV. *Exp. Fluids.* 54:1625.

Garcia-Mayoral R, Jimenez J (2011) Drag reduction by riblets. *Phi. Trans. R. Soc. A.* 369: 1412-1427

Goldstein D, Handler R, Sirovich L (1995) Direct numerical simulation of turbulent flow over a modelled riblet covered surface. *J. Fluid Mech.* 302:333-376

Guala M, Metzger M, Mckeon BJ (2011) Interactions within the turbulent boundary layer at high Reynolds number. J. *Fluid Mech.* 666: 573-604

Guala M, Tomkins CD, Christensen KT, Adrian RJ (2012) Vortex organization in a turbulent boundary layer overlying sparse roughness elements. *Journal of Hydraulic Research* 50:465–481.

Hama FR, (1954) Boundary layer characteristics for smooth and rough surfaces. *Trans.Soc.Naval Archit.Marine Engre* 62: 333-358

Hama FR, Long JD, Hegarthy JC (1957) On transition from laminar to turbulent flow. *J. Appl. Phys* 28-4:388-394

Hambleton WT (2007) Experimental study of coherent events in laminar and turbulent boundary layers. *PhD Thesis*, University of Minnesota

Head MR, Bandyopadhyay P (1981) New aspects of turbulent boundary-layer structure. *J. Fluid Mech.*,107: 297-338

Hefner JN, Anders JB, Bushnell DM (1983) Alteration of outer flow structures for turbulent drag reduction. *AIAA Journa*l 83-0193

Hutchins N, Choi KS (2002) Towards a greater understanding of turbulent skin friction reduction. In: *Proceedings of ASME Fluid Engineering Conference*, Montreal, Quebec, Canada

Hutchins N, Ganapathisubramani B, Marusic I (2005) Spanwise periodicitiy and the existence of very large scale coherence in turbulent boundary layers. *4th International Symposium on Turbulence and Shear Flow Phenomena*, Williamsburg, Virginia.

Hutchins N, Marusic I (2007a) Evidence of very long meandering features in the logarithmic region of turbulent boundary layers. *J. Fluid Mech* 579: 1-28

Hutchins N, Marusic I (2007b) Large-scale influences in near-wall turbulence. *Philosophical Transactions of the Royal Society A.* 365: 647-664

Jacobi I, McKeon BJ (2011) New perspectives on the impulsive roughness-perturbation of a turbulent boundary layer. *J. Fluid Mech.* 677:179–203

Jiménez J (1998) The largest scales of turbulent wall flows. *CTR Annual Research Briefs*

Jiménez J (2004) Turbulent Flows Over Rough Walls. *Annu. Rev. Fluid Mech.* 36:173–196.

Jodai Y, Elsinga GE (2016) Experimental observation of hairpin auto-generation events in a turbulent boundary layer. *J. Fluid Mech.* 795:611-633.

Kawamura T, Hiwada M, Hibino T, Mabuchi T, Kumada M (1984) Flow around a finite circular cylinder on a flat plate. *Bulletin of the JSME* 27:2142-2150

Kevin, Monty JP, Bai HL, Pathikonda G, Nugroho B, Barros JM, Christensen KT, Hutchins N (2017) Cross-stream stereoscopic particle image velocimetry of a modified turbulent boundary layer over directional surface pattern. *J. Fluid Mech.* 813: 412-435

Kim K, Sung HJ, Adrian RJ (2008) Effects of background noise on generating coherent packets of hairpin vortices. *Physics of Fluids* 20(10)

Kim KC, Adrian RJ (1999) Very large-scale motion in the outer layer. *Physics of Fluids.* 11(2)

Kline SJ, Reynolds WC, Schraub FA, Rundstadler PW (1967) The structure of turbulent boundary layers. *J. Fluid Mech.* 30: 741-773

Lee J, Lee JH, Choi J, Sung HJ (2014) Spatial organization of large and very large scale motions in a turbulent channel flow. *J.Fluid Mech.* 749: 818-840

Lee JH, Sung HJ (2011) Very-large-scale motions in a turbulent boundary layer. *J. Fluid Mech.* 673:80 – 120

Lee SJ, Kim HB (1999) Laboratory measurements of velocity and turbulence field behind porous fences. *Journal of Wind Engineering and Industrial Aerodynamics* 80:311-326

Lee SJ, Lee SH (2001) Flow field analysis of a turbulent boundary layer over a riblet surface. *Exp Fluids.* 30: 153-166

Lin J, Laval JP, Foucaut JM, Stanislas M (2008) Quantitative characterization of coherent structures in the buffer layer of near-wall turbulence. Part 1: streaks. *Exp. Fluids*. 45:999-1013.

Marusic I (2001) On the role of large-scale structures in wall turbulence. *Physics of Fluids.* 13(3)

Marusic I, Mathis R, Hutchins N (2010) High Reynolds number effects in wall turbulence. *International Journal of Heat and Fluid Flow.* 31: 418 – 428

Marusic I, Perry AE (1995) A wall-wake model for the turbulence structure of boundary layers. Part 2. Further experimental support. *J. Fluid Mech.* 298: 361-388

Mathis R, Hutchins N, Marusic I (2009) Large-scale amplitude modulation of the small-scale structures in turbulent boundary layers. *J. Fluid Mech.* 628: 311-337

Mathis R, Marusic I, Hutchins N, Sreenivasan KR (2011) The relationship between the velocity skewness and the amplitude modulation of the small scale by the large scale in turbulent boundary layers. *Physics of Fluids* 23: 121702

Meinhart CD, Adrian RJ (1995) On the existence of uniform momentum zones in a turbulent boundary layer. *Physics of Fluids.* 7(4)

Monty JP, Allen JJ, Lien K, Chong MS (2011) Modification of the large scale features of high Reynolds number wall turbulence by passive surface obtrusions. *Exp. Fluids* 51: 1755-1763

Nolan KP, Zaki TA (2013) Conditional sampling of transitionary boundary layers in pressure gradients. *J. Fluid Mech.* 728: 306-339

Nugroho B, Hutchins N, Monty JP (2013) Large-scale spanwise periodicity in a turbulent boundary layer induced by highly ordered and directional surface roughness. *International Journal of Heat and Fluid Flow,* 41:90-102

Offen GR, Kline SJ (1975) A proposed model of the bursting process in turbulent boundary layers. *J. Fluid Mech.,* 70(2):209-228

Ortiz-Dueñas C, Ryan MD, Longmire EK (2011) Modification of Turbulent Boundary Layer Structure Using Immersed Wall- Mounted Cylinders. In: *Proc. Turbulent Shear Flow Phenomena VIII*, Ottawa

Park CW, Lee SJ (2000) Free end effects on the near wake flow structure behind a finite circular cylinder. *Journal of Wind Engineering and Industrial Aerodynamics.* 88: 231-246

Park CW, Lee SJ (2003) Flow structure around two finite circular cylinders located in an atmospheric boundary layer: side-by-side arrangement. *Journal of Fluids and Structures.* 17: 1043-105

Pattenden RJ, Turnock SR, Zhang X (2005) Measurements of the flow over a low-aspect-ratio cylinder mounted on a ground plane. *Exp. Fluids.* 39: 10-21

Perry AE, Chong MS (1982) On the mechanism of wall turbulence. *J. Fluid Mech.* 119: 173-217

Plesniak MW, Nagib HM (1985) Net drag reduction in turbulent boundary layers resulting from optimized manipulation. In*: AIAA Shear Flow Control Conference, Boulder, CO,* Paper No. AIAA-85-0518, March 12-14

Pope SB (2000) Turbulent flows. Cambridge University Press

Robinson SK (1991) Coherent motions in the turbulent boundary layer. *Annual Review of Fluid Mechanics*., 23:601-639

Robinson SK, Kline SJ, Spalart PR (1989) A review of quasi-coherent structures in a numerically simulated turbulent boundary layer. *NASA Technical Memorandum,* 102191

Rodríguez-López E, Bruce PJK, Buxton ORH (2016) Near field development of artificially generated high Reynolds number turbulent boundary layers. *Physical Review Fluids* 1:074401

Rodríguez-López E, Bruce PJK, Buxton ORH (2016) On the formation mechanisms of artificially generated high Reynolds number turbulent boundary layers. *Boundary-Layer Meteorology* 160:201-224

Ryan MD (2011) Planar and volumetric measurements downstream of cylinders immersed in a turbulent boundary layer. *Master's Thesis*, University of Minnesota.

Ryan MD, Ortiz-Dueñas C, Longmire EK (2011) Effects of simple wall-mounted cylinder arrangements on a turbulent boundary layer. *AIAA Journal* 49(10):2210–2220

Saikrishnan N, Marusic I, Longmire EK (2006) Assessment of dual plane PIV measurements in wall turbulence using DNS data. *Exp Fluids*. 41:265 – 278

Sakamoto H, Arie M (1983) Vortex shedding from a rectangular prism and a circular cylinder placed vertically in a turbulent boundary layer. *J. Fluid Mech.* 126:147-165

Savill AM, Mumford JC (1988) Manipulation of turbulent boundary layers by outer-layer devices: skin-friction and flow-visualization results. *J. Fluid Mech.* 191:389-418

Schofield WH, Logan E (1990) Turbulent shear flow over surface mounted obstacles. *Journal of Fluid Engineering* 112:376 – 385

Schröder A, Geisler R, Staack K, Elsinga GE, Scarano F, Wieneke B, Henning A, Poelma C, Westerweel J (2011) Eulerian and Lagrangian views of a turbulent boundary layer flow using time-resolved Tomographic PIV. *Exp. Fluids.* 50:1071-1091

Smits AJ, Wood DH (1985) The response of turbulent boundary layers to sudden perturbations. *Ann. Rev. Fluid Mech* 17: 321-58

Sillero JA, Jiménez J, Moser RD (2013) One-point statistics for turbulent wall-bounded flows at Reynolds numbers up to $\delta+ \sim 2000$. *Physics of Fluids* 25:105102

Smith CR, Walker JDA, Haidari AH, Sobrun U (1991) On the dynamics of near-wall turbulence. *Phil. Trans. R. Soc. Lond. A* 336:131-175

Squire DT, Morill-Winter C, Hutchins N, Schultz MP, Klewicki JC, Marusic I (2016) Comparison of turbulent boundary layers over smooth and rough surfaces up to high Reynolds numbers. *J. Fluid Mech.* 795: 210 – 240

Stellmacher M, Obermayer K (2000) A new particle tracking algorithm based on deterministic annealing and alternative distance measures. *Exp. Fluids* 28: 506-518.

Sumner D (2013) Flow above the free end of a surface-mounted finite-height circular cylinder: A review. *Journal of Fluids and Structures*. 43: 41-63

Sumner D, Heseltine JL, Dansereau OJP (2004) Wake structure of a finite circular cylinder of small aspect ratio. *Exp. Fluids* 37: 720-730

Sumner D, Wong SST, Price SJ, Païdoussis MP (1999) Fluid behavior of side-by-side circular cylinders in steady cross-flow. *Journal of Fluid Structures*. 13: 309-338

Tan YM, Longmire EK (2015) On the reorganization of perturbed hairpin packets in a turbulent boundary layer. In: *Proceedings 11th International symposium on particle image velocimetry*, Santa Barbara, CA

Tan YM (2014) Effects of an array of cylinders immersed in a turbulent boundary layer. *Master's Plan B Report*. University of Minnesota.

Tomkins CD (2001) The structure of turbulence over smooth and rough walls. *PhD Thesis*, University of Illinois at Urbana Champaign

Tomkins CD, Adrian RJ (2003) Spanwise structure and scale growth in turbulent boundary layers. *J. Fluid Mech.* 490: 37-74

Tomkins CD, Adrian RJ (2005) Energetic spanwise modes in the logarithmic layer of a turbulent boundary layer. *J. Fluid Mech.*, 545:141-162

Townsend AA (1976) The structure of turbulent shear flows. 2nd ed. Cambridge University Press.

Tutkun M, George WK, Delville J, Stanislas M, Johansson PBV, Foucaut JM, Coudert S (2015) Two-point correlations in high Reynolds number flat plate turbulent boundary layers. *Journal of Turbulence.* 10: 1-23

Vanderwel C, Ganapathisubramani B (2015) Effects of spanwise spacing on large-scale secondary flows in rough-wall turbulent boundary layers. *J.Fluid Mech.* 774: R2

Volino RJ, Schultz MP, Flack KA (2007) Turbulence structure in rough and smooth wall boundary layers. *J. Fluid Mech.* 592: 263-293

Wallace JM, Eckelmann H, Brodkey RS (1972) The wall region in turbulent shear flow. *J. Fluid Mech.*, 54: 39-48

Walsh, MJ (1980) Drag characteristics of V-groove and transverse curvature riblets. Viscous drag reduction (ed. Hough GR). *AIAA*

Walsh, MJ (1990) Riblets. Viscous drag reduction in boundary layers. *AIAA.* A91-12688 02-34

Wang HF, Zhou Y, Chan CK, Lam KS (2006) Effect of initial conditions on interaction between a boundary layer and a wall-mounted finite length cylinder wake. *Physics of Fluids*. 18: 065106

Wark CE, Nagib HM (1989) relation between outer structures and wall-layer events in boundary layers with and without manipulation. *Proc. 2nd IUTAM Symp. on Structure of Turbulence and Drag Reduction*, Zurich Switzerland (ed. A.Gyr). Springer, pp 467-474

Wark CE, Nagib HM (1990) Relation between outer structure and wall layer events in boundary layers with and without manipulation. In *structure of turbulence and drag reduction* ed A.Gyr Springer-Verlag Berlin

Wark CE, Naguib MA, Nagib HM (1990) Effect of plate manipulators on coherent structures in a turbulent boundary layer. *AIAA Journal*. 28-1877

Wilkinson SP, Anders JB, Lazos BS, Bushnell DM (1988) Turbulent drag reduction research at NASA Langley – progress and plans. *International Journal of Heat and Fluid Flow* 9:266-277

Woodcock JD, Marusic I (2015) The statistical behavior of attached eddies. *Physics of Fluids* 27:015104

Wu Y, Christensen KT (2006) Population trends of spanwise vortices in wall turbulence. *J. Fluid Mech.* 568: 55–76.

Wu Y, Christensen KT (2010) Spatial structure of a turbulent boundary layer with irregular surface roughness. *J. Fluid Mech.* 655: 380–418

Yajnik KS, Acharya M (1979) Non-equilibrium effects in a turbulent boundary layer due to the destruction of large eddies. *Structure & Mechanisms of Turbulence.* Vol 1: 249. Lect. Notes in Phys. No. 76, Springer-Verlag.

Zheng S, Longmire EK (2014) Perturbing vortex packets in a turbulent boundary layer. *J. Fluid Mech.* 748:368–398

Zhou J, Adrian RJ, Balachandar S (1996) Autogeneration of near-wall vortical structures in channel flow. *Physics of Fluids*, 8(1)

Zhou J, Adrian RJ, Balachandar S, Kendall TM (1999) Mechanisms for generating coherent packets of hairpin vortices in channel flow. *J. Fluid Mech.* 387:353–396